APPLICATION AND DEVELOPMENT OF FINITE ELEMENT TECHNIQUES FOR TRANSDUCER DESIGN AND ANALYSIS

by

CLIVE BAYLISS

A thesis submitted to the
Faculty of Engineering
of the
University of Birmingham,
for the degree of
Doctor of Philosophy

School of Electronic and Electrical Engineering
The University of Birmingham
Birmingham B15 2TT
England

July 1998

SYNOPSIS

Ocean acoustic tomography (OAT) is a method for mapping the physical characteristics of the world's oceans. This technique enables the properties of a region of ocean – its temperatures, salinities, densities, and current speeds – to be inferred by measuring the propagation times of pulses transmitted between an array of transducers that surround the region. Central to the development of OAT is the availability of low frequency (< 500 Hz), low Q (< 4), light (< 250 kg), and efficient (> 50 %) sound sources that can operated at depths in excess of 500 m.

Following a review of transducer motor and flextensional transformer technologies, the class I flextensional transducer driven by a piezoelectric ceramic stack is selected as being suitable for OAT. Finite element (FE) techniques are applied to the design of this transducer. By observing the change in pertinent performance characteristics of the device in response to altering various design parameters a set of design rules is established. In applying these rules an OAT projector has been designed. A scaled prototype has been constructed and the measured performance characteristics concur with FE predictions. Based on these results a full-scale device is expected to meet the requirements for an OAT projector, with the exception of weight, though this has to be verified.

In order to accurately determine the performance characteristics of a transducer it is essential to know the phenomena that limit the acoustic power output of the transducer; these could be one or more of the following: (a) cavitation, (b) electrical failure, (c) mechanical failure, (d) thermal failure. Power limitations arising from (a) or (b) can be determined from empirical data, whilst those arising from (c) or (d) are best determined using numerical methods. FE software is readily obtainable for assessing the mechanical behaviour of transducers, however, no commercial software is currently available for determining thermal behaviour. To this end new FE software has been developed and applied to the analysis of various transducers. Experimental results are presented to validate the accuracy of this new software.

ACKNOWLEDGEMENTS

I would like to take this opportunity to thank Dr. D. T. I. Francis for his guidance and support. I would also like to acknowledge Prof. R. F. W. Coates, Dr. L. S. Wang, Mr. R. Stoner, and other members of the Acoustics Group for providing many enlightening discussions. Of immense help was the technical support provided by Mr. K. Slade and other employees of the mechanical workshop in the construction and assembly of the 2.5 kHz partially free-flooded class I flextensional transducer. I would also like to acknowledge the enthusiastic general technical support provided by Mr. A. Yates. Finally, I would like to express gratitude to P. Ericson at Reson System in Denmark for the construction of the 5 kHz air-backed class I flextensional transducer.

This study has been supported by the University of Birmingham and by the European Communities under the LOFTOMO (Low Frequency Transducer for Ocean Acoustic Tomography) contract MAS2-CT91-0010-C.

CONTENTS

Appendices

Chapter 1

INTRODUCTION

1.1 Motivation

Since the early 1980s the design and development of low-frequency, high-power, underwater acoustic sound sources has become a high priority for the oceanographer as well as for the military. In the field of antisubmarine warfare, the effectiveness of passive sonar detection systems has diminished due to advances in the acoustic quietening of submarines. This has led to interest in low-frequency active detection systems operating in the frequency range between 100 Hz and 1 kHz. Also new fields in oceanography, involving the circulation patterns of the world's oceans, have started to be investigated. One technique being employed is ocean acoustic tomography, which provides information on sound speed as well as other physical parameters in oceanic basins; another is the tracking of freely drifting floats over very long distances, for the analysis of deep oceanic water circulation. Central to the development of these techniques is the availability of low-frequency sound sources.

This thesis will be concerned mainly with the application of numerical methods in the development of low-frequency transducers. The main motivation for research is the lack of suitable transducers that can fulfil all the performance requirements for tomographic applications.

Classically the design of transducers has relied on the use of a lumped-element approach. The method relies on the basic assumption that the transducer can be represented by a number of mass elements interconnected by springs and dampers. By recognising that these mechanical components can be transformed into equivalent electrical components, it is possible to represent the transducer by an equivalent electrical circuit. Standard network analysis can then be applied to obtain design factors such as resonance frequency, bandwidth, acoustic power output, and efficiency.

Derivation and computation of the various parts of an equivalent circuit requires a detailed knowledge of the electrical and elastic properties of all parts of the vibrating system. This is fairly easy to do for a transducer of simple geometry; however, for many low-frequency transducers which employ flexing motions or cavity resonances the task becomes significantly more difficult and analysis is best carried out using numerical methods. Even when an equivalent circuit has been generated it might not be a very good representation of the behaviour of the transducer under all circumstances. This is evident even with simplistic transducer designs. Furthermore, equivalent circuits cannot provide information about the mechanical or acoustic behaviour of transducers.

In the last decade the application of finite element (FE) techniques to the design of underwater acoustic transducers has progressively increased. This is essentially due to the increasing availability of powerful personal computers. FE analysis can provide the designer with a wealth of accurate data regarding the behaviour of a transducer. In addition to the electrical response of the transducer, information is obtained about the acoustic and mechanical behaviour.

A number of FE software packages are commercially available, some of which are dedicated to the design of underwater transducers. Also many research groups in the public sector (for example, universities) involved in underwater acoustics have their own software. The Acoustics Group at the University of Birmingham is no exception, having two such packages available, TransCAD which can model axi-symmetrical structures, and the more powerful PHOEBE which can model 3-dimensional structures. Thus, we can make use of existing software to aid in the transducer design process.

Another important area of transducer design involves determining the maximum power that a given design can handle. This is crucial if the specification of a transducer is to be accurately defined. The maximum acoustic power output of a transducer will be limited either by the properties of the acoustic medium or the internal features of the design. More specifically the limitation will be dictated by one of the following: (a) cavitation, (b) electrical failure, (c) mechanical failure, or (d) thermal failure. The phenomenon of cavitation gives rise to the formation of gas bubbles in the water medium at the vibrating surface of the transducer. This has a severely detrimental effect on the operation of the transducer and is best avoided. The theoretical cavitation limit can be readily calculated. However, the threshold can be much higher

than the theoretical limit and typically the limit is determined from empirical data. Electrical limits are imposed by dielectric breakdown. The limiting potential is particularly difficult to define and one usually relies on the previous experience of transducer designers. Mechanical limitations are caused by fatigue failure, and this implies calculating the dynamic stresses within the transducer. However, the fatigue limit of materials is known to be affected by the presence of static stresses. These may be present due to deformation of the transducer caused by hydrostatic pressure, or thermomechanical stresses. To this end it is necessary to calculate the static and dynamic stresses within a transducer, both of which are best tackled using numerical methods. Finally, thermal limitations are imposed by materials which are effected by heat; for example, glue joints commonly used in transducers will begin to denature at 80 °C. Heat is generated by losses within the components of the transducer. This will give rise to an increase in temperature within the transducer, which if excessive could limit the maximum power output. Obviously the extent of this temperature rise depends on the heat-transfer design of the transducer. Here two problems have to be solved. Firstly the heat generated within the components of the transducer will need to be determined and secondly, the resulting temperature rise will need to be derived. Again these are most easily tackled using numerical methods.

Typically, the previously mentioned commercial packages can be used to calculate the stresses within a transducer, though maybe not thermomechanical stresses. However, at the time of writing the author is not aware of a commercially available software package that can analyse the thermal behaviour of a transducer. In fact the author is only aware of one paper which describes the modelling of heat dissipation and resulting thermal evolution in transducers using FE techniques [1.1], although the results presented were not verified experimentally.

Thus, a further area for research is the power limitations of transducers, especially the investigation of thermal behaviour.

1.2 Ocean Acoustic Tomography

A complex structure of motions, driven by winds, solar heat and tides, is continually at play in the ocean interior. The motions range from current and tidal patterns of planetary scale, through inter-mediate scale processes like internal waves, to small scale turbulence of sub-millimetre size. An appreciation of this complex and multi-connected system must form the basis of any understanding of the oceans.

The components of the general circulation of the ocean are known as meso and gyre scale phenomena. Gyre scale phenomena are large rotating circulation patterns of roughly 1000 km in extent. Within these massive areas of swirling water there can be found smaller mesoscale phenomena of 100 km in size. By analogy to the atmosphere, the mesoscale variability may be likened to ocean weather.

The ocean circulation is difficult to monitor with conventional oceanographic instruments because of its large spatial extent and slow time scales of variation. Even for an area as small as 1 square megametre (1000 km x 1000 km), several full-time vessels, or several hundred fixed moorings, are required.

To overcome the difficulties of conventional techniques, W. Munk and C. Wunsch proposed in 1979 that tomography be adapted to measuring the physical properties of the ocean [1.2]. The technique consists of measuring the travel time of acoustic sound pulses between multiple points which are interpreted to provide information about the intervening ocean (figure 1.1) – its temperatures, salinities, densities, and current speeds.

The travel time of the pulses is proportional to the average sound speed and can be inverted to reveal the intervening sound speed structure. Simultaneous transmission between two points permits measurement of currents; the difference in travel times between signals propagating in opposite directions is proportional to the average component of water velocity.

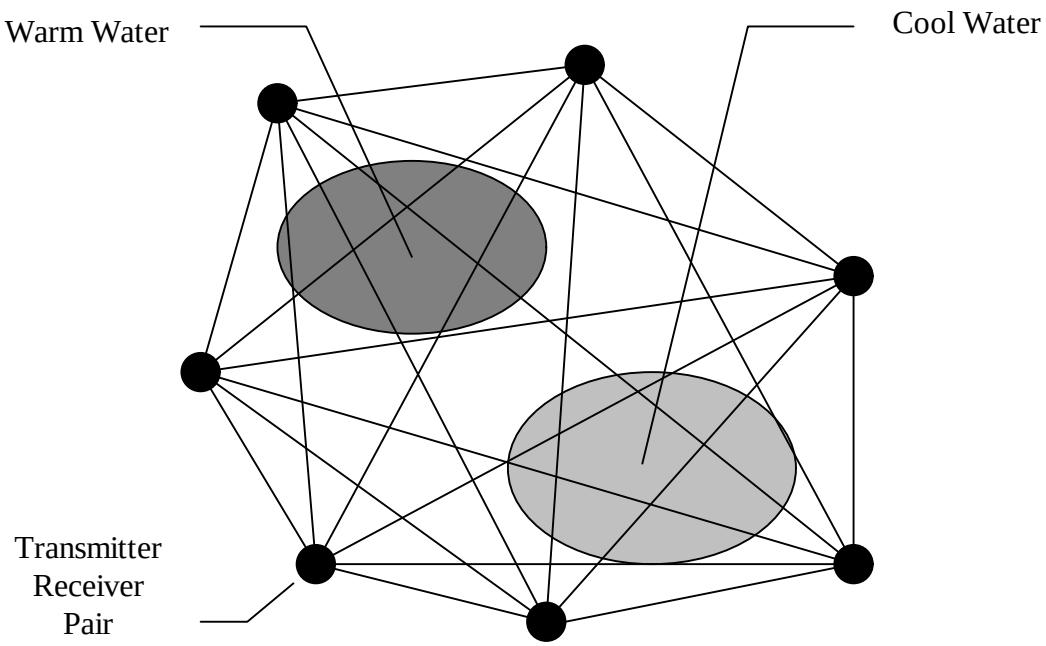

Figure 1.1. Transmitters pulse acoustic energy to receivers along many paths. Inhomogeneities in the ocean alter the sound speed causing variability in travel time of the pulses. Inversion algorithms allow the derivation of a sound speed map.

Horizontal resolution is determined solely by the distribution of moored transmitter and receiver pairs; the amount of data increases as the square of the number of moorings. Vertical resolution arises naturally as a consequence of the ocean's vertical sound speed profile [1.3]. The speed of sound is a function of temperature, salinity, and pressure. In mid-latitudes sound speed initially decreases with depth as the ocean temperature drops until the effects of pressure reverse the trend, where the effects of salinity are second order. The resulting sound channel, or waveguide created by the temperature inversion, is known as the SOFAR channel. The sound travels by a variety of ray paths connecting a source and receiver, known as multipath propagation. Each multipath follows a unique course through the ocean, and thus each has a unique arrival time and arrival angle.

Observation of a wide sea area requires the use of low-frequency sound sources to prevent significant signal attenuation. High frequencies, in the order of kilohertz, are rapidly attenuated by chemical processes and molecular motions in the water. Signals above 10 kHz can barely be detected at 10 km; in contrast, those below 100 Hz can easily cover thousands of kilometres without significant energy losses. Unfortunately, low-frequency sound sources tend to be large,

heavy, cumbersome devices, with equally undesirable transmission characteristics. Moreover these devices are prohibitively expensive.

1.3 Transducer Design Criteria

The lack of suitable acoustic sources has been cited [1.4, 1.5] as perhaps the most important factor limiting wider application of ocean acoustic tomography. Such sources need to operate at low frequencies over a large bandwidth to facilitate good multipath resolution, both of which are difficult to realise in a compact device. High power operation for improved signal-to-noise ratio with good efficiency for prolonged battery operation are of secondary importance. A further consideration is the ability of the device to operate at depth, between 500 and 2000 metres [1.6].

M. Letiche, *et al.*, [1.7] propose the following specification for ocean acoustic tomography sources.

- Centre frequency 250 Hz – 500 Hz
- Operating depth > 500 m
- Total mass < 250 kg
- Q-factor < 4
- Source level > 190 dB re 1 μPa @ 1 m
- Efficiency > 50%

The work in this these was carried out as part of a wider project, LOFTOMO (Low Frequency Transducer for Ocean Acoustic Tomography); initial work by the partners identified three likely technologies – capped ring, Janus-Helmholtz, and flextensional. The University of Birmingham was tasked with investigating the last of these. Thus, this thesis will consider only this form of low frequency projector.

1.4 Objectives

Ocean acoustic tomography is a means to determine the physical characteristics of the world's oceans. Central to the development of this technique is the availability of low-cost acoustic transducers with adequate transmission characteristics. In the past a general lack of design rules for such transducers, stemming largely from the complex nature of the behaviour of the devices

themselves, has limited the capability of generating good acoustic signals into the water for tomographic applications.

The main aim of this research is to use FE techniques to design an ocean acoustic tomography source that matches or improves upon the specification proposed by M. Letiche, *et al*. [1.7]. The initial design process will make use of established FE techniques. The assessment of the cause of power limitation within the transducer will require the development of new software to determine if thermal effects are significant. This software will use FE techniques to compute the power dissipated within the various components of the transducer and the resulting thermal temperature rise under continuous waveform (CW) operation.

To achieve these aims a number of goals will have to be attained, namely to

- review the currently available flextensional transducer designs which could be adapted for use as an ocean acoustic tomography source,
- analyse the most suitable transducer technology using the numerical software, PHOEBE, and establish the influence of the main design parameters on the performance characteristics,
- review the causes of power limitations in piezoelectric transducers and develop a general method, using finite element techniques, for determining whether power will be thermally limited,
- analyse the thermal behaviour of the transducer using the developed software,
- construct prototype devices to confirm the validity of the numerical methods.

1.5 Thesis Outline

The remainder of the thesis is arranged as follows.

Chapter Two—At the heart of any electro-acoustic transducer is a mechanism for converting electrical energy into mechanical energy. In this chapter the principle transduction mechanisms, or motor technologies, suitable for low-frequency transducers are examined, namely, piezoelectric, electrostrictive, and magnetostrictive transduction.

Chapter Three—Reviews current flextensional transformer technologies. The purpose of the transformers is to improve the coupling from the high impedance motor to the low impedance water load. This has the effect of reducing the quality factor and hence increasing the transmission bandwidth.

Chapter Four—Introduces the established finite element and boundary element techniques that, when combined, form a powerful tool for the electrical, mechanical, and acoustic analysis of transducers.

Chapter Five—Describes the modelling of a class I flextensional transducer. Results are presented that indicate the dependence of the transducer's performance on various design parameters.

Chapter Six—Reports on the engineering considerations which effect the design of class I flextensional transducers.

Chapter Seven—A design is proposed which satisfies the frequency, acoustic power output, quality factor, but not weight or depth, for the projector specification of M. Letiche, *et al*., [1.7]. Experimental data from a prototype device is compared with performance characteristics predicted from numerical modelling.

Chapter Eight—A second design is proposed which may overcome depth limitations at the expense of weight. Experimental data from a prototype device is compared with performance characteristics predicted from numerical modelling.

Chapter Nine—Reviews the various phenomena that limit the power output of piezoelectric transducers. Methods for accessing the significance of each phenomena, using finite element techniques or estimations, are described.

Chapter Ten—Describes FE techniques that can be used to examine the power dissipated in the various components of a transducer and the resulting thermal effects, namely the flow of heat and distribution of temperature in the steady-state.

Chapter Eleven—The thermal characteristics of two transducers are assessed, namely, a Tonpilz transducer, and a flextensional transducer. The steady-state temperature under CW operation is predicted using FE techniques. These results are compared with experimental findings. Finally, the power limitation mechanisms for each transducer are presented along with an estimate of the maximum acoustic power that may be safely radiated.

Chapter Twelve—Concludes the research presented in the thesis and offers suggestions for further work.

1.6 References

[1.1] W. Steichen, G. Vanderborck, and Y. Lagier, 'Determination of Power Limits of a High Frequency Transducer Using the Finite Element Method', in *Power Sonics and Ultrasonic Transducers Design*, B. Hamonic and J.-N. Decarpigny, Eds., (Springer-Verlag, 1988), 160-174.

[1.2] W. Munk and C. Wunsch, 'Ocean Acoustic Tomography: A Scheme for Large Scale Monitoring', *Deep-Sea Research*, 26, 123-161, (1979).

[1.3] R. J. Urick, *Principles of Underwater Sound*, 3rd Edition, (McGraw-Hill Book Company, 1983), 111-120.

[1.4] R. C. Spindel and P. F. Worcester, 'Ocean Acoustic Tomography Programs: Accomplishments and Plans', *Proc. OCEANS '90*, 1-10, (1990).

[1.5] P. F. Worcester, B. D. Cornuelle, and R. C. Spindel, 'A Review of Ocean Acoustic Tomography: 1987-1990', *Reviews of Geophysics*, Supplement, 557-570, (1991).

[1.6] R. Person, 'Transducer Needs for Oceanography', in *Proc. Power Transducers for Sonics and Ultrasonics*, B. F. Hamonic, O. B. Wilson, and J.-N. Decarpigny, eds. (Springer-Verlag, 1991), 14-21.

[1.7] M. Letiche, R. Coates, S. Marselli, L. Bjørnø, and P. Eriksen, 'Low Frequency Transducers for Ocean Acoustic Tomography', in *Proc. Underwater Acoustics*, L. Bjørnø, ed., (European Commission, 1994), Vol. 1, 531-536.

Chapter 2

MOTOR TECHNOLOGIES

2.1 Introduction

At the heart of any electro-acoustic transducer is a mechanism for converting electrical energy to mechanical energy (table 2.1), and vice versa.

Suitable materials must be able to expand or contract under the control of an external stimulus. Generally materials with these properties fall into two categories, defined by whether they are stimulated by an electric field or a magnetic field. The material's response to the stimulus is either linear or quadratic, depending on whether mechanical strain is directly proportional or proportional to the square of the applied electrical signal respectively. If the electrical signal is sinusoidal of the form

$$E(t) = E_e \cos(\omega t) \tag{2.1}$$

a square-law material produces a strain proportional to

$$E(t) = \left[E_e \cos(\omega t)\right]^2 \tag{2.2}$$

The response is not sensitive to the direction of the applied electrical signal and thus varies at twice the applied frequency.

Table 2.1. Electro-mechanical mechanisms.

Electric field types		Magnetic field types	
Type	Response	Type	Response
Piezoelectric	Linear	Electrodynamic	Linear
Dielectric	Quadratic	Electromagnetic	Quadratic
Electrostrictive	Quadratic	Magnetostrictive	Quadratic

If signal distortion is acceptable, square-law materials can simply be driven at a frequency of one half the required frequency. However, a near-linear response can be obtained by applying a biasing quantity E_o to the sinusoidal signal. This 'polarises' the strain response of the material, which becomes proportional to,

$$\left[E_o + E_e \cos(\omega t)\right]^2 = E_o^2 + 2E_e E_o \cos(\omega t) + E_e^2 \cos^2(\omega t) \tag{2.3}$$

If E_o is large in comparison to E_e then the final term of equation (2.3) can be ignored and quasi-linear operation is obtained.

In this chapter piezoelectricity, electrostriction, and magnetostriction are described (for an overview see [2.1-2.4]). The suitability of materials exhibiting these phenomena are assessed for use as the driving element in flextensional transducers.

2.2 Piezoelectricity

The phenomenon of 'pressure electricity' was first observed by Pierre and Jacques Curie in the 1880s [2.5] (for history see [2.6-2.8]). They showed that when certain types of crystals are deformed by mechanical pressure they develop electrical potentials. This behaviour, which is spontaneous in several natural or manmade crystals such as quartz or Rochelle-salt, is due to the crystalline structure. Mechanical action provokes the appearance of an electrical dipole in each crystalline unit cell of the material by shifting the centres of the positive and negative charges, as shown in figure 2.1.

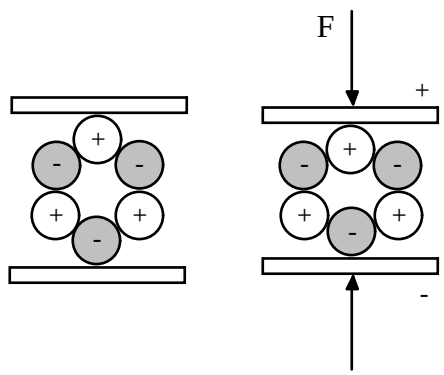

Figure 2.1. Piezoelectric action in Rochelle-salt showing separation of charge centres under stress.

This is the direct piezoelectric effect. Conversely, when an electric field is applied to a crystal it undergoes a physical deformation. This is the converse piezoelectric effect and is a thermodynamic consequence of the direct effect.

Besides the crystals mentioned above, an important group of piezoelectric materials are the piezoelectric ceramics [2.9, 2.10]. These were originally investigated in the early 1950s because of their ferroelectric properties. A ferroelectric material has a spontaneous electric polarisation, due to a lack of symmetry in its ionic structure, which can be reversed by an applied electric field. As a consequence, the material has a high dielectric constant and exhibits hysteresis. This behaviour is analogous to that of ferromagnetic materials, and hence ceramic piezoelectric materials are typically referred to as ferroelectric materials. In contrast to naturally occurring piezoelectric crystals, ferroelectric ceramics are polycrystalline materials with the perovskite crystal structure – a tetragonal/rhombhedral structure very close to a cubic.

Many processes are involved in the production of piezoelectric ceramics. The raw materials, in powdered form, are mixed together and then heated to form a compound. This process is commonly referred to as ‘calcing’. The calcined powder is then ground into very fine particles that are moulded into the desired shape. This requires the addition of a binding agent which holds the particles together prior to firing.

Ceramic particles may be formed into many shapes, including bars, plates, discs, rings, cylinders, and hemispheres. The formed shape is then bisque-fired at low temperatures in order to drive-out the binder and provide some mechanical strength. The second firing, or ‘high firing’ completes the chemical bonding of the constituent materials. Electrodes are applied to the desired surfaces, and a final firing bonds the electrode material to the ceramic surfaces.

At this stage the ceramic may be regarded as a mass of minute crystallites, randomly oriented. The ceramic material is therefore isotropic and will exhibit no piezoelectric effect because of this random orientation.

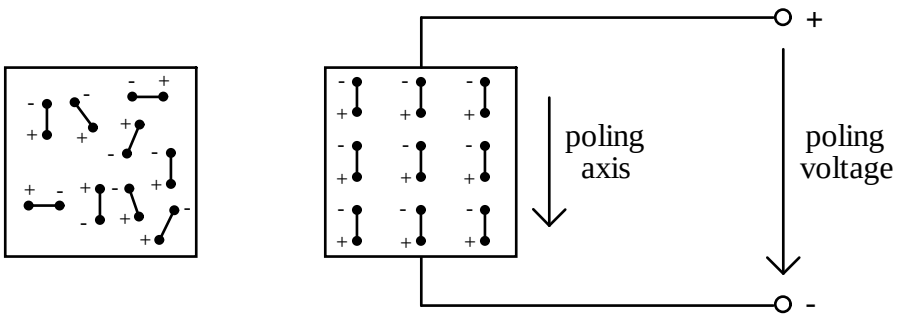

(a) (b)

Figure 2.2. Electric dipoles in the piezoelectric material (a) before and (b) after polarisation (ideal conditions).

For each ceramic material there exists a characteristic Curie temperature. Above the Curie temperature electric dipoles inside the material exist in random orientations. The material becomes paraelectric. By exploiting this property ceramic materials can be made piezoelectric in a chosen direction by a 'poling' process. The ceramic is heated in a dielectric oil bath and a large electric field is applied across its electrodes. This results in an aligning of the dipoles within the material in the direction most closely aligned with the field. Figure 2.2 shows how the poling process affects the ceramic (ideal conditions).

The poling process in piezoelectric ceramics is susceptible to ageing or the loss of piezoelectric sensitivity with time. Like other forms of decay, piezoelectric ageing is a logarithmic function of time and the exact rate defines the change in the material parameters per decade.

2.2.1 Piezoelectric Relationships

The combined mechanical and electrical behaviour of piezoelectric material [2.1-2.3, 2.7, 2.11] is defined by

$$\{S\} = \left[s^E\right]\{T\} + \left[d\right]^{\mathrm{T}}\{E\} \tag{2.4a}$$

$$\{D\} = \left[d\right]\{T\} + \left[\varepsilon^T\right]\{E\} \tag{2.4b}$$

where $\{S\}$ is the stress vector, $\{T\}$ is the strain vector, $\{E\}$ is the electric field strength vector,

$\{D\}$ is electric flux density vector, [s] is the elastic compliance matrix, [d] is the piezoelectric strain matrix, and [ε] is the dielectric matrix.

Alternatively, with strain and electric field as the independent variables, the equations may be written as

$$\{T\} = \left[c^E\right]\{S\} - [e]^{\mathrm{T}}\{E\} \tag{2.5a}$$

$$\{D\} = [e]\{S\} + \left[\varepsilon^S\right]\{E\} \tag{2.5b}$$

where [e] is a piezoelectric stress matrix.

Further forms exist, taking other combinations of quantities as independent variables [2.3, 2.7].

2.2.2 The Piezoelectric Coupling Coefficient

The performance of a piezoelectric ceramic is commonly rated according to its coupling coefficient [2.12], which indicates the ability of the material to convert electrical energy into mechanical energy. The coupling coefficient k is defined as the ratio of mutual elastic and dielectric energy density U_m to the geometric mean of the elastic strain energy density U_e and the dielectric energy density U_d:

$$k = \frac{U_m}{\sqrt{U_e U_d}} \tag{2.6}$$

This is typically in the order of 50 per cent. The coupling coefficient should not be confused with efficiency, which is often in excess of 90 per cent. Nevertheless, when converting electrical to mechanical energy, it is desirable to use materials with high coupling coefficients.

The total energy density is defined as,

$$U = \tfrac{1}{2}\{S\}\{T\} + \tfrac{1}{2}\{D\}\{E\} \tag{2.7}$$

Using equations (2.4a, 2.4b), equation (2.7) may be written as,

$$U = \tfrac{1}{2}\{T\}^{\mathrm{T}}\left[s^E\right]\{T\} + \tfrac{1}{2}\left(\{T\}^{\mathrm{T}}[d]\{E\} + \{E\}^{\mathrm{T}}[d]\{T\}\right) + \tfrac{1}{2}\{E\}^{\mathrm{T}}\left[\varepsilon^T\right]\{E\} \tag{2.8}$$

or

$$U = U_e + 2U_m + U_d \tag{2.9}$$

As an example consider a piezoelectric material, such as PZT-4, manufactured in ring form and poled in the 3- or z-direction. The coupling coefficient of interest is

$$k_{33} = \frac{d_{33}}{\sqrt{\varepsilon_{33}^{T} s_{33}^{E}}} \tag{2.10}$$

2.2.3 Properties of Piezoelectric Ceramics

Poled ferroelectric ceramics follow the same elasto-electric matrix as class 6*mm* crystals from the hexagonal system [2.7]. This class has one sixfold axis of symmetry (taken to be along the polarisation direction) and six symmetry planes parallel to that axis. Thus the elastic matrix has the following form,

$$\begin{bmatrix} s_{11} & s_{12} & s_{13} & 0 & 0 & 0 \\ s_{12} & s_{11} & s_{13} & 0 & 0 & 0 \\ s_{13} & s_{13} & s_{33} & 0 & 0 & 0 \\ 0 & 0 & 0 & s_{44} & 0 & 0 \\ 0 & 0 & 0 & 0 & s_{44} & 0 \\ 0 & 0 & 0 & 0 & 0 & 2(s_{11} - s_{12}) \end{bmatrix} \tag{2.11}$$

the piezoelectric constant matrix has the form,

$$\begin{bmatrix} 0 & 0 & 0 & 0 & d_{15} & 0 \\ 0 & 0 & 0 & d_{15} & 0 & 0 \\ d_{31} & d_{31} & d_{33} & 0 & 0 & 0 \end{bmatrix} \tag{2.12}$$

and the dielectric constant matrix has the form,

$$\begin{bmatrix} \varepsilon_{11} & 0 & 0 \\ 0 & \varepsilon_{11} & 0 \\ 0 & 0 & \varepsilon_{33} \end{bmatrix} \tag{2.13}$$

There are many ceramic compositions used today. The properties of these compositions can vary significantly from one manufacturer to the next. Additionally, fluctuations occur from batch to batch and even within a given batch. This is due to slight chemical differences, variations in density, inhomogeneous chemical compositions, variation in grain size, varying response to the poling treatment, and so forth.

Problems of comparing products from different ceramic manufactures led to the development of a military specification for transducer ceramics. This classifies ceramics into four basic types,

Type I Hard lead zirconate-titanate with a Curie temperature equal to or greater than 310ºC

Type II Soft lead zirconate-titanate with a Curie temperature equal to or greater than 330ºC

Type III Very hard lead zirconate-titanate with a Curie temperature equal to or greater than 330ºC

Type IV Barium titanate with nominal additives of 5 percent calcium titanate and 0.5 percent cobalt carbonate as necessary to obtain a Curie temperature equal to or greater than 100ºC

The terms ‘hard’ and ‘soft’ refer to the composition type. Hard materials are not easily poled or de-poled except at elevated temperatures. This stability is accompanied by low dielectric loss and makes these materials particularly suitable for projector which run at high continuous power levels. Soft materials are more readily poled or de-poled. They have high electro-mechanical coupling coefficients but also high dielectric loss, making these materials suitable for hydrophones, or pulsed projectors requiring high acoustic output. Table 2.2 lists typical low signal data for the Navy Type piezoelectric ceramic compositions at room temperature (25 °C).

The principal disadvantage of piezoelectric ceramic materials occurs when they are used at low frequencies. At these frequencies their capacitive nature means they posses a high impedance, and this requires a large transformer to be used to provide the high drive voltage and inductance needed to match the static capacitance of the ceramic. In addition, piezoelectric ceramic materials are brittle (good compressive strength and poor tensile strength) and must be operated under compressive pre-stress so that they are never subject to tension, even at highest drive levels.

Table 2.2. Properties of Navy Type Ceramics. Values are typical low signal levels at 25 °C and are taken from references [2.3, 2.7] and Vernitron, Ltd. data sheets.

		Navy Type			
		I	II	III	IV
		Vernitron Type			
		PZT-4™	PZT-5A™	PZT-8™	Ceramic-B™
Parameter	Units				
k_p		(-)0.58	(-)0.60	(-)0.50	(-)0.33
k_{31}		(-)0.33	(-)0.34	(-)0.30	(-)0.19
k_{33}		0.70	0.70	0.64	0.48
k_{15}		0.71	0.68	0.55	0.48
k_t		0.51	0.48	0.48	0.38
$\varepsilon_{33}^{T} / \varepsilon_0$		1300	1700	1020	1200
$\varepsilon_{33}^{S} / \varepsilon_0$		635	830	582	910
$\varepsilon_{11}^{T} / \varepsilon_0$		1475	1730	1291	1300
$\varepsilon_{11}^{S} / \varepsilon_0$		730	916	898	1000
d_{31}	10^{-12} C N^{-1}	-123	-171	-97.4	-58
d_{33}		289	374	225	149
d_{15}		496	584	333	242
s_{11}^{E}	10^{-12} m^2 N^{-1}	12.3	16.4	11.5	8.6
s_{12}^{E}		-4.05	-5.74	-3.38	-2.6
s_{13}^{E}		-5.31	-7.22	-4.69	-2.7
s_{33}^{E}		15.5	18.8	13.5	9.1
s_{44}^{E}		39.0	47.5	31.9	22.2
s_{66}		32.7	44.3	27.8	22.4
e_{31}	C m^{-2}	-5.2	-5.4	-4.0	-3.1
e_{33}		15.1	15.8	13.8	13.5
e_{15}		12.7	12.3	10.4	10.9
c_{11}^{E}	10^{10} N m^{-2}	13.9	12.1	13.7	15.8
c_{12}^{E}		7.78	7.52	6.97	6.9
c_{13}^{E}		7.43	11.1	7.16	6.75
c_{33}^{E}		11.5	7.54	12.4	15.0
c_{44}^{E}		2.56	2.11	3.14	4.5
c_{66}		3.06	2.26	3.37	4.5
Density	10^3 kg m^{-3}	7.5	7.75	7.6	5.555
Q_m		500	75	1000	400
Q_e		250	50	250	170
Curie point	°C	328	365	300	115
T_{max}	°C	200	250	175	—
Heat Capacity	J kg^{-1} °C^{-1}	420	420	420	500
Thermal Conductivity	W m^{-1} °C^{-1}	2.1	1.5	2.1	2.5

2.3 Electrostriction

Electrostriction is a second order effect found in almost all dielectric material. The phenomenon is very pronounced in the class of dielectrics known as ferroelectrics. Due to a lack of symmetry in the ionic structure of these materials, electric dipoles are formed spontaneously. These dipoles have a preferred orientation within certain localised regions or domains. Usually, under normal conditions, the domains are randomly oriented throughout the material and the overall electric moment is zero. On application of an electric field the domains rotate towards the direction of the field. Since the unit cell length of the structure is slightly longer along the dipole direction than in the orthogonal directions, there is an accompanying expansion parallel to the field axis. Application of a reverse field also results in an expansion of the material. Figure 2.3 shows that the curve of strain against field strength approximately follows a square law, until saturation begins to limit the strain.

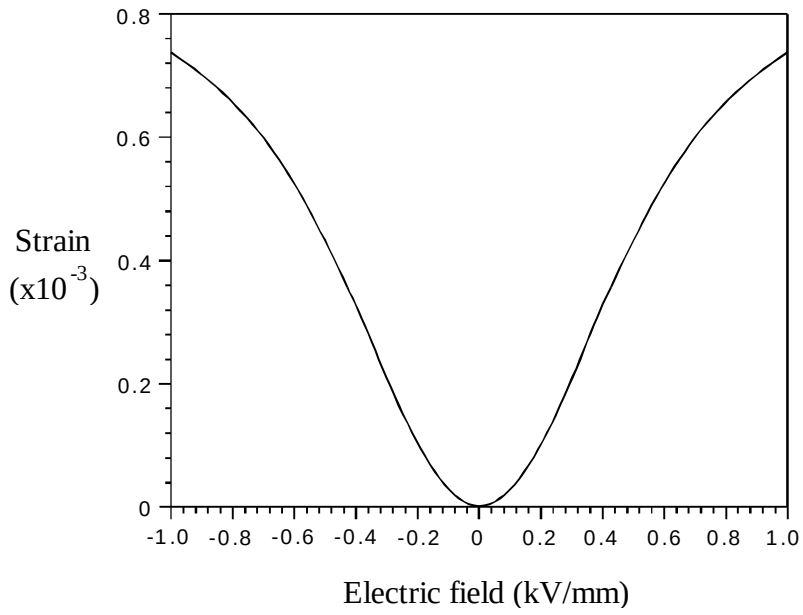

Figure 2.3. Strain vs. electric field for electrostrictive ceramic ESC-1 [2.13].

A quasi-linear response is achieved by applying a steady electric field. This shifts the material's response to a portion of the strain vs. electric field curve that is reasonable linear. Once polarised, the properties of electrostrictive materials are similar to those of piezoelectric materials and equations (2.4-2.12) may be used to describe their behaviour. However, since the value of ε is dependent on the intensity of the bias field the constants *d* and *e* must be specified for a given field strength.

2.3.1 Properties of Electrostrictive Ceramics

Electrostrictive ceramics offer the possibility of greater power output per unit volume than piezoelectric ceramics. This is due to the high maximum strain (approximately 4 times that of a piezoelectric ceramic, and akin with 'giant' magnetostrictive materials [2.14]). Electrostrictive ceramics can be shaped into disks, plates, and rings using conventional manufacturing techniques. In addition, electrostrictive materials do not have a remnant polarisation, they do not require poling and can therefore be fabricated into non-conventional shapes.

Temperature affects the permitivity and dielectrical loss ($\tan \delta_e$) in electrostrictive ceramics. The permitivity rises with increasing temperature to a maximum, at which point the electrical losses decrease dramatically (figures 2.4 and 2.5 respectively).

Both piezoelectric and electrostrictive ceramics require a high drive voltage. Thus the transformer requirements for low frequency operation adds significantly to the overall weight. Electrostrictive ceramics introduce a further complication in that a d.c. bias must be supplied in parallel with the a.c. drive to achieve a near linear output.

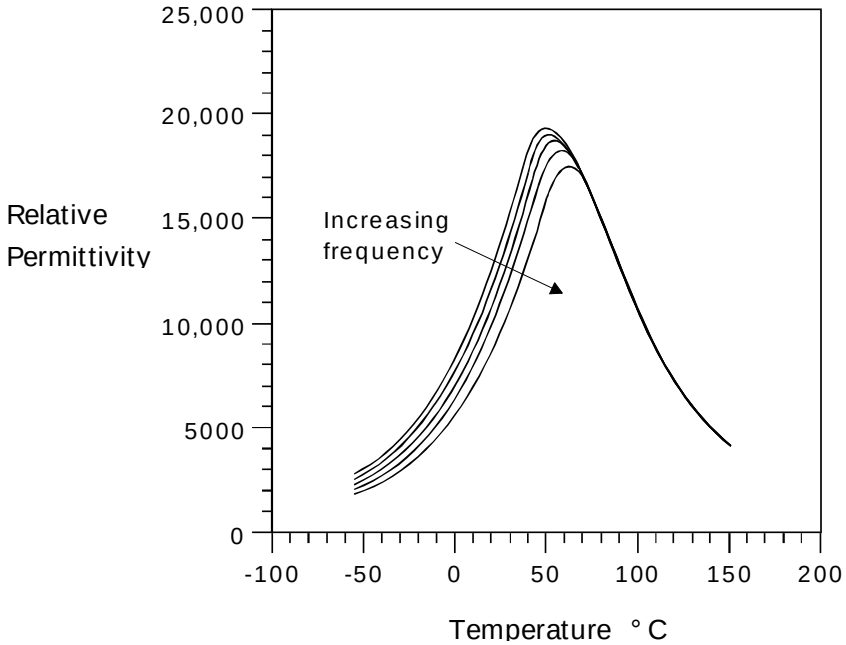

Figure 2.4. Relative permittivity vs. temperature for electrostrictive ceramic ESC-1 [2.13].

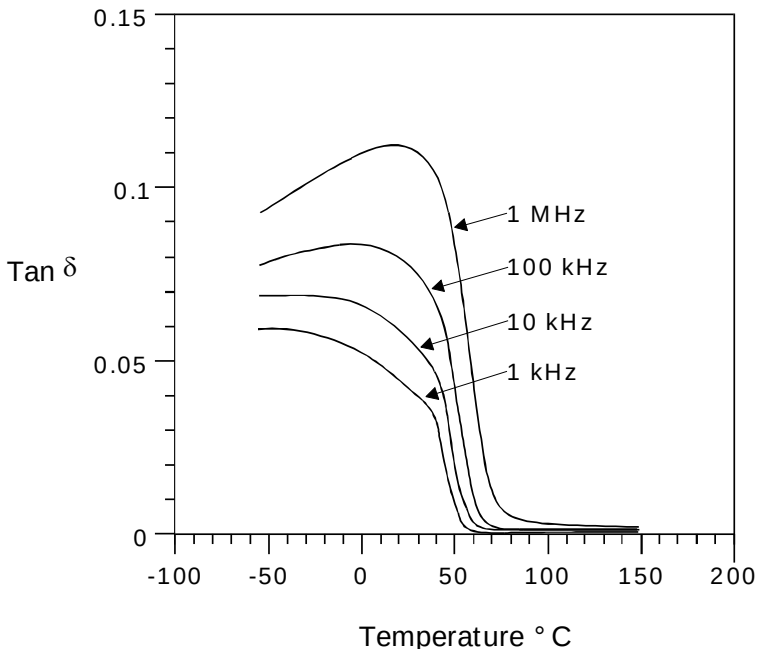

Figure 2.5. Electric loss factor vs. temperature for electrostrictive ceramic ESC-1 [2.13].

2.4 Magnetostriction

The magnetostrictive effect was first observed by C. Page in 1837 and studied quantitatively by J. Joule in the 1840s. However, the phenomenon was not used in any significant way until the 1930s and 1940s when it became important in the construction of sonar projectors.

Before the 1950s the magnetostrictive effect exhibited by the ferromagnetic metal nickel, and alloys of nickel, cobalt, and iron (e.g. Permendur) was predominately exploited as the driving element in sonar transducers. With the discovery of the piezoelectric qualities of barium-titanate and lead-zicronate-titanate, polarised ferroelectric ceramics quickly replaced other forms of transducer material. However, the development of 'giant' magnetostrictive rare earth materials [2.15, 2.16] has prompted further investigation into their potential to supersede piezoelectric ceramic materials in low-frequency transducer designs [2.17-2.22].

Research in the early 1970s at the Naval Ordinance Laboratory (NOL) (now NSWC) in America resulted in the discovery that the maximum strains exhibited by binary alloys composed of certain rare earth elements and iron, known as 'Terfenol' ($TbFe_2$), were 10 to 100 times greater than that of nickel (table 2.3). However, due to the large magnetocrystalline anisotropy of Terfenol the application of large magnetic fields is required to realise the high strains. The addition of dysprosium to the original formulation of Terfenol produces a ternary alloy, known as 'Terfenol-D' ($Tb_{0.3}Dy_{0.7}Fe_{1.93}$), that exhibits a much lower anisotropy and thus reduces the required drive field.

Ferromagnetic materials are characterised by the formation of magnetic domains, each consisting of a volume of material in which exchange forces cause alignment of magnetic moments in a single direction. In the absence of other forces, this alignment occurs along preferred crystallographic directions. The crystal aligning forces can, however, be overcome by external forces, and the energy needed to do this is called the magneto-crystalline anisotropic energy.

Ferromagnetic materials change in dimension, exhibiting magnetostriction, when individual domains are forced into alignment by an external energy source. This is due to interactions between magnetic moments in adjacent domains. If repulsive, these cause an expansion of the

host material in the direction of repulsion (positive magnetostriction), and if attractive, cause a contraction of host material in the direction of attraction (negative magnetostriction). Figure 2.6 shows possible graphs of strain against field strength, for positive and negative magnetostriction; the curves approximately follow a square law, until saturation begins to limit the strain.

A near-linear strain vs. magnetic field response can be obtained with magnetostrictive materials by applying a constant magnetic bias, and superimposing the drive signal. The magnetic biasing can be supplied by one of two methods, or a combination of both. In the first method, permanent magnets surround the magnetostrictive element; however, this technique is limited to applications that require only a modest biasing field. In the second method, a coil carrying direct current is used to generate the biasing field. A secondary coil, in addition to the drive coil, may be used for this purpose. Alternatively, by addition of a direct current component to the alternating current excitation signal a single coil may be used to generate both the bias and excitation fields.

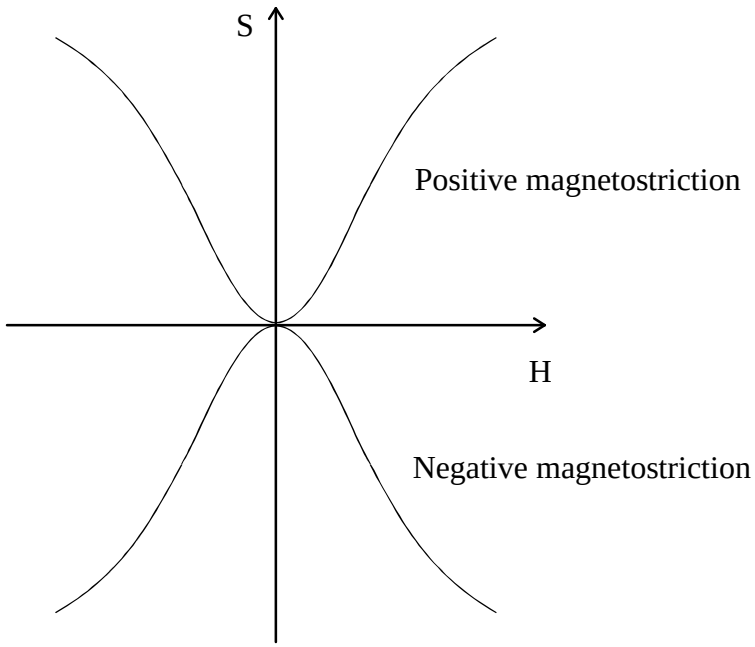

Figure 2.6. Magnetostrictive strain *S* as a function of the magnetic field strength *H*.

2.4.1 Magnetostrictive Relationships

The combined mechanical and magnetic behaviour of polarised magnetostrictive material [2.3, 2.7] is defined by

$$\{S\} = [s^H]\{T\} + [d]^{\mathrm{T}}\{H\} \tag{2.14a}$$

$$\{B\} = [d]\{T\} + [\mu^T]\{H\} \tag{2.14b}$$

where $\{H\}$ is the magnetic field strength vector, $\{B\}$ is the magnetic flux density vector, $[d]$ is the piezomagnetic strain matrix, and $[\mu]$ is the permeabiliy matrix.

Alternatively, with strain and magnetic field as the independent variables, the equations may be written as

$$\{T\} = [c^H]\{S\} - [e]^{\mathrm{T}}\{H\} \tag{2.15a}$$

$$\{B\} = [e]\{S\} + [\mu^S]\{H\} \tag{2.15b}$$

where $[e]$ is a piezomagnetic stress matrix.

Other equations exist, taking other pairs of independent variables [2.3, 2.7].

2.4.2 The Magnetomechanical Coupling Coefficient

As with piezoelectric ceramics, the coupling coefficient is of greatest significance when assessing the potential performance of a magnetostrictive material for transducer applications. It indicates the ability of the material to convert magnetic energy into mechanical energy and vice versa. The coupling coefficient k is defined as the ratio of the mutual energy density W_m to the geometric mean of the elastic energy density W_e and the magnetic field energy W_f,

$$k = \frac{W_m}{\sqrt{W_e W_f}} \tag{2.16}$$

The total energy density is defined as,

$$W = \tfrac{1}{2}\{S\}\{T\} + \tfrac{1}{2}\{B\}\{H\} \tag{2.17}$$

Using equations (2.14a, 2.14b), equation (2.17) may be written as,

$$W = \tfrac{1}{2}\{T\}^{\mathrm{T}}\left[s^{H}\right]\{T\} + \tfrac{1}{2}\left(\{T\}^{\mathrm{T}}[d]\{H\} + \{H\}^{\mathrm{T}}[d]\{T\}\right) + \tfrac{1}{2}\{H\}^{\mathrm{T}}\left[\mu^{T}\right]\{H\} \qquad (2.18)$$

or

$$W = W_e + 2W_m + W_f \qquad (2.19)$$

As an example consider a magnetostrictive material, such as Terfenol-D, which is manufactured in rod form with the cylinder axis along the 3- or z-direction. The cylindrical shape of the material implies that applications will use the longitudinal excitation mode. Thus the coupling coefficient of interest is,

$$k_{33} = \frac{d_{33}}{\sqrt{s_{33}^{H}\mu_{33}^{T}}} \qquad (2.20)$$

2.4.3 Properties of Rare Earth Alloys

As with electrostrictive materials, magnetostrictive rare earth alloys offer the possibility of greater power output per volume of material. This is due to high maximum strain (approximately 4 times that of a piezoelectric ceramic, and akin with electrostrictive materials).

Magnetostrictive materials are driven by current rather than by voltage. Thus they are well suited to modern power amplifiers and can be driven directly through a series matching capacitor. However, the low operating efficiency of magnetostrictive rare earth alloys is the principle factor limiting its wider application. Low efficiency is the result of power losses within the drive material and excitation coil. The most obvious cause of ohmic loss is in the coil where current flowing though the windings produces heat due to the resistivity of the conductor. Losses also occur in the drive material due to eddy currents and hysteresis.

The properties of a ternary alloy of terbium-dysprosium-iron (Terfenol) are compared with other magnetostrictive material in table 2.3.

Table 2.3. Properties of magnetostrictive materials [2.23].

Property	Units	Nickel	Permendur	Terfenol
k_{33} (opt.)		0.15-0.31	0.20-0.37	0.60
d_{33} (opt.)	10^{-9} Wb N^{-1}	-3.1	14-30	—
μ_{33}^{S} / μ_o (opt.)		22	80	4
H (opt.)	10^{2} A m^{-1}	7-10	25	160
c_{33}^{B}	10^{10} Pa	21	22	5
Magnetostrain	10^{-6}	-33	70	1100
Resistivity	ohm m	$7x10^{-8}$	$30x10^{-8}$	$60x10^{-8}$
Density	10^{3} kg m^{-3}	8.8	8.2	9.2
Curie point	°C	358	980	375

2.5 Conclusions

The acoustic power obtained from a given sonar projector is ultimately limited by the energy density of the driver material and its efficiency [2.14]. Energy density is determined for a given material by its Young's Modulus and its induced strain. Effectively this energy density U for electromechanical ceramics is given by,

$$U = \frac{\varepsilon^2 E}{2} \tag{2.21}$$

where strain ε is directly proportional to the effective d_{33} coefficient of the material, and E is the Young's Modulus.

The relative performance of Navy III (piezoelectric material), Terfenol-D (giant magnetostrictive alloy), and PMN-X (electrostrictive material) is compared in table 2.4. It can be seen that Terfenol-D and PMN-X produce far greater strains than the piezoelectric material. However, the desirable properties of both these materials are accompanied by several less desirable traits. Giant magnetostrictive materials are usually afflicted by low efficiencies while electrostrictive ceramics are highly sensitive to temperature and frequency. Both types of material also exhibit a quadratic relationship between strain and field.

Table 2.4. Comparison of the energy densities of sonar driver materials [2.14].

Material	Micro-strain (ε)	Young's modulus (GPa)	Energy Density (J/m^3)
Navy III	250	71	2,200
Terfenol-D	1000	30	15,000
PMN-X	800	70	22,500

The electroacoustic efficiency requirement for an ocean acoustic tomography source is greater than 50 per cent. This favours the use of a piezoelectric or electrostrictive ceramics, rather than magnetostrictive material, for which high efficiencies are more difficult to achieve. Moreover, since the power requirements are moderate, the main advantage of electrostrictive and magnetostrictive materials no longer applies. Thus, for the purpose of this study no overall advantage can be gained by the use of an electrostrictive or magnetostrictive material, and therefore a piezoelectric motor will be used in this research.

The main characteristics that have affected a choice of a motor material for use in flextensional transducers are summarised in table 2.5.

Table 2.5. A comparative assessment of motor materials suitable for driving a flextensional transducers.

Material	Advantages	Disadvantages
Piezoelectric ceramics	• Linear strain response • High efficiency • Low cost	• High impedance
Electrostrictive ceramics	• Large maximum strain • Large energy density • High efficiency	• Quadratic strain response • Temperature and frequency dependent properties • High impedance • High cost
Magnetostrictive rare earth alloys	• Large maximum strain • Large energy density • Low impedance	• Quadratic strain response • Low efficiency • Very brittle • High cost

2.7 References

[2.1] D. Stansfield, *Underwater Electroacoustic Transducers*, (Bath University Press and Institute of Acoustics, 1990), Chapter 3.

[2.2] D. G. Tucker and B. K. Gazey, *Applied Underwater Acoustics*, (Pergamon Press Ltd., 1966), Chapter 5.

[2.3] O. B. Wilson, *Introduction to Theory and Design of Sonar Transducers*, (Peninsula Publishing, 1988), Chapters 3, 4, and 7.

[2.4] F. V. Hunt, *Electroacoustics*, (American Institute of Physics, 1954), Chapter 1.

[2.5] J. Curie and P. Curie, *C. R. Acad. Sci. Paris*, 91, 294 (1880); 91, 383 (1880).

[2.6] W. P. Mason, 'Piezoelectricity, its History and Applications', *J. Acoust. Soc. Am.*, 70(6), 1561-1566, (1981).

[2.7] D. A. Berlincourt, D. R. Curran, and H. Jaffe, 'Piezoelectric and Piezomagnetic Materials and their Function in Transducers', in *Physical Acoustics*, 1(a), W. P. Mason, ed., (Academic Press, 1964), 170-270.

[2.8] C. S. Brown, R. C. Kell, R. Taylor, and L. A. Thomas, 'Piezoelectric Materials: A Review of Progress', *Proc. IEE*, 109(B), 99-114, (1962).

[2.9] D. Berlincourt, 'Piezoelectric Ceramics: Charateristics and Applications', *J. Acoust. Soc. Am.*, 70(6), 1586-1595, (1981).

[2.10] H. Jaffe and D. A. Berlincourt, 'Piezoelectric Transducer Materials', *Proc. IEEE*, 53(10), 1372-1386, (1965).

[2.11] R. C. Dorf, *The Electrical Engineering Handbook*, (CRC Press, 1993), 1087-1097.

[2.12] D. Stansfield, *Underwater Electroacoustic Transducers*, (Bath University Press and Institute of Acoustics, 1990), 49.

[2.13] Morgan Matroc Ltd. (Unilator Division), *Electrostrictive Ceramic (ESC1)*, data sheet, (1993).

[2.14] S. M. Pilgrim, M. Massuda, J. D. Prodey, and J. M. Hock, 'Electrostrictive Sonar Drivers for Flextensional Transducers', in *Transducers for Sonics and Ultrasonics*, M. D. McCollum, B. F. Hamonic, and O. B. Wilson, eds, (Technomic Publishing Co., Inc, 1993), 95-102.

[2.15] R. W. Timme, 'Magnetomechanical Characteristics of a Terbium-Holmium-Iron Alloy', *J. Acoust. Soc. Am.*, 59(2), 459-464, (1976).

[2.16] D. McMasters, 'Magnetostrictive Materials', in *Power Transducers for Sonics and Ultrasonics*, B. Harmonic, O. B. Wilson, and J. N. Decarpigny, eds., (Spring-Verlag, 1991), 125-131.

[2.17] G. A. Steel, 'A 2-kHz Magnetostrictive Transducer', in *Transducers for Sonics and Ultrasonics*, M. D. McCollum, B. F. Hamonic, and O. B. Wilson, eds, (Technomic Publishing Co., Inc, 1993), 250-258.

[2.18] C. J. Purcell, 'Terfenol Driver for the Barrel-Stave Projector', in *Transducers for Sonics and Ultrasonics*, M. D. McCollum, B. F. Hamonic, and O. B. Wilson, eds, (Technomic Publishing Co., Inc, 1993), 160-169.

[2.19] J. R. Oswin and A. Maskery, 'Magnetostriction in Flextensional Transducers', *Proc. I. O. A.*, 9(2), 23-30, (1987).

[2.20] M. B. Moffett, A. E. Clark, M. Wun-Fogle, J. Linberg, J. P. Teter, and E. A. McLaughlin, 'Characterization of Terfenol-D for Magnetostrictive Transducers', *J. Acoust. Soc. Am.*, 89(3), 1448-1455, (1991).

[2.21] R. W. Timme and S. W. Meeks, 'Magnetostrictive Underwater Sound Transducers', *Journal De Physique*, 40(5), 280-285, (1979).

[2.22] G. A. Steel and J. R. Oswin, 'A Magnetostrictive Transducer Design', in *Power Transducers for Sonics and Ultrasonics*, B. Harmonic, O. B. Wilson, and J. N. Decarpigny, eds., (Spring-Verlag, 1991), 152-161.

[2.23] D. Stansfield, *Underwater Electroacoustic Transducers*, (Bath University Press and Institute of Acoustics, 1990), 66-67.

Chapter 3

FLEXTENSIONAL TECHNOLOGIES

3.1 Introduction

The designing of low-frequency, high-power, underwater sound sources poses several difficulties [3.1-3.8]. These are related to the size of the device and the required submergence depth.

In order to obtain sufficient acoustic power, it is common practice to drive the projector around its fundamental resonance frequency, and hence its size is inversely proportional to the working frequency [3.3]. Traditional ultrasonic transducers tend to become prohibitively massive for frequencies lower than 1 kHz. This is especially true of longitudinal vibrators, as demonstrated by Woollett [3.8] and summarised in table 3.1. The large size of these devices, which is a direct consequence of the high stiffness of the piezoelectric ceramic stack, can be significantly reduced by utilising materials with higher compliance such as Terfenol, which has a Young's modulus of approximately one third that of piezoelectric ceramics. A more general technique, however, is to employ transduction mechanisms that utilise flexural or radial modes of vibration.

Table 3.1. The characteristics of the Tonpilz transducer at different design frequencies. In each case, the in-water mechanical Q is equal to 5 and the intensity over the font face is 1 W cm^{-2}.

Resonance frequency (Hz)	Headmass diameter (m)	Total length (m)	Total weight (kg)	Power (W)	Peak displacement (mm)
5000	0.12	0.3	12	113	0.0051
1000	0.6	1.5	1500	2800	0.026
500	1.2	3.0	12000	11300	0.051
100	6	15.0	1500000	280000	0.26

Table 3.2. Pressure release mechanisms for low-frequency transducers.

Depth	Technique
< 100 m	Self-supporting structures
< 200 m	Water-filled bladder
< 1000 m	Compliant tubes in oil
> 1000 m	Liquid filled

The miniaturisation of low-frequency projectors has allowed transducers to have small dimensions compared with the in-water acoustic wavelength of the sound produced. As a consequence the acoustic loading is poor and hence the transfer of mechanical power at the surface of the device is inefficient. This implies a demand for large volume velocities, and thus high electrical and mechanical driving levels. The reduced fluid loading is also associated with narrow bandwidths. To effect the large volume velocities it is preferable for the interior of the transducer to be compliant. This has serious implications when the device has to operate at deep submergence levels. To allow the transducer to withstand the external water pressure some form of pressure equalisation must be used. The chosen mechanism is highly dependent on the submergence depth at which the device must operate. Table 3.2 compares the most common techniques used to combat hydrostatic pressure.

At great depths, in the order of thousands of metres, transducers have to be liquid-filled. The transducer then becomes effectively independent of operating depth. The liquid fill, however, provides essentially no pressure release and this generally has an adverse effect on the electro-acoustic characteristics of the transducer, which can result in a strong decrease in transmission levels, accompanied by a reduced bandwidth. For depths of operation less than a thousand metres, compliant tubes can be integrated with the liquid-filled cavity [3.9-3.11]. The sealed, air-filled, metal oval tubes reduce the effective stiffness of the cavity, which in turn restores adequate acoustic efficiencies. The potential performance improves with decreasing depth, since, with reduced hydrostatic pressure the tubes can be mechanically weaker and hence more compliant.

For modest depths, below 200 m, an internal water bladder can be used [3.12-3.16]. The bladder, which is open to the sea, expands with increasing external water pressure and compresses the internal air, supplying the necessary pressure compensation. At shallow depths of the order of a

hundred metres, it is often possible to eliminate the need for pressure compensation, since the transducer may be structurally strong enough to withstand the hydrostatic pressure unaided [3.17, 3.18].

The name ‘flextensional’ accurately describes the mechanical workings of a subdivision of electroacoustical transducers that are particularly suited to low-frequency operation. At such frequencies the transducer is compact and has a good power-to-weight ratio; they are able to deliver medium-to-high acoustic power at frequencies above 100 Hz. This is due to the mechanical amplification produced by the inherent shape of the mechanical shell, which results in large volume displacements from comparatively small strains in the driving mechanism; that is, electrical excitation of the ceramic stack produces an extensional (and contractional) motion which is transmitted to the surrounding medium through the flexural motion of the shell with a large mechanical amplification. Therefore, in the most general sense, the shell flexes and the stack extends – hence the name flextensional.

The operating frequency of the flextensional transducer is generally the first mechanical resonance of the device, which corresponds to the first symmetrical flexure mode of the shell. At this frequency the dimensions of the transducer are often considerably smaller than the in-water acoustic wavelength and thus the acoustical behaviour of the transducer is that of a non-directive monopole source.

The flextensional concept most commonly consists of a piezoelectric stack, a mechanical shell and, depending on the particular design under consideration, an internal pressure release system. A common requirement is that the shell be slit, or built up from staves to allow the shell to flex easily, thus reducing the resonance frequency and usually increasing acoustic power capability. The piezoelectric stack is generally driven at a frequency lower than its first longitudinal resonance frequency and thus high-drive conditions are sought. As a result, a maximum volume of active material is always required and this can lead to difficulties in obtaining high pre-stress levels: compressive pre-stress is required so that the driver motor is never subjected to tension even at highest drive levels. Classically, pre-stressing is achieved by using a piezoelectric stack that is slightly longer than the inner length of the major axis of the shell. The stack is inserted parallel to the major axis while the shell is mechanically deformed by an external force. On removal of this force the stored energy in the shell applies compressive force to the piezoelectric stack. A

judicious choice of stack length, taking account of the shell stiffness, results in the correct pre-stress value. Alternatively, pre-stress can be obtained by use of tie rods [3.19, 3.20]. These rods are designed to have sufficient static tensile strength without adding more than a small part to the total dynamic stiffness of the vibrating system.

The following chapter reviews the range of flextensional transducers in some detail. The review begins with the pioneering work of H. Hayes and W. J. Toulis. The various forms of the flextensional transducer are then described and the classification schemes used to identify them are reviewed. This is proceeded by an extensive literature review for each type of flextensional transducer. An overview of these and other low-frequency sound sources may be found in references [3.1-3.8].

3.2 The Birth of the Flextensional Transducer

The flextensional transducer concept is often attributed to W. J. Toulis who patented the "Flexural-Extensional Electromechanical Transducer" in 1966 [3.21, 3.22]. However, work by Harvey Hayes, predating Toulis' work by several decades, led to the construction of the first flextensional transducer in 1929. The massive air transducer was built and tested at the Naval Research Laboratories (NRL) under Hayes' guidance. This resulted in a 1936 patent "Sound Generating and Directing Apparatus" [3.23] which describes the theory and design of an archer's 'bow' type of transducer, now known as a class IV flextensional transducer (figure 3.1). This used a magnetostrictive drive mechanism within an oval shell to produce a 'lever' amplification effect. Hayes intended that his electrically driven device would replace the much larger pneumatically driven foghorns of the time. However, the contemporary superiority of the ring transducer resulted in funding being diverted away from flextensional transducer research and this was compounded by a reduction of staff at the NRL.

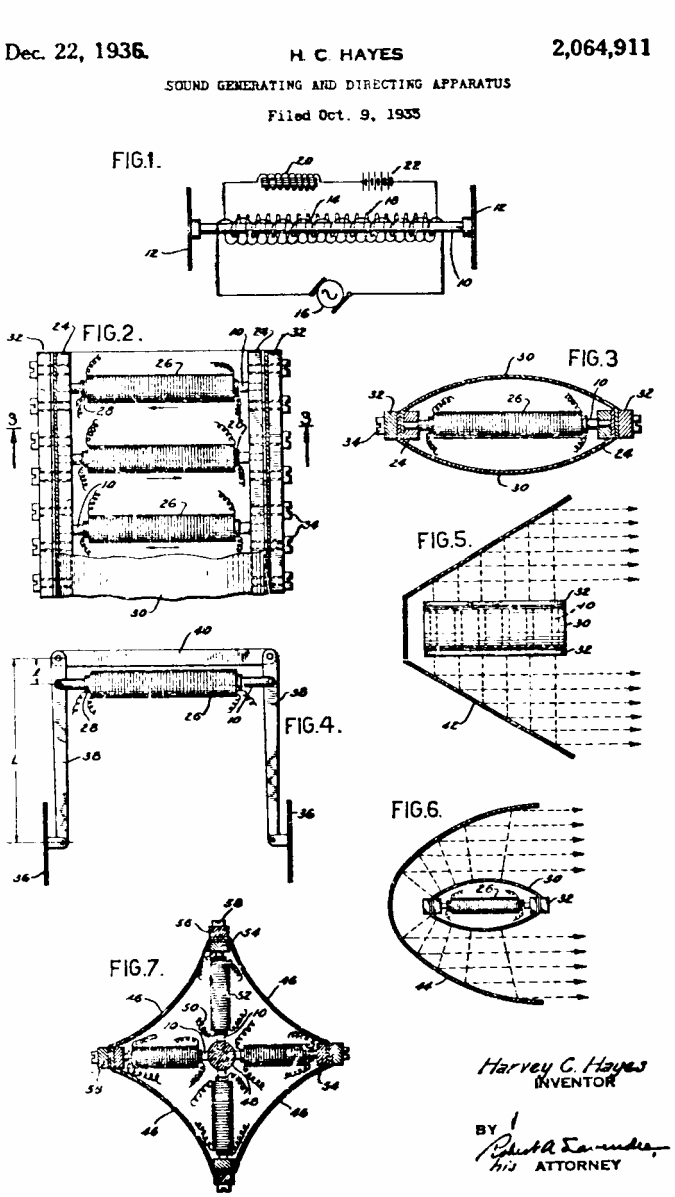

Figure 3.1. Illustration sheet from H. C. Hayes' 1936 patent [3.23] of a foghorn flextensional transducer (picture taken from reference 3.24).

3.3 The Re-birth of the Flextensional Transducer

The flextensional concept lay dormant until the middle-to-late 1950s when Toulis began investigating and developing the transducer. His work on flextensional transducers is reported by Kenneth Rolt [3.24] to have evolved from his investigations into compliant tubes [3.25, 3.26].

Although his early work on flextensional transducers was never published in open literature he first mentioned a flextensional transducer in a paper on effective transducer coupling [3.27] and again in a paper discussing acoustic-backing techniques [3.28]. Having realised the device's potential as a compact low-frequency acoustic projector he filed two patents. One patent [3.21] dealt with the transducer design (figure 3.2), while the other [3.22] covered a fluid-filled internal pressure compensation using compliant tubes for the same transducer. The Toulis design was in principle identical to that of Hayes, the crucial difference being that the Toulis transducer operated underwater and was excited by a piezoelectric stack. A lack of knowledge of Hayes' earlier work resulted in the flextensional concept being attributed to Toulis. This still holds true today.

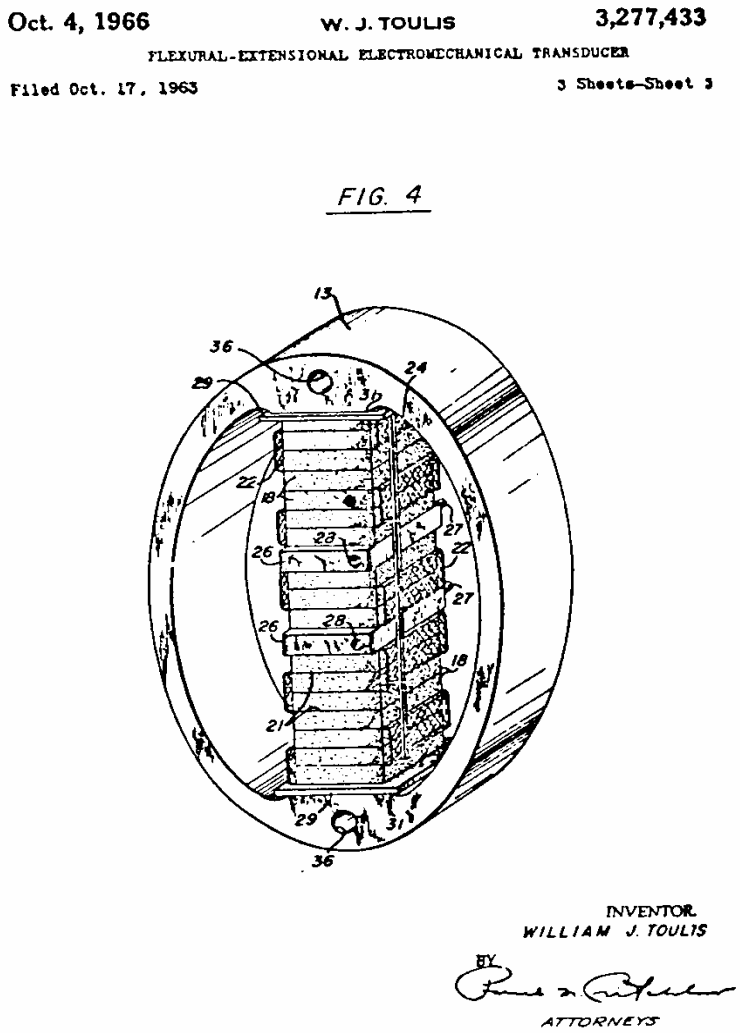
Oct. 4, 1966 W. J. TOULIS 3,277,433

FLEXURAL-EXTENSIONAL ELECTROMECHANICAL TRANSDUCER

Filed Oct. 17, 1963 3 Sheets-Sheet 3

FIG. 4

INVENTOR.
WILLIAM J. TOULIS
BY
ATTORNEYS

Figure 3.2. Sketch from W. J. Toulis' 1966 patent [3.21] of a ceramic-driven oval shell flextensional transducer (picture taken from reference 3.24).

3.4 Flextensional Transducer Classification Schemes

Currently there are two accepted classification schemes, namely those of 'Brigham-Royster' and 'Pagliarini-White'. This may seem strange when one considers that there are only a handful of possible flextensional transducer designs and this can often lead to confusion. It is therefore necessary to declare which scheme is being used when one talks about flextensional transducers.

The Pagliarini-White scheme [3.18, 3.19], as shown in figure 3.3, distinguishes class morphologically; that is, the distinction between the four classes is based on shape.

The Brigham-Royster scheme [3.24, 3.29], as shown in figure 3.4, distinguishes its classes by two methods. Class I, class IV, and class V, are distinguished by shape, while class I, class II, and class III, are distinguished by pragmatic criteria; class II is a high power version of class I and class III is a broad-band version of class I. It may be noted that the class I and class IV classifications in both schemes are identical. Also, the class V in the Brigham-Royster classification is equivalent to the class II in the Pagliarini-White classification.

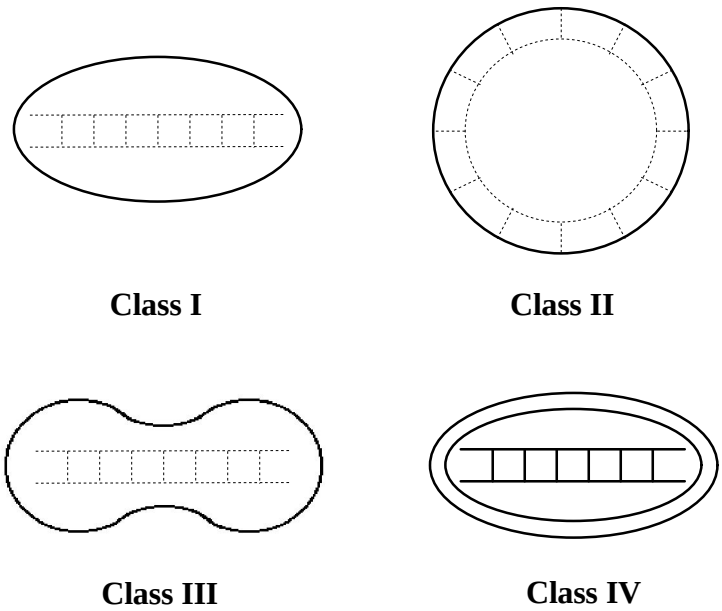

Figure 3.3. The Pagliarini-White classification scheme.

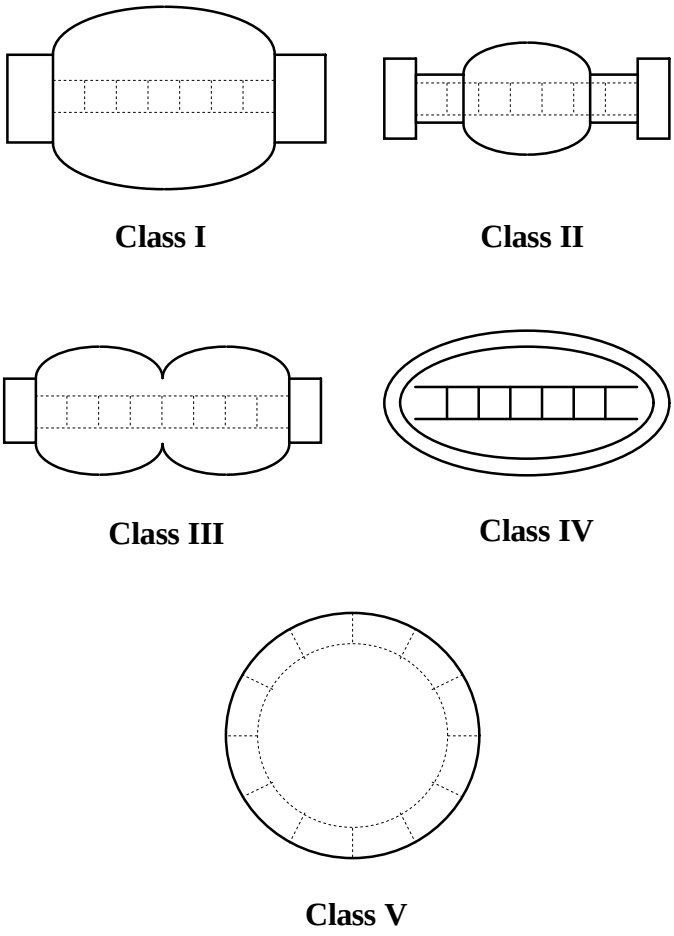

Figure 3.4. The Brigham-Royster classification scheme.

D. F. Jones [3.30] describes the confusion created by the underlying inconsistencies that exist in both classification schemes and a simplified alternative is proposed. This simplified scheme, based on the Pagliarini-White classification, contains only three classes, class I, class II, and class IV. The class III category is dropped on the grounds that it is an inverted form of the class I category. Such a classification scheme is preferable since ambiguity is removed. Each class would cover concave and convex shell geometries, high-power versions, and dual-shell broad- bandwidth versions. However, the author finds that the class V Brigham-Royster transducer classification is deeply entrenched in the literature. Thus, unless otherwise stated, a simplified Brigham-Royster classification scheme will be adopted in this thesis: the simplified scheme contains only three classes, class I, class IV, and class V.

3.5 Class I Flextensional Transducer

The class I flextensional transducer, otherwise known as the barrel-stave transducer, was one of the first to find an application [3.31]. The transducer usually consists of a piezoelectric stack and a surrounding mechanical shell that is cylindrical in nature. The shell, which is usually slotted or segmented, is coupled to the driver motor through the end plates. Excitation of the stack results in extensional motion of the end plates in the axial direction, which is transformed into radial motion via flexure of the surrounding shell. The volume velocity associated with the radial motion can be several times that due to the extensional motion.

The first 'successful' application of the flextensional concept was the so-called University of Miami flextensional transducer system built by North American Aviation, Inc., Columbus Division [3.9]. The device, which consists of a 30 inch piezoelectric stack housed within a convex aluminium shell, has an in-water resonance frequency of approximately 420 Hz, an in-water mechanical quality factor of 9, and a transmitting voltage response of 142.0 dB re. 1 μPa V^{-1} @ 1 m. The ceramic stack was protected with an oil-filled boot that permitted free-flooding of the transducer. A second, but much larger, oil-filled boot surrounded the entire transducer assembly for improved leakage and corrosion protection. Since the transducer was fluid-filled it had compliant tubes fitted within the cavity to provide essential pressure release to the radiating diaphragms. The inclusion of the tubes resulted in a depth-dependent and depth-limited transducer operation. Under free-flood conditions the transducer was found to have an acoustical power conversion efficiency of over 80 per cent; however the addition of the external boot resulted in a marked degradation in efficiency, down to approximately 50 per cent.

To determine the basic principles that govern the operation of the class I flextensional transducer, Royster developed a computer-modelling technique based on a mathematical model representation [3.32, 3.33]. The model, which is based on the University of Miami transducer, approximates the transducer though the consideration of three distinct problems: the mechanical shell, the piezoelectric stack, and the surrounding medium. The mechanical shell vibration problem is simplified by representing the shell as a framework consisting of a series of bars and joints. Thus the infinite number of degrees of freedom of the continuous shell has been reduced to a finite number, allowing solution by use of finite-difference equations. The piezoelectric stack wave equation is solved in terms of an arbitrary terminal impedance. Finally, the acoustic radiation

problem is solved by numerical evaluation of the Helmholtz integral for the farfield and nearfield pressure distributions. Taken together, the three components allow the transducer model to be constructed. The theoretical results obtained from the computer simulations were reported to be comparable with experimental data. Royster also presented the effect of certain geometrical parameters on pertinent performance characteristics: the resonance frequency, the sound-pressure level, and the quality factor. In a later paper [3.29] Royster states that the numerical model indicates that the minimum practical mechanical quality factor lies between 5 and 6. In addition, the model yielded data that indicated that the eigenvalues for the radiation modes of a typical design are, in general, too distant from each other to achieve a practical broad-band capability by varying the geometrical characteristics.

Several variations on the standard convex class I flextensional transducer exist. The first is a high power variant, commonly known as the Brigham-Royster class II flextensional transducer. The shell of this type of device is designed to have long cylindrical end sections that will allow a sufficient volume of ceramic to be accommodated to produce the required acoustic power output. The second variant is a broad-band dual-shell design, otherwise known as a Brigham-Royster class III flextensional transducer. The device, which looks like a graft of two different sized shells (hence the name ‘dual-shell’), forms a double-resonance shell system. By having two closely spaced resonance modes a broadened acoustic bandwidth is achieved.

Surprisingly, the success of the University of Miami transducer failed to generate interest in the class I flextensional transducer and support for the device shifted in favour of the contemporary class IV design. However, several companies have recently built the concave form of the class I flextensional transducer, which was patented by H. C. Merchant in 1966 [3.34], in response to DREA (Defence Research Establishment Atlantic) interest.

The in-house developments of research into the concave device by the DREA have been documented in recent papers by D. F. Jones [3.30] and C. J. Purcell [3.35]. Jones assesses the performance parameters for a number of barrel-stave projector designs, with various concave shell geometries; this includes solid shells, slotted shells, and staved shells. All the projectors contained a piezoelectric ceramic stack driver element that had been wrapped in fibreglass for shock hardening and moisture protection. The solid shell design required a shell with elastic properties such that it is stiff in the axial direction and compliant in the hoop direction in order to achieve a

low-frequency flexural mode; hence, a composite shell consisting of axially aligned boron fibres impregnated with urethane resin was employed. Testing of the solid shell design showed that it did exhibit a low resonance frequency but the source level and efficiency were both poor. The slotted, and staved, shell designs, which were constructed from aluminium, required a rubber boot to prevent the ingress of sea water though the gaps in the shell. Jones compared the performance of the DREA staved projector with a similar commercial projector, the Sparton Model 03BA1100. The commercial transducer was found to outperform the DREA design; Jones attributes this to the superior booting technique used on the Sparton. Results presented for the slotted projector indicated that the optimum number of slots is 12. However, Jones suggests that the effects of hydrostatic pressure may be more pronounced on a shell with 12 slots than the effects on shells with fewer slots, and hence 8 to 10 slots may be desirable. Purcell's paper [3.35] investigated the potential of the "giant" magnetostrictive rare-earth alloy Terfonal-D as a possible replacement for piezoelectric ceramics. The performance of a prototype device fitted with a Terfonal-D driver was compared with one powered by a ceramic driver. The experimental results proved to be disappointing, however; in particular the efficiency was very low (only 7 per cent).

An interesting variant of the concave form of the class I flextensional transducer was developed by Frank Abbott [3.36] (figure 3.5). The device, typically, was composed of six staves fashioned around a central stack assembly. The staves were not of simple concave construction, since the centre included a large piston to create a cylindrical shape and provide extra mass loading needed to lower the resonance frequency of the device. The staves were shaped in such a way that their central regions could bend and their entire outer faces move radially in response to longitudinal extension of the stack.

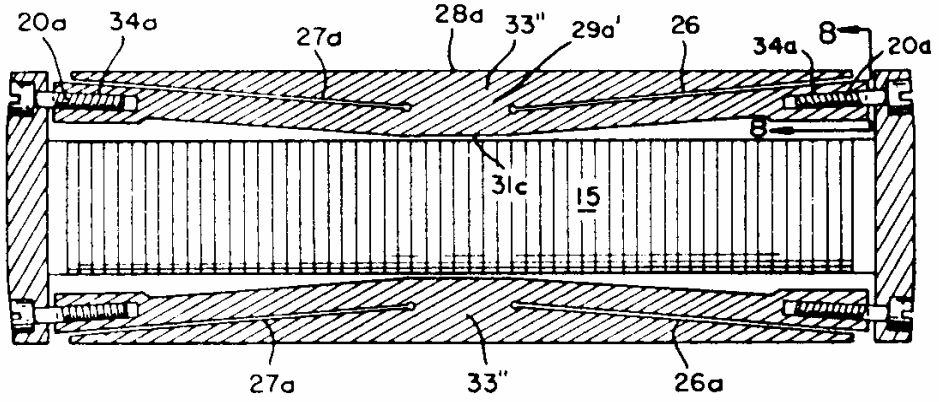

Figure 3.5. Sketch from F. R. Abbott's 1971 patent [3.36] of a ceramic-driven flextensional transducer (picture taken from review of patent [3.36]).

3.6 Class IV Flextensional Transducer

Over the years a great deal of effort has been spent in advancing the understanding of the class IV flextensional transducer and this has resulted in many technological innovations. This is clearly evident from the amount of literature on the subject.

The class IV flextensional transducer, as conceived by Hayes and later patented as an underwater sound source by Toulis, is currently the most well-known and most often-used flextensional design. The device typically consists of an elliptical mechanical shell that is driven by an internal stack of piezoelectric ceramic bars: variants of the class IV geometry include the circular shell, the flat-oval shell [3.29], and the concave shell or Merchant (figure 3.6) [3.34].

Computer modelling techniques were developed concurrently by Royster [3.37, 3.38] and Brigham [3.39-3.41], the latter reporting excellent agreement between theoretical and experimental data.

Brigham continued to study the class IV flextensional transducer. A comprehensive mathematical model was developed to describe the dynamic behaviour of the flextensional by the general techniques of wave mechanics [3.42]. Brigham used a simple model of the ceramic bar, differential equations for an oval ring with free ends to describe the radiating shell, and elliptic

radiation functions combined with an infinite-cylinder model for the radiated pressure field. Reasonable agreement between theory and experimental data was claimed. A later paper [3.43] investigates the effects of shell geometry and materials based on the results yielded from an equivalent circuit model that was not described in the paper. Recently Brigham has presented a simplified theoretical model that was developed in the 1970s [3.44].

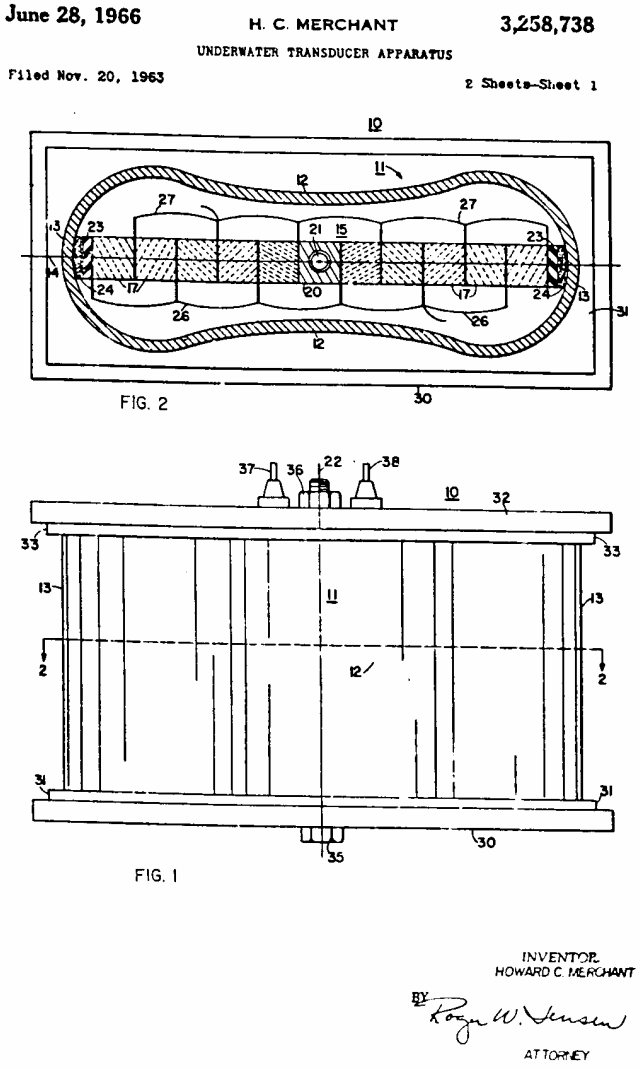

Figure 3.6. Sketch from H. C. Merchant's 1966 patent [3.34] of a ceramic-driven, concave shell flextensional transducer (picture taken from reference 3.24).

The first successful production run of air-backed underwater flextensional transducers were produced by Sanders Associates in 1977 for the Wide Track Sonar Program. The design and performance of this transducer are described by Pagliarini and White [3.45]. Measured data was shown to closely match the predicted results, yet the method of calculating these predictions has not been published. In a later paper [3.46] a number of empirical formulae derived from simple theory were quoted, but the derivation was not included.

An overview of the design principles for the class IV structure is discussed by Oswin, *et al*. [3.17, 3.18] and Bromfield [3.47]. The effects of the many variables on the performance of the device are explored; shell materials, shell thickness, and the ratio of the shell major axis to minor axis are covered. The limitations on operating frequency and power imposed by submersion depth are also explained.

Various solutions have been proposed to overcome the effects of pressure. Thomson-Sintra ASM have developed a dynamic filter [3.48, 3.49] that is integrated in the middle of the drive stack. The compliance of the filter is low compared with the stack under dynamic conditions; conversely it is high under static conditions. The maximum functional depth is consequently limited to the mechanical strength of the shell. Nevertheless, the transducer is still air-backed and its resonance frequency will be depth dependent. Hardie describes the use of a free-flood rubber bladder as a simple means of providing an internal counter pressure [3.15]. The bladder reduces the tendency for the resonance frequency to shift with changes in operating depth by countering the hydrostatic loading of the transducer. This scheme for countering the external pressure effects was found to be effective for depths up to one half the catastrophic buckling depth of the device. For unlimited depth capability Oswin and Steel propose a flextensional-Helmholtz device [3.50].

The class IV flextensional transducer has been subject to many design innovations over the years. Dahlstrom incorporated stress bolts into the ceramic stack assembly [3.51] (figure 3.7). This configuration eliminates the requirement for the elliptical shell to be stiff enough to apply sufficient pre-stress for high drive operation at depth. The Tocquet projector [3.52] is manufactured in the style of a Tonpilz transducer (figure 3.8). One end of the ceramic stack is

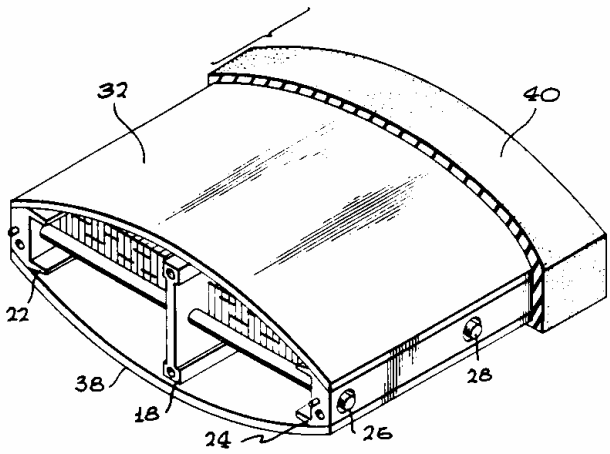

Figure 3.7. Sketch from a patent by D. K. Dahlstrom, M. E. Fife, and C. R. Judy [3.51] of a flextensional transducer with a ceramic stack assembly that incorporates stress bolts (picture taken from review of patent [3.51]).

connected to the elliptical shell and the other end is loaded with a large counter weight. Designs by Rolt [3.53, 3.54] (figure 3.9) and Inone [3.55] incorporate 'hinges' into the high stress areas of the shell, thus changing the nature of the stress distributions. Unfortunately the hinges are subject to very high stresses and may lead to mechanical failure in long term operation. The outboard-driven flextensional patent by Porzio [3.56], as the title suggests, places the ceramic stack on the outside of the elliptic shell (figure 3.10). This configuration allows much larger volumes of active materials to be employed, which enables the generation of greater acoustic power. Additionally, the pre-stress on the stack is a minimum at the surface and increases with depth. An alternative method of generating increased acoustic power is to replace the piezoelectric ceramic stack with magnetostrictive alloy rods [3.57] or an electrostrictive ceramic stack [3.58]. Although the reported data demonstrate the promise of these materials, prototype designs that have incorporated them have only met with limited success, and their future usefulness remains to be demonstrated.

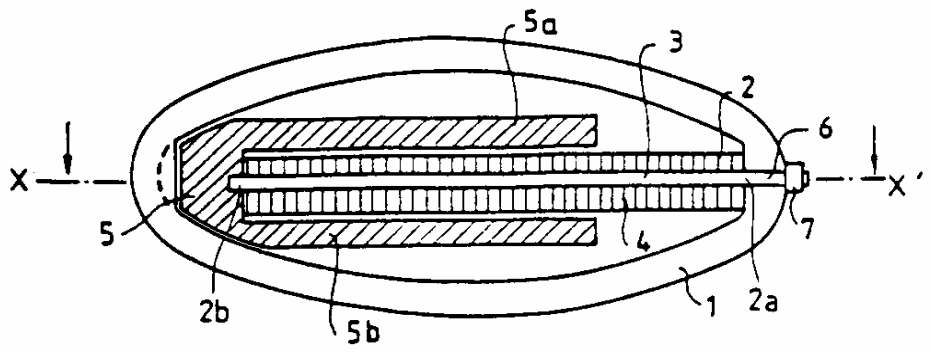

Figure 3.8. Sketch from a patent by B. Tocquet and M. Letiche [3.52] of a Tonpilz style flextensional transducer (picture taken from review of patent [3.52]).

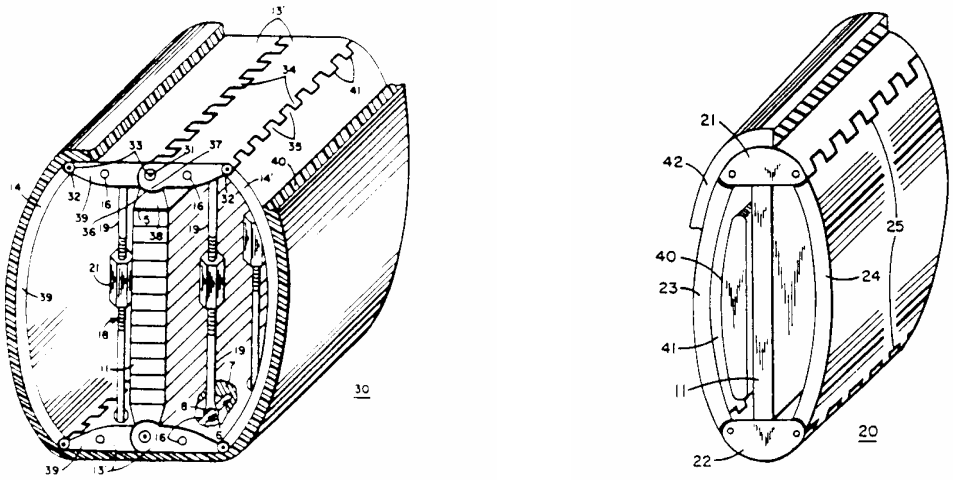

Figure 3.9. Sketches from K. D. Rolt's 1989 and 1991 patents [3.53, 3.54] of flextensional transducers with hinged shells (pictures taken from review of patents [3.53, 3.54]).

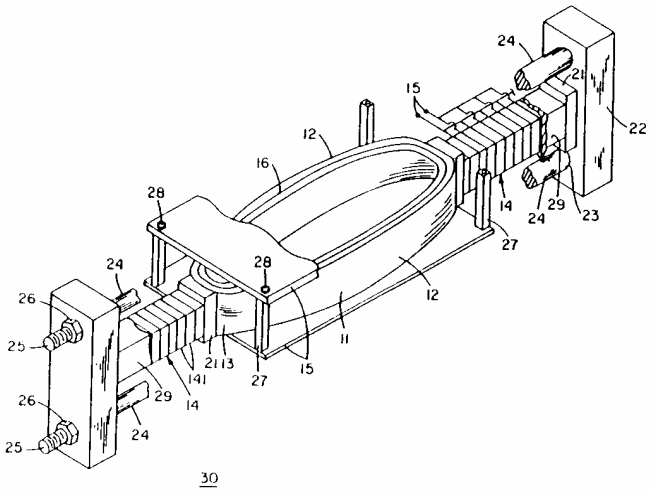

Figure 3.10. Sketch from R. Porzio's 1990 patent [3.56] of an outboard-driven flextensional transducer (picture taken from review of patent [3.56]).

3.7 Class V Flextensional Transducer

The class V flextensional transducer, otherwise known as the ring-shell transducer, was patented in 1955 by F. A. Abbott [3.59], who was at the time a colleague of Toulis at Naval Electronics Laboratory (NEL, and now called the Naval Ocean Systems Centre, NOSC). The device consists of a pair of convex, or concave, metallic membranes that are cemented to the sides of a piezoelectric ceramic ring (figure 3.11). The ring is excited radially by electrodes on its inner and outer cylindrical surfaces. As it expands, it stretches the membranes, resulting in perpendicular movements of a greatly magnified amplitude. Abbott also described a method for moderate pressure compensation, in which the collapse of the transducer's shell membranes under ocean pressure is prevented by injecting the transducer with compressed gas.

The transducer described by Abbott used a monolithic and radially polarised ring that is characteristic of high frequency devices where dimensions are small. In the case of low-frequency, high-power sources, a segmented ring comprising of tangentially polarised ceramics is employed. The segmented ring is pre-stressed by an external glass fibre wrapping.

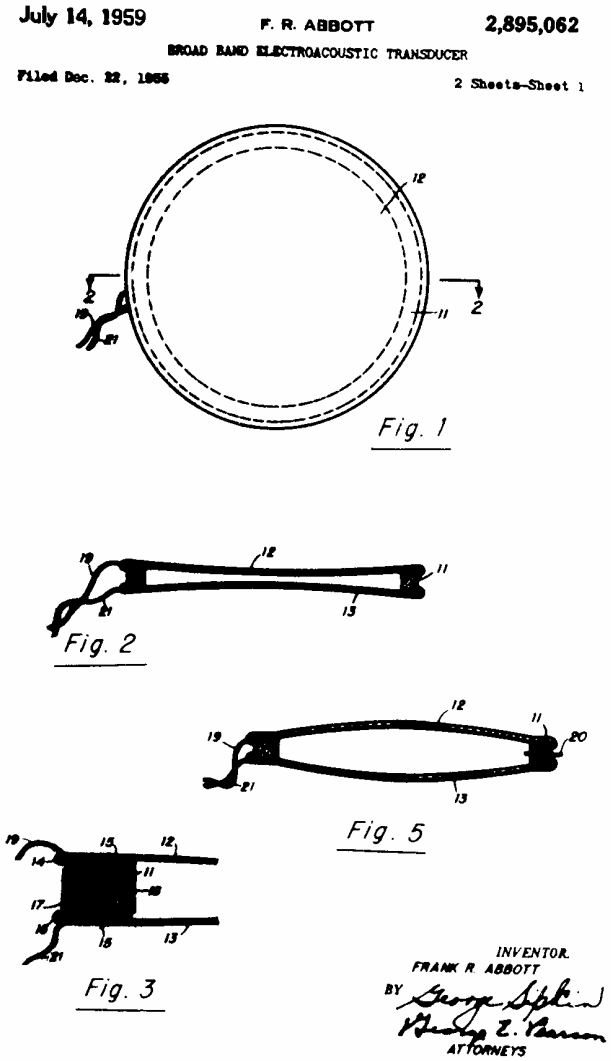
July 14, 1959 F. R. ABBOTT 2,895,062

BROAD BAND ELECTROACOUSTIC TRANSDUCER

Filed Dec. 22, 1955 2 Sheets-Sheet 1

Fig. 1

Fig. 2

Fig. 5

Fig. 3

INVENTOR.
FRANK R. ABBOTT
BY George Apley
Harding E. Parmer
ATTORNEYS

Figure 3.11. Illustration sheet from F. R. Abbott's 1959 patent [3.59] of a ceramic-driven flextensional transducer (picture taken from reference 3.24).

An alternative to the segmented ring has been proposed by K. Anifrani and D. Boucher [3.60]. Their ring consists of eight metal ring segments on which conventional cylindrical ceramic stacks are mounted; the arrangement forms an inscribed polygon (figure 3.12). The ceramics are driven in parallel in their thickness mode, and the stacks are pre-stressed by central bolts. Anifrani and Boucher state that their design combines the advantages of simple construction and easy pre-stressing.

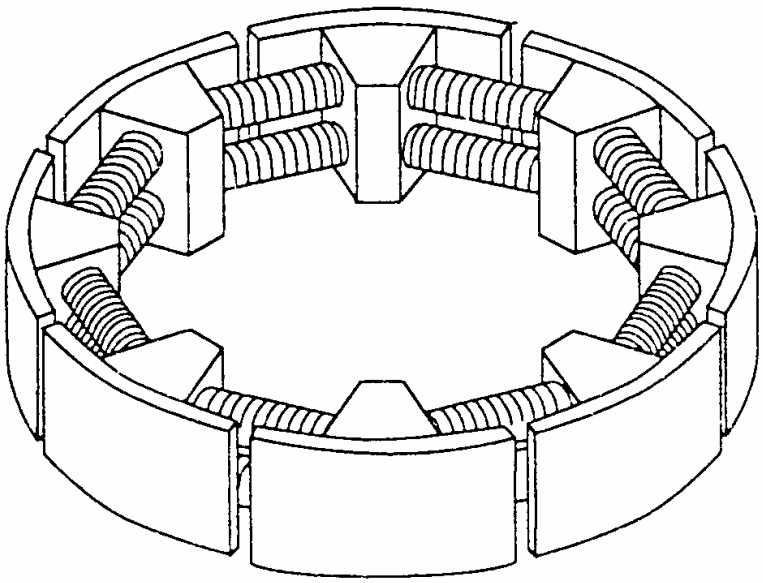

Figure 3.12. Sketch of a polygonal ring conceived by K. Anifrani and D. Boucher (picture taken from reference 3.60).

As with the other classes of flextensional transducers, Royster, *et al.*, pioneered the computer modelling of the class V flextensional transducer [3.61, 3.62]. Royster's model approximates the transducer through the consideration of three distinct problems. The vibration problem is solved using a finite-difference model to approximate the shell. The piezoelectric ring, which has an arbitrary impedance on its boundary, is solved using Bessel functions. Finally, the acoustic radiation problem is solved using a surface source distribution method. Taken together the three components allow a model of the transducer to be constructed. Royster found the results computed from the mathematical model to be a 'good' approximation when compared with experimental data.

Today computer modelling makes extensive use of the finite-element method. Commercially-available packages have made it easy for the transducer designer to study the resonance modes, velocity profiles, static and dynamic stresses, and the acoustic output of flextensional transducers.

Anifrani and Boucher used the finite-element program ATILA to model their new transducer designs [3.60]. They presented in-air and in-water analyses for two types of transducer utilising the novel octagonal ring arrangement, the symmetrical type comprising of two shells, and the asymmetrical type with only one shell. Additionally, the effect of altering shell curvature for convex and concave configurations was also analysed.

B. A. Armstrong and G. W. McMahon used the finite-element program MAVART to design a ring-shell projector [3.12-3.15]. The transducer was intended to be used for low-frequency, high-power operation at moderate depths. Pressure compensation is provided by an internal water bladder that increases the effective operating depth. The bladder, which is open to the sea, expands with the ingress of water and compresses the internal air, supplying the necessary pressure compensation without seriously impeding the motion of the shell. The maximum operating depth of the transducer with an internal fill pressure of 4 atmospheres absolute has been estimated at 300 metres.

M. Letiche and P. La Scala used ETAx, an axisymmetrical numerical approach that combines the finite element and boundary element methods, to refine an equivalent circuit model [3.63]. The transducer employs a mechanical filter between the shell and the segmented ceramic ring that effectively makes the piezoceramic pre-stress independent of hydrostatic pressure, thereby providing pressure compensation. The mechanical filter, a polyurethane material, is very compliant under static conditions to compensate for shell deformation under the action of hydrostatic pressure but stiff enough in dynamic conditions to provide a good coupling between the driver and the shell. The maximum operating depth of the transducer has been defined as 1000 metres.

3.8 Other Flextensional Transducer Designs

Previously it was shown that the flextensional concept originated from Hayes. In addition to constructing the later-day equivalent of the class IV flextensional transducer, he also built another variety of flextensional. The transducer consisted of four oscillating plates driven at their corners by four magnetostrictive elements attached to a common central member; thus the shell is configured as a four pointed star and the drive elements are arranged in a cross-shaped formation

(figure 3.1). Excitation of the magnetostrictive elements results in flexure of the plates that is accompanied by in-phase breathing of the plates and their interconnecting ends.

Abbott exploited the four-sided flextensional for underwater use (figure 3.13) [3.64]. However, apart from replacing the magnetostrictive drive elements with ceramic stacks, the design is effectively identical to that of Hayes.

Butler extended the four-sided flextensional principle to encompass transducers with three or more sides [3.65].

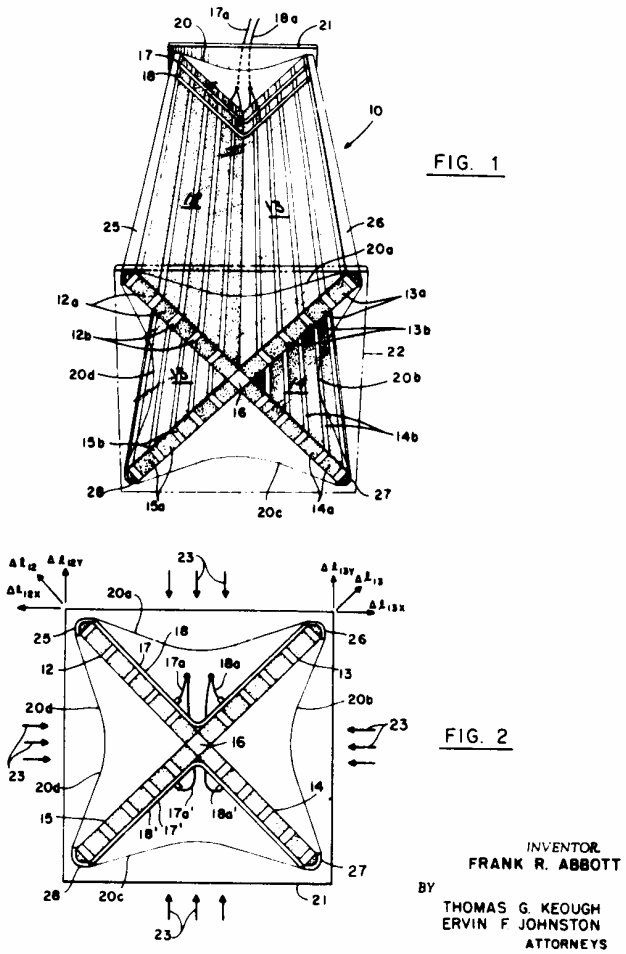

Figure 3.13. Sketch from F. R. Abbott's 1972 patent [3.64] of a ceramic-driven four-sided flextensional transducer (picture taken from reference 3.24).

A ceramic-driven four-sided prototype transducer has been built and tested by the Submarine Signal Division of the Raytheon Company. The device, described by Butler and Rolt [3.66], has a diameter of 25 inches, an in-water frequency of approximately 1 kHz, an in-water mechanical quality factor of 3, and a transmitting voltage response of 133 dB re. 1 μPa V^{-1} @ 1 m.

3.9 Conclusions

A variety of flextensional transducer designs have been considered in this chapter for application as an ocean acoustic tomography source. The main characteristics that have affected a choice of transducer technology are summarised in table 3.3. Of the possible transducer designs, the class I flextensional, otherwise known as the 'barrel-staved' flextensional, shows particular promise since the technology has been utilised for a similar application. The shape of the device means that it is readily suited to arrangement in a vertical line array to achieve horizontal directivity and so reduce unwanted acoustic energy transmission to the ocean floor and sea surface. It is also anticipated that of all the flextensional designs the class I transducer will offer the best chance of meeting the depth requirements. Techniques of modifying the design so that it can operate in deep water at depths of over 100 metres are explored later in this thesis.

The University of Miami transducer was the first successful application of the flextensional concept. This class I device fails to meet the performance criteria for an ocean acoustic tomography source on account of its high mechanical quality factor of over twice the requisite value. Furthermore, results derived from Roysters' computer model, based on an approximate mathematical theory, indicate that the minimum practical quality factor is somewhat higher than the required value. However, due to the limited nature of his model there is a need to use methods that can more precisely determine whether such performance specification can be met.

Improved performance predictions can be obtained from finite element modelling. Although this technique has been applied extensively to class IV and V flextensional transducers, it has not been used comprehensively to analyse the mechanical behaviour of the class I design.

Table 3.3. A comparative assessment of flextensional technologies suitable for ocean acoustic tomography.

Flextensional technology	Advantages	Disadvantages
Class I	• Has been applied to a similar application • Suited to vertical line array configuration • Free-flooded design possible	• Difficult construction • Limited understanding of the class I design
Class IV	• Well understood design • Simplest construction	• Most difficult to provide internal pressure equalisation
Class V	• Understood design • Suited to vertical line array configuration	• Comparatively expensive • Most difficult construction • Difficult to provide internal pressure equalisation

The literature review has shown that there is an insufficient understanding of the workings of the class I flextensional transducer. In this thesis the effects of varying the geometry of a typical transducer observed from calculations using the finite element method coupled with the boundary element method are presented. This should greatly increase the understanding of the basic governing parameters and help produce improved transducer designs.

3.10 References

[3.1] D. Stansfield, *Underwater Electroacoustic Transducers*, (Bath University Press and Institute of Acoustics, 1990), Chapter 11.

[3.2] O. B. Wilson, *Introduction to Theory and Design of Sonar Transducers*, (Peninsula Publishing, 1988), Chapter 6.

[3.3] J.-N. Decarpigny, B. Hamonic, and O. B. Wilson, 'The Design of Low-Frequency Underwater Acoustic Projectors: Present Status and Future Trends', *IEEE J. Oceanic Eng.*, 16(1), 107-122, (1991).

[3.4] R. Timme, A. M. Young, and J. E. Blue, 'Transducer Needs for Low Frequency Sonar', in *Power Transducers for Sonics and Ultrasonics*, B. Harmonic, O. B. Wilson, and J.-N. Decarpigny, eds., (Springer-Verlag, 1988), 143-159.

[3.5] D. Boucher, 'New Soultions for Low Frequency Sonar Projectors', in *Transducers for Sonics and Ultrasonics*, M. D. McCollum, B. F. Hamonic, and O. B. Wilson, eds., (Technomic Publishing Co. Inc., 1993), 17-37.

[3.6] D. Boucher, 'Trends and Problems in Low Frequency Sonar Projector Design', in *Proc. Power Sonic and Ultrasonic Transducers Design*, B. Hamonic and J.-N. Decarpigny, eds., (Spring-Verlag, 1988), 100-120.

[3.7] R. S. Woollett, 'Trends and Problems in Sonar Transducer Design', *IEEE Trans. Ultrasonics Eng.*, 10, 116-124, (1963).

[3.8] R. S. Woollett, 'Basic Problems Caused by Depth and Size Constraints in Low-Frequency Underwater Transducers', *J. Acoust. Soc. Am.*, 68(4), 1031-1037, (1980).

[3.9] M. Kronengold and W. J. Toulis, 'Directional 420-Hz Sound Source', *IEEE Trans. Geoscience Electronics*, 6(4), 204-211, (1968).

[3.10] Y. Le Gall, D. Boucher, X. Lurton, and A. M. Bruneau, 'Optimization of the Janus-Helmholtz Transducer for Ocean Acoustic Tomography', in *Proc. Underwater Acoustics*, L. Bjørnø, ed., (European Commission, 1994), Vol. 1, 527-530.

[3.11] Y. Le Gall, D. Boucher, X. Lurton, and A. M. Bruneau, 'Great Depth, High Efficiency, Broadband, Reliable Low Frequency Transducer for Acoustical Tomography', *Proc. OCEANS '94* , 2, 284-288, (1994).

[3.12] G. W. McMahon and B. A. Armstrong, 'A Pressure-compensated Ring-Shell Projector', *Conf. Proc. I. O. A.*, Transducers for Sonar Applications, 9.1-9.8, (1980).

[3.13] B. A. Armstrong and G. W. McMahon, 'Discussion of the Finite-Element Modelling and Performance of Ring-Shell Projectors', *IEE Proceedings*, 131(F), 275-279, (1984).

[3.14] G. W. McMahon, 'Ring-Shell Projector', U. S. Patent 4,858,206, (15 August 1989); reviewed in *J. Acoust. Soc. Am.*, 87(4), 1834, (1990).

[3.15] G. W. McMahon, 'The Ring-Shell Flextensional Transducer (Class V)', in *Power Transducers for Sonics and Ultrasonics*, B. Harmonic, O. B. Wilson, and J. N. Decarpigny, eds., (Spring-Verlag, 1991), 60-74.

[3.16] D. J. W. Hardie, 'The Effect of Depth Pressure on a Flextensional Transducer', *Proc. I. O. A.*, 12(4), 40-48, (1990).

[3.17] J. R. Oswin and A. Turner, 'Design Limitations of Aluminium Shell, Class IV Flextensional Transducers', *Proc. I. O. A.*, 6(3), 94-101, (1984).

[3.18] J. Oswin and J. Dunn, 'Frequency, Power, and Depth Performance of Class IV Flextensional Transducers', in *Power Sonic and Ultrasonic Transducers*, B. Hamonic and J.-N. Decarpigny, eds., (Springer-Verlag, 1987), 121-133.

[3.19] H. B. Miller, 'Composite Electromechanical Transducer', U.S. Patent 2,930,912 (29 March 1960); reviewed in *J. Acoust. Soc. Am.*, 33(11), 1648, (1961).

[3.20] H. B. Miller, 'Origin of Mechanical Bias for Transducers', *J. Acoust. Soc. Am.*, 35(9), 1455, (1963).

[3.21] W. J. Toulis, 'Flexural-Extensional Electromechanical Transducer', U.S. Patent 3,277,433 (4 October 1966); reviewed in *J. Acoust. Soc. Am.*, 41(3), 764, (1967).

[3.22] W. J. Toulis, 'Flexural-Extensional Electromechanical Transducer', U.S. Patent 3,274,537 (20 September 1966); reviewed in *J. Acoust. Soc. Am.*, 41(3), 764, (1967).

[3.23] H. C. Hayes, 'Sound Generating and Directing Apparatus', U.S. Patent 2,064,911 (22 December 1936).

[3.24] K. D. Rolt, 'History of the Flextensional Electroacoustic Transducer', *J. Acoust. Soc. Am.*, 87(3), 1340-1349, (1990).

[3.25] W. J. Toulis, 'Acoustic Refraction and Scattering with Compliant Elements. I. Measurements in Water', *J. Acoust. Soc. Am.*, 21(9), 1021-1026, (1957).

[3.26] W. J. Toulis, 'Acoustic Refraction and Scattering with Compliant Elements. II. Analysis', *J. Acoust. Soc. Am.*, 29(6), 1027-1033, (1957).

[3.27] W. J. Toulis, 'Electromechanical Coupling and Composite Transducers', *J. Acoust. Soc. Am.*, 35(1), 74-80, (1963); R. S. Woollett, 'Comments on "Electromechanical Coupling and Composite Transducers"', *J. Acoust. Soc. Am.*, 35(11), 1837-1838, (1963); W. J. Toulis, 'Auther's Response to Comments by R. S. Woollett', *J. Acoust. Soc. Am.*, 35(11), 1838, (1963).

[3.28] W. J. Toulis, 'Acoustic-Backing Techniques for Transducers and Radiators', *J. Acoust. Soc. Am.*, 37(2), 250-256, (1965); L. H. Royster, 'Comments on "Acoustic-Backing Techniques for Transducers and Radiators," by W. J. Toulis', *J. Acoust. Soc. Am.*, 37(6), 1152-1153, (1965); L. H. Royster, 'Predicting the Effective Dynamic Coupling Coefficient of the Flextensional Transducer (preliminary Design Considerations)', *J. Acoust. Soc. Am.*, 38(5), 879-880, (1965).

[3.29] L. H. Royster, 'The Flextensional Concept: A New Approach to the Design of Underwater Acoustic Transducers', *Applied Acoustics*, 3, 117-126, (1970).

[3.30] D. F. Jones, 'Flextensional Barrel-Stave Projectors', in *Transducers for Sonics and Ultrasonics*, M. D. McCollum, B. F. Hamonic, and O. B. Wilson, eds., (Lancaster, PA: Technomic Publishing Co. Inc., 1993), 150-159.

[3.31] E. F. Rynne, 'Innovative Approaches for Generating High Power, Low Frequency Sound', in *Transducers for Sonics and Ultrasonics*, M. D. McCollum, B. F. Hamonic, and O. B. Wilson, eds., (Lancaster, PA: Technomic Publishing Co. Inc., 1993), 38-49.

[3.32] L. H. Royster, 'Flextensional Underwater Acoustic Transducer', *J. Acoust. Soc. Am.*, 43(3), 671-682, (1969).

[3.33] J. N. Boone, L. H. Royster, and R. A. Nelson, 'Mathematical Model for a Class II Flextensional Underwater Acoustic Transducer', *J. Acoust. Soc. Am.*, 47(1), 71 (abs), (1970).

[3.34] H. C. Merchant, 'Underwater Transducer Apparatus', U. S. Patent 3,258,738, (28 June 1966).

[3.35] C. J. Purcell, 'Terfenol Driver for the Barrel-Stave Projector', in *Transducers for Sonics and Ultrasonics*, M. D. McCollum, B. F. Hamonic, and O. B. Wilson, eds., (Technomic Publishing Co. Inc., 1993), 160-169.

[3.36] F. R. Abbott, 'High Fidelity Underwater Music Projector', U. S. Patent 3,718,897 (27 May 1971); reviewed in *J. Acoust. Soc. Am.*, 54(2), 568, (1973).

[3.37] J. R. Ruledge and L. H. Royster, 'Mathematical Model for the Class II Flextensional Transducer', *J. Acoust. Soc. Am.*, 50(1), 141 (abs), (1971).

[3.38] J. R. Rutledge and L. H. Royster, 'Approximate Model for Predicting Operational Parameters of the Class IV Flextensional Underwater Transducer', *J. Acoust. Soc. Am.*, 51(1), 82 (abs), (1972).

[3.39] G. A. Brigham, 'Computer Modeling of Oval Flextensional Underwater Transducer', *J. Acoust. Soc. Am.*, 50(1), 141 (abs), (1971).

[3.40] G. A. Brigham, 'An Equivalent Circuit for Oval, Flextensional Transducers', *J. Acoust. Soc. Am.*, 51(1), 141 (abs), (1971).

[3.41] G. A. Brigham, 'In-plane Free Vibrations of Tapered Oval Rings', *J. Acoust. Soc. Am.*, 54(2), 451-460, (1973).

[3.42] G. Brigham, 'Analysis of the Class-IV Flextensional Transducer by use of Wave Mechanics' *J. Acoust. Soc. Am.*, 56(1), 31-39, (1974).

[3.43] G. Brigham and B. Glass, 'Present Status in Flextensional Transducer Technology', *J. Acoust. Soc. Am.*, 68(4), 1046-1052, (1980).

[3.44] G. Brigham amd B. McTaggart, 'A Simplified Design Technique for Closed Shell Flextensional Devices', *Proc. U.D.T.*, 481-487, (1990).

[3.45] J. A. Pagliarini and R. P. White, 'A Small, Wide-Band, Low-Frequency, High-Power Sound Source Utilising the Flextensional Transducer Concept', *Proc. OCEANS '78* , 333-338, (1978).

[3.46] W. J. Marshall, J. A. Pagliarini, and R. P. White, 'Advances in Flextensional Transducer Design', *Proc. OCEANS '79.*, 124-129, (1979).

[3.47] G. Bromfield, 'Class IV Flextensional Transducers', in *Power Transducers for Sonics and Ultrasonics*, B. Harmonic, O. B. Wilson, and J. N. Decarpigny, eds., (Heidelburg: Spring-Verlag, 1991), 48-59.

[3.48] Y. Lagier, Th. Mazyer, D. Guyomar, Ph. Dufourcq, and P. Ventura, 'Flextensional Transducer Modelling', *Proc. U. D. T.*, 778-783, (1990).

[3.49] P. Dufourcq, J. Adda, M. Letiche, and E. Sernit, 'Transducers for Great Depths', in *Power Transducers for Sonics and Ultrasonics*, B. Harmonic, O. B. Wilson, and J. N. Decarpigny, eds., (Heidelburg: Spring-Verlag, 1991), 75-85.

[3.50] J. Oswin and G. A. Steel, 'Flextensional Transducers with Unlimited Depth Capability', *Proc. I. O. A.*, 12(4), 13-20, (1990).

[3.51] D. K. Dahlstrom, M. E. Fife, and C. R. Judy, 'Underwater Transducer', U. S. Patent 4,764,907 (16 August 1988); review in *J. Acoust. Soc. Am.*, 85(3), 1389, (1389).

[3.52] B. Tocquet and M. Letiche, 'Flextensional Transducer', U. S. Patent 4,970,706 (13 November 1990); reviewed in *J. Acoust. Soc. Am.*, 91(1), 539, (1992).

[3.53] K. D. Rolt, 'Flextensional Electroacoustic Transducer with Hydrostactically Compression-Loaded Driver', U. S. Patent 4,862,429 (29 August 1989); reviewed in *J. Acoust. Soc. Am.*, 87(4), 1828, (1990).

[3.54] K. D. Rolt, 'Hinge-Modified Flextensional Transducer', U. S. Patent 4,932,008 (5 June 1990); reviewed in *J. Acoust. Soc. Am.*, 89(4), 1843, (1991).

[3.55] T. Inoue and T. Nada, 'Underwater Low-Frequency Ultrasonic Wave Transmitter', U. S. Patent 4,706,230 (10 November 1987); reviewed in *J. Acoust. Soc. Am.*, 83(6), 2470, (1988).

[3.56] R. Porzio, 'Outboard-Driven Flextensional Transducer', U. S. Patent 4,894,811 (16 January 1990); review in *J. Acoust. Soc. Am.*, 90(4), 2215, (1991).

[3.57] J. R. Oswin and A. Maskery, 'Magnetostriction in Flextensional Transducers', *Proc. I. O. A.*, 9(2), 23-30, (1987).

[3.58] S. M. Pilgrim, M. Massuda, J. D. Prodey, and J. M. Hock, 'Electrostrictive Sonar Drivers for Flextensional Transducers', in *Transducers for Sonics and Ultrasonics*, M. D. McCollum, B. F. Hamonic, and O. B. Wilson, eds, (Lancaster, PA: Technomic Publishing Co., Inc, 1993), 95-102.

[3.59] F. R. Abbott, 'Broad Band Electroacoustic Transducer', U.S. Patent 2,895,062 (14 July 1959); reviewed in *J. Acoust. Soc. Am.*, 32(1), 310, (1960).

[3.60] K. Anifrani and D. Boucher, 'New Designs of Class V Flextensional Transducers using the ATILA Code', *Proc. I. O. A.*, 12(4), 21-30, (1990).

[3.61] J. N. Boone, L. H. Royster, and R. A. Nelson, 'Mathematical Model for a Class V Flextensional Underwater Acoustic Transducer', *J. Acoust. Soc. Am.*, 47(1), 71 (abs), (1970).

[3.62] R. A. Nelson and L. H. Royster, 'Development of a Mathematical Model for the Class V Flextensional Underwater Acoustic Transducer', *J. Acoust. Soc. Am.* 49(5), 1609-1620, (1971).

[3.63] M. Letiche and P. La Scala, 'Great Depth Class V Flextensional Transducer', in *Transducers for Sonics and Ultrasonics*, M. D. McCollum, B. F. Hamonic, and O. B. Wilson, eds., (Lancaster, PA: Technomic Publishing Co. Inc., 1993), 142-149.

[3.64] F. A. Abbott, 'Low Frequency Electroceramic Sonar Transducer', U. S. Patent 3,659,258 (25 April 1972); reviewed in *J. Acoust. Soc. Am.*, 52(4), 1972, (1972).

[3.65] J. L. Butler, 'Flextensional Transducer', U. S. Patent 4,742,499 (3 May 1988); reviewed in *J. Acoust. Soc. Am.*, 84(5), 1968, (1988).

[3.66] J. L. Butler and D. Rolt, 'A Four-sided Flextensional Transducer', *J. Acoust. Soc. Am.*, 83(Suppl. 1), S19, (1988).

Chapter 4

NUMERICAL METHODS IN TRANSDUCTION

4.1 Introduction

Partial differential equations arise in connection with various physical and geometrical problems when the function involved depends on two or more independent variables. Important areas include fluid and solid mechanics, heat transfer, electromagnetic theory and other physical and engineering problems. The natural vibration of a structure is of primary importance to the transducer designer. In general, practical problems often lead to differential equations that cannot be 'simply' solved or a solution obtained in closed form, and a technique for approximating the numerical value or values of the solution must be employed [4.1-4.3]. Such techniques come under the collective title of 'numerical analysis', and with the development of fast computers and effective software, many previously unsolvable problems can now be approximated to a high degree of accuracy.

The finite element method [4.4, 4.5] is a numerical approach that can be used for the accurate solution of complex engineering problems. The method was first developed in 1956 for the analysis of aircraft structures. Within a decade it was soon recognised that the finite element technique could be applied to the solution of many other classes of problems. The development of a numerical treatment for piezoelectric elements [4.6, 4.7] has allowed the finite element method to be applied to the field of electro-acoustic transducer design. Transducer designers are increasingly exploiting the technique to model the highly complex geometry of low-frequency projectors.

The effect of fluid loading is highly significant to the in-water behaviour of a transducer. In general the main effects are to introduce damping and increase the inertia of the structure, lowering the resonance frequencies. One way of numerically determining the effect of loading is to extend the finite element model into the fluid [4.8-4.10]. However, the boundary element method offers a more appropriate approach [4.6, 4.11, 4.12].

The boundary element method is a relatively recent development in the field of numerical analysis. It was first used to model acoustic problems in the 1960s [4.13-4.17]. The method solves the acoustic wave equation by transforming it into an integral equation over the surface of the structure; that is, the method solves for the unknowns on the radiating surface rather than throughout the fluid region.

In this chapter the numerical analysis techniques, as used for the modelling of acoustic transducers, are summarised.

4.2 The Finite Element Method

In the finite element method the structure or domain is divided into a finite number of smaller subregions or finite elements. These elements describe a mesh, where the 'coarseness' of the mesh determines the accuracy of the solution; hence, an increased number of elements within the mesh produces an improved approximation to the solution. As the number of elements used to model the domain tends to infinity, the accuracy of the solution approaches that of the differential equation. However, an exact solution is not possible due to the presence of rounding errors, which depend on the number of significant figures used to represent a real number.

Each element is defined by a discrete number of points or nodes that are situated on the element boundaries and are common to adjacent elements. These nodal points are given by co-ordinates relative to a set of global axes (x, y, z). The geometry of each element is defined in terms of these co-ordinates by shape functions that map the points onto a local co-ordinate system. The mapped nodal points are given by co-ordinates relative to a set of local axes (ξ, η, ζ).

Inside a given element the physical quantities of interest are expressed as the combination of values at the element nodes. With regard to transducer modelling, the physical quantities of interest are the mechanical displacement in the passive or active elastic components, and the

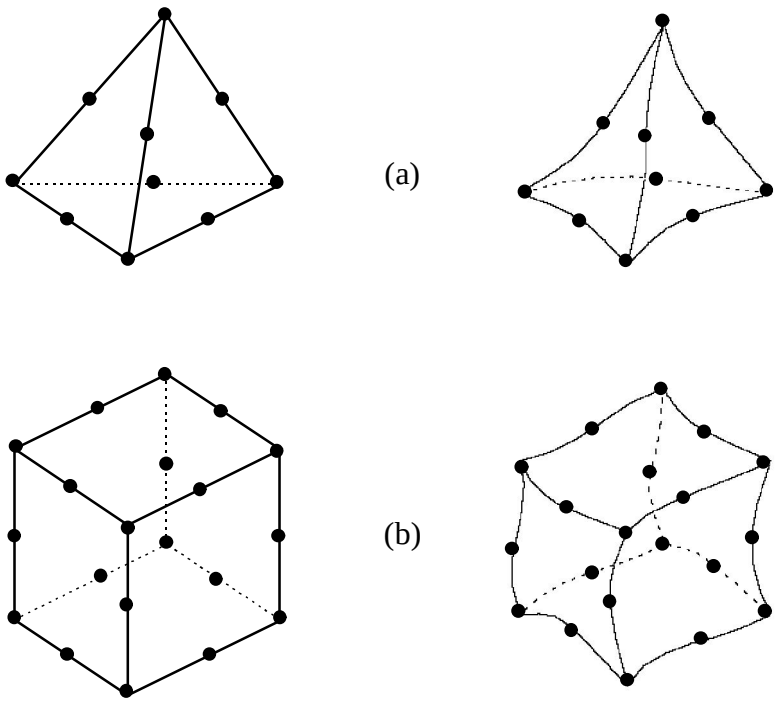

Figure 4.1. Three-dimensional second-order finite elements. (a) Master tetrahedron, 10 nodes in local space (ξ, η, ζ), and actual tetrahedron, 10 nodes in global space (x, y, z). (b) Master hexahedron, 20 nodes in local space (ξ, η, ζ), and actual hexahedron, 20 nodes in global space (x, y, z).

electrical potential in the piezoelectric parts. The combination coefficients, known as interpolation functions, are expressed in terms of the local co-ordinates of the element. A common choice is to use second order quadratic functions, which require nodes to be placed at the corners and mid-points of the edges of the element (figure 4.1). If the same interpolation functions are used for all the physical quantities, the element is said to be isoparametric.

4.2.1 Virtual Work

The electroelastic finite element equations are derived by applying the principles of minimum virtual work [4.7]. The work done by external forces $\{F_A\}$ when displacement and strain change by small amounts, $\{\delta u\}$ and $\{\delta S\}$ respectively, must equal the change in the potential and kinetic energies. Thus

$$\{\delta u\}\{F_A\} = \int_V \{\delta S\}^{\mathrm{T}}\{T\}dV + \rho\int_V \{\delta u\}\{\ddot{u}\}dV \tag{4.1a}$$

where $\{T\}$ is the stress vector and ρ is the material density.

The work done by the applied charges $\{Q\}$ when the potential and electric field change by small amounts, $\{\delta\phi\}$ and $\{\delta E\}$ respectively, equals the change in electrical potential energy within the volume. Thus

$$\{\delta\phi\}\{Q\} = \int_V \{\delta E\}^{\mathrm{T}}\{D\}dV \tag{4.1b}$$

where $\{D\}$ is the dielectric displacement vector.

Substituting the piezoelectric relationships for stress and electric flux density given in Chapter 2,

$$\{T\} = [c^E]\{S\} - [e]^{\mathrm{T}}\{E\} \tag{4.2a}$$

$$\{D\} = [e]\{S\} + [\varepsilon^S]\{E\} \tag{4.2b}$$

into equations (4.1a) and (4.1b), respectively, we obtain

$$\{\delta u\}^{\mathrm{T}}\{F_A\} = \int_V \{\delta S\}^{\mathrm{T}}[c^E]\{S\}dV - \int_V \{\delta S\}^{\mathrm{T}}[e]^{\mathrm{T}}\{E\}dV + \int_V \{\delta u\}^{\mathrm{T}}\rho\{\ddot{u}\}dV \tag{4.3a}$$

$$\{\delta\phi\}^{\mathrm{T}}\{Q\} = \int_V \{\delta E\}^{\mathrm{T}}[e]\{S\} + \int_V \{\delta E\}^{\mathrm{T}}[\varepsilon^S]\{E\}dV \tag{4.3b}$$

4.2.2 Representation of Losses by Complex Numbers

In practice, energy losses occur in all materials, in the sense that a portion of the mechanical and electrical energy is converted to heat rather than into the required acoustic energy. In a piezoelectric material, excited by an alternating electric field, losses can be phenomenologically separated into three components. These include elastic and dielectric hysteresis effects. A third loss component in piezoelectric materials has also been identified, which represents imperfect piezoelectric energy conversion [4.18]; however, data for such losses are not generally available.

To take into account internal losses, we introduce complex values for material coefficients and constants. This gives a good representation of ordinary losses if we assume harmonic time

dependence. Extraordinary losses (non-linearities) are not explicitly modelled. However, they may be artificially included in the imaginary part of the material coefficients and constants.

Thus the elastic stiffness coefficient matrix, the piezoelectric stress constant matrix, and the dielectric constant matrix are defined respectively as,

$$\left[c^E\right] = \left[c_x^E\right] - j\left[c_y^E\right] \tag{4.4a}$$

$$\left[e\right] = \left[e_x\right] - j\left[e_y\right] \tag{4.4b}$$

$$\left[\varepsilon^S\right] = \left[\varepsilon_x^S\right] - j\left[\varepsilon_y^S\right] \tag{4.4c}$$

It should be noted that the imaginary parts of the above coefficients and constants are required to be negative as this corresponds to negative phase angle and hence positive loss [4.18].

A major problem is finding reliable values for the imaginary part of the material coefficients and constants. When manufacturer's data are available, material losses are usually expressed by loss tangents or quality factors. These elastic, piezoelectric, or dielectric loss values are related to their respective complex coefficients or constants in the following manner;

$$\tan\left(\delta_m\right) = \frac{1}{Q_m} = -\frac{\Im m\left[c^E\right]}{\Re e\left[c^E\right]} \tag{4.5a}$$

$$\tan\left(\delta_p\right) = \frac{1}{Q_p} = -\frac{\Im m\left[e\right]}{\Re e\left[e\right]} \tag{4.5b}$$

$$\tan\left(\delta_e\right) = \frac{1}{Q_e} = -\frac{\Im m\left[\varepsilon^S\right]}{\Re e\left[\varepsilon^S\right]} \tag{4.5c}$$

4.2.3 Finite Element Formulation

To generate the electroelastic matrix relations for a finite element, the displacement and potential are expressed in term of *n* nodal values via interpolation functions [4.4] N_u and N_ϕ

$$\left\{u\right\} = \left[N_u\right]\left\{u_n\right\} \tag{4.6a}$$

$$\left\{\phi\right\} = \left\langle N_\phi\right\rangle\left\{\phi_n\right\} \tag{4.6b}$$

where

$$\left[N_u\right]=\begin{bmatrix} N_1 & 0 & 0 & \cdot & \cdot & \cdot & N_n & 0 & 0 \\ 0 & N_1 & 0 & \cdot & \cdot & \cdot & 0 & N_n & 0 \\ 0 & 0 & N_1 & \cdot & \cdot & \cdot & 0 & 0 & N_n \end{bmatrix}$$

$$\left\langle N_\phi \right\rangle = \left\langle N_1 \quad \cdot \quad \cdot \quad \cdot \quad N_n \right\rangle$$

Differentiating equations (4.6a) and (4.6b) yields expressions for the strains and electric field (negative potential gradient)

$$\{S\} = \left[B_u\right]\{u_n\} \tag{4.7a}$$

$$\{E\} = -\left[B_\phi\right]\{\phi_n\} \tag{4.7b}$$

where

$$\left[B_u\right]=\begin{bmatrix} \frac{\partial N_1}{\partial x} & 0 & 0 & \cdot & \cdot & \cdot & \frac{\partial N_n}{\partial x} & 0 & 0 \\ 0 & \frac{\partial N_1}{\partial y} & 0 & \cdot & \cdot & \cdot & 0 & \frac{\partial N_n}{\partial y} & 0 \\ 0 & 0 & \frac{\partial N_1}{\partial z} & \cdot & \cdot & \cdot & 0 & 0 & \frac{\partial N_n}{\partial z} \\ 0 & \frac{\partial N_1}{\partial z} & \frac{\partial N_1}{\partial y} & \cdot & \cdot & \cdot & 0 & \frac{\partial N_n}{\partial z} & \frac{\partial N_n}{\partial y} \\ \frac{\partial N_1}{\partial z} & 0 & \frac{\partial N_1}{\partial x} & \cdot & \cdot & \cdot & \frac{\partial N_n}{\partial z} & 0 & \frac{\partial N_n}{\partial x} \\ \frac{\partial N_1}{\partial y} & \frac{\partial N_1}{\partial x} & 0 & \cdot & \cdot & \cdot & \frac{\partial N_n}{\partial y} & \frac{\partial N_n}{\partial x} & 0 \end{bmatrix}$$

$$\left[B_\phi\right]=\begin{bmatrix} \frac{\partial N_1}{\partial x} & \cdot & \cdot & \cdot & \frac{\partial N_n}{\partial x} \\ \frac{\partial N_1}{\partial y} & \cdot & \cdot & \cdot & \frac{\partial N_n}{\partial y} \\ \frac{\partial N_1}{\partial z} & \cdot & \cdot & \cdot & \frac{\partial N_n}{\partial z} \end{bmatrix}$$

Using the above relationships, the energy equations (4.3a) and (4.3b) can be rewritten as follows

$$\{F_A\} = \left[K_{uu}\right]\{u_n\} + \left[K_{u\phi}\right]\{\phi_n\} + \left[M\right]\{\ddot{u}_n\} \tag{4.8a}$$

$$\{-Q\} = \left[K_{\phi u}\right]\{u_n\} + \left[K_{\phi\phi}\right]\{\phi_n\} \tag{4.8b}$$

where

$$\left[K_{uu}\right] = \int_V \left[B_u\right]^{\mathrm{T}} \left[c^E\right] \left[B_u\right] dV$$

$$\left[K_{u\phi}\right] = \int_V \left[B_u\right]^{\mathrm{T}} \left[e\right] \left[B_\phi\right] dV$$

$$\left[K_{\phi u}\right] = \int_V \left[B_\phi\right]^{\mathrm{T}} \left[e\right] \left[B_u\right] dV$$

$$\left[K_{\phi\phi}\right] = -\int_V \left[B_\phi\right]^{\mathrm{T}} \left[\varepsilon^E\right] \left[B_\phi\right] dV$$

and

$$\left[M\right] = \rho \int_V \left[N_u\right]^{\mathrm{T}} \left[N_u\right] dV$$

The matrices $[K_{uu}]$, $[K_{u\phi}]$, $[K_{\phi u}]$, and $[K_{\phi\phi}]$, are referred to as the mechanical, piezoelectric, transposed piezoelectric, and dielectric stiffness matrices respectively. Matrix $[M]$ is referred to as the mass matrix.

By performing a static condensation of the $\{\phi\}$ degrees of freedom, equations (4.8a) and (4.8b) can be rewritten as

$$\left[M\right]\left\{\ddot{u}_n\right\} + \left[K\right]\left\{u_n\right\} = \left\{F\right\} \tag{4.9}$$

where $[K]$ is the condensed electroelastic stiffness matrix

$$\left[K\right] = \left[K_{uu}\right] - \left[K_{u\phi}\right]\left[K_{\phi\phi}\right]^{-1}\left[K_{\phi u}\right]$$

and $\{F\}$ is the corresponding electromechanical forcing function

$$\left\{F\right\} = \left\{F_A\right\} - \left[K_{u\phi}\right]\left[K_{\phi\phi}\right]^{-1}\left\{-Q\right\}$$

For harmonic vibration at a frequency ω, in radians per second, equation (4.9) becomes (time factor $e^{j\omega t}$ understood)

$$\left[-\omega^2\left[M\right] + \left[K\right]\right]\left\{u_n\right\} = \left\{F\right\} \tag{4.10}$$

Prior to solution of equation (4.10) the number of unknown quantities is reduced by applying boundary conditions and other fixities. For example, the nodal components of potential can be taken to be zero on the earth electrode surfaces and at any point outside the piezoelectric elements. Additionally, geometrical symmetry, either axial or mirror, may be exploited to further reduce the number of unknowns.

The solution of the reduced or modified form of equation (4.10) can be accomplished by using a standard method, such as Gauss elimination, or LU decomposition, provided that all the external forces and charges can be specified. For a transducer operating in air there is assumed to be no external loading and hence the external forces are equal to zero. The charges are set to a nominal value on the non-earthed electrode surfaces and zero elsewhere.

Once nodal values of displacement and electric potential have been determined, strain and electric field strength can be found from equations (4.7a) and (4.7b) respectively, and then stress and electric flux density from equations (4.2a) and (4.2b) respectively.

The solution values for electric potential at the non-earthed electrodes can also be used to derive the admittance response. The relationship between admittance Y and electric potential ϕ is given by

$$Y = \frac{i}{\phi} \tag{4.11}$$

where i is electric current and is defined as (time factor $e^{j\omega t}$ understood)

$$i = \frac{\partial Q}{\partial t} = j\omega Q \tag{4.12}$$

Thus,

$$Y = j\omega \frac{Q}{\phi} \tag{4.13}$$

The admittance may be decomposed into its real and imaginary components, its conductance G and susceptance B, so that

$$Y = G + jB \tag{4.14}$$

The inverse of the admittance is the impedance Z; that is,

$$Z = \frac{1}{Y} \tag{4.15}$$

This may also be broken down into its real and imaginary components, its resistance R and reactance X, so that

$$Z = R + jX \tag{4.16}$$

It will often be useful to be able to convert between the resistance and reactance components and the conductance and susceptance components. Thus,

$$R + jX = \frac{1}{G + jB} = \frac{G - jB}{G^2 + B^2}$$

Equating the real and imaginary parts, we have

$$R = \frac{G}{G^2 + B^2} \tag{4.17a}$$

$$X = \frac{-B}{G^2 + B^2} \tag{4.17b}$$

Similarly, it can be shown that

$$G = \frac{R}{R^2 + X^2} \tag{4.18a}$$

$$B = \frac{-X}{R^2 + X^2} \tag{4.18b}$$

4.3 The Boundary Element Method

By contrast with the finite element method only the surfaces of the structure need be discretised. Thus, the three-dimensional problem is reduced to a two-dimensional one. As with finite elements, the geometry of each boundary element, which is defined by a discrete number of nodes, is mapped onto a local co-ordinate system. The physical quantities of interest on the structure's surface are expressed in terms of the values at the nodal points by interpolation functions. Again, quadratic isoparametric elements (figure 4.2) are preferred as the same interpolation functions can be implemented for both the physical quantity approximation and the global-to-local geometrical transformation.

In the case of a vibrating surface surrounded by an infinite region of compressible fluid the requirement is to solve the wave equation

$$\nabla^2\theta - \frac{\ddot{\theta}}{c^2} = 0 \tag{4.19}$$

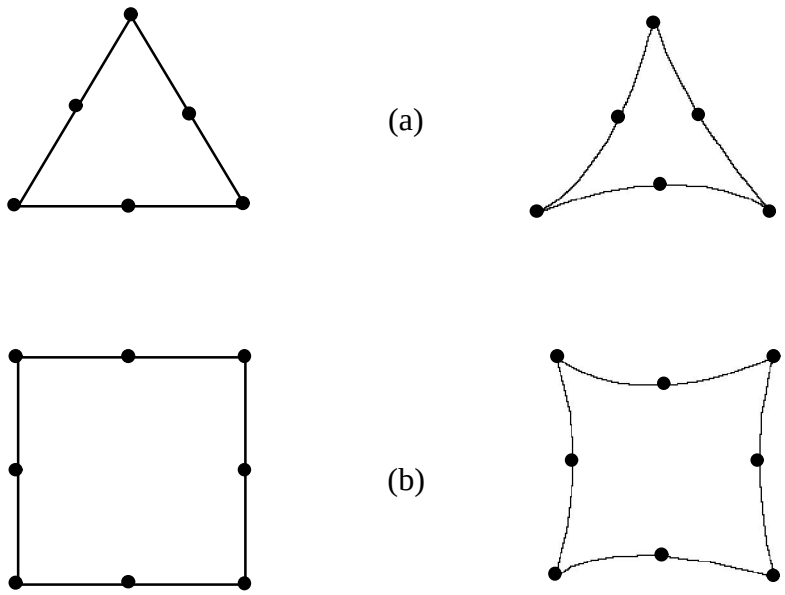

Figure 4.2. Two-dimensional second-order finite elements. (a) Master trigon, 6 nodes in local space (ξ, η, ζ), and actual trigon, 6 nodes in global space (x, y, z). (b) Master tetragon, 8 nodes in local space (ξ, η, ζ), and actual tetragon, 8 nodes in global space (x, y, z).

where θ is the acoustic pressure and c is the sound speed in the fluid. For steady state harmonic problems (time variation $e^{j\omega t}$) this reduces to the Helmholtz equation

$$\left(\nabla^2 + k^2\right)\theta = 0 \tag{4.20}$$

where $k = \omega/c$ is the wavenumber and ω is the frequency in radians per second. The radiation condition

$$\lim_{r\to\infty} \int \left(\frac{\partial \theta}{\partial r} + jk\theta \right)^2 dS = 0 \tag{4.21}$$

where S is the total surface area, ensures that the pressure field consists only of outgoing waves. Finally the Neumann boundary condition

$$\frac{\partial \theta}{\partial n} = -j\omega\rho\dot{u} \tag{4.22}$$

where ρ is the fluid density, enforces continuity of normal velocity $\dot{u}$ on the vibrating surface.

Using Green's integral theorem, the Helmholtz equation can be represented by an integral form in which the pressure at any point p is obtained in terms of an integral over the radiating surface

[4.11, 4.12, 4.19]; with the inclusion of an incident pressure term $\theta_{inc}(p)$ this takes the following form:

$$\int_S \left\{ \theta(p) \frac{\partial G_k(p,q)}{\partial n_q} - G_k(p,q) \frac{\partial \theta(q)}{\partial n_q} \right\} dS_q = \beta(p)\theta(p) - \theta_{inc}(p) \tag{4.23}$$

where G_k is the free space Green's function

$$G_k(p,q) = \frac{e^{-jkr}}{4\pi r}, \qquad r = |p-q|$$

and the value of β depends on the position of p: for p inside S, $\beta(p) = 0$; for p outside S, $\beta(p) = 1$; for p on S, $4\pi\beta(p) =$ solid angle occupied by the fluid at p.

The coefficient matrices, as in the finite element method, are assembled by calculating the element contributions. The element contributions are obtained by the evaluation of the surface integral (4.23) in terms of pressure θ and normal pressure gradients $\partial\theta/\partial n$. The response matrices of the individual elements are then assembled in a systematic fashion and with the Neumann boundary condition (4.22) enforced the system matrix can be written as

$$[A]\{\theta\} = [B]\{v\} - \{\theta_{inc}\} \tag{4.24}$$

where [*A*] and [*B*] are global matrices given by integral expressions [4.11, 4.12]. For a surface with a prescribed velocity distribution this equation can be solved for the surface pressures. The acoustic pressure at any point in the field can then be determined numerically using the external form of the Helmholtz equation (4.23). For the fluid-structure interaction problem the surface velocities are unknown and equation (4.24) must be solved simultaneously with the finite element equation (4.10).

4.4 The Combined Method

For fluid-structure interaction problems the boundary element equation must be solved simultaneously with the finite element equation [4.19]. There are two main possibilities for linking the equations, the structure-variable methodology, and the fluid-variable methodology [4.20]. In the first, the boundary element equation is inverted and then substituted into the finite element equation. In the latter, the finite element equation is inverted and then substituted into the boundary element equation. The former approach is preferred as the integration of the two

numerical methods is simpler. A further benefit of the structure-variable approach is that secondary fluid regions can be included.

The structure-variable methodology will now be described since this is the method used by the author. The fluid interaction force F_l is related to the acoustic pressure on the surface θ by the coupling matrix L [4.20] such that

$$\{F_l\} = \pm[L]\{\theta\} \tag{4.25}$$

where (+) corresponds to an internal fluid region and (–) corresponds to an external fluid region. The boundary element equation (4.24) is inverted

$$\{\theta\} = j\omega[A]^{-1}[B]\{u\} - [A]^{-1}\{\theta_{inc}\} \tag{4.26}$$

where the velocity vector $\{\dot{u}\}$ has been replaced by the node displacement vector $\{u\}$ using the expression

$$\{\dot{u}\} = j\omega\{u\} \tag{4.27}$$

F_l is then substituted into the finite element equation (4.10), to obtain

$$\left[-\omega^2[M]+[K]+ j\omega[L][A]^{-1}[B]\right]\{u\} = \{F\} + \left[[L][A]^{-1}\right]\{\theta_{inc}\} \tag{4.28}$$

As in the standard finite element method, the solution of equation (4.28) can be accomplished by using one of the standard linear algebra methods, such as Gauss elimination, or LU decomposition. Once nodal values of displacement and electric potential have been determined, strain and electric field strength can be found from equations (4.7a) and (4.7b) respectively, and then stress and electric flux density from equations (4.2a) and (4.2b) respectively. Solutions for the displacements also enable the surface pressures to be determined from equation (4.26), while the electric potential at the non-earthed electrodes can be used to derive the electrical admittance. Using equation (4.23) it is possible to calculate the acoustic pressure at any point in the field, thereby allowing the beam pattern and the projector voltage sensitivity on the acoustic axis to be found. The total acoustic power output can be determined by a surface integration. The ratio of the acoustic power and the electrical power gives the efficiency of the transducer, and by comparing acoustic power with the projector voltage sensitivity on the acoustic axis it is possible to calculate the directivity index of the transducer. Finally, when the analysis is performed over a suitable frequency range information regarding the resonance frequencies and bandwidths of the structure can be evaluated.

4.5 References

[4.1] J. N. Decarpigny, B. Hamonic, and O. B. Wilson, 'The Design of Low-Frequency Underwater Acoustic Projectors: Present Status and Future Trends', *IEEE J. Oceanic Eng.*, 16(1), 107-122, (1991).

[4.2] G. W. Benthien, 'The Direction of Transducer and Array Modeling in the 1990s', in *Transducers for Sonics and Ultrasonics*, M. D. McCollum, B. F. Hamonic, and O. B. Wilson, eds., (Lancaster, PA: Technomic Publishing Co. Inc., 1993), 66-76.

[4.3] R. Coates, 'Modeling Acoustic Transducers: Problems and Some Possible Solutions', *IEEE OCEANS '90*, 544-549, (1990).

[4.4] O. C. Zienkiewicz, 'The Finite Element Method', (McGraw-Hill, 1977).

[4.5] B. V. Smith, 'Finite Element Principles', *Proc. I. O. A.*, 10(9), 16-37, (1988).

[4.6] P. C. Macey, 'Fluid Loading and Piezoelectric Elements', *Proc. I. O. A.*, 10(9), 79-104, (1988).

[4.7] H. Allik and T. J. R. Hughes, 'Finite Element Method for Piezoelectric Vibration', *Int. J. Num. Meth. Eng.*, 2, 151-157, (1970).

[4.8] B. Hamonic, J. C. Debus, J. N. Decarpigny, D. Boucher, and B. Tocquet, 'Analysis of a Radiating Thin-Shell Sonar Transducer using the Finite Element Method', *J. Acoust. Soc. Am.*, 86(4), 1245-1253, (1989).

[4.9] J. N. Decarpigny, J. C. Debus, B. Hamonic, R. Bossut, P. Tierce, D. Morel, D. Boucher, and B. Tocquet, 'Finite Element Analysis of Low Frequency Sonar Transducers', *Proc. I. O. A.*, 9(2), 42-51, (1987).

[4.10] R. Bossut and J. N. Decarpigny, 'Finite Element Modeling of Radiating Structures using Dipolar Damping Elements', *J. Acoust. Soc. Am.*, 86(4), 1234-1244, (1989).

[4.11] D. T. I. Francis, 'A Gradient Formulation of the Helmholtz Integral Equation for Acoustic Radiation and Scattering', *J. Acoust. Soc. Am.*, 93(4), 1700-1709, (1993).

[4.12] D. T. I. Francis, 'A Boundary-Element Method for the Analysis of the Acoustic Field in Three-Dimensional Fluid-Structure Interaction Problems', *Proc. I. O. A.*, 12(4), 76-84, (1990).

[4.13] L. H. Chen and D. G. Schweikert, 'Sound Radiating from an Arbitrary Body', *J. Acoust. Soc. Am.*, 35, 1626-1632, (1963).

[4.14] G. Chertock, 'Sound Radiation from Vibrating Surfaces', *J. Acoust. Soc. Am.*, 36, 1305-1313, (1964).

[4.15] L. G. Coupley, 'Integral Equation Method for Radiation from Vibrating Bodies', *J. Acoust. Soc. Am.*, 41, 807-816, (1967).

[4.16] L. G. Coupley, 'Fundamental Results Concerning Integral Representations in Acoustic Radiation', *J. Acoust. Soc. Am.*, 44, 28-32, (1968).

[4.17] H. A. Schenck, 'Improved Integral Formulation for Acoustic Radiation Problem', *J. Acoust. Soc. Am.*, 44, 41-58, (1968).

[4.18] R. Holland, 'Representation of Dielectric, Elastic, and Piezoelectric Losses by Complex Coefficients', *IEEE Trans. on Sonics and Ultrasonics*, SU-14(1), 18-20,1967.

[4.19] R. P. Shaw, 'Coupling Boundary Integral Equation Methods to "Other" Numerical Techniques', in *Recent Advances in Boundary Element Methods*, C. A. Brebbia, ed., (Pentech Press, 1978), 137-147.

[4.20] I. C. Mathews, 'Numerical Techniques for Three-Dimensional Steady-State Fluid-Structure Interaction', *J. Acoust. Soc. Am.*, 79(5), 1317-1325, (1986).

Chapter 5

STRUCTURAL ANALYSIS

5.1 Introduction

Flextensional transducer technology has attracted considerable interest over the past two decades. Recently, research into underwater sound for applications in ocean acoustic tomography has renewed interest in the class I flextensional transducer, otherwise known as the 'barrel-stave' flextensional. This projector combines low-frequency, wide-bandwidth, high-efficiency, high-power operation with lightweight and compact geometry.

To design these projectors, the mathematical analysis is difficult and the optimisation is complicated by the large number of variables that need to be considered. The class I flextensional has previously been investigated using a theoretical approach as long ago as the 1960s. Since then, the development of the finite element and boundary element methods has provided superior numerical approximation tools for structural and acoustic analysis respectively. When these methods are combined a solution for submerged vibrating structures can be obtained with the effect of fluid loading taken into account.

The numerical analysis of acoustic transducers has becoming increasingly popular with the advent of cheap, powerful, personal computers. This has led to an increased understanding of the general principles that govern the operation of such devices. This technique has not been applied extensively to predict the performance of class I flextensional transducers. In this chapter the software package PHOEBE – a coupled finite element and boundary element software package for modelling of acoustic transducers, available within the Acoustics Group at the University of Birmingham – is summarised. Numerical modelling of a class I flextensional transducer is described and subsequent results from calculations are presented. A rigorous examination of the influence of the various design parameters on the transducer's performance is undertaken. More specifically, the design parameters investigated relate to the shell design, and the radius of the end-

plates. However, due to the infinite design possibilities, even when considering this limited set of parameters, the number of geometries has necessarily been restricted.

5.2 PHOEBE

A number of specialised numerical analysis packages now exist in the commercial and public sector that are dedicated to the design of electroacoustic transducers. The structure of these finite element or boundary element solution systems generally involves three distinct modules: (1) the pre-processor module; (2) the solution processor module; (3) the post-processor module. The pre-processor module deals with all the information necessary for the analysis of the problem. The module must accomplish three functions: (1) description of the geometry of the object; (2) mesh generation; (3) definition of the regions and the boundaries. The post-processor module outputs the relevant information. The module must perform two tasks: (1) extraction of significant information; (2) graphical presentation of numerical data.

PHOEBE [5.1, 5.2] is a three-dimensional transducer analysis package. This software, which runs on an IBM-compatible personal computer in the MS-DOS environment, was developed by S. S. Jarng and D. T. I. Francis at the University of Birmingham. PHOEBE uses a combined finite element and boundary element method that permits in-air and in-water modelling. Twenty-node quadratic isoparametric brick elements are implemented for the finite element mesh and the exposed faces of these elements, which represent the radiating face of the structure, are the boundary elements.

The pre-processor is rudimentary and requires the user to follow a lengthy set-up procedure that includes manual meshing. Provision does exist to exploit rotational and mirror symmetry and thus in symmetrical structures the number of elements in the mesh can be reduced. Nevertheless the procedure is still time-consuming and prone to error.

The post-processor produces numerical data files for the projector voltage sensitivity, electrical impedance, acoustic power, directivity pattern, node displacements, and mode shapes.

5.3 Analysis of a Slotted-Shell Flextensional Transducer

The first form of the class I flextensional transducer that is considered is the slotted shell type. In this style, the shell is circular in the hoop direction and incorporates a number of slots of uniform width that 'cut' the curved section of the shell to reduce the shell hoop stiffness. With this configuration the resonance frequency of the device is lowered and the acoustic power output is increased. In addition, the tendency for the shell to buckle under operation is reduced. The shell which is no longer solid, is open to the surrounding sea. However, the ingress of water is easily prevented by enclosing the transducer in a rubber boot. Unfortunately, the addition of the rubber boot presents a serious depth limitation; at depths above 100 metres the water pressure is great enough to force the rubber into the slots and this adversely effects the transducer's performance.

The structure on which the modelling has been based is shown in figure 5.1. The device is shown in concave form, although both concave and convex shells have been modelled. In designing a numerical model a balance has to be struck between its accuracy and the time required to generate a set of results. In this case the purpose of the model is to reveal the influence of the various design parameters on the transducer's performance rather than produce highly accurate results. Thus to reduce the computational demands, the model has been simplified by the omission of the pre-stress bolt and rubber boot. The simplified model consists of two end-plates, a shell, and a ceramic stack. In addition, an insulator is incorporated at each end of the stack to provide electrical isolation. The piezoelectric driving stack consists of eight ceramic rings (25 mm thick) connected by glue joints (0.1 mm thick). By utilising a small number of thick ceramic rings the performance degrading effect of glue joints is minimised (see Chapter 6, Section 6.4 for more details).

The initial 'base' values of the structure's dimensions are listed in table 5.1 and the standard materials and their properties in table 5.2. In all cases, unless otherwise specified, these dimensions and materials apply.

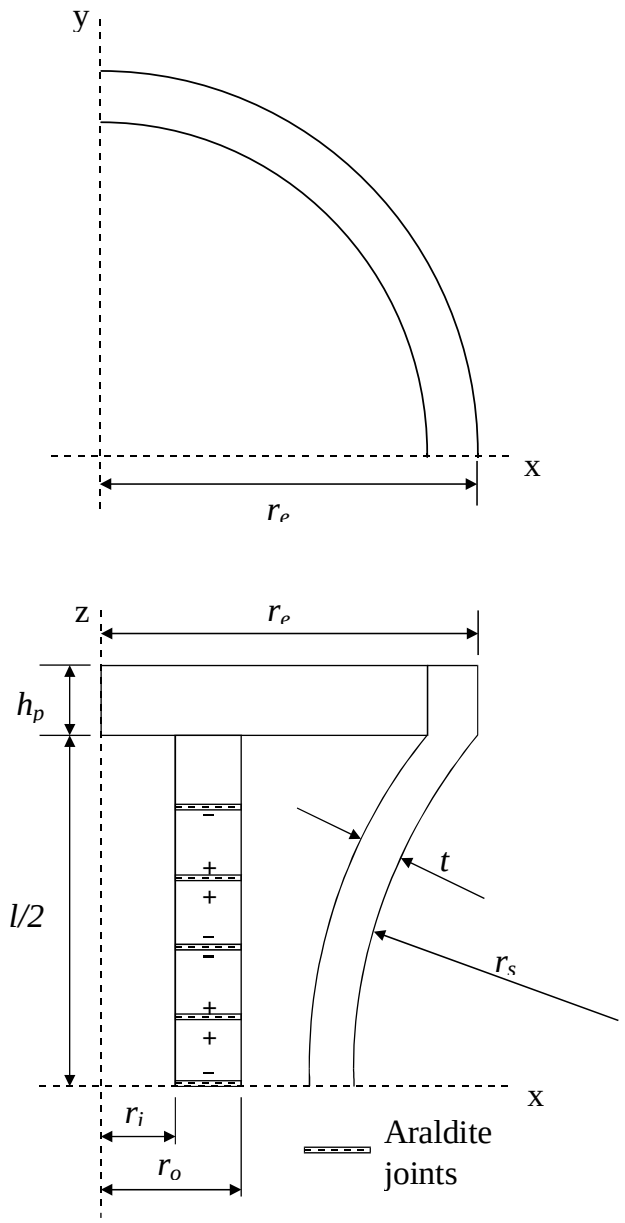

Figure 5.1. Geometric parameters of a slotted-shell transducer.

Table 5.1. Geometric parameters and their base values.

Parameter	Description	Base value
$c = 1/r_s$	Curvature of shell profile >0 for convex shell <0 for concave shell	4 m^{-1}
t	Shell thickness	15 mm
ℓ	Length between end-plates	250 mm
r_e	Radius at end of device	85 mm
h_p	End-plate thickness	30 mm
r_i	Inner radius of stack	20 mm
r_o	Outer radius of stack	40 mm
n	Order of rotational symmetry	12
s	Size ratio (scale factor applied to all linear dimensions of a given design)	(1)

Table 5.2. Standard materials and their properties.

Part	Material	Density (kg m^{-3})	Young's modulus (10^3 MPa)	Poisson's ratio	Mechanical quality factor Q_m
Ceramic	PZT-4™	See table 2.2			
Insulator	MACOR™	2520	140.0	0.29	500
End-plate	Steel	7960	193.0	0.31	10000
Shell	Aluminium	2710	68.91	0.30	1000
Glue joints	Araldite	1180	6.5	0.40	10

5.3.1 Mesh Generation

The finite element and boundary element modelling software, PHOEBE, has been used to compute the results presented in this thesis. As previously stated (Section 5.2), PHOEBE has no built-in mesh generation facilities and thus requires the user to supply the finite element and boundary element meshes. Each element in the mesh must constitute only one material and as far as possible resemble a cuboid. In addition, the largest linear dimension of any given element should preferably be less than a third of the acoustic wavelength in the material in order for the quadratic interpolation to provide a good approximation. This requirement is easily satisfied in the case of flextensional transducers, where the dimensions are small compared with the radiated acoustic wavelength.

Figure 5.2 depicts the complete structural mesh (for clarity the hidden lines have been removed) which consists of 528 elements. However, by invoking rotational symmetry, the order of which depends on the number of slots, and mirror symmetry in the xy-plane, it is possible to reduce the structural mesh to a half-segment (figure 5.3) that contains only 22 elements, consisting of 9 shell elements, 3 end-plate elements, 1 insulator element, 5 glue elements, and 4 ceramic elements. The boundary element mesh is taken as consisting of the exposed faces of the finite element mesh, and comprises 13 elements. To generate these meshes by hand is time consuming and prone to error. To overcome this problem the author has written a computer program that will generate meshes for any given class I flextensional transducer design presented in this thesis.

5.3.2 Preliminary Results

The fundamental in-air and in-water resonance frequencies for a slotted-shell transducer with the stated base dimensions are identified from the in-air (figure 5.4) and in-water (figure 5.5) admittance responses, respectively. Thus, the fundamental in-air resonance occurs at a frequency of 1570 Hz and the fundamental in-water resonance occurs at a frequency of 952 Hz.

The relative displacement field at the in-water resonance frequency is shown in figure 5.6. The diagram depicts the 'displaced' position relative to the at rest position. The displacement position is exaggerated by an arbitrary scale factor to allow it to be easily viewed. The piezoelectric stack, which converts electrical energy to mechanical energy (as an expansion and contraction motion) acts on the end-plates and thereby causes the shell to flex. In may be noted that the convex shell geometry causes the shell to move inwards with the expansion of the stack, thus the motion of the end-plates is 180° out of phase with the radiating shell. This appears to contradict the requirement that displacements over the surface should be in phase for maximum acoustic power radiation. However, the volume displacement over the end-plates is an order of magnitude smaller than that over the shell.

At higher resonance frequencies the 'flapping' motion of the shell tends to produce a cancellation effect in water that leads to inefficient operation. Thus, only the fundamental mode is of interest.

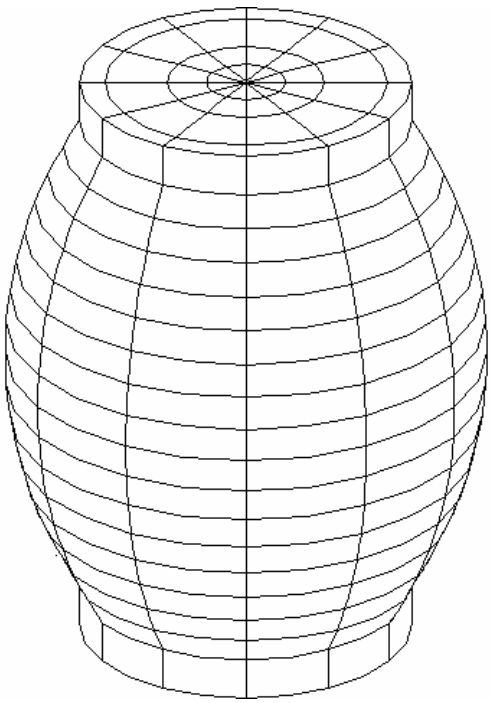

Figure 5.2. Structural mesh of the ‘base’ slotted-shell transducer.

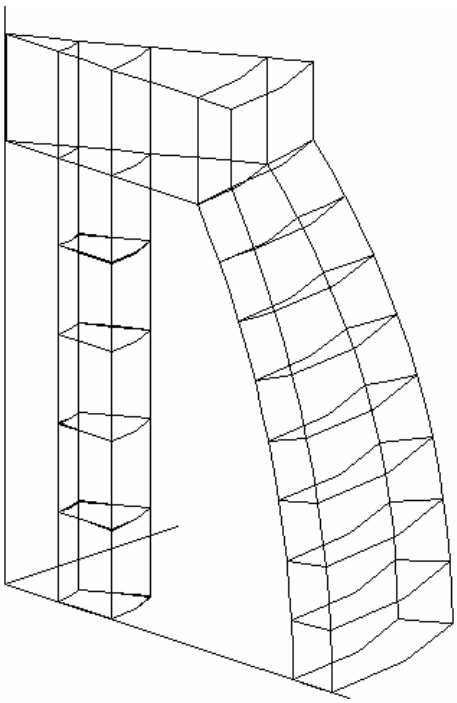

Figure 5.3. Half-segment mesh of the ‘base’ slotted-shell transducer.

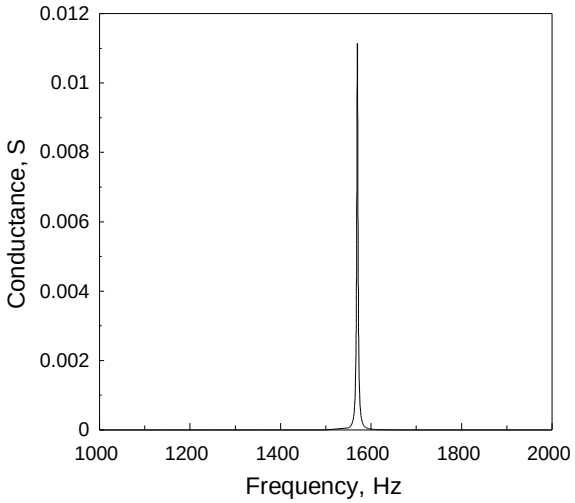

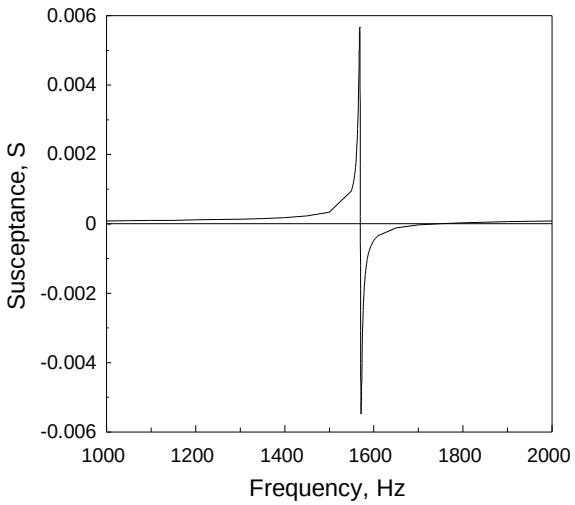

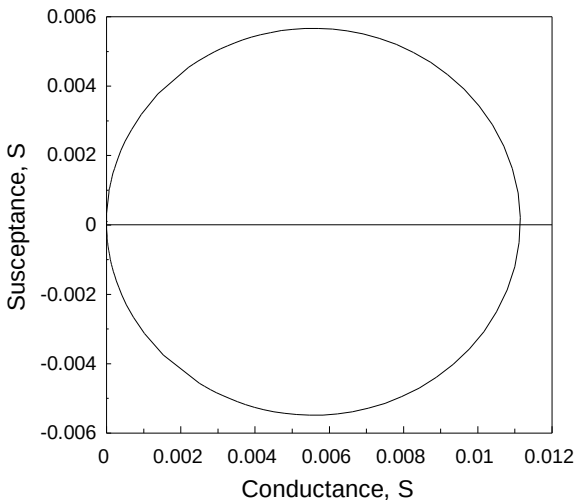

Figure 5.4. In-air admittance response for the 'base' slotted-shell transducer

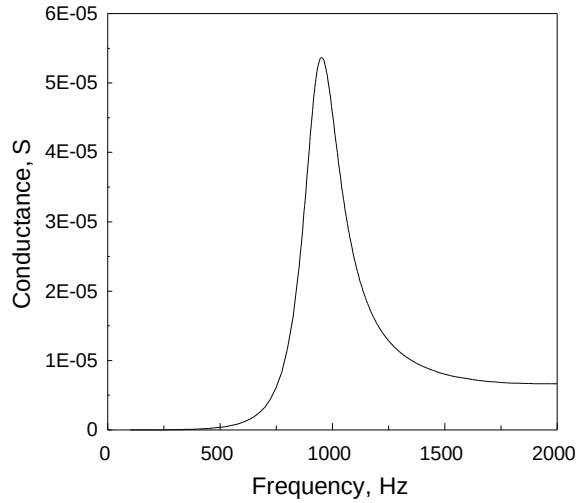

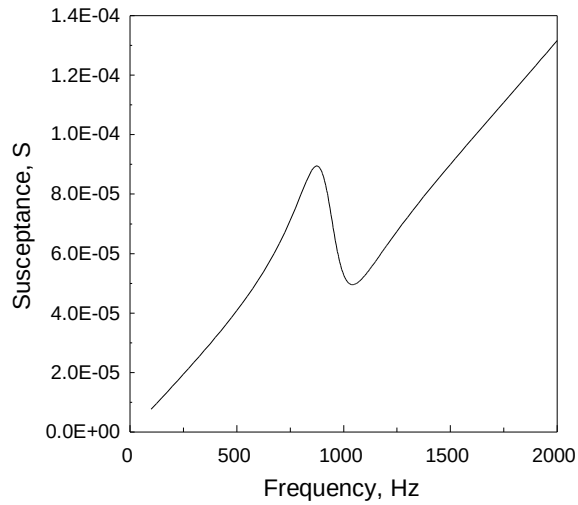

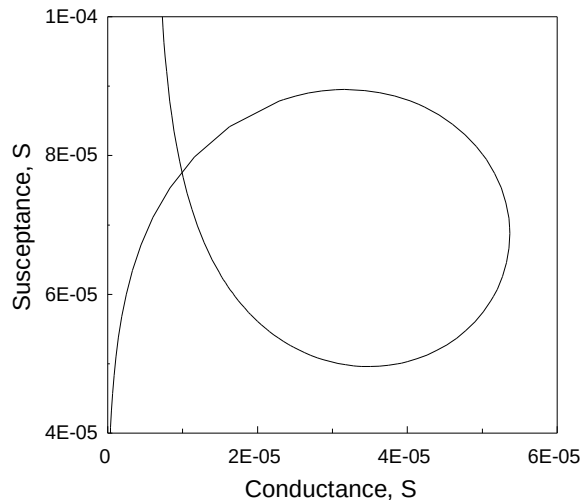

Figure 5.5. In-water admittance response for the 'base' slotted-shell transducer.

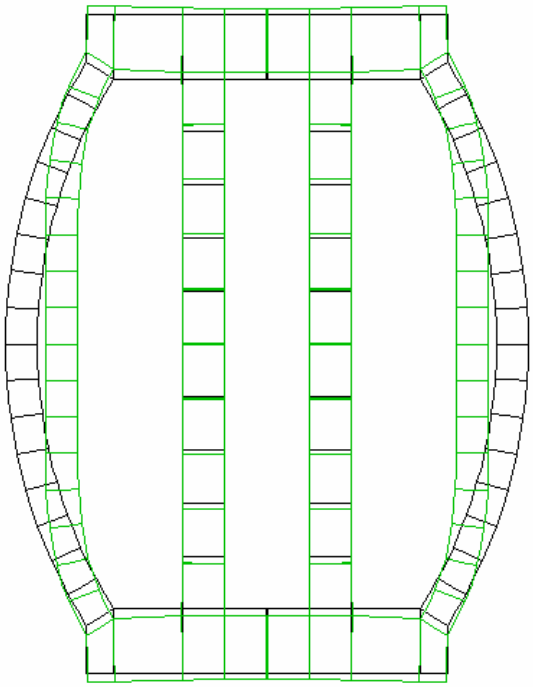

Figure 5.6. In-water relative displacement field for the 'base' slotted-shell transducer. Solid lines—at rest position. Dotted lines—displaced position.

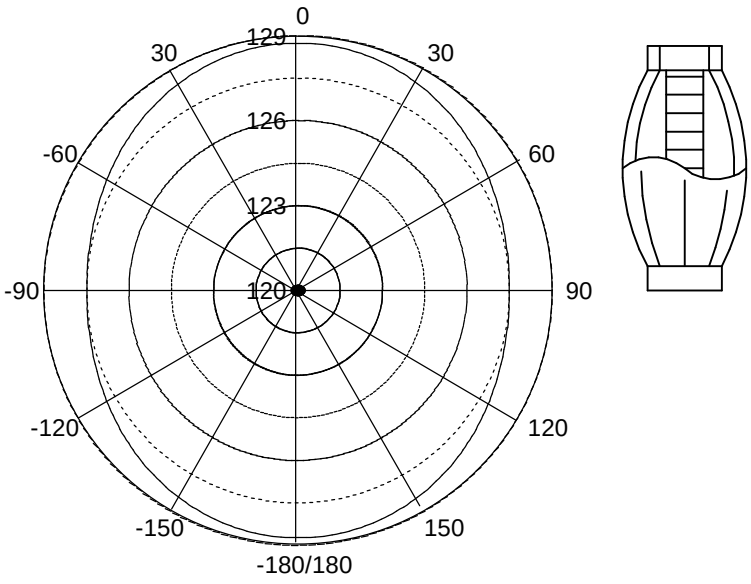

Figure 5.7. Far field sound pressure *vs.* direction in the vertical plane for the 'base' slotted-shell transducer (dB re. 1 μPa V^{-1} @ 1 m).

The polar plot of the far field sound pressure in the vertical plane, is shown figure 5.7. The pressures were computed at 10 m and scaled to dB re. 1 μPa V^{-1} @ 1 m. The difference between the maximum and minimum pressure is less than 3 dB, which demonstrates that the transducer is omnidirectional. This is to be expected as the transducer is small compared with the resonance wavelength.

The maximum acoustic power output is another important parameter. The factor which limits power in a piezoelectric transducer may have different origins: an electrical origin, a mechanical origin, or a thermal origin[†]. Depending on the transducer design and the required operating conditions, one of the above limitations will be encountered. However, for most applications, it is reasonable to assume that the acoustic power output is limited by the maximum electrical field that can be safely applied to the ceramic stack before electrical breakdown or depoling occurs. A conservative limiting electrical field of 200 kV r.m.s. m^{-1} is suggested in ref. [5.3], and this value is used to determine the maximum acoustic power output.

The acoustic output of a transducer is commonly rated according to its source level, SL, which represents its strength as an acoustic source. The relationship between acoustic power and source level is

$$\mathrm{SL}\left(\text{dB re. } 1\mu\text{Pa @ } 1\text{m}\right) = 170.9 + 10\log\left(P_a\right) + \mathrm{DI} \tag{5.1}$$

where DI is the directivity index of the transducer [5.4] (DI = 0 for omnidirectional sources).

The transducer's in-water performance characteristics are summarised in table 5.3.

Table 5.3. In-water performance characteristics of the 'base' slotted-shell transducer.

Parameter	Description	Value
f	Fundamental resonance frequency	952 Hz
P_a	Peak acoustic power	1327 W
SL	Source level	202.1 dB re. 1 μPa @ 1 m
η_{ea}	Efficiency	99.2 %
B	Bandwidth	221 Hz
Q	Q-factor	4.3

[†] Power limitations are discussed in Chapter 9.

Finally figures 5.8 and 5.9 compare the normalised radiation impedance seen by the flextensional transducer with that calculated for a spherical source with the same surface area. The radiation impedance of a spherical source is given [5.5] by

$$Z_r = ka\rho cA_S\left[\frac{ka + j}{1+(ka)^2}\right] \tag{5.2}$$

where $k = 2\pi f/c$ is the wavenumber (f is the frequency and c is the sound speed in the medium), a is a characteristic length (radius of the sphere), and A_S is the surface area. Equation (5.2) can be normalised by extracting a factor ρcA_S, resulting in an expression solely in terms of the dimensionless variable ka.

The radiation impedance seen by the sphere may be regarded as the ideal. From figures 5.8 and 5.9 we can see that the resistive load seen by the flextensional transducer is approximately half that seen by a sphere of equivalent surface area. The reactive load is similar in both cases. We can quantify these results by introducing some simple mechanical terms which have general applicability rather than depending on the particulars of a design. If the drive to a transducer is such as to generate a constant piston velocity, independent of frequency, then the output power P is given by

$$P = u^2 R_r \tag{5.3}$$

where u is the r.m.s. velocity of displacement of the radiating surface and R_r is the radiation resistance. This says that power is proportional to the radiation resistance. The mechanical quality factor Q is given by

$$Q = \frac{2\pi f M_e}{R_r} \tag{5.4}$$

where f is the resonance frequency and M_e is the effective vibrating mass. This says that power is inversely proportional to the radiation resistance.

The radiation reactance X_r may be thought of as an additional vibrating mass. This ‘extra’ mass has the effect of reducing the resonance frequency and increasing the mechanical quality factor.

Thus, the radiation resistance sets the upper limits of power and Q-factor.

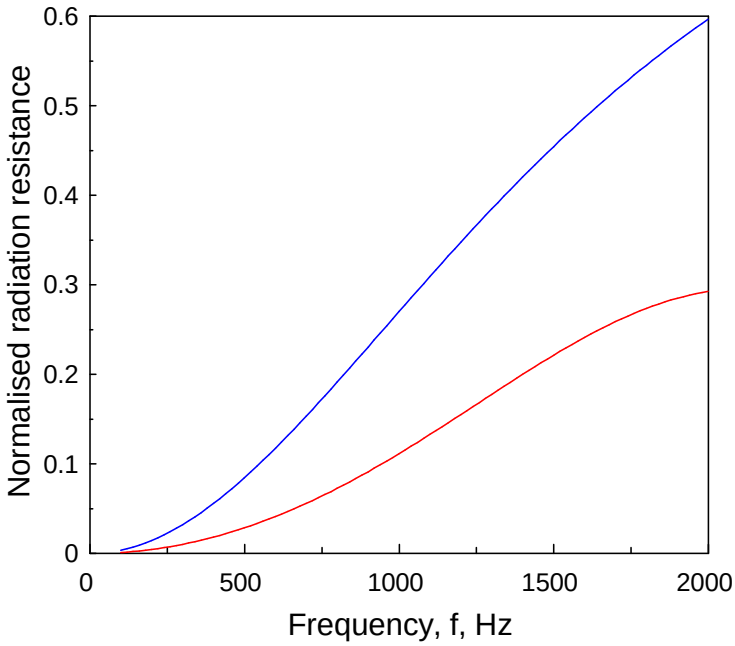

Figure 5.8. Normalised radiation resistance. Red line—flextensional transducer. Blue line—sphere with equivalent surface area.

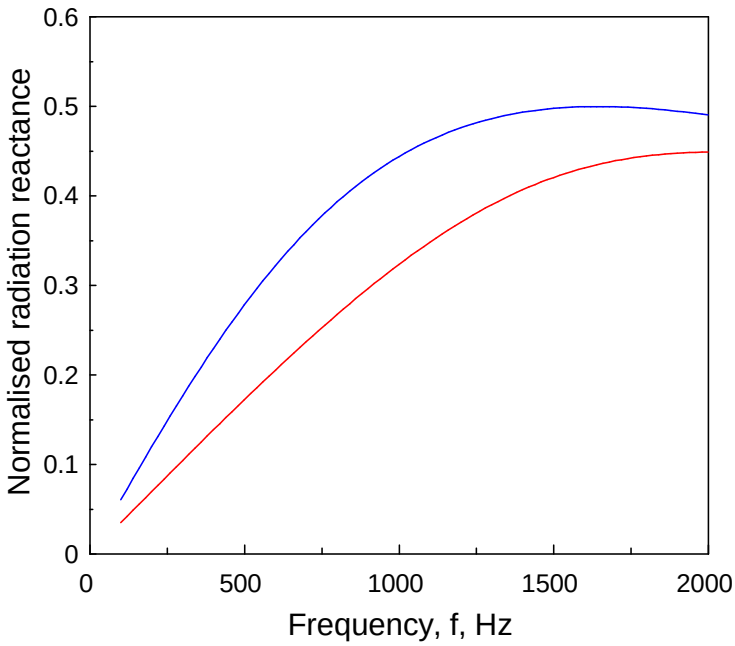

Figure 5.9. Normalised radiation reactance. Red line—flextensional transducer. Blue line—sphere with equivalent surface area.

The following section first examines the effect of scaling and then assesses the relationship between the geometry of the shell and the performance of the transducer. The performance characteristics of interest have been limited to resonance frequency, acoustic power, and quality factor.

5.3.3 Effects of Scaling

It is a well-known feature of acoustic problems that the governing equations can be written in terms of a dimensionless variable *ka* [5.6, 5.7]. Hence, for two geometrically similar problems the same solution applies if *ka* is unchanged. Thus, when scaling a particular design by a factor *s*, the resonance frequency varies in inverse proportion to the linear dimensions. The bandwidth, being the difference between two frequencies, also varies inversely, so the quality factor *Q* will remain constant. The limiting potential is proportional to the scaling factor, while the solution for conductance at the scaled resonance frequency is unchanged. The acoustic power *P* is therefore proportional to the square of the limiting potential and hence to the square of the linear dimension. The relationships are therefore,

$$f \propto \frac{1}{s} \tag{5.5a}$$

$$P \propto s^2 \tag{5.5b}$$

$$Q \propto 1 \tag{5.5c}$$

These relationships have been confirmed numerically: as shown in figure 5.10, the computed results support the theory within the accuracy of the numerical method.

The scaling relationships provide a useful simplification for the design process, in that they allow the effect of scaling a particular design to be predicted easily. In particular, if a design is obtained that satisfies the quality factor requirement, it can then be scaled to meet the required frequency. It should be noted that these relationships assume that all aspects of the design are scaled equally. In practice, certain features, for example the glue joints, may not scale precisely and some departure from the relationships may be expected.

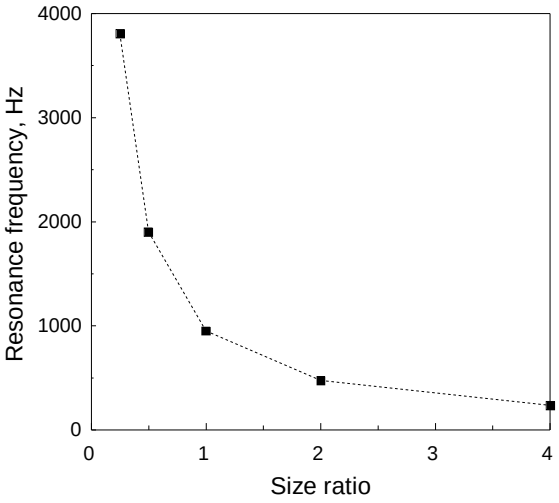

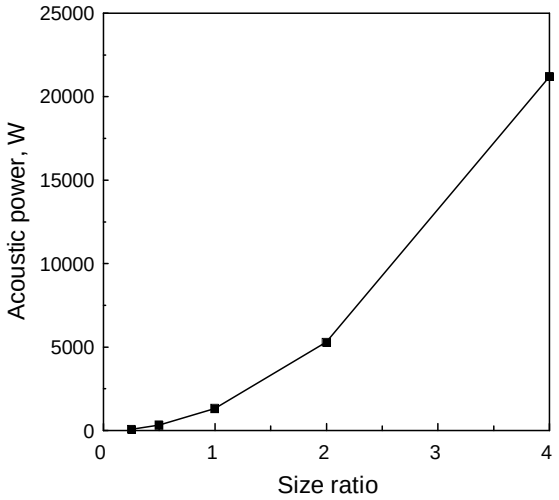

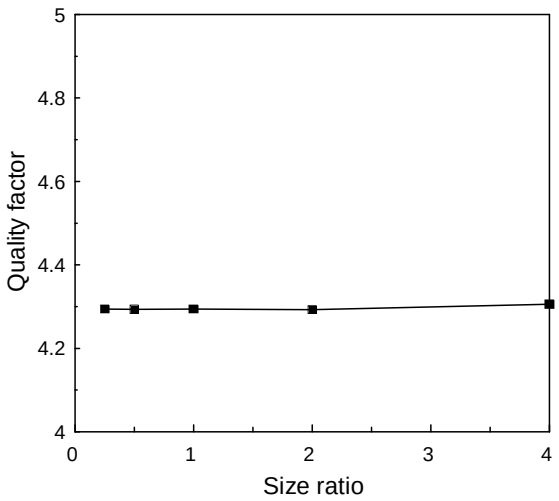

Figure 5.10. Effect on performance characteristics of scaling all dimensions.

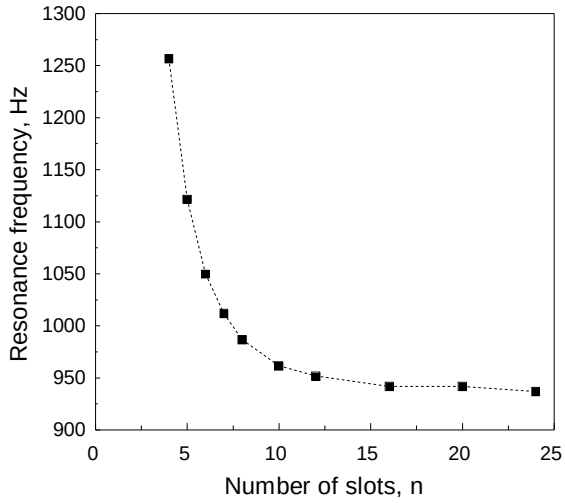

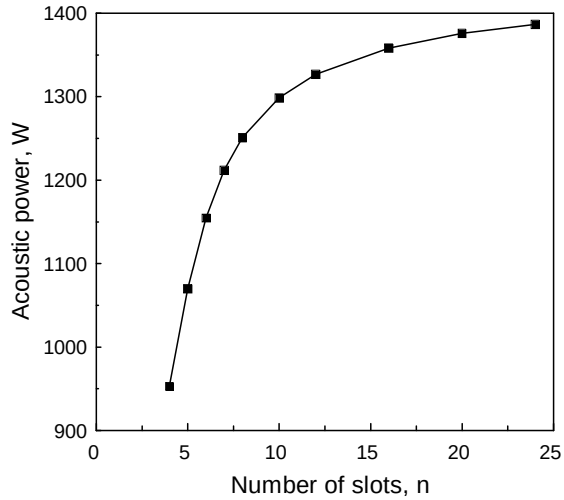

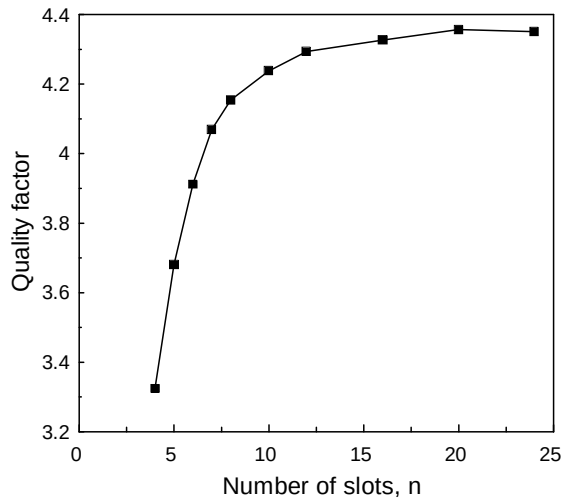

Figure 5.11. Variation of performance characteristics with the number of slots, *n*; all other parameters equal to their base values.

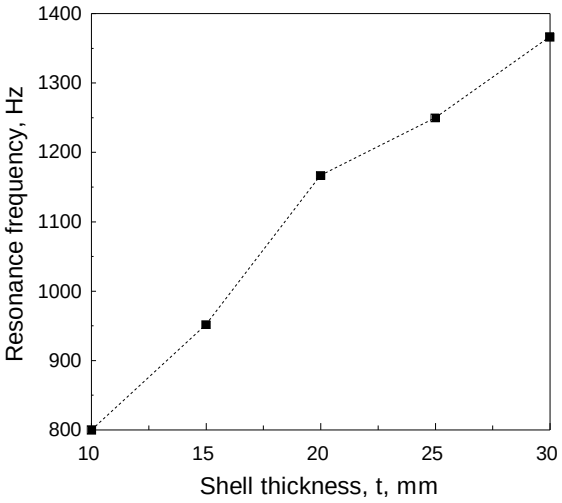

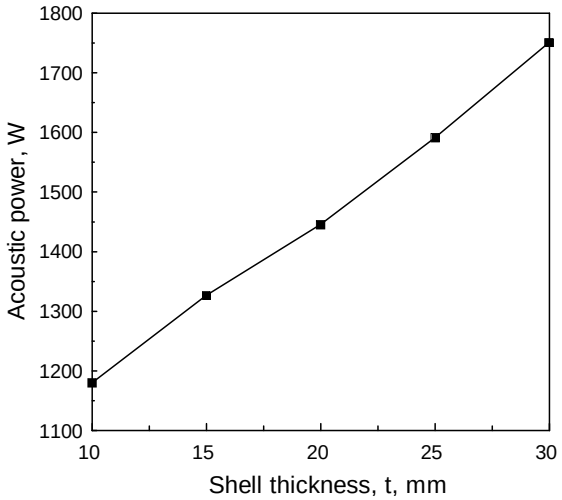

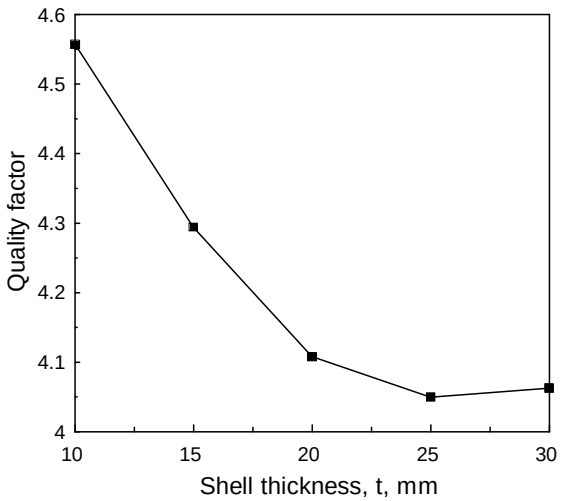

Figure 5.12. Variation of performance characteristics with shell thickness, *t*; all other parameters equal to their base values.

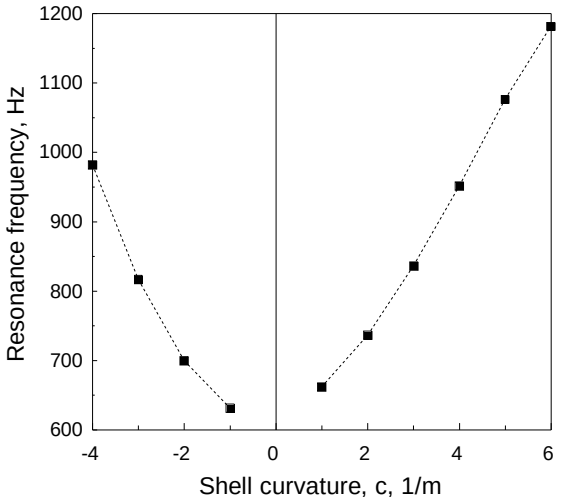

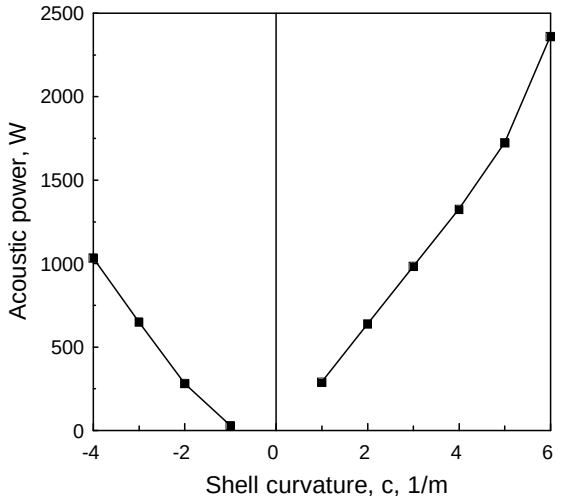

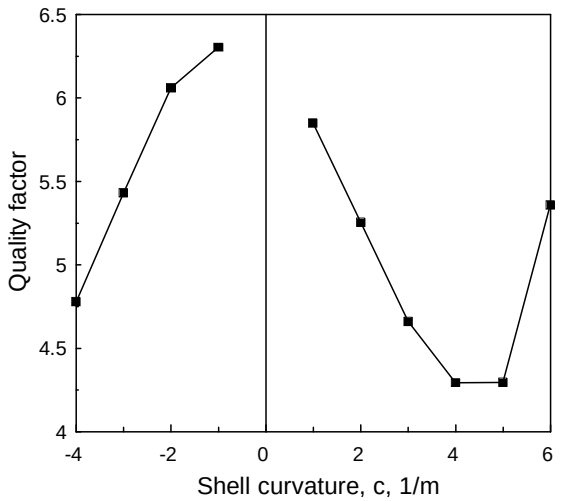

Figure 5.13. Variation of performance characteristics with shell curvature, *c*; all other parameters equal to their base values.

5.3.4 Effects of Varying the Geometry of the Shell

In this section the effects of varying the parameters of the shell about the base values are examined. This includes the number of slots in the shell, the shell thickness, and the shell curvature. The assessment of changing these parameters is biased towards the target specification of low-frequency, high-power, and low quality factor. The quality factor of the device is of paramount importance, since the required resonance frequency can be obtained by means of scaling, as previously explained, and acoustic power generally exceeds requirements. However, a low ratio of resonance frequency to size is desirable if size and weight are to be minimised.

The effect of varying the number of slots in the shell is shown in figure 5.11. As the number is increased, the flexural stiffness of the shell decreases, resulting in lower resonance frequencies. At the same time, the greater compliance of the staves permits them to vibrate at larger amplitudes; thus the acoustic power output increases. The increase in the quality factor may be attributed to the decrease in the radiation loading, which is the main source of damping in the system, as the resonance frequency decreases. The trend levels off at twelve slots; increasing the number of slots beyond this value only has a marginal effect. Since low-frequency and high-power are performance goals the optimum number of slots would appear to be twelve. However, one must also be aware that in reducing the flexural stiffness of the shell, it becomes weaker and increasingly susceptible to the effects of hydrostatic pressure. Thus, depending on the depth of operation, it may be preferable to employ eight to ten slots. These theoretical results reflect experimental results presented by D. F. Jones [5.8], though for a concave rather than convex device.

The performance characteristics for varying shell thickness are shown in figure 5.12. As the shell becomes thicker and stiffer, the resonance frequency increases. Acoustic power is also seen to increase. The quality factor reaches a minimum for a shell thickness of 25 mm.

Figure 5.13 shows the variation in resonance frequency, power capability and quality factor for varying shell curvature. Positive curvatures indicate a convex shell geometry, while negative values denote concave profiles. There is a practical limit to the curvature of a concave device imposed by the need for clearance between the shell and the driving stack. In the case of convex shell geometry, the resonance frequency and acoustic power increase with increasing curvature. The quality factor reaches an optimum value for a shell curvature of 4 m^{-1}. The results for the concave shell approximately mirror those of the convex shell, but with slightly increased quality factor and reduced power capability. The gap between the results arises from the difficulty of obtaining reliable values for small magnitudes of curvature. This is caused by the low response of the flexural mode of the shell when it is nearly straight.

5.4 Analysis of a Staved-Shell Flextensional Transducer

In the previous section results were presented for a class I flextensional transducer with a slotted shell that is circular in the hoop direction. In this section a similar device with a staved shell configuration is considered.

The structure on which the modelling has been based is illustrated in figure 5.14. The shell of the transducer is of segmented design; that is, the shell consists of a number of sections known as staves. These are curved in the axial direction but flat in the hoop direction. This configuration has the same advantages as the slotted shell arrangement, in that the hoop stiffness of the shell is reduced, and hence the resonance frequency of the device is lowered and acoustic power output is increased. The staves are coupled to the piezoelectric ceramic stack through metal end-plates. The end-plates are polygonal in shape since the internal and external surfaces of each stave are flat in the hoop direction. Since the device is polygonal in the hoop direction the radius at the end of the device, r_e, refers to the average radius. The driver stack is taken to consist of eight ceramic rings that are connected by glue joints of nominal thickness. An insulator at each end of the piezoelectric stack makes up the required length between the end-plates.

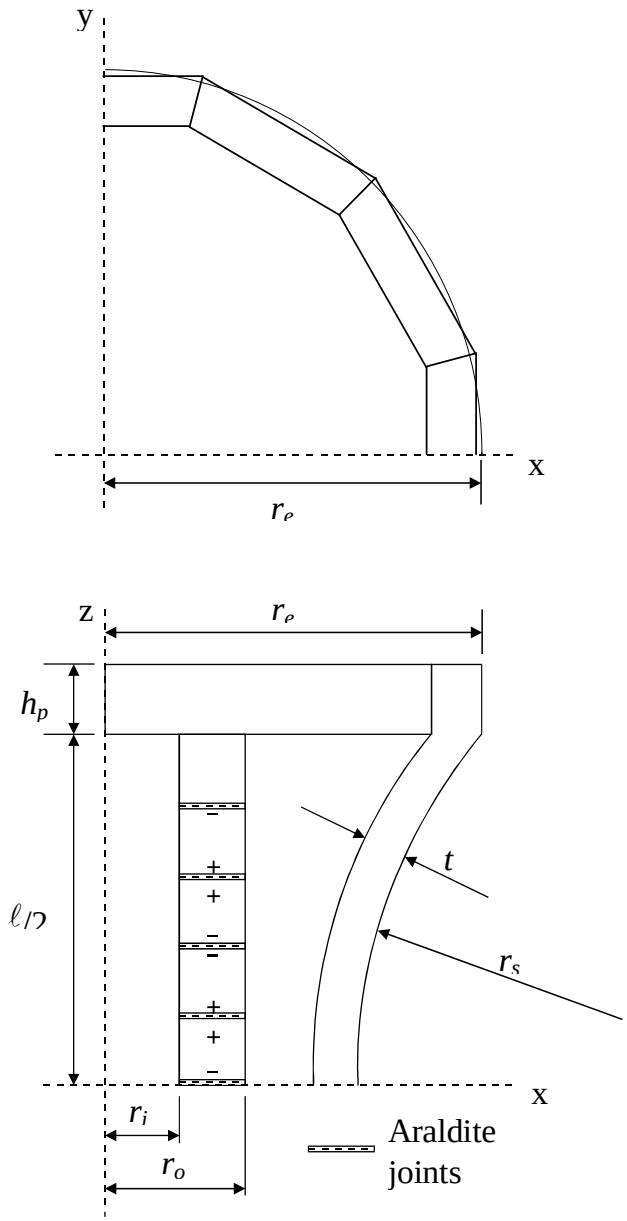

Figure 5.14. Geometric parameters of a staved-shell transducer.

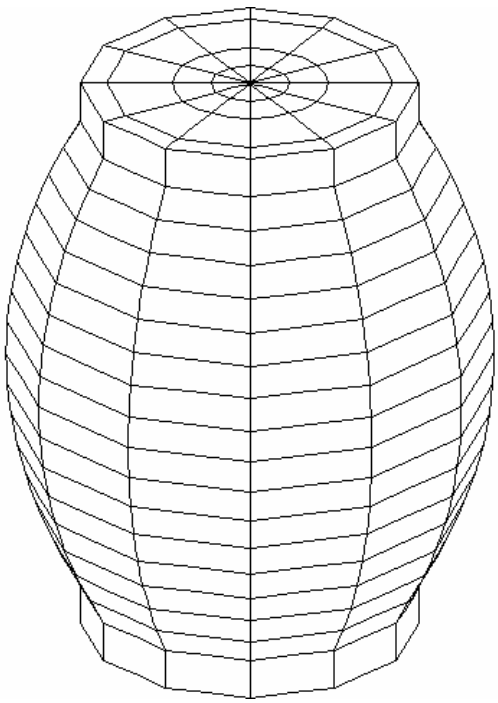

Figure 5.15. Structural mesh of the ‘base’ staved-shell transducer.

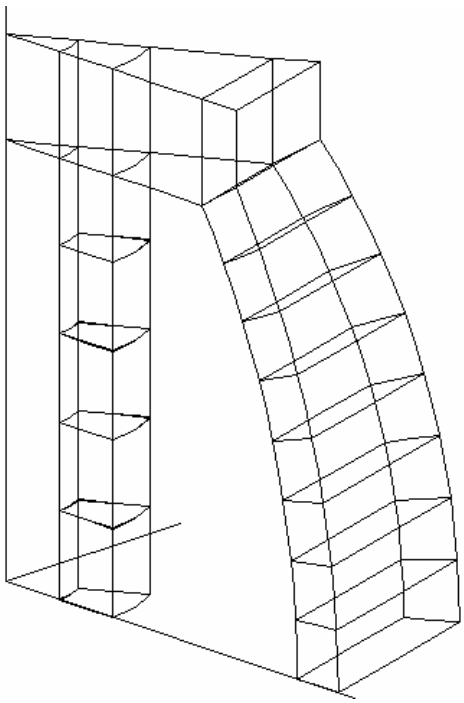

Figure 5.16. Half-segment mesh of the ‘base’ staved-shell transducer.

The initial 'base' values of the structure's dimensions and the base materials are identical to those employed for the slotted shell transducer model. Consistency between the slotted shell and the staved shell models has been maintained so that a comparison between the two designs can be readily made.

The model is transformed into a finite element mesh containing 528 elements (figure 5.15 – hidden lines have been removed). As before, by invoking rotational symmetry, the order of which depends on the number of staves, and mirror symmetry in the xy-plane, it is possible to reduce the structural mesh to a half-segment (figure 5.16) that contains only 22 elements, with the boundary element mesh comprising 13 elements.

5.4.1 Preliminary Results

The in-water performance characteristics are summarised in table 5.4. The results indicate that the performance of a staved-shell transducer is comparable to that of an equivalent slotted-shell device. However, the characteristics of the staved-shell design are preferred as the device exhibits a lower resonance frequency, albeit at the expense of a reduced maximum acoustic power output. The decreased resonance frequency is due to the reduced stiffness of the shell; that is, the staves, being flat in the hoop direction, are less stiff in flexure in comparison to the sections of the slotted-shell, which are curved in the hoop direction.

Table 5.4. In-water performance characteristics of the 'base' staved-shell transducer.

Parameter	Description	Value
f	Fundamental resonance frequency	925 Hz
P_a	Peak acoustic power	1273 W
SL	Source level	201.9 dB re. 1 μPa @ 1 m
η_{ea}	Efficiency	99.1 %
B	Bandwidth	215 Hz
Q	Q-factor	4.3

5.4.2 Effects of Varying the Material Properties of the Staves

The material properties of the shell, principally density and Young's modulus, greatly influence the resonance frequency, acoustic power output, and quality factor.

The density ρ of a material is defined as its mass m per unit volume V. Thus

$$\rho = \frac{m}{V} \tag{5.6}$$

Young's Modulus E is defined as the ratio of tensile stress S (force F per unit area A) to tensile strain T (change in length $\Delta\ell$ per unit length ℓ). Thus

$$E = \frac{S}{T} = \frac{F/A}{\Delta\ell/\ell} \tag{5.7}$$

When a tensile stress is applied to a material it experiences a tensile strain; that is, it extends in the longitudinal direction. The magnitude of this extension is defined by the Young's Modulus of the material. As the material extends it becomes thinner. Poisson's ratio σ is the name given to the ratio of change in diameter Δr per unit diameter r to change in length $\Delta\ell$ per unit length ℓ. Thus

$$\sigma = \frac{\Delta r/r}{\Delta\ell/\ell} \tag{5.8}$$

An approximate value of 0.3 is typical for metallic material.

To investigate the influence of the material properties, density and Young's Modulus, on the performance characteristics of the transducer a set of hypothetical materials was devised. The values for density and Young's Modulus were varied over the range of 1000 kg m^{-3} to 10000 kg m^{-3} and 1 GPa to 100 GPa respectively. Poisson's ratio is fixed to 0.3 for all the imaginary materials.

The effects of the stave material on the in-water resonance frequency, maximum acoustic power, and quality factor are indicated in figure 5.17. The results indicate that the ideal material for low frequency applications has a low stiffness and a high density. Conversely, in order to maximise the acoustic bandwidth (low quality factor) the material must have a high stiffness and a low density.

Table 5.5. Comparison of a number of candidate stave materials.

Material	Density	Young's Modulus	Resonance Frequency	Acoustic Power	Quality factor
Steel	Highest	Highest	Higher	Highest	Highest
Titanium	Higher	High	High	Higher	Higher
Aluminium	High	Low	Medium	Medium	High
S-Glass	Medium	Medium	Low	Low	Medium
E-Glass	Low	Lower	Lower	Lower	Low
Epoxy Resin	Lowest	Lowest	Lowest	Lowest	Lower
Carbon Fibre	Lower	Higher	Highest	High	Lowest

Maximum acoustic power output requires a material of high stiffness and density. These trends agree with previously published results for the class IV flextensional transducer [5.9-5.11].

Table 5.5 gives a comparison of the effect on transducer performance in water for a number of candidate stave materials. The materials are listed in descending order of quality factor; that is, steel has the highest value while the carbon fibre composite has the lowest value.

In the subsequent sections three stave materials are considered, stainless steel, aluminium, and epoxy resin. The properties of these materials are listed in table 5.6. Stainless steel offers a high power output, but at the cost of a high resonance frequency and a low bandwidth, and hence is of less use unless its high strength is needed. Conversely, epoxy resin yields a low resonance frequency and wide bandwidth but only for low acoustic power. Generally, aluminium offers an acceptable compromise between stainless steel and epoxy resin materials.

Table 5.6. Stave materials.

Material	Density ($kg\ m^{-3}$)	Young's modulus (10^3 MPa)	Poisson's ratio	Mechanical quality factor Q_m
Stainless Steel	7960	193.0	0.31	10000
Aluminium	2710	68.91	0.30	1000
Resin	1130	8.86	0.40	100

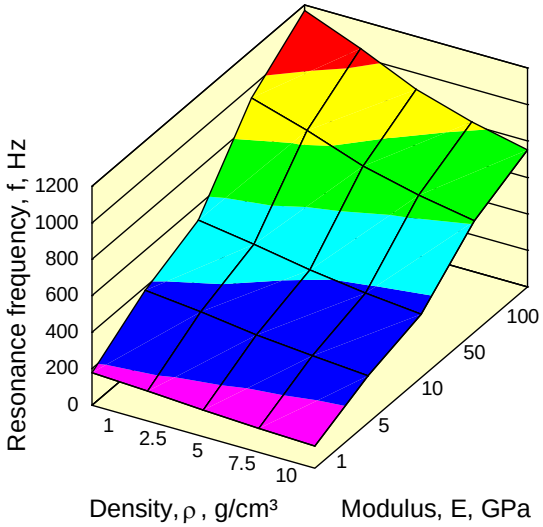

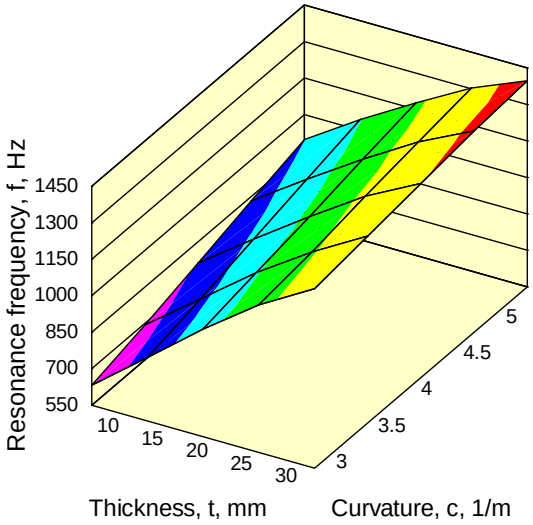

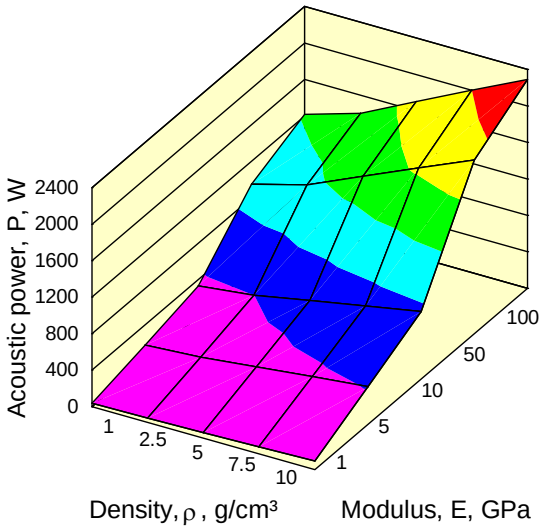

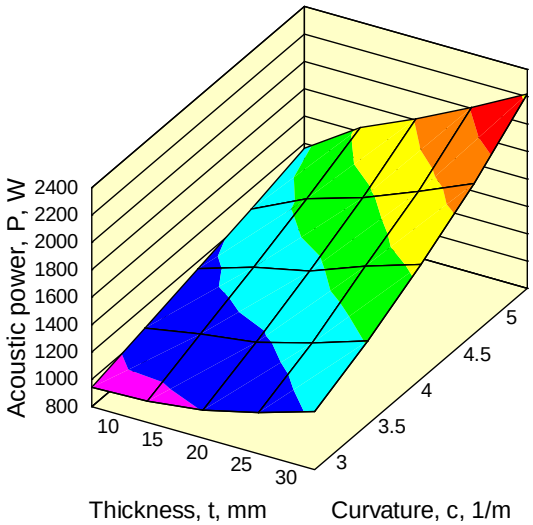

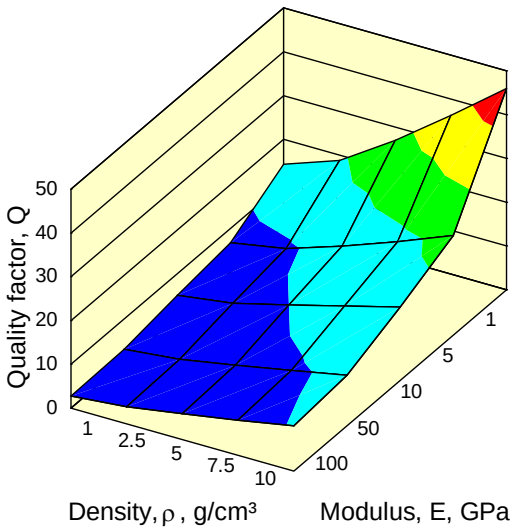

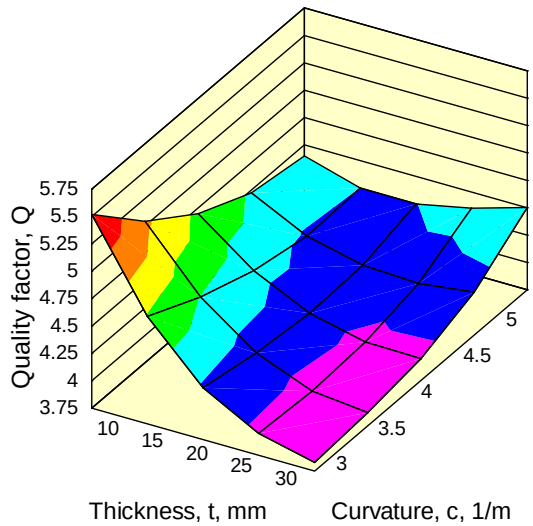

Figure 5.17. Variation of performance characteristics with density and Young's modulus.

Figure 5.18. Variation of performance characteristics with stave thickness and curvature.

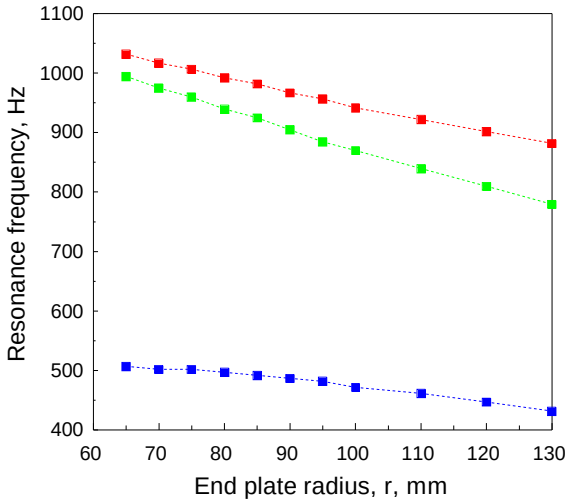

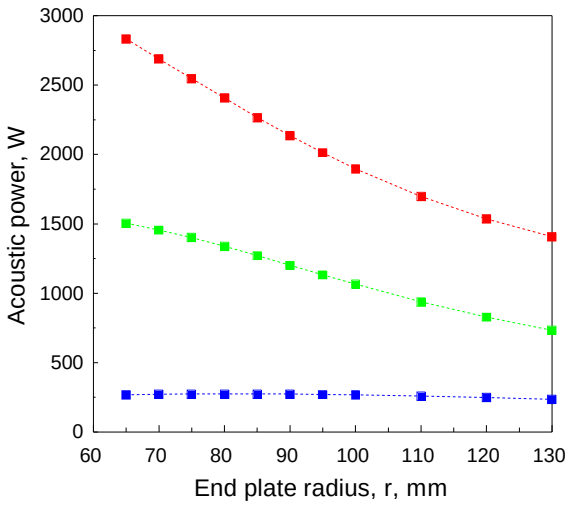

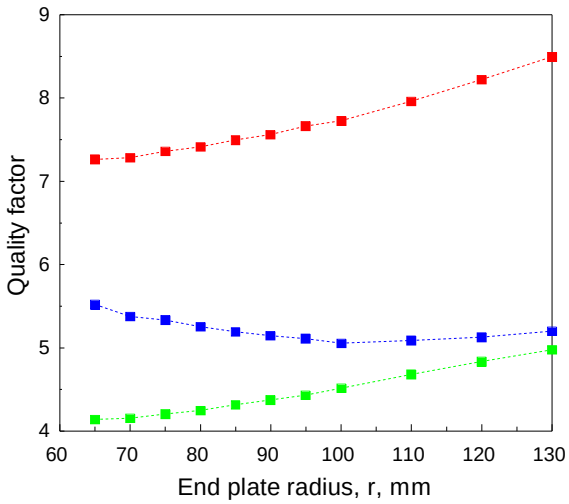

Figure 5.19. Variation of performance characteristics with end-plate radius, *r*; all other parameters equal to their base values.

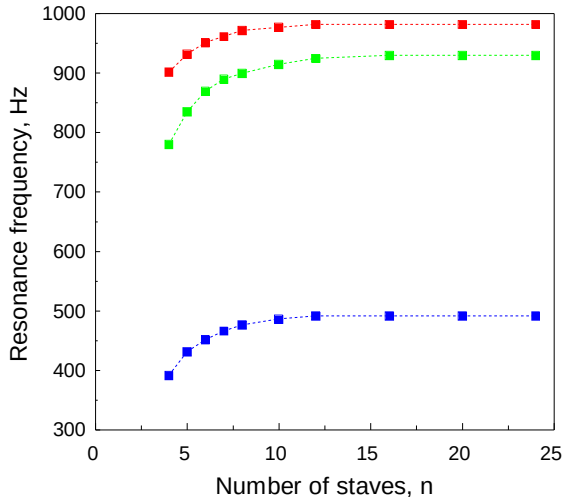

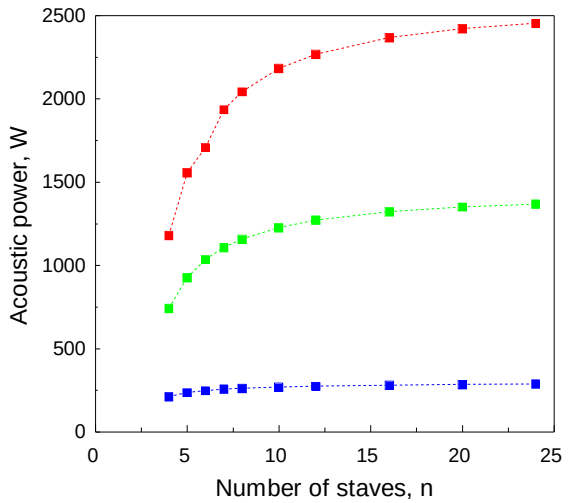

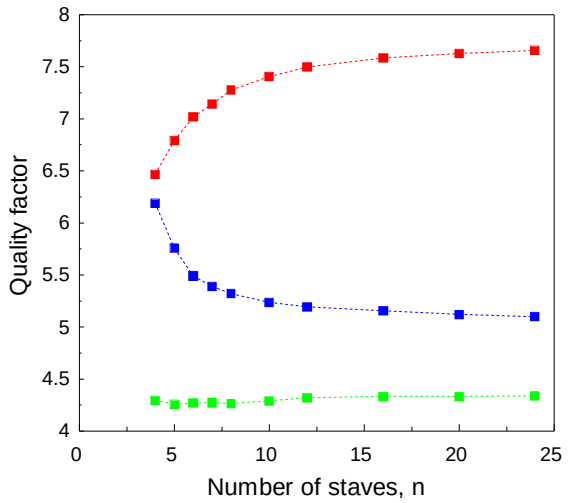

Figure 5.20. Variation of performance characteristics with the number of stave, *n*; all other parameters equal to their base values.

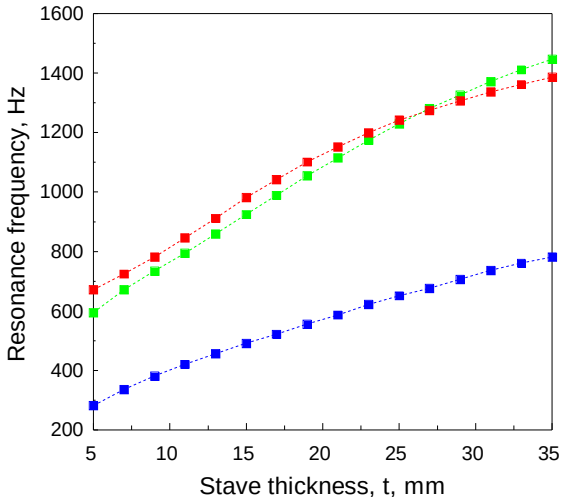

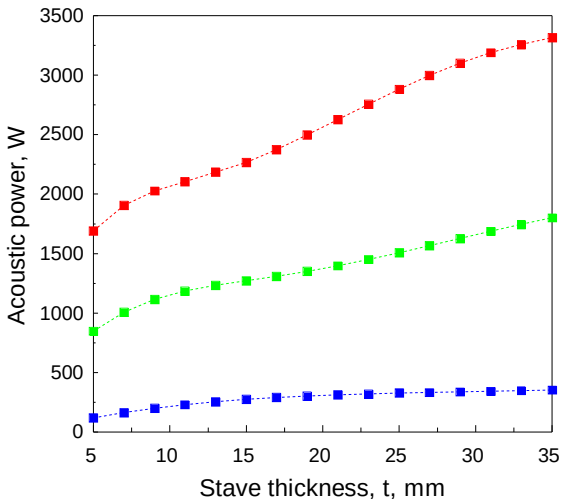

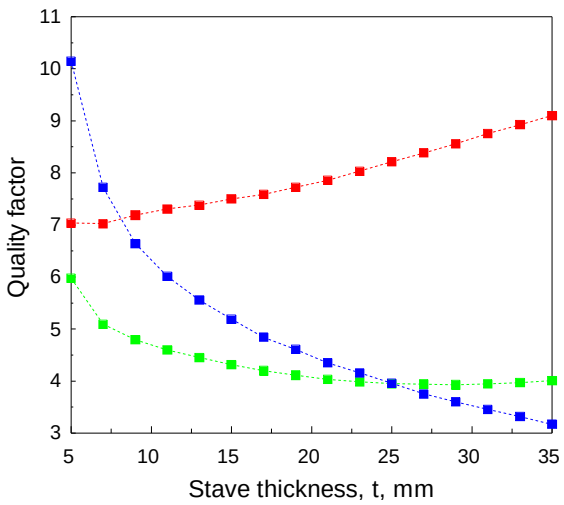

Figure 5.21. Variation of performance characteristics with stave thickness, *t*; all other parameters equal to their base values.

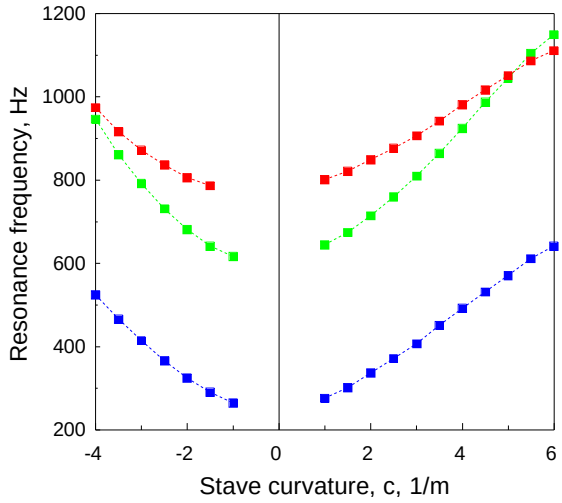

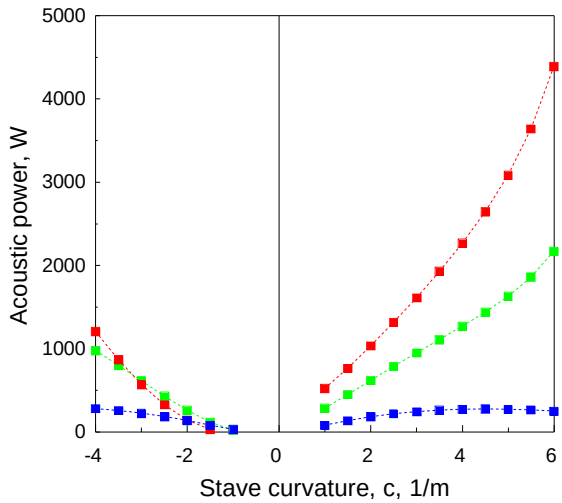

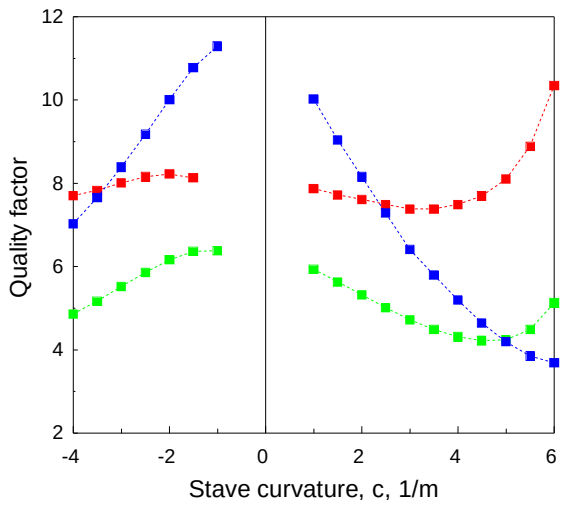

Figure 5.22. Variation of performance characteristics with stave curvature, *c*; all other parameters equal to their base values.

5.4.3 Effects of Varying the Radius of the End-Plates

In this section the effects of varying the radius at the end of the transducer is examined for three stave materials – stainless steel, aluminium, and epoxy resin. The results are presented in a graphical format which allows easy identification of the trends. The colours red, green, and blue are used respectively to represent the aforementioned materials in the figures.

Increasing the radius at the end of the transducer extends the radiating area of the staves, and might be expected to increase the acoustic power capability and reduce the quality factor. However, the results presented in figure 5.19 indicate the reverse. An explanation of this behaviour is that the end-plates act as 'de-coupling' elements. That is, the function of the end-plates is to transfer the energy produced by the driving stack to the radiating shell. As the radius of the plates is increased they becomes less stiff and therefore less effective at transferring power to the staves. In the case of the epoxy resin material, the stiffness of the end-plates is much greater than that of the staves, so that the de-coupling effect only becomes apparent when the radius of the end-plates is large.

Expanding the area of the transducer also increases the water loading and hence reduces the resonance frequency and this is verified by the results.

5.4.4 Effects of Varying the Geometry of the Staves

In this section the effects of varying the stave parameters about the base values are examined for the three stave materials. These parameters consist of the number of staves, and the thickness and curvature of the staves.

The effect of varying the number of staves is observed for a constant radiating area. This is achieved by keeping the average radius at the end of the device constant. Figure 5.20 indicates that increasing the number of staves has the effect of increasing the resonance frequency and acoustic power. The effect on quality factor is variable; for steel, aluminium, and epoxy resin stave materials the quality factor increases, does not noticeably change, and decreases respectively. It is likely that the end-plates play a part in determining this response [5.4].

Increasing the number of staves beyond eight only has a marginal effect, and it would appear that this number of staves provides a reasonable compromise between retaining simplicity of construction and the transducer's performance.

The effects of altering the thickness of the staves is shown in figure 5.21. As the staves become thicker and thus stiffer, the resonance frequency increases, as does the acoustic power. For aluminium staves, the quality factor reaches a minimum for a stave thickness of 30 mm; for the other materials the minimum, if it exists, is beyond the range considered.

Figure 5.22 shows the variation in resonance frequency, power capability and quality factor for varying shell curvature. Negative curvatures are included to illustrate the performance for the concave shell profile. The results indicate that for the convex shell configuration, resonance frequency and acoustic power increase with increasing curvature. In the case of steel and aluminium staved-shells the quality factor reaches a minimum value. The minimum for epoxy resin, if it exists, lies outside the range considered.

Further analysis of thickness and curvature for a shell composed of aluminium staves reveals that the two parameters are inter-dependent in their influence on the performance characteristics of the transducer. Figure 5.18 illustrate the variation in performance for a grid of values of these parameters. As previously described, increasing the thickness and curvature leads to an increased resonance frequency and acoustic power output. However, for a given stave thickness there is an optimum value of the curvature for a minimum value of quality factor. The relationship between the parameters and minimum quality factor appears to be linear within the range of shell profiles modelled; thin staves are required to be highly curved for an optimum value of quality factor, whereas thicker staves should be somewhat less curved.

5.5 Conclusions

The combined finite element and boundary element method has been used to assess the performance of a number of class I flextensional transducer design configurations.

Early in the modelling process the scaling principles for resonant systems were confirmed. These imply that the resonance frequency of a given design can be changed by scaling all dimensions

proportional to the reciprocal of frequency. The effect on the other parameters of the transducer can also be determined.

Further simulations reveal that the performance of a slotted-shell flextensional transducer converges with that of an equivalent staved-shell device as the number of staves is increased. However, for a practical number of staves the staved-shell transducer has been found to offer superior performance characteristics. Indeed the effect on the performance of the device as a result of changing the number of slots or staves was minimal except when very few slots or staves were employed (< 8). In addition, the convex form of the device has been found to offer superior performance compared to the concave case, because it offers a lower quality factor and higher power output. However, the concave shell may still be preferred for shallow water (<100 m) applications, as the device is self-biasing; that is, the hydrostatic pressure acting on the concave shell compresses the stack and safeguards it against the damaging effects of tension. For deep water applications, some form of depth compensation must be incorporated, and this consideration no longer applies.

Analysis of the effect of changing the thickness and curvature of an aluminium shell revealed that the two parameters are inter-dependent in their influence on the performance characteristics of the transducer. Thin staves are required to be highly curved for an optimum value of quality factor, whereas a thicker stave can be somewhat less curved. This relationship appears to be linear within the range of shell profiles modelled.

The choice of shell material depends on the required objective. For low resonance frequency a material with low stiffness and a high density is required, while for low quality factor the opposite – high stiffness and a low density – is needed. For high acoustic power the material should have both high stiffness and high density.

In addition to investigating the effect of changing the material properties and geometry of the shell, the impact of altering the end-plates was studied. It was found that superior performance is obtained when the stiffness of the end-plates is significantly greater than that of the shell. That is, stiffer end-plates improve the coupling between the piezoelectric stack and the shell which results in superior energy transfer. The implication of this was that the end-plates must be made from a material that has a high Young's modulus, such as steel. It also suggested that the radius of the

end-plate should be minimised in order to reduce weight. These requirements would favour the use of a convex shell since the concave shell requires clearance from the stack and hence larger and thicker end-plates.

From the results presented in this chapter a design process can be discerned. The process is as follows: (a) select a shell material that approximately meets the desired performance characteristics; (b) select a shell type, either slotted or staved; (c) select a shell profile, either convex or concave; (d) optimise the thickness and curvature of the shell for very stiff end-plates; (e) reduce the stiffness of the end-plates as much as possible while maintaining performance; (f) scale the dimensions to obtain the required resonance frequency.

In conclusion, the choice of design parameters depends on the importance attached to each objective (frequency, power, and quality factor) and some compromise will have to be made.

5.6 References

[5.1] S. S. Jarng, D. T. I. Francis, J. R. Dunn, and B. V. Smith, 'Optimization of Sonar Transducers using a Coupled FE-BE Method', *Proc. I. O. A.*, 12(4), 57-65, (1990).

[5.2] B. V. Smith, R. L. Mansfield, D. T. I. Francis, and J. R. Dunn, 'The Design of a 100-kHz Wideband Sonar Transducer', in *Transducers for Sonics and Ultrasonics*, M. D. McCollum, B. F. Hamonic, and O. B. Wilson, eds., (Lancaster, PA: Technomic Publishing Co. Inc., 1993), 231-238.

[5.3] D. Stansfield, *Underwater Electroacoustic Transducers*, (Bath University Press and Institute of Acoustics, 1990), 183-184.

[5.4] D. Stansfield, *Underwater Electroacoustic Transducers*, (Bath University Press and Institute of Acoustics, 1990), 29-33.

[5.5] D. Stansfield, *Underwater Electroacoustic Transducers*, (Bath University Press and Institute of Acoustics, 1990), 150.

[5.6] D. T. I. Francis, C. Bayliss, J. A. Ahmad, and R. F. W. Coates, 'The Development of a Low Frequency Barrel-Stave Transducer for Tomographic Applications using Finite Element and Boundary Element Modelling', *Proc. OCEANS '94*, 371-376, (1994).

[5.7] R. S. Woollett, 'Power Limitations of Sonic Transducers', *IEEE Trans. Sonics Ultrasonics*, 15(4), 21-227, (1968).

[5.8] D. F. Jones, 'Flextensional Barrel-Stave Projectors', in *Transducers for Sonics and Ultrasonics*, M. D. McCollum, B. F. Hamonic, and O. B. Wilson, eds., (Lancaster, PA: Technomic Publishing Co. Inc., 1993), 150-159.

[5.9] W. J. Marshall, J. A. Pagliarini, and R. P. White, 'Advances in Flextensional Transducer Design', *Proc. OCEANS '79.*, 124-129, (1979).

[5.10] J. Oswin and J. Dunn, 'Frequency, Power and Depth Performance of Class IV Flextensional Transducers', in *Power Sonic and Ultrasonic Transducer Design*, B. Hamonic, and J. N. Decarpigny, eds., (Berlin: Springer-Verlag, 1988), 121-133.

[5.11] G. Bromfield, 'Class IV Flextensional Transducers', in *Power Transducers for Sonics and Ultrasonics*, B. Harmonic, O. B. Wilson, and J. N. Decarpigny, eds., (Heidelburg: Spring-Verlag, 1991), 48-59.

Chapter 6

DESIGN CONSIDERATIONS

6.1 Introduction

In the previous chapter parameter-based numerical analysis of a class I flextensional transducer was presented. The model used did not include a centre bolt or a rubber boot (not required if the transducer is free-flooded), both of which are essential components of a working transducer. In this chapter we will consider the practical engineering aspects of converting a theoretical design into a physical device.

The flextensional transducer can be considered to consist of a number of individual parts. These include the shell, rubber boot, stack, centre bolt, end-plates, and end-caps. The following sections focus on the various engineering aspects that affect the design of the more complex of these components. In some cases a number of options are reported, and it is then up to the designer to decide which method is most appropriate (in most cases the preferred technique is suggested in the text).

6.2 Shell Construction

The most fundamental design issue affecting the manufacturing of the shell of a flextensional transducer is the joining between the staves and the end-plates. In the finite element model the coupling between these components is assumed to be perfect. However, in practice, the joining can be far from ideal and can adversely affect the performance of the transducer.

The simplest joint, and typically the one most commonly employed, is a single bolt joint. In this configuration the shell to end-plate coupling is determined by the friction between the two surfaces. The coupling may be enhanced by securing the staves to the end-plate with epoxy resin and bolts. A more elegant solution is to utilise keyway joints. In this arrangement the staves

effectively 'lock' into the end-plates. However, this improvement comes at a price. To implement keyway joints requires much tighter manufacturing tolerance and hence higher fabrication costs.

The method of manufacturing the staves is dependent on the chosen material. Staves made from a composite material, such as glass-reinforced-plastic (GRP), necessitates the use of a mould. The fibrous reinforcing material is arranged inside the mould such that strands run the length of the stave. The mould is filled with resin. The resin, which should normally be degassed before application to remove an air bubbles, may have to be forced into the mould under pressure. Once the resin is set any required machining may be carried out.

Aluminium staves are considerably easier to fabricate. The stave can simply be machined from a solid block. However, if a large number of transducers are to be produced it may be more cost effective to cast the staves before machining, although the risk of casting defects may be significant.

In order to minimise manufacturing costs it is preferable to construct the shell from the minimum number of staves as is practicable. Thus, from the numerical analysis performed in the previous chapter, it would appear that a choice of eight staves offers the most satisfactory compromise between simplicity of the shell and the performance of the device.

6.3 Rubber Boot

The staves are designed such that when they are fastened to the transducer, axial gaps of uniform width (approximately 1 mm) are left between adjacent staves. As explained in the previous chapter, these gaps are required in order allow the transducer to function correctly. However, they introduce an added complication. In the air-backed form, the shell of the transducer must be covered with a rubber boot (typically neoprene rubber) to prevent the ingress of water into the transducer.

The simplest booting technology consists of a tubular rubber section which is stretched over the shell of the transducer and bonded to the end-plates. However, this configuration is far from ideal as boot flapping and other undesirable effects are known to occur [6.1]. A superior and more

costly technique involves the fabrication of a boot that follows the contours of the shell. This is bonded onto the surface of the shell. In both approaches great care must be taken to ensure a perfect mating between the boot and the shell, since even tiny air bubbles under the rubber can have a dramatic effect on the performance of the transducer.

6.4 Stack Construction

The stack is assembled from a number of piezoelectric rings, cemented together. Electrodes are sandwiched between the rings to allow the electric field to be applied. Insulators are usually placed at either end of the stack to provide electrical isolation. An insulator is also commonly fitted around the centre bolt to eliminate the possibility of flashover between the bolt and the surrounding piezoelectric rings.

In designing the stack a number of considerations need to be taken into account. If the stack is composed of a large number of rings the number of glue–electrode joints will be high. This will have the undesirable effect of reducing the stiffness of the stack, which in turn reduces the electro-mechanical coupling and increases the mechanical dissipation.

If the number of ceramic rings used to construct the stack is reduced the effect of the joints is minimised. However, for a stack comprising n ceramic rings of thickness t and cross-sectional area A connected in parallel, the capacitance C is given by

$$C = \frac{\varepsilon_{33}^{T} An}{t} \tag{6.1}$$

where ε is the permittivity. If the number of rings is low, the capacitance of the stack will be low and its impedance high. As the impedance of the transducer increases, so must the size and weight of the transformer that matches the high impedance transducer to the low impedance of a power amplifier. A higher impedance must also result in higher drive voltages on the transducer side, requiring careful construction of the transformer and choice of electrical components on the transducer side (cables and connectors).

The number of ceramic rings chosen is thus a compromise between the electro-mechanical coupling and impedance.

A further consideration is the cost of the piezoelectric rings. Most manufacturers of piezoelectric ceramics produce a standard range of products. A suitable product can normally be found from this range. When the required dimensions cannot be compromised many manufacturers can machine custom-sized-ceramics, although these will undoubtedly come at a premium.

The materials most commonly found to be suitable to bond the piezoelectric rings together are the epoxy resins. The epoxy resin manufacturers generally specify curing conditions and optimum joint thickness for achieving maximum tensile strength. Although joints in a pre-stressed stack should never be in tension, the greatest reliability of the transducer is obtained when high bond strengths of at least 10 MPa are achieved [6.2].

Each joint needs to incorporate some form of electrode as well as provide mechanical bonding between rings. A typical solution involves the use of either copper or brass shims. Each shim has the same internal and external diameters as the ceramic rings. A tag is left on the external edge to permit the attachment of electrical leads. Braided conductors may be used to reduce the chances of fatigue failure of the leads.

The problem with using solid shims is the difficulty in controlling the joint thickness, and it may be hard to obtain consistent results. Greater control over joint thickness can be achieved by using a thin gauze of Monel metal. Electrical connections can be made in a similar manner to that used for solid shims, that is, leaving a tag on the external edge. However, such a joint may be susceptible to fatigue failure in high power applications [6.3]. A more reliable technique is to use reinforcing brass rings. These rings, which have an inside diameter just larger than the outside diameter of the ceramic rings, are spot welded together in pairs with a layer of gauze sandwiched between them [6.3].

Another possible technique is to cut two chains of shims from metal gauze. Each shim in a chain is joined to the next by a thin strip of gauze that is long enough to span the thickness of two ceramic rings. Several layers of insulation tape must be wrapped around the connecting strips to provide electrical insulation. The two chains may then be woven, perpendicular to each other,

between the ceramic rings. The first chain is woven between the odd numbered joints and the second links the even numbered joints. In this way only two electrical connections are required, hence minimising the number of soldered contacts and thus failure points.

It is usually desirable to arrange that the stack be balanced about earth; that is, an even number of ceramics are employed and the electrical connections at both ends are connected to earth. With this arrangement the stack may be directly inserted into the transducer. However, connecting the whole transducer to earth runs the risk of electrolytic corrosion at the interface between dissimilar metals. Such problems are avoided by electrically insulating the stack from earth and hence insulators are usually inserted between the stack and the end-plates. The insulators should preferably have similar properties and dimensions to those of the ceramic rings. Machineable ceramics, such as MACOR, are particularly suitable.

An insulator is also commonly fitted around the centre bolt to prevent flash-over from the piezoelectric rings to the bolt. This insulator may also usefully serve as a jig to locate the rings and electrodes whilst the stack is being assembled, and thus must be manufactured from a material which is reasonably stiff and can be machined to an acceptable tolerance (typically a plastic such as Nylon).

6.5 Centre Bolt

The function of the centre bolt is to prevent the piezoelectric stack being subjected to tensile stress during the positive phase of the alternating stress cycle. Thus, the bolt must apply a compressive force which is greater than the peak alternating force within the stack. The required force that must be exerted by the bolt can be ascertained from finite element and boundary element calculations. From these calculations the bolt material and cross-sectional area may be determined.

The peak tensile force within the stack may be deduced from the peak amplitude of vibration of the stack at resonance. The finite element and boundary element software, PHOEBE, calculates the complex values of displacement at the nodes for a drive voltage of 1 V peak. Thus, the peak displacement is given by

$$|u|_{1\text{ V peak}} = \sqrt{u^* u} \tag{6.2}$$

where u is the complex value of displacement at the end of the stack. Assuming that maximum drive conditions are sought, and the acoustic output of the transducer is limited by the maximum electrical field that can safely be applied to the piezoelectric rings (200 kV r.m.s. m^{-1}), the peak displacement in the stack at maximum drive conditions is given by

$$|u|_{200\text{ kV r.m.s. m}^{-1}} = |u|_{1\text{ V peak}} \left(\sqrt{2}\right) 200000t \tag{6.3}$$

This corresponds to a peak tensile force of

$$F_s = \frac{c_{33}^E A_s |u|_{200\text{ kV r.m.s. m}^{-1}}}{\ell_s} \tag{6.4}$$

where ℓ_s is the length of the stack and is the product of the number of rings n times the thickness of a single ring t (that is, $\ell_s = nt$), c is the compliance of the ceramic, and A_s is the cross-sectional-area of the stack. This is the minimum compressive force that the centre bolt must apply. However, it is advisable to allow a significant safety margin. As a general rule, it is recommended that the compressive force should be of the order of twice the peak value of the alternating force in the stack at resonance [6.4].

The bolt has the undesirable effect of tending to restrict the motion of the transducer. However, this can be tolerated if the stiffness of the bolt is considerable less than that of the stack. Let the ratio of the stack stiffness K_s (ignoring the effects of the glue–electrode joints) to the bolt stiffness K_b be denoted by k. Then,

$$k = \frac{K_s}{K_b} = \frac{E_s A_s}{\ell_s} \frac{\ell_b}{E_b A_b} \tag{6.5}$$

where E_s and E_b, A_s and A_b, and ℓ_s and ℓ_b, are the stack and bolt elastic modulus, cross-sectional-area, and length, respectively. For a practical bolt design the stiffness of the bolt should be an order of magnitude less than that of the stack (that is, $k \geq 10$) so as to not excessively inhibit the motion of the transducer.

Table 6.1. Candidate centre bolt materials.

Material	Tensile strength (MPa)	Fatigue limit (MPa)	Density (kg m^{-3})	Young's modulus (10^3 MPa)	Poisson's ratio
High tensile steel	1500	620	7850	207	0.29
Stainless steel	880	370	7750	210	0.31
Beryllium copper	1300	290	8840	127	0.29

The bolt must also be strong enough to safely apply the required compressive force. The static stress in the bolt $T_b(static)$ for an applied compressive force F_b is given by

$$T_b(static) = \frac{F_b}{A_b} \tag{6.6}$$

where A_b is the cross-sectional-area of the bolt core. Superimposed on this is the alternating force produced by the stack and this results in a peak stress within the bolt $T_b(peak)$ of

$$T_b(peak) = T_b(static)\left[1 + \frac{1}{2k}\right] \tag{6.7}$$

Since the stresses in a transducer are dynamic, the requirement for a centre bolt is a material that has a high fatigue limit. A number of candidate bolt materials are listed in table 6.1. It should be noted that the fatigue limits quoted are for alternating stresses that are symmetrical and centred about zero. However, in the centre bolt the dynamic stresses are added to the static stress; that is, the alternating stresses cycle about the static stress. A reliable guide for combined stresses such as these does not exist [6.5], though an approximation for the fatigue limit $T_f(m)$ of a material when it is loaded by a mean stress T_m is given by the equation

$$T_f(m) = T_f(0)\left[1 - \frac{T_m}{T_t}\right] \tag{6.8}$$

where $T_f(0)$ is the fatigue limit for zero mean stress, and T_t is the tensile strength.

At this point, having determined the static compressive force that the bolt must exert and chosen a suitable material, one can establish the required cross-sectional-area of the core of the bolt. Since $T_b(peak) \le T_f(m)$ the minimum cross-section area of the bolt core A_{min} is given by

$$A_{\min} = \frac{F_b\left[1+\dfrac{T_f(m)}{T_t}\right]}{T_f(m) - \dfrac{F_b E_b \ell_s}{2E_s \ell_b A_s}} \tag{6.9}$$

In practice, since this value is the absolute minimum, a bolt with a core slightly larger should be chosen in order to reduce the possibility of fatigue failure. On the other hand, an excessively large bolt should be avoided as this will decrease the stack to bolt stiffness ratio and lessen the acoustic power output.

Having determined the force that the centre bolt must exert, we must consider how it can accurately be applied. An obvious method is to use a torque wrench. The required torque T may be calculated by the following formula:

$$T = F_b \frac{\mu\cos(\theta)+\sin(\theta)}{\cos(\theta)-\mu\sin(\theta)} r \tag{6.10}$$

where

$$\theta = \arctan\left(\frac{\text{thread pitch}}{\text{circumference}}\right)$$

r is the radius of the bolt, and μ is the friction coefficient. The problem with using this method is determining the friction coefficient; typical values of μ for a steel to steel interface have been quoted as 0.8 for a clean surface, down to 0.16 for a lubricated surface [6.6]. Thus, the friction coefficient is an unknown quantity, which can only be estimated, and the method is hence not a viable technique for applying a known force.

A more reliable technique is to measure the 'stretch' put on the bolt. The extension of the bolt u_b of length ℓ_b and elastic modulus E_b when subject to a tensile stress T_b is given by

$$u_b = \frac{T_b(static)\ell_b}{E_b} \tag{6.11}$$

By means of a dial gauge on the end of the bolt it should be possible to measure the extension of the bolt to accuracy of within 1 μm.

An alternative method of ensuring that the desired force is applied is to measure the stress applied to the stack directly, by measuring the voltage generated piezoelectrically in the ceramic. The stack can be considered as a capacitance connected in parallel to a very large resistance. Thus, the voltage across the stack at time *t* after a compressive force has been applied is

$$v(t) = v(0)e^{-t/\tau} \tag{6.12}$$

where $v(0)$ is the instantaneous voltage generated and τ is the time constant; they are respectively defined as

$$v(0) = \frac{Q}{C} = \frac{d_{33}F_b}{\varepsilon_{33}^T A_s}t$$

$$\tau = RC = \rho\varepsilon_{33}^T$$

where ρ is the resistivity of the ceramic. The symbols Q, C and R, represent the instantaneous charge generated across the stack, and the resistance and capacitance of the stack, and are respectively defined as

$$Q = d_{33}F_b n$$

$$C = \frac{\varepsilon_{33}^T An}{t}$$

$$R = \frac{\rho t}{An}$$

Typical values for the time constant of several piezoelectric ceramics are listed in table 6.2. From these figures the technique would appear to be perfectly plausible, assuming that the device used to measure the voltage generated is capable of measuring high voltages of the order of kilovolts, and has a very high input impedance (for example, an electrostatic volt meter). However, environmental conditions, such as moisture in the air, cause charge to leak away which severely reduces the time constant, making the method unfeasible.

Table 6.2. Time constants for several piezoelectric ceramics at 25 °C.

	Navy Type			
	I	II	III	IV
	Vernitron Type			
	PZT-4™	PZT-5A™	PZT-8™	Ceramic-B™
Time constant, τ	> 100	> 2000	≈ 90	> 100

If the effective capacitance of the stack could somehow be amplified, the above technique could be made to work. The reasoning behind this is that the voltage generated across the stack is inversely proportional to its capacitance and low voltages result in low leakage currents.

While it is not possible to increase the capacitance of the stack, it is possible to transfer charge. A circuit which accomplishes this is the integrator, shown in figure 6.1. The input current v_{in}/R flows through C, and because the inverting input of the operational amplifier (op-amp) is a virtual ground, the output voltage is given by

$$-C\frac{d}{dt}\left(v_{out}\right) = \frac{v_{in}}{R} = i_{in} = \frac{d}{dt}\left(Q\right)$$

or

$$v_{out} = \frac{Q}{C} \tag{6.13}$$

where Q is the instantaneous charge generated in the stack. The value of C should be chosen to give an output voltage in the permissible range of the op-amp (for example, 10 V).

For accurate results, high quality components must be used, that is, an ultra-low-input-current op-amp and a low-leakage capacitor. For example, an 'electrometer' op-amp can have an input current as low as 10 fA, and a high-quality 1 μF capacitor can have a leakage resistance greater than 100 GΩ. Thus the integrator keeps stray currents at the summing junction below 100 pA (for a worst case 10 V full-scale output), corresponding to an output dv/dt of less than 0.1 mV s^{-1}.

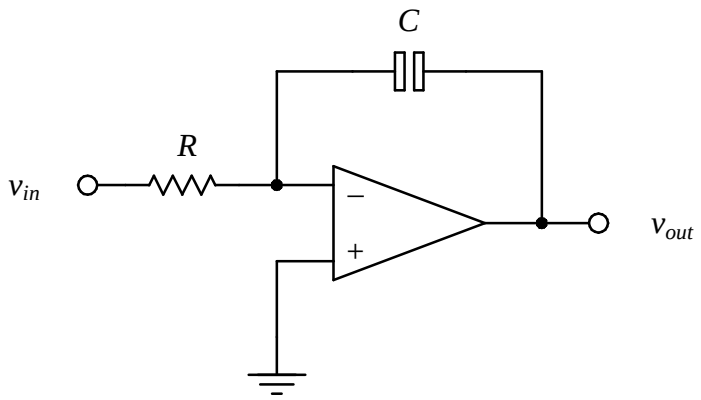

Figure 6.1. Integrator circuit.

One problem with the circuit shown in figure 6.1 is that the output tends to wander off, even with the input grounded. This is because there is no direct current feedback path. The problem can be minimised by using an op-amp with low input current and offsets, trimming the op-amp input offset voltage, and using large R and C values. As an example, a laser-trimmed op-amp will typically have an offset voltage of 200 μV and, used in an integrator with R = 10 kΩ and C = 1 μF, will produce an output drift of approximately 20 mV s^{-1}.

Many of the techniques discussed here will be used in the construction of two prototype transducers, reported in the following chapters.

6.6 References

[6.1] D. F. Jones, 'Flextensional Barrel-Stave Projectors', in *Transducers for Sonics and Ultrasonics*, M. D. McCollum, B. F. Hamonic, and O. B. Wilson, eds., (Lancaster, PA: Technomic Publishing Co. Inc., 1993), 150-159.

[6.2] D. Stansfield, *Underwater Electroacoustic Transducers*, (Bath University Press and Institute of Acoustics, 1990), 207.

[6.3] D. Stansfield, *Underwater Electroacoustic Transducers*, (Bath University Press and Institute of Acoustics, 1990), 208.

[6.4] D. Stansfield, *Underwater Electroacoustic Transducers*, (Bath University Press and Institute of Acoustics, 1990), 188.

[6.5] D. Stansfield, *Underwater Electroacoustic Transducers*, (Bath University Press and Institute of Acoustics, 1990), 211.

[6.6] E. Oberg and F. D. Jones, *Machinery's Handbook*, 18th Edition, (Machinery Publishers, Co., 1969), 522.

Chapter 7

AN AIR-BACKED DESIGN

7.1 Introduction

This chapter is concerned with the design and development of a transducer that is suitable for use as an ocean acoustic tomography sound source. In the first section a transducer design is developed, based on analytical work presented in Chapter 5, which meets the frequency, quality factor, acoustic power, and efficiency requirements, but fails to achieve the specified weight and operating depth. Subsequent sections report the construction and testing of a scaled version of this transducer design.

7.2 A Transducer Design Suitable for Ocean Acoustic Tomography

In this section a transducer design suitable for ocean acoustic tomography is presented. The materials and dimensions of the transducer have been selected to meet the specification presented in Chapter 1:

- Centre frequency 250 Hz - 500 Hz
- Operating depth > 500 m
- Total mass < 250 kg
- Q-factor < 4
- Source level > 190 dB re. 1 μPa @ 1 m
- Efficiency > 50%

Since the device is air-backed its maximum operating depth is restricted to approximately 100 m. Methods for overcoming this limitation are discussed in the next chapter.

The low quality factor requirements favour a light and compliant shell material, such as epoxy resin over aluminium or steel. Unfortunately the acoustic power output of such a shell is low. Higher output levels can be achieved from materials of higher stiffness and density, such as steel, but at the expense of quality factor and size. Thus, aluminium, which offers improved acoustic power output over epoxy resin materials for an adequately sized device that is capable of

operating over a reasonable bandwidth (low quality factor), is the preferred material. The transducer materials selected are the original base materials (table 5.2).

Since the required resonance frequency can be obtained simply by applying the scaling laws, defined in Chapter 5, and the acoustic power capability is well satisfied, the primary consideration has been to optimise the device for a low quality factor. Table 7.1 lists the chosen dimensions derived from the previous results, with the design then scaled to provide a resonance frequency of 500 Hz.

It should be noted that the design presented is based on a set of previously modelled dimensions that most accurately matched the requirements, and that minor improvements on the basis of the graphical results could be made. For example, it may be desirable to reduce the number of staves to eight to decrease the complexity of the device. In addition, there are many way to reduce the quality factor, but unfortunately this has the adverse effect of increasing the resonance frequency and hence the size of the device.

The weights of the components of the device are listed in table 7.2; these have been determined from the known densities and the element volumes calculated by numerical integration in the finite element method. These weights are scaled by the factor s^3 for the full-scale design.

Table 7.1. Proposed dimensions.

Base Design				Scaled Design			
Parameter values		Performance characteristics		Parameter values		Performance characteristics	
c	3 m^{-1}	f	1160 Hz	c	1.3 m^{-1}	f	500 Hz
t	25 mm	P_a	1.1 kW	t	58 mm	P_a	2.5 kW
ℓ	250 mm	η_{ea}	0.99 (99 %)	ℓ	580 mm	η_{ea}	0.99 (99 %)
r_e	85 mm	Q	3.95	r_e	197.2 mm	Q	3.95
h_p	30 mm			h_p	69.6 mm		
r_i	20 mm			r_i	46.4 mm		
r_o	40 mm			r_o	92.8 mm		
n	12			n	12		
s	1			s	2.32		

Table 7.2. Weight of transducer

Part	Density ($kg\ m^{-3}$)	Volume ($10^{-3}\ m^3$)	Weight (kg)	Quantity	Total weight (kg)
Ceramic ring	7500	1.177	8.827	8	70.613
Insulator	2520	1.177	2.966	2	5.932
Endplate	7960	4.656	37.062	2	74.124
Shell	2710	49.593	134.398	1	134.398
					≈ 285

The total weight of the transducer is approximately 285 kg, just 35 kg over the specification value. By slightly altering the dimensions of the endplate it should be possible to achieve the target weight with only a marginal impact on the transducer's performance. Another method of reducing the weight of the device is to use thinner staves. However, this results in an increased quality factor.

It is anticipated that the size and weight of the transducer could be significantly reduced by considering an alternative shell material. A prudent choice would be a composite glass-fibre and epoxy resin material. Such a material, which has been rejected due to predicted lower acoustic power output and manufacturing difficulties, would produce a considerably smaller and lighter device. However, the optimisation and implementation of a composite shell requires further investigation.

7.3 A 5 kHz Air-Backed Flextensional Transducer

The transducer design that was presented previously in this chapter has been scaled to approximately 1/10 size to give a resonance frequency of around 5 kHz. Using the scaled dimensions as a guideline, P. Ericson at Reson System in Denmark assembled a prototype device. A scaled version of the device has been built, rather than the 500 Hz ocean acoustic tomography sound source, in order to allow the essential concepts to be validated without excessive development and testing costs.

7.3.1 Construction Details

Technical schematics and a comprehensive parts list for the 5 kHz air-backed transducer can be found in Appendix B. The cross-section view of the prototype device is repeated in figure 7.1 and the main dimensions and materials are listed in tables 7.3 and 7.4 respectively. It may be noted that the number of staves has been reduced to simplify the design. The eight staves were machined from aluminium bar and secured to the steel end-plates using bolts with countersunk heads. The end-plates are octagonal in shape since each stave is flat in the hoop direction. Axial slits of uniform width (~1 mm) are left between adjacent staves which allow them to move independently. The ingress of water though these gaps is prevented by stretching a tubular rubber boot over the shell and then bonding it to the end plates. Electrical connections are mounted on one of the end-plates, and the other provides access to the central pre-stress bolt.

Figures 7.2-7.4 depict photographs of the assembled transducer prior to the application of the rubber boot. Figure 7.2 shows the transducer with its axis horizontal. In figure 7.3 the electrical connections can clearly be seen protruding from the 'top' end-plate, while figure 7.4 shows the reverse angle shot of the countersunk head of the pre-stress bolt situated at the centre of the 'bottom' end-plate.

Table 7.3. Main transducer dimensions.

Parameter	Description	Value (mm)
r_s	Radius of curvature of the staves	70
t	Shell thickness	6
ℓ	Length between end plates	60
r_e	Radius at end of device	20
h_p	End-plate thickness	10
r_i	Inner radius of stack	4
r_o	Outer radius of stack	10
n	Order of rotational symmetry	8

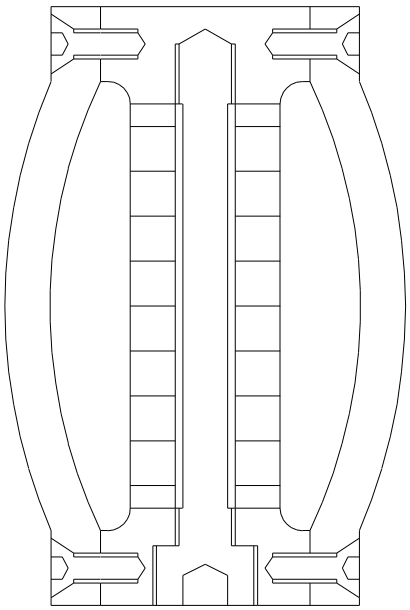

Figure 7.1. Technical drawing of the 5 kHz air-backed flextensional transducer (scale 1 : 1).

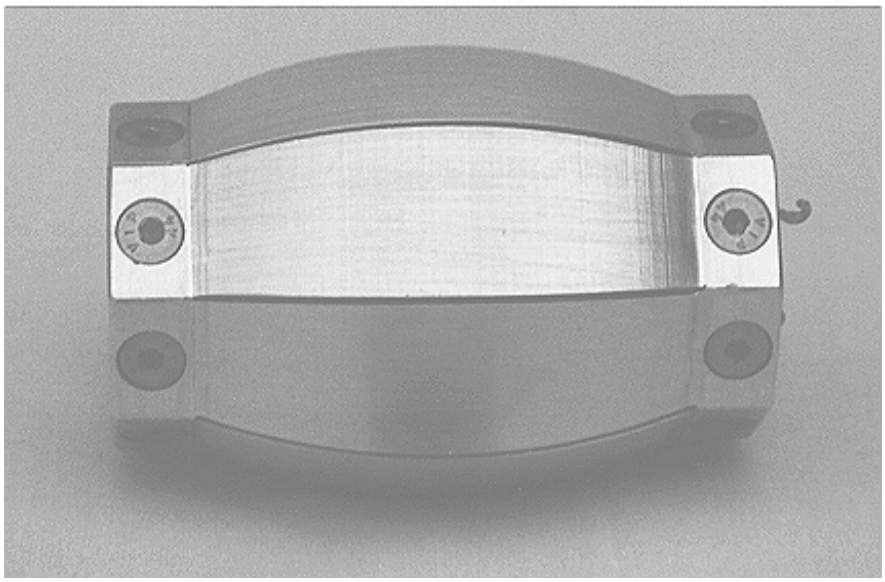

Figure 7.2. 5 kHz air-backed flextensional transducer (horizontal view).

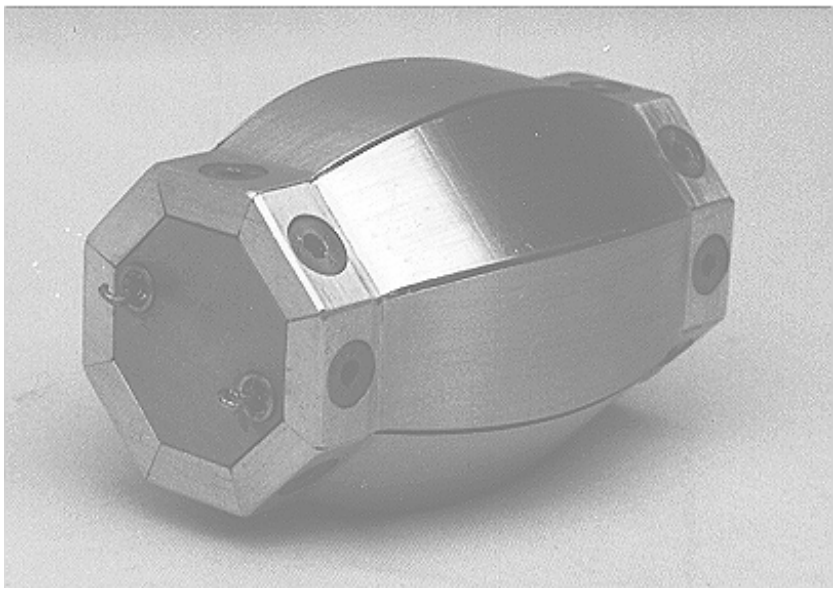

Figure 7.3. 5 kHz air-backed flextensional transducer (view of electrical contacts).

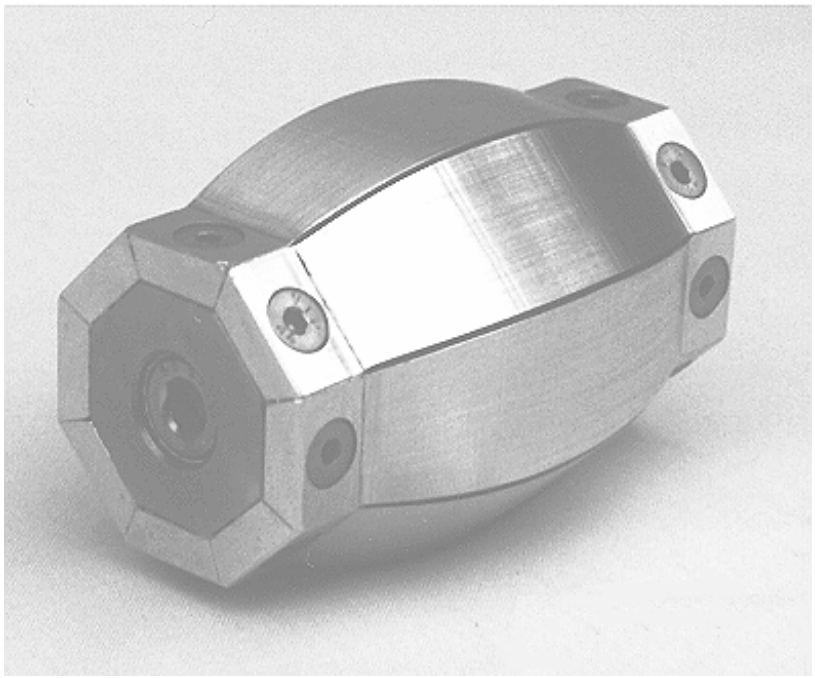

Figure 7.4. 5 kHz air-backed flextensional transducer (view of centre bolt).

Table 7.4. Main transducer materials.

Part	Material	Density (kg m^{-3})	Young's modulus (10^3 MPa)	Poisson's ratio	Mechanical quality factor Q_m
Ceramic	PZT-4™	See table 2.2			
Insulator	MACOR™	2520	140.0	0.29	500
End-plate	Mild Steel	7700	195.0	0.28	2000
Stave	Aluminium	2710	68.91	0.30	1000
Joint	—	1180	6.5	0.40	100

7.3.2 Results

The theoretical and experimental electrical responses of the prototype projector are shown in figures 7.5 through to 7.12 respectively. Many of the methods used to derive values from these responses are described in ref. [7.1].

The theoretical electrical responses are predicted from finite element and boundary element calculations, while the actual electrical responses of the prototype projector have been measured using a Hewlett Packard 4192A LF Impedance Analyser with a broad frequency range of 5 Hz to 13 MHz. The analyser is connected though an IEEE-488 parallel interface to an IBM-compatible personal computer. The computer is used to set the impedance analyser to sweep through the frequency band of interest and record the admittance response over this range.

The in-air admittance response was observed over the frequency range of 0.1 kHz to 10 kHz in steps of 10 Hz. The conductance curve, presented in figure 7.6, indicated that the fundamental in-air resonance occurs at the frequency of 7140 ± 5 Hz. This compares favourably with the frequency of 7223 ± 0.5 Hz predicted from the numerically generated response shown in figure 7.5, an approximate discrepancy of only 1.16 %.

Using the relationship between admittance and impedance, presented in Chapter 4, Section 4.2.3, it is possible to convert the admittance responses to impedance responses. The resistance curve then allows the frequency of the in-air anti-resonance to be detected. When both the frequency of resonance and anti-resonance are known the coupling coefficient can be calculated [7.1].

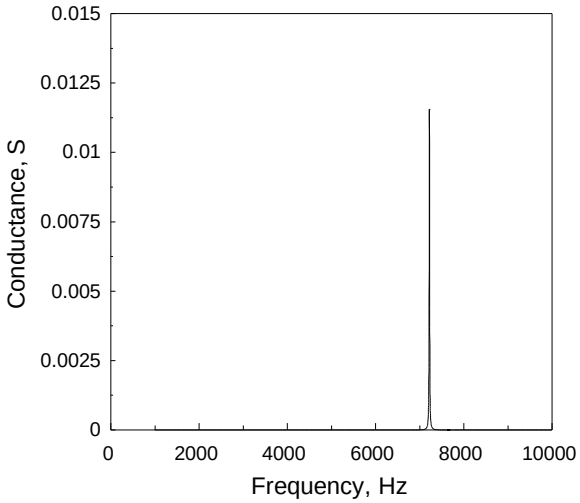

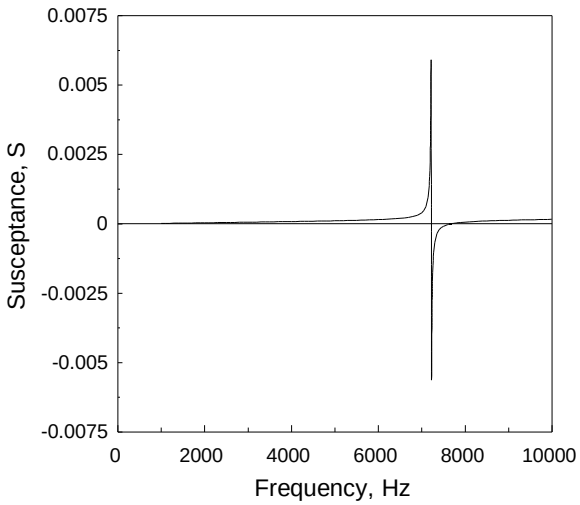

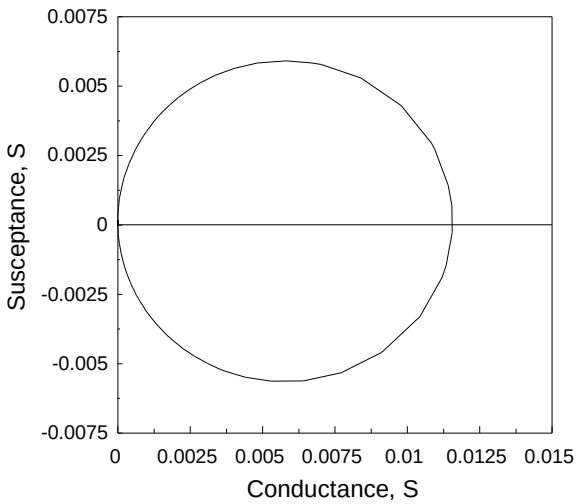

Figure 7.5. Theoretical in-air admittance response.

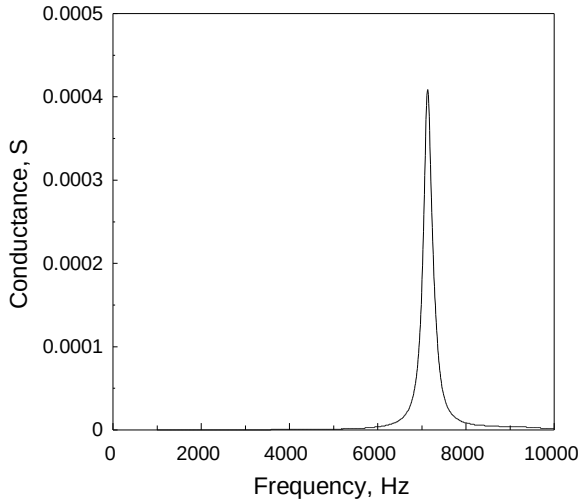

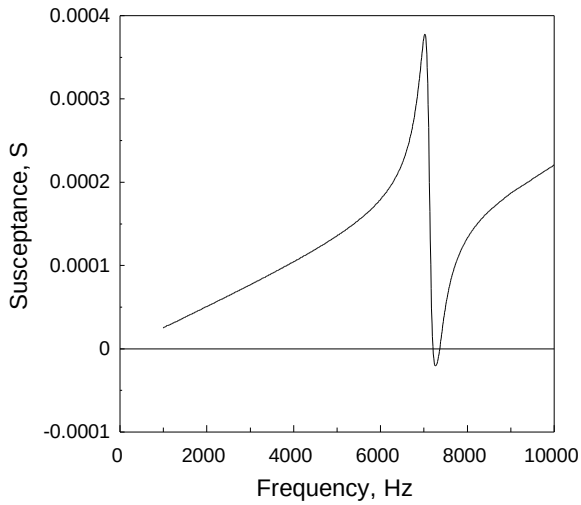

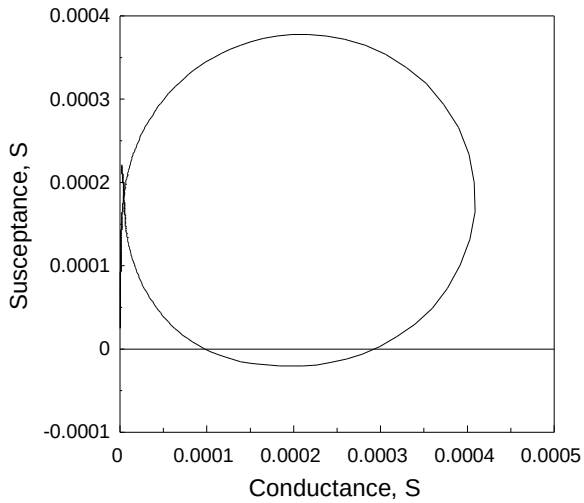

Figure 7.6. Measured in-air admittance response.

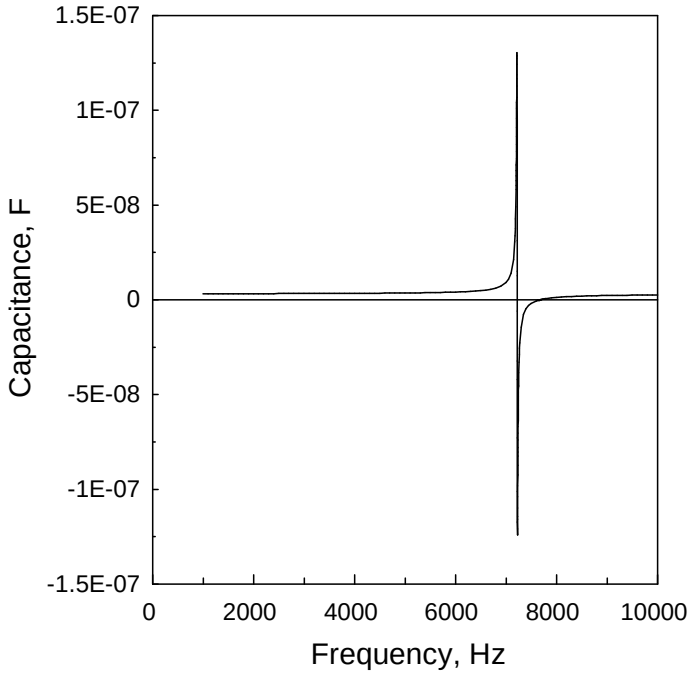

Figure 7.7. Theoretical in-air capacitance response.

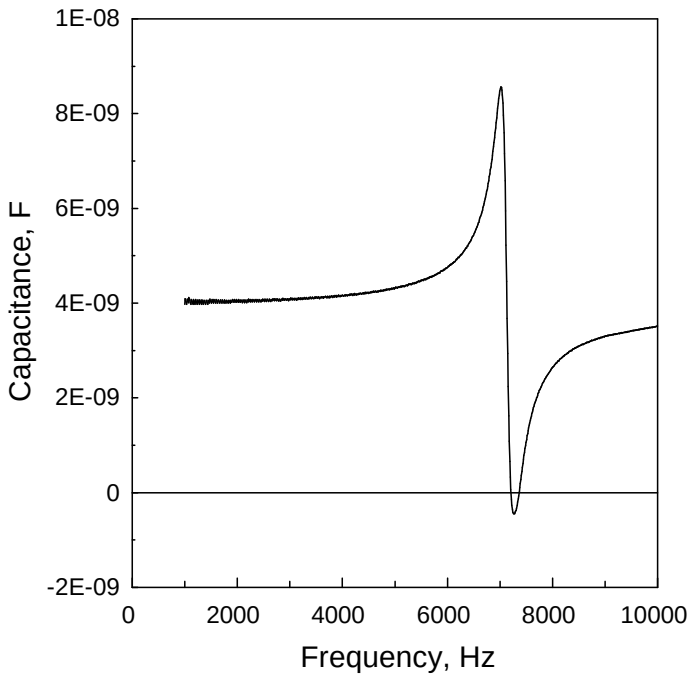

Figure 7.8. Measured in-air capacitance response.

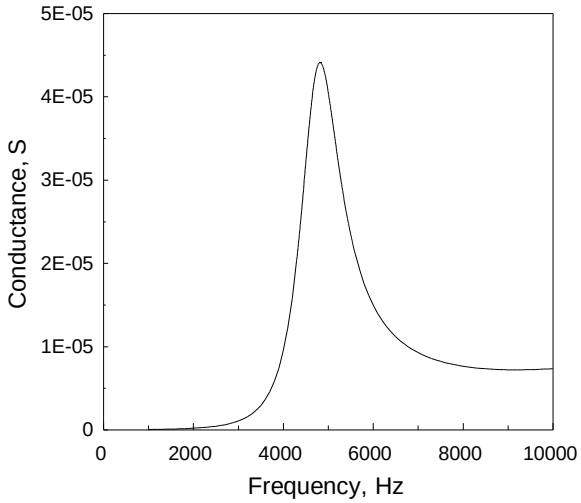

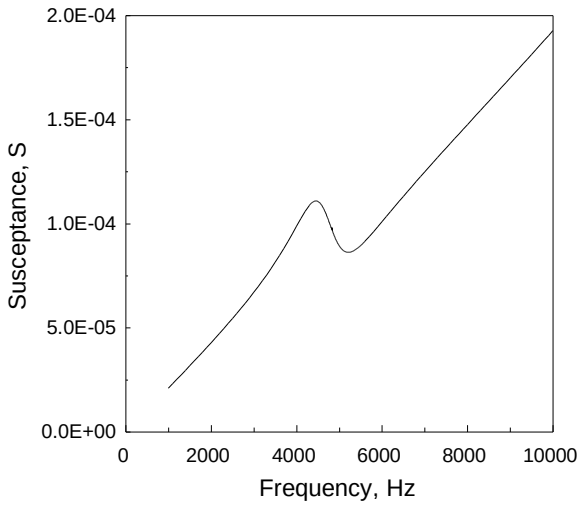

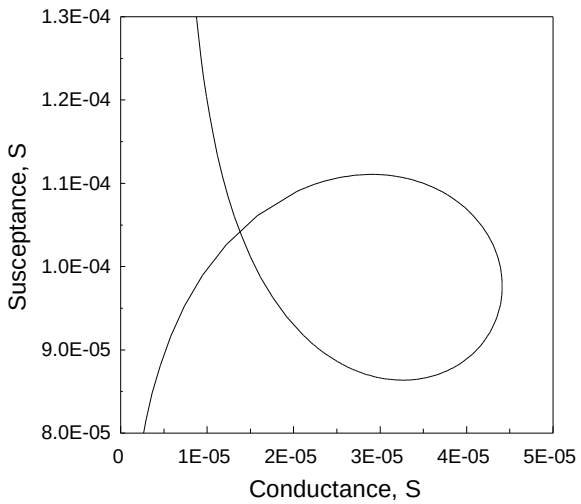

Figure 7.9. Theoretical in-water admittance response.

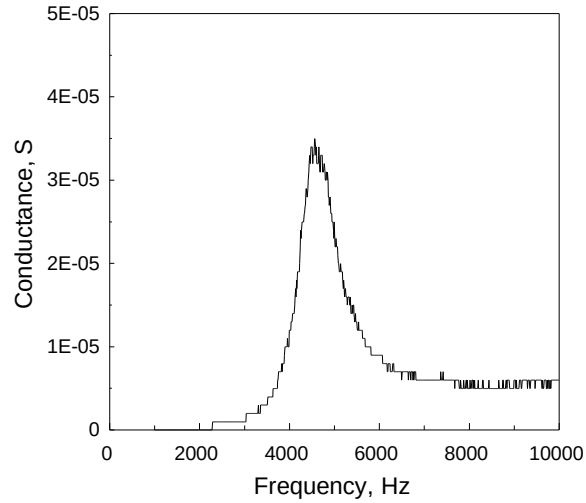

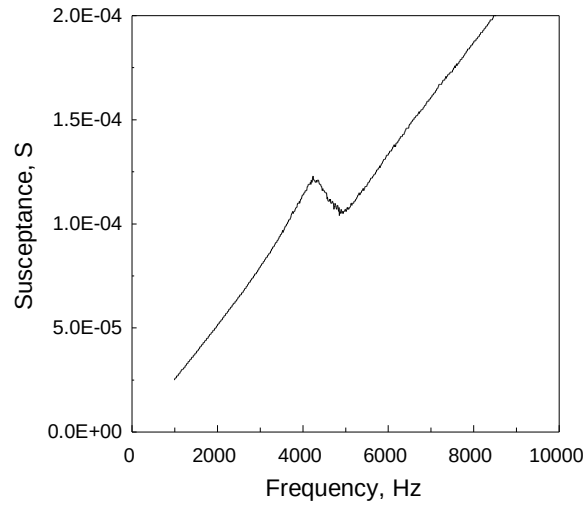

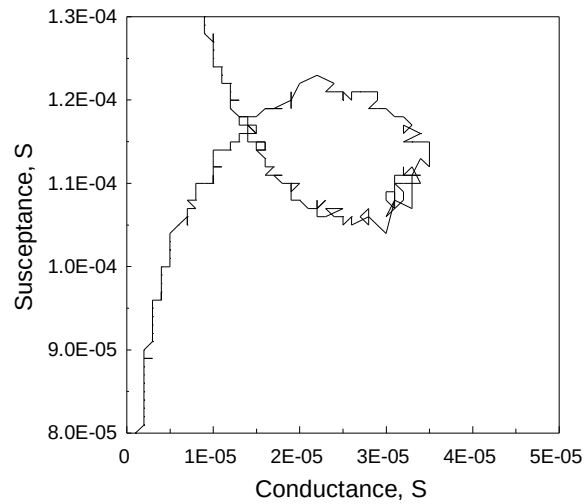

Figure 7.10. Measured in-water admittance response.

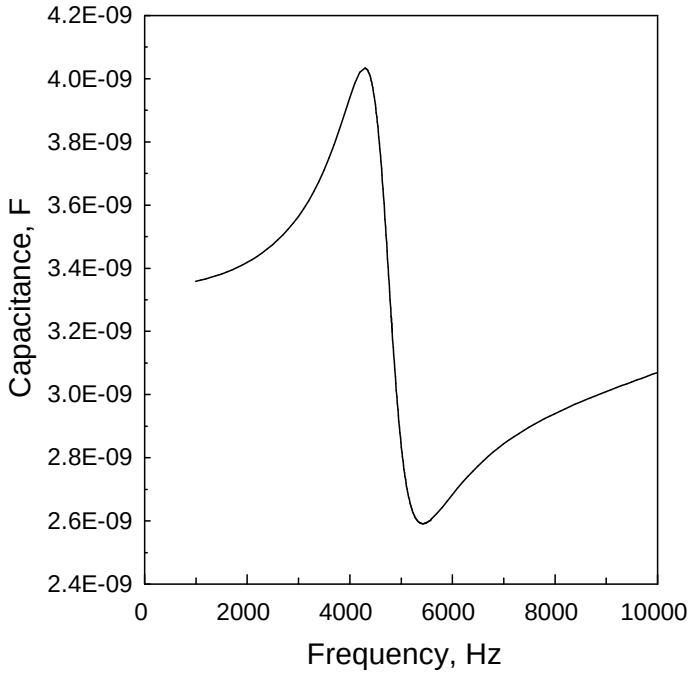

Figure 7.11. Theoretical in-water capacitance response.

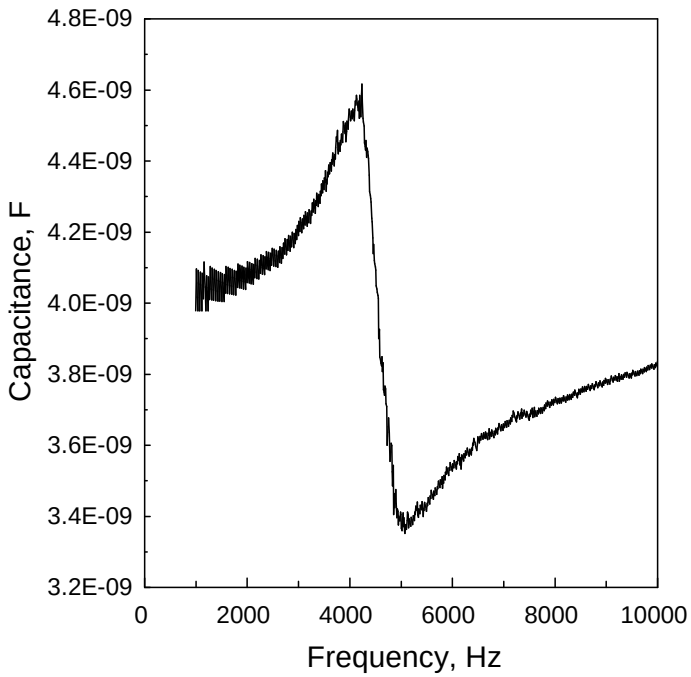

Figure 7.12. Measured in-water capacitance response.

It is found that the anti-resonance occurred at a frequency of 7430 ± 5 Hz. This corresponds to a predicted anti-resonance of 7655 ± 0.5 Hz, a discrepancy of 3.03 %. Using the following equation

$$k^2 = 1 - \left(\frac{f_{resonance}}{f_{anti-resonance}} \right)^2 \tag{7.3}$$

the coupling coefficient k^2 is found to be 0.110 for the theoretical model and 0.0765 for the actual device. An explanation for the reduced electro-mechanical coupling in the prototype transducer will be deferred for the moment.

The transducer capacitance can also be derived from the admittance response; the variation with frequency is given by

$$C = \frac{B}{2\pi f} \tag{7.4}$$

The predicted and measured capacitance responses are shown in figures 7.9 and 7.10 respectively. As expected, the capacitance well below resonance is effectively constant, 3.35 nF @ 1 kHz predicted, 4.05 nF @ 1 kHz actual device. The measured low-frequency capacitance C_{LF} conforms almost exactly to the value calculated using equation (7.1). At frequencies above the resonance both the predicted and measured responses follow the ideal behaviour within the frequency range explored, becoming asymptotic to a constant value equal to the capacitance at resonance.

It may be observed that the measured in-air electrical responses at resonance are not as sharp as predicted and the peak values are significantly reduced. This variation is almost certainly due to greater mechanical damping in the structure than that found in the finite element model. The lack of damping in the numerical model can be attributed to a number of factors; (a) the omission of the rubber boot, (b) assumption of perfect coupling between the end-plates and the staves, (c) the omission of the centre bolt, (d) the variation of the material properties from their expected values.

The effect of the extra damping is to reduce the mechanical quality factor and the coupling coefficient. These and other important parameters that can be derived from the in-air electrical responses, predicted and measured, are listed in table 7.5.

Table 7.5. Parameters derived directly from in-air electrical responses.

Parameter	Theoretical value	Experimental value
f_{air}	7223 ± 0.5 Hz	7140 ± 5 Hz
k^2	0.110	0.0765
Q_m	657	30
G_m	11.55 mS	409 μS
C_{LF}	3.35 nF	4.05 nF
tan δ_e	0.003	0.008

Table 7.6. Components of the in-air equivalent circuit.

Parameter	Theoretical value	Experimental value
L_m	1.321 H	1.624 H
C_m	367 pF	306 pF
R_m	86.4 Ω	2.4 kΩ
C_e	2.98 nF	3.694 nF
R_e	2 MΩ	700 kΩ

The measured value for the electrical loss factor (tan δ_e) is somewhat higher than the manufacturer's quoted value of 0.004, while the predicted value is slightly lower. These discrepancies are probably caused by difficulties in measuring low conductance values in the first case, and the approximations inherent in the finite element treatment in the second case.

Table 7.6 lists the components of an in-air equivalent circuit that can be derived from the parameters listed in table 7.5, as explained in ref. [7.1]. All the components, excluding the mechanical resistance R_m, compare favourable. The large discrepancy between the values for R_m is a direct effect of the high level of mechanical damping associated with the experimental results.

The measurement of the in-water electrical response was performed in a manner similar to that used for the in-air case. The radiating surface of the projector was first chemically cleaned with a detergent (washing-up liquid) to remove any grease to which air bubbles might adhere when the transducer is immersed in water. The transducer was then suspended in the centre of an acoustic tank of dimensions 30 feet by 12 feet by 10 feet. Even when the surface of the transducer has been degreased it is likely that some air bubbles will cling to the surface of the transducer. Thus,

several hours were allowed to pass between introducing the projector to the tank and measuring the electrical response to ensure that the transducer surface was fully 'wetted' [7.2]; that is, the air bubbles that initially adhere to the surface of the transducer as it is immersed in water have dissipated.

The measured response, shown in figure 7.12, is rather noisy due to the limited accuracy of the measuring equipment. However, it indicates that the fundamental in-water resonance frequency occurs at 4700 Hz ± 5 Hz, which is in general agreement with the predicted resonance frequency of 4819 Hz ± 0.5 Hz observed from the computed response presented in figure 7.11, an approximate discrepancy of 2.53 %. It may be noted that the admittance levels at resonance compare far more favourably in water than they do in air. This is because in air the radiation resistance can be considered to be negligible, and thus the only source of damping is that in the structure. In water, however, the radiation resistance is usually much greater than the internal mechanical losses and hence considerably increases the overall damping.

Table 7.7 summarises performance characteristics taken from the predicted and measured in-water admittance responses. It may be noted that the clamped capacitance can be measured directly from the in-water capacitance response (see figures 7.13 and 7.14). This is possible since the variation of capacitance with frequency in water is much more gradual than in air. Values of 3.226 nF predicted, and 3.759 nF measured, compare favourable with previously calculated values for the clamped capacitance.

Table 7.7. Parameters derived directly from in-water electrical responses.

Parameter	Theoretical value	Experimental value
f_{water}	4819 Hz ± 0.5 Hz	4700 Hz ± 5 Hz
Q_M	3.95	4.0
G_M	40.5 μS	30 μS
G_{max}	44.1 μS	33 μS
C_e	3.226 nF	3.759 nF

Table 7.8. Efficiencies.

Parameter	Theoretical value	Experimental value
η_{ma}	99.6 %	91.9 %
η_{em}	91.8 %	90.9 %
η_{ea}	91.4 %	83.5 %

Using equivalent circuit methods it is possible to estimate the efficiency of a transducer from its in-air and in-water admittance responses [7.1]. Table 7.8 lists the predicted and measured mechanical-acoustic, electro-mechanical, and electro-acoustic efficiencies. The actual device is seen to be approximately 8 % less efficient than predicted. Again this difference can be attributed to the higher level of internal damping in the transducer than expected. Another factor is the limited accuracy of the measuring equipment which has a resolution of 1 μS.

7.4 Conclusions

In this chapter the initial development of a transducer suitable for ocean acoustic tomography has been detailed. A design was presented which met virtually all the requirements, with the exception of the weight and operating depth. Since the proposed transducer was air-backed it had to be covered with a rubber boot to prevent water from entering the transducer. The requirement for a boot limits the maximum operating depth of this design to approximately 100 metres, the depth at which the boot is forced into the gaps between the staves.

A scaled prototype transducer based on the air-backed transducer design has been built and experimentally assessed. The in-air and in-water admittance responses of the device have been measured on a digital impedance analyser. The performance characteristics, in both cases, compare favourably with the values predicted from finite element and boundary element calculations. In particular, the resonance frequencies, show very good agreement. The peak values of the measured responses, however, were somewhat lower than those predicted. This discrepancy between the theoretical and experimental results is attributed to an increased level of damping in the transducer than that found in the finite element and boundary element model. The

lack of damping in the numerical model resulted in an overestimation of the efficiency of the device.

7.5 References

[7.1] D. Stansfield, *Underwater Electroacoustic Transducers*, (Bath University Press and Institute of Acoustics, 1990), Chapter 4.

[7.2] D. Stansfield, *Underwater Electroacoustic Transducers*, (Bath University Press and Institute of Acoustics, 1990), 260.

Chapter 8

A FREE-FLOODED DESIGN

8.1 Introduction

The work described in the previous chapter was carried out for an air-backed transducer design. The specification for an ocean acoustic tomography source requires an operational depth in excess of 500 metres. Methods of providing depth capability have been considered in Chapter 3, but thus far no attempt has been made at modelling such a configuration. Of the possible methods, two are considered to be appropriate for the class I flextensional transducer geometry when required to operate at a depth of 500 metres: (a) operating the transducer as a free-flooded device, with the inclusion of compliant tubes to reduce the internal impedance [8.1]; (b) operating the transducer as a free-flooded device, using a compliant material, such as a closed-cell foam, to partially fill the interior in order to reduce the internal loading on the shell [8.2].

Both solutions modify the performance as predicted by existing work, and the extent of this modification needs to be established. It is anticipated that the depth compensation schemes will have the effect of increasing the resonance frequency because of the increased internal stiffness [8.3-8.5]. An increase of the resonance frequency is undesirable, since a larger, and hence heavier, device is required to produce a given resonance frequency in comparison to an air-backed device. It is predicted that the acoustic power output and efficiency will be reduced because of the increase in internal stiffness, which will result in work being done in compressing the internal fluid fill, and because of losses within the cavity. The loss in the internal fluid is likely to be insignificant, except in the gaps between the staves where large amplitude fluid motion might occur. Loss in the compliant elements will depend on the material used – foam materials being more lossy than steel or aluminium tubes. The effect on bandwidth is more difficult to predict, because of the competing influences of increasing the internal stiffness, mass loading and internal damping.

In this section, the construction of a partially free-flooded transducer, incorporating an internal foam compliant region, is described. This device was machined and assembled at the University of Birmingham. A brief description of the procedures and techniques used to assemble the transducer are given.

As with the air-backed transducer, theoretical and experimental analysis of the partially free-flooded device is presented. However, due to the low operating frequency of the device it was necessary to calibrate the transducer in a deep water site and a brief description of the set-up required to undertake these experiments is given.

8.2 2.5 kHz Partially Free-Flooded Flextensional Transducer

The new transducer design is loosely based on the original air-backed design. The dimensions have been scaled to approximately 1/3 size, which would be expected to result in a resonance frequency of around 1.5 kHz assuming that the device is used in an air-backed configuration. However, it will be seen that flooding the device, even with the inclusion of compliant components, has a dramatic effect of its performance, producing a considerable increase in the frequency of resonance and 3 dB bandwidth while reducing acoustic power output and efficiency.

The major design modification is the inclusion of an internal compliant region. The choice of foam for this region is restricted by a number of criteria. Firstly, the foam must be impervious to water, and this implies a closed-cell structure. Secondly, the foam should be as compliant as possible. However, the more compliant foams are structurally weaker and thus the limiting factor is the required operating depth. Table 8.1 lists a selection of foams from the Plasticell range. The maximum depth quoted is for a material under static compression. However, if as intended, the foam is to be fitted inside a transducer, it will subjected to an alternating pressure superimposed on the ambient pressure and this must be taken into consideration. As the required operating depth of the transducer is 500 metres, the Plasticell D300 material was selected. Finally, since we require the cavity to be as compliant as possible, a maximum volume of foam material is always sought after. Thus, the gap between the compliant region and the staves must be minimised.

Table 8.1. Plasticell foam materials.

Material	Density (kg m^{-3})	Young's modulus (MPa)	Poisson's ratio	Mechanical quality factor Q_m	Maximum depth (m)
D40	40	21.5	0.3	160	30
D55	55	38.1	0.3	160	75
D75	75	61.3	0.3	160	140
D100	100	90.4	0.3	160	190
D300	300	357	0.3	160	875
D400	400	470	0.3	160	1380

The compliant foam material is only available in sheet form, and hence due to the limited thickness available this region is comprised of a number of layers in the axial direction. Each layer is machined into discs of the required dimensions. Then the outer surface of each disc is shaped so that it follows the profile of the inner surface of the staves less 1 mm, to allow a gap between the two.

In addition to incorporating an internal foam compliant region which allows operation at depths up to at least 500 metres, a number of other minor modifications have been made to the design which slightly improve the performance of the transducer. The most notable change is in the connection between the end-plates. With the first prototype transducer the staves were simply secured to the end-plates with bolts. The staves were therefore liable to slide, introducing friction losses. As explained in Chapter 6, Section 6.2, the coupling between the staves and the end-plates can be improved by employing keyway joints, and such joints have been incorporated in this second prototype device.

Other changes include, reducing the radius of the end-plates, which also improves the coupling between the staves and the end-plates, and using staves with a slightly tapered profile. Tapered staves, which are slightly thicker at the midriff than at the ends, offer a similar performance to conventional staves of greater mass and thus help to reduce the weight of the transducer.

8.2.1 Construction Details

The technical drawings and a comprehensive parts list for the 2.5 kHz free-flooded transducer can be found in Appendix B. The schematic of the cross-sectional view of the assembled transducer is repeated in figure 8.1 and the main dimensions and materials are listed in tables 8.2 and 8.3 respectively.

The stack was formed from 26 PZT-4 ceramic rings. In addition, a MACOR ring of the same dimensions as the piezoelectric rings were fitted at each end of the stack to ensure electrical isolation. A nylon tube was placed through the centre of the stack to prevent flash-over to the bolt. Electrical contacts with the silvered surfaces of the piezoelectric ceramics were made using Monel metal gauze. The technique of using two chains was implemented, as described in Section 6.4.

Table 8.2. Main transducer dimensions.

Parameter	Description	Value (mm)
r_{si}	Inner radius of curvature of the staves	183
r_{so}	Outer radius of curvature of the staves	172
g_s	Gap between staves	1
g_c	Cavity gap	1
t	Shell thickness at midriff	12
ℓ	Length between end plates	170
r_e	Radius at end of device	46.4
h_p	End-plate thickness	25
r_i	Inner radius of stack	10
r_o	Outer radius of stack	25
n	Order of rotational symmetry	8

Table 8.3. Main transducer materials and their properties.

Part	Material	Density (kg m^{-3})	Young's modulus (10^3 MPa)	Poisson's ratio	Mechanical quality factor Q_m
Ceramic	PZT-4™	See table 2.2			
Insulator	MACOR™	2520	140.0	0.29	500
End-plate	Stainless	7960	193.0	0.31	10000
Foam	D300	300	0.357	0.30	160
Stave	Aluminium	2710	68.91	0.30	1000

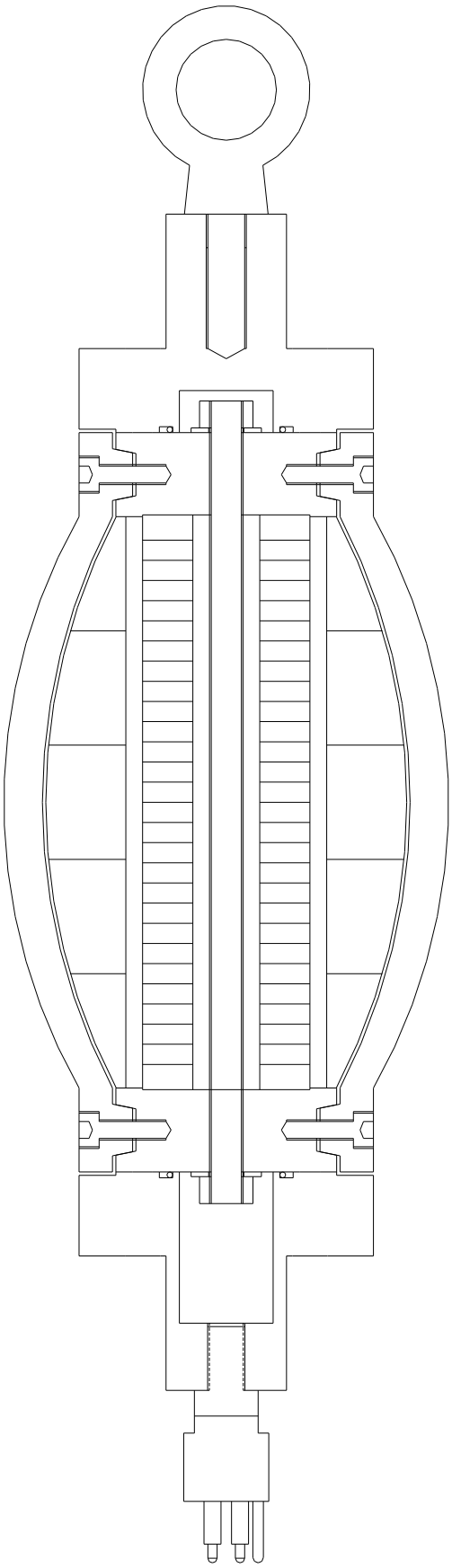

Figure 8.1. Technical drawing of the 2.5 kHz free-flooded prototype transducer (scale 1 : 2).

Prior to assembling the stack, all the components (PZT-4 rings, MACOR rings, gauze, and nylon tube) were degreased by immersing them in 5 % DECON 75 solution in an ultrasonic bath and then rinsed in acetone to remove the cleaning solution. This preparation process is essential if high quality glue joints are to be realised. It also reduces electrical leakage currents along the surface of the piezoelectric rings and reduces the chance of flash-over between the electrodes.

The glue was mixed in the correct proportions of resin and hardener, as specified by the manufacturer, and then evacuated until the majority of the trapped air had boiled off. This process minimises the air trapped in the glue joints, and helps achieve a strong bond strength. Air bubbles in the glue joints will weaken the bond strength; they also increase the compliance of the stack and hence degrade the electro-mechanical coupling. The glue used was ARALDITE 2019. This is a low viscosity glue and was chosen since it is the only one in the ARALDITE range which has an adequately long cure time (90 minutes working time) such that the stack could be assembled. Also, the use of a runny glue is advantageous since it is easier to remove the trapped air and hence helps to ensure good quality joints.

The stack was assembled using the nylon tube as a jig to locate the rings and electrodes. The outer diameter of the tube was just large enough to ensure that the rings fitted snugly around it. A MACOR insulation ring was fitted at one end, around the top of the tube. The stack was built up on top of the MACOR ring, with Monel metal gauze chains being appropriately woven between the piezoelectric ceramics. Before each new element was fitted the nylon tube was gently tapped up through the rings until enough tubing protruded from the topmost ring to accommodate another ring. The stack was complete with the fitting of another MACOR ring.

Having completed the stack, one end was glued onto the ‘bottom’ end-plate which is designed to accommodate the electrical connection to the stack. To ensure that the correct glue joint thickness was achieved, a Monel metal gauze ring was inserted between the end-plate and stack. The other end-plate was placed on the opposite end of the stack but was not glued in place. A length of studding was placed though the centre of the entirety to ensure that all the components were correctly located. The whole assembly was then placed in a hydraulic press and compressed by a pressure of 1000 psi, expelling the excess glue out of the joints.

The stack was left under compression for 96 hours until the glue had cured. It was then taken out of the press and the loose end-plate and studding removed. Two electrical wires were run though the 'bottom' end-plate and then soldered onto the gauze chains. The compliant region was then centred around the stack and glued to the 'bottom' end-plate using a quick setting epoxy resin. When the glue had cured the region between the stack and foam was filled with a potting compound, SCOTCHCAST. This bonded the compliant region to the stack and also provided a waterproof layer.

The assembly, thus far, was mounted and centred on a length of studding that was approximately one and a half times longer than required. At the 'bottom' end-plate, a nut and washer were brought to bear against its surface. The remaining studding protruding from the nut was clamped tightly in a lathe chuck. At this point the 'top' end-plate was glued onto the free-end of the stack. Once again a ring of Monel metal gauze was used to control the glue joint thickness. Another set of nut and washer were loosely tightened onto this end-plate. The remaining studding at this end of the assembly was then run though a lathe steady, enabling the device to be held level. Obviously it was essential that both end-plates aligned precisely, and this was accomplished by clamping the end-plates together, as shown in figure 8.2. Finally, the required compressive pressure of 1000 psi was applied to the stack. This was achieved by mounted a clock dial gauge on the lathe saddle such that it was just touching the end of the centre bolt. Then by tightening the nut pressing on the 'top' end-plate, thereby stretching the centre bolt, the required force was applied, interpreted though the reading on the dial gauge which measured the extension of the bolt.

After curing of the glue, the jig clamping the end-plates was removed. Opposite staves were then inserted into the relevant slots in the end-plates and loosely bolted on. Inserting the staves in pairs helped to ensure that forces acting on the device were symmetrical. Once all the staves had been located, the bolts were fully tightened. The transducer could then be removed from the lathe and the excess studding cut off.

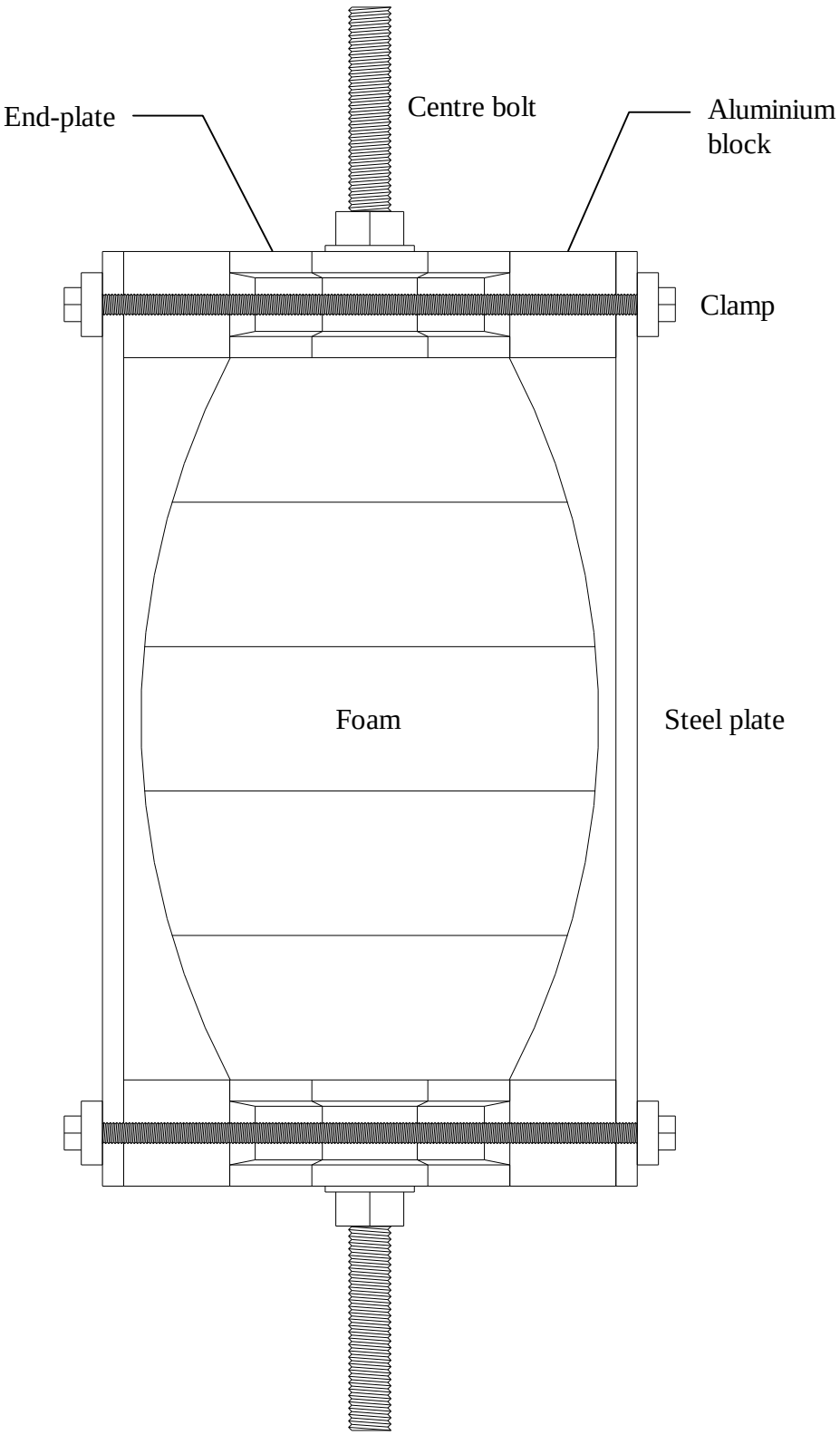

Figure 8.2. Clamping arrangement used to ensure that both end-plates aligned. Two mild steel plates span between the end-plates. These are mounted on aluminium blocks so that the plates clear the compliant foam region. The plates are then clamped in place at each end, thus aligning the two end-plates.

The final assembly process was to bolt the end-caps onto the end-plates. The 'bottom' end-cap incorporated a 4-pin WET-CON connector, which facilitated the connection of the electrode wires to the outside world, while the 'top' end-cap was fitted with a eye-bolt, which provided a means of suspending the transducer. Photographs of the completed device are shown in figures 8.3, 8.4, and 8.5.

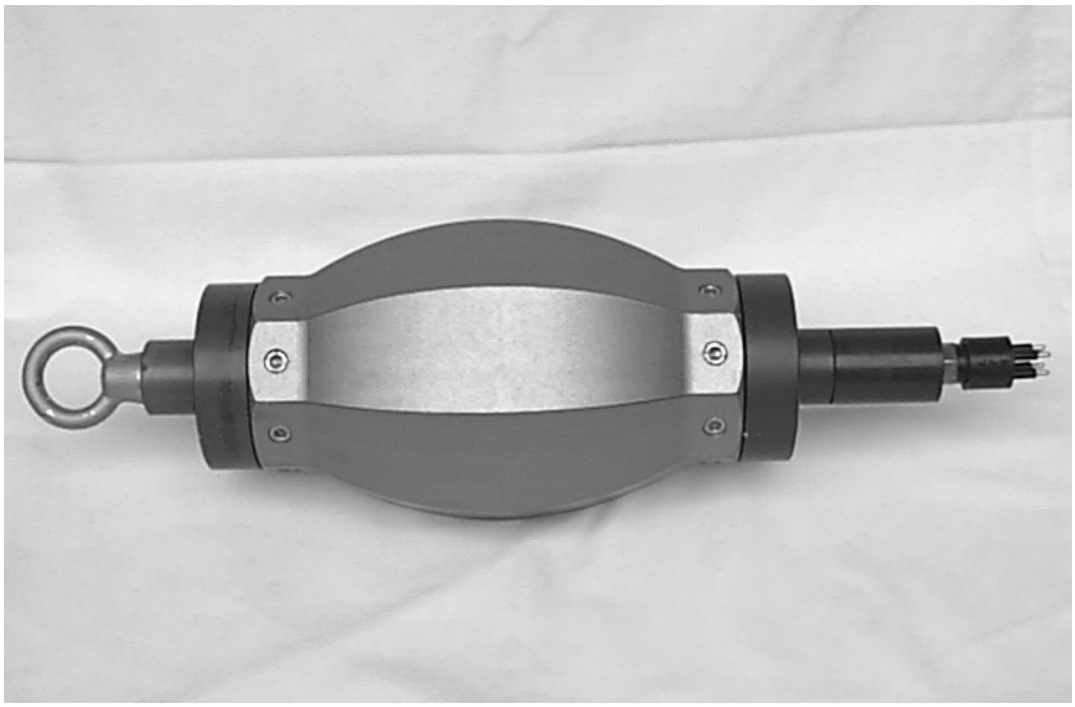

Figure 8.3. 2.5 kHz free-flooded flextensional transducer (horizontal view).

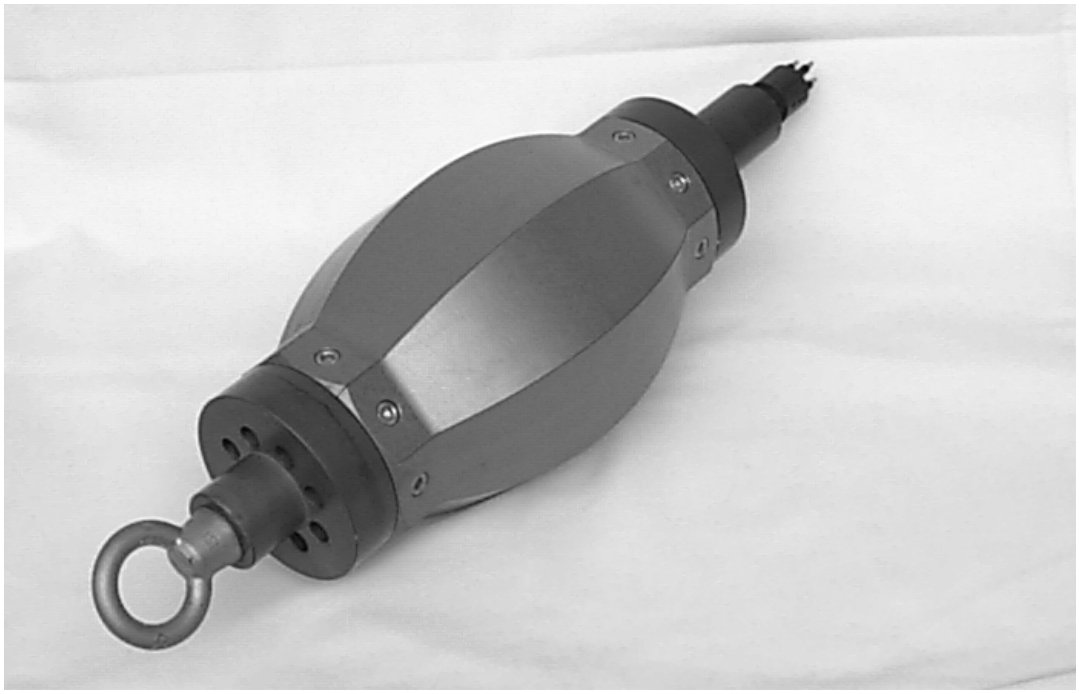

Figure 8.4. 2.5 kHz free-flooded flextensional transducer (view of eye-bolt).

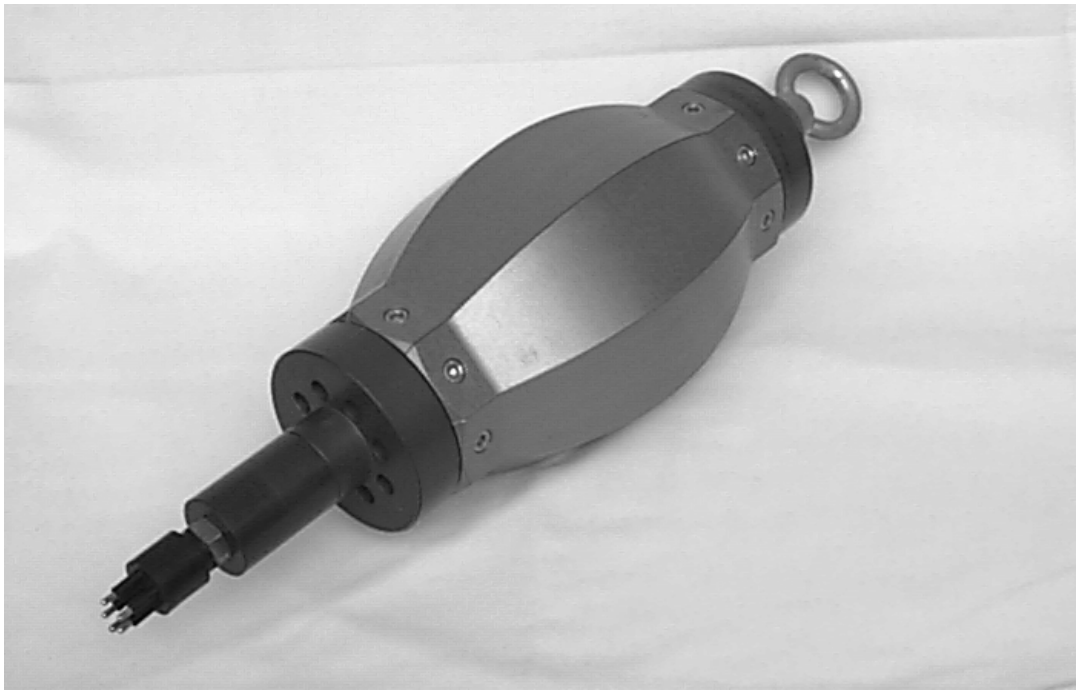

Figure 8.5. 2.5 kHz free-flooded flextensional transducer (view of electrical connector).

8.2.2 Finite Element and Boundary Element Results

In this section finite element and boundary element results are presented for this second prototype transducer.

Figure 8.6 shows the mesh for the transducer in the air-filled configuration. The mesh is a one-eighth segment of the upper half of the transducer. As with the meshes described in Chapter 5, the implementation of this reduced structural mesh is made possible by realising rotational symmetry about the z-axis, and mirror symmetry in the xy-plane.

The mesh is similar to those used in Chapter 5, but with the inclusion of a compliant region. Ten elements have been used to represent half the stack; one MACOR element, four PZT-4 elements, and 5 glue joints. In the actual transducer, a half stack consists of one MACOR ring and thirteen PZT-4 rings with glue joints binding the component together. In light of the reduced number of stack elements in the numerical model the glue joints have been scaled to match the volume present in the constructed transducer.

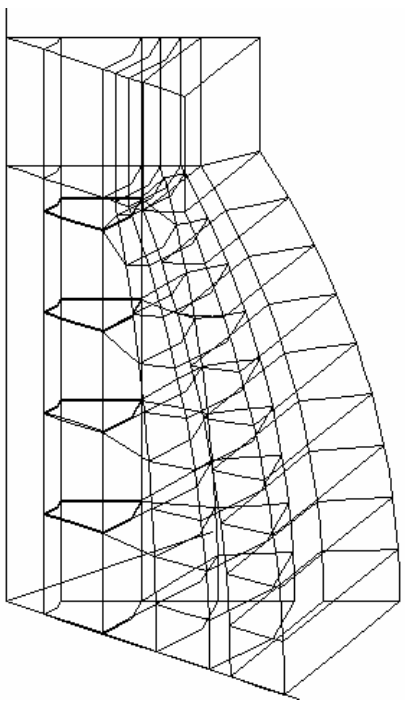

Figure 8.6. Segment mesh of the air-backed version of the transducer.

The effect of using less piezoelectric elements in the model causes the finite element and boundary element calculation to produce scaled values for the admittance and sound pressures. However, the scaling factors can easily be determined.

Replacing n ceramic elements by n_{model} while keeping total length constant means that for equivalent conditions the current scales by a factor of n_{model}/n, since the elements are electrically in parallel. The thickness of the elements and therefore the voltage across them are scaled by the inverse factor n/n_{model}. The, the true admittance Y (= current/voltage) is scaled by the factor $(n_{model}/n)^2$, that is

$$Y = Y_{model}\left(\frac{n}{n_{model}}\right)^2 \tag{8.1}$$

where Y_{model} is the admittance calculated for the model with n_{model} piezoelectric elements rather than the true number n.

The acoustic output of the model is calculated assuming a 1 V peak input across the piezoelectric elements of the model. Since this is equivalent to an input voltage n_{model}/n in the actual device, the true sound pressure p with respect to 1 V peak input is given by

$$p = p_{model}\left(\frac{n}{n_{model}}\right) \tag{8.2}$$

where p_{model} is the calculated pressure. Alternatively, in decibel form

$$\mathrm{S} = 20\log_{10}\left(p_{model}\right) + 20\log_{10}\left(\frac{n}{n_{model}}\right) + 120 \tag{8.3}$$

Figures 8.7 and 8.8 show respectively the corrected in-water conductance and capacitance responses of the air-backed version of the transducer. Table 8.4 summarises performance characteristics calculated from these responses, while table 8.5 list the components of an equivalent electrical circuit.

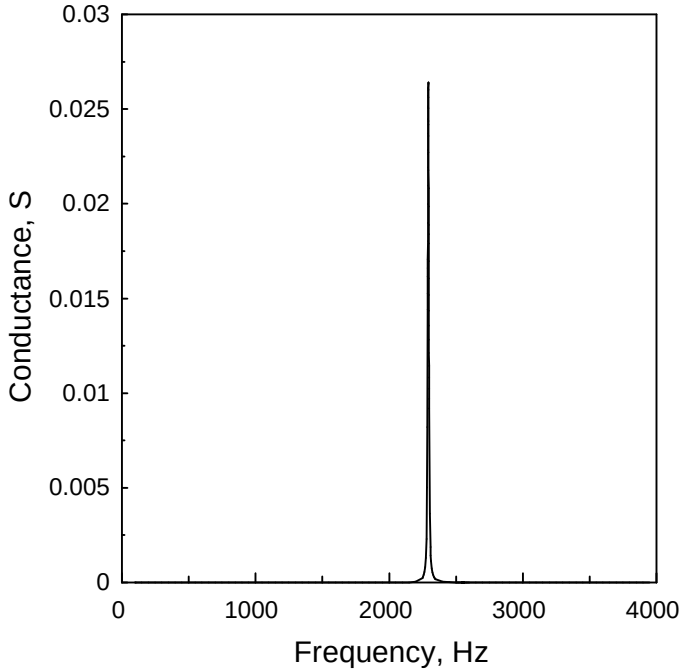

Figure 8.7. Predicted in-air conductance response.

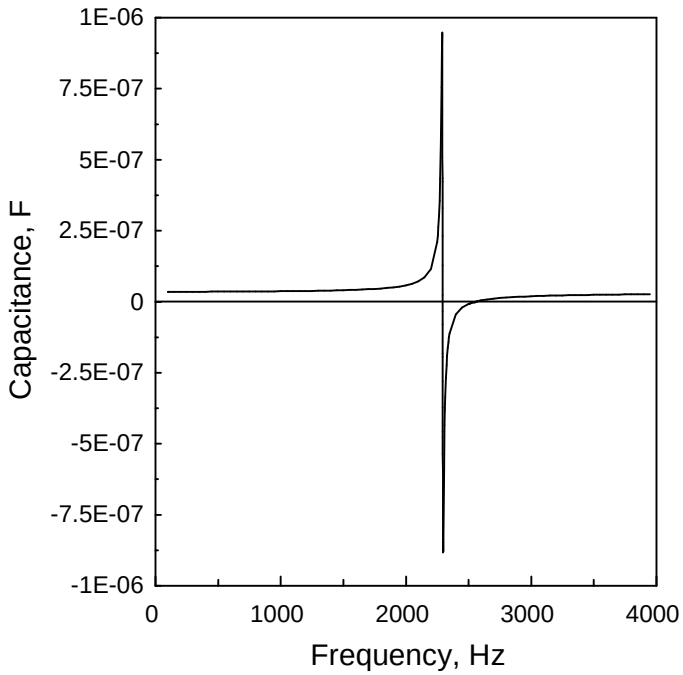

Figure 8.8. Predicted in-air capacitance response.

Table 8.4. Parameters derived directly from the predicted in-air electrical responses.

Parameter	Value
f_{air}	2294 ± 0.5 Hz
k^2	0.191
Q_m	258
G_m	26.42 mS
C_{LF}	36.0 nF
$\tan \delta_e$	0.003

Table 8.5. Components of the in-air equivalent circuit.

Parameter	Value
L_m	0.7 H
C_m	6.876 nF
R_m	37.85 Ω
C_e	29.12 nF
R_e	250 kΩ

Having analysed the in-air performance of the transducer we now need to consider its behaviour when operated as a free-flooded device. Figure 8.9 shows the mesh for the transducer in the free-flooded configuration. The mesh is identical to that used for the air-backed configuration, but with the addition of water elements between the staves and the compliant region.

Figures 8.10 and 8.11 show the in-water conductance and capacitance responses of the free-flooded version of the transducer, respectively. From these it can be seen that the transducer behaves in a curious manner over the frequency range around 3.8 kHz. Figures 8.12 and 8.13 depict the relative displacement field at the fundamental in-water resonance frequency and the frequency of 3.8 kHz respectively. The displacement field at resonance shows the foam moving in unison with the staves at the midriff. At the frequency of 3.8 kHz the motion of the internal region dominates, indicating that this is a cavity resonance rather than a stave resonance; all the power is being utilised in moving the fluid. It is possible that this cavity resonance is an artefact of the numerical treatment as it is not observed in practice.

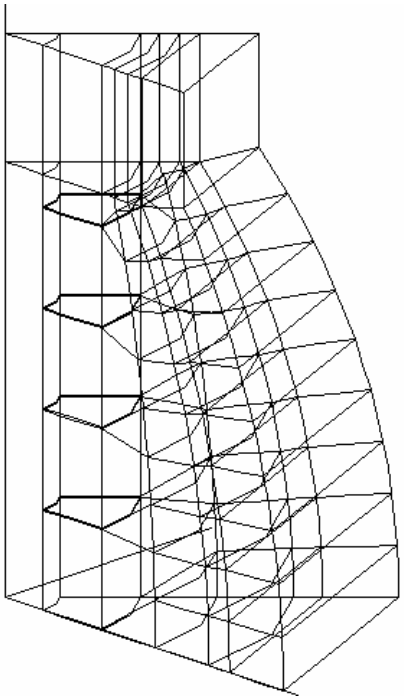

Figure 8.9. Segment mesh of the partially free-flooded version of the transducer.

If these results for the free-flooded device are compared with those of an equivalent air-backed configuration there is a observed significant increase in the frequency of resonance (up from 1430 Hz to 2610 Hz) and an increase in the 3 dB bandwidth (up from 310 Hz to 770 Hz) with a corresponding decrease in the quality factor. The increase in resonance frequency can be attributed to the greater internal stiffness. The reduction of the quality factor is due at least in part to the high level of damping in the compliant region. This can also be seen in the reduced peak conductance value (down from 543 μS to 413 μS). Table 8.6 summarises the performance characteristics.

Table 8.6. Parameters derived directly from the predicted in-water electrical response.

Parameter	Value
f_{water}	2610 Hz ± 5 Hz
$B(-3\text{ dB})$	770 Hz
Q_M	3.12
G_{max}	413 μS
C_e	64 nF

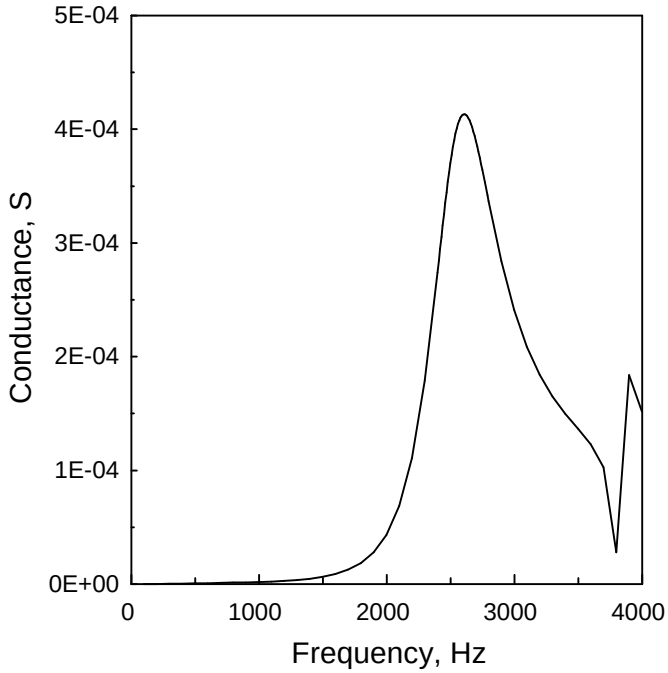

Figure 8.10. Predicted in-water conductance response.

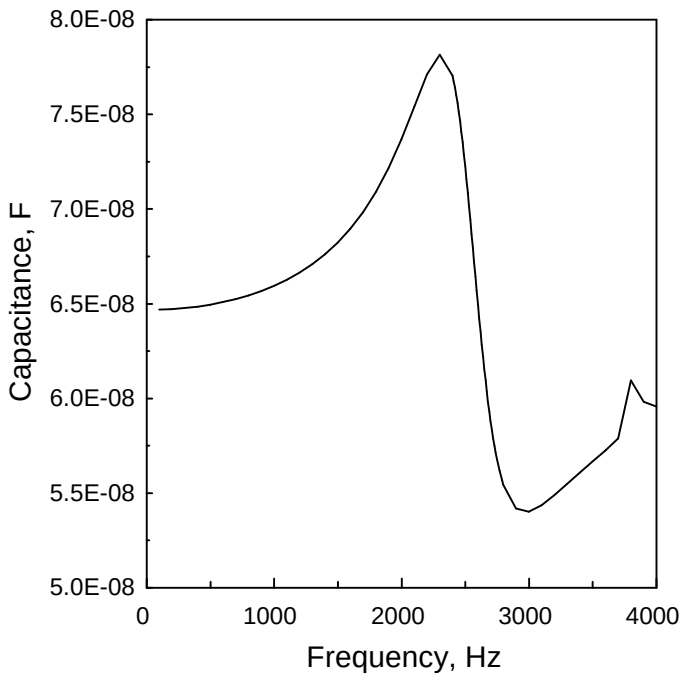

Figure 8.11. Predicted in-water capacitance response.

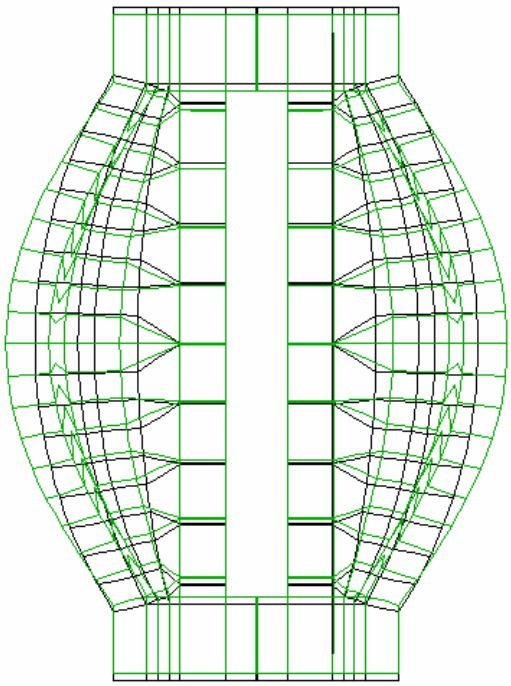

Figure 8.12. Predicted in-water relative displacement field of the 2.5 kHz partially free-flooded transducer at resonance (2.61 kHz). Solid lines—at-rest position. Dotted lines—displaced position.

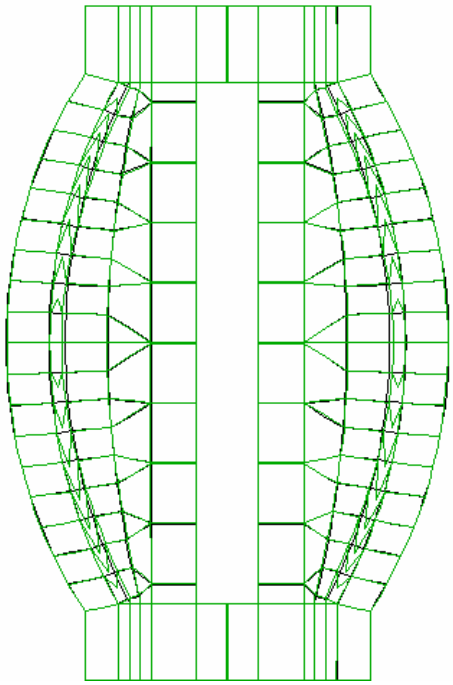

Figure 8.13. Predicted in-water relative displacement field of the 2.5 kHz partially free-flooded transducer at 3.8 kHz. Solid lines—at-rest position. Dotted lines—displaced position.

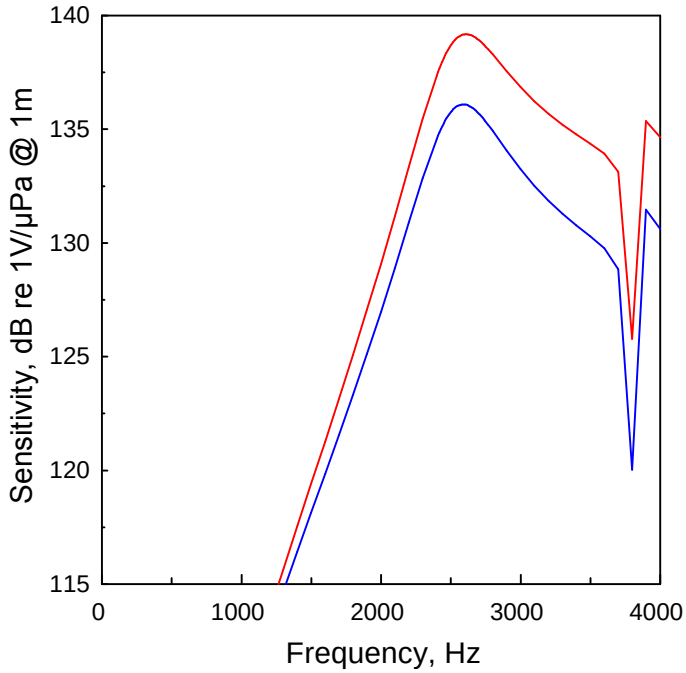

Figure 8.14. Predicted projector voltage sensitivity response of the partially free-flooded version of the transducer. Red—response in the z-direction. Blue—response in the x-direction.

In addition to the in-water admittance response, we can also analyse the behaviour of the transducer from its projector voltage sensitivity response, shown in figure 8.14. The figure shows the sensitivity response in the z-direction and the x-direction. It can be seen that the two responses are almost identical below resonance. At resonance there is a 3 dB variation between the two responses, and hence the transducer can only just be considered to be omni-directional. Above the resonance frequency the response in the z-direction falls off slightly less quickly than the response in the x-direction. Thus the quality factor based on the sensitivity response in the z-direction is slightly less than that based on response in the x-direction. Beyond the resonance frequency we again see a sharp dip in the responses, caused by the cavity resonance.

Table 8.7 summarises the results for the free-flooded version of the transducer with an internal compliant region determined from sensitivity responses.

Table 8.7. Parameters determined from the predicted in-water acoustic responses.

Parameter	Value
f	2610 Hz ± 10 Hz
$B_{x-direction}(-3\text{ dB})$	708
$Q_{x\text{-}direction}$	3.69
$S_{x-direction}$	136.1 dB re 1 V/μPa @ 1 m
$B_{z-direction}(-3\text{ dB})$	775 Hz
$Q_{z-direction}$	3.37
$S_{z-direction}$	139.2 dB re 1 V/μPa @ 1 m
η_{ea}	97.2 %

8.4.3 Transducer Calibration

The in-air conductance and capacitance responses of the transducer are shown in figures 8.15 and 8.16 respectively. Table 8.8 summarises performance characteristics calculated from these responses, while table 8.9 list the components of an equivalent electrical circuit.

Comparing the predicted and measured results it is seen that the same basic differences occur between the various parameters as they did for the 5 kHz air-backed flextensional transducer discussed in the previous chapter. That is, the numerical model has slightly overestimated the resonance frequency and underestimated the structural damping.

In-water calibration of the second prototype transducer presented a number of problems that stemmed from the low operating frequency. The size of the acoustic test tank at the University of Birmingham prohibits the use of frequencies below several kilohertz. Thus, it was necessary to test the transducer in a larger expanse of water. The nearest suitable site was a flooded quarry. The quarry has a maximum depth of 30 metres at its centre, and is several hundred metres across.

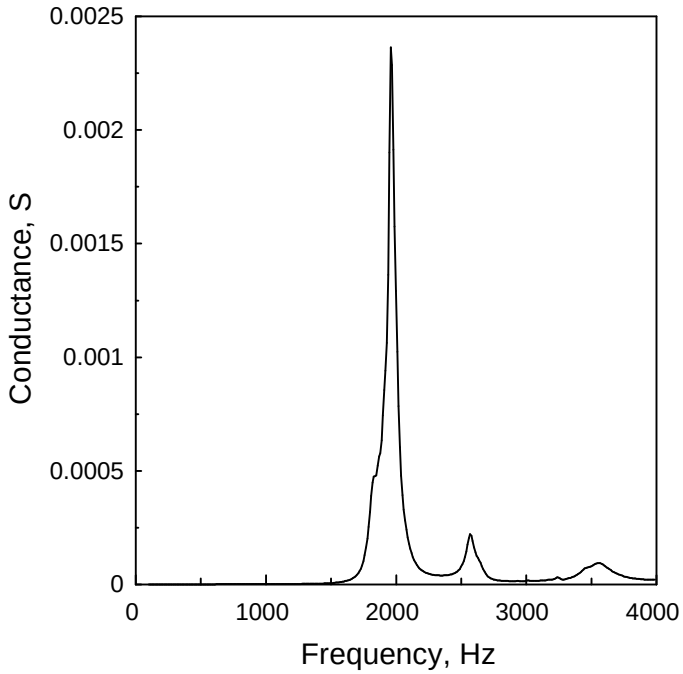

Figure 8.15. Measured in-air conductance response.

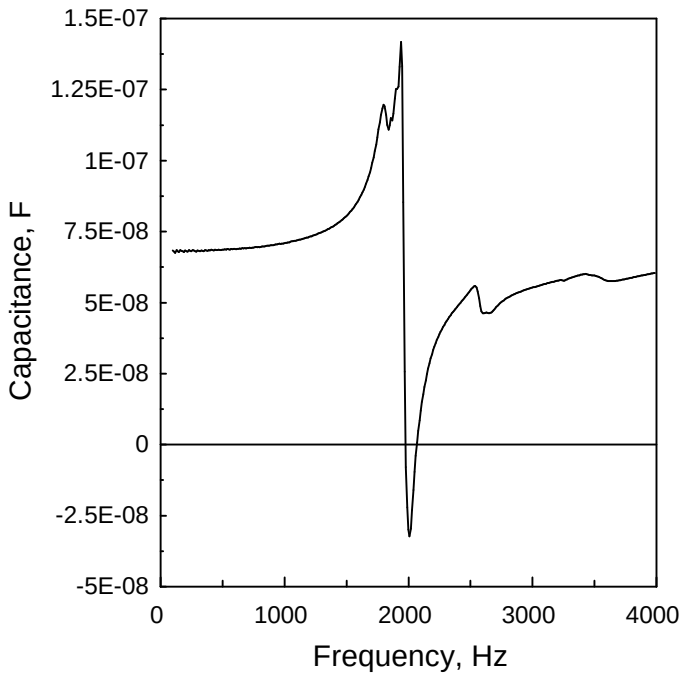

Figure 8.16. Measured in-air capacitance response.

Table 8.8. Parameters derived directly from the measured in-air responses.

Parameter	Value
f_{air}	1964 ± 0.5 Hz
k^2	0.421
Q_m	29
G_m	2.364 mS
C_{LF}	68.0 nF
tan δ_e	0.007

Table 8.9. Components of the in-air equivalent circuit.

Parameter	Value
L_m	0.23 H
C_m	28.63 nF
R_m	424.89 Ω
C_e	39.37 nF
R_e	100 kΩ

The main difficulty with field-trails is the alignment of the transducer and hydrophone in precisely specified positions, a task normally easily achieved in a test tank. In order to be able to take measurements of projector voltage sensitivity on the axes of the transducer a 'calibration' frame was constructed, shown in outline in figure 8.17. This 2-metre-square aluminium frame enabled the transducer to be precisely positioned in its centre. Hydrophones were mounted on the z-axis and x-axis of the transducer to take the measurements. The frame was suspended from two, 2 metre lengths of rope connected to eye-bolts mounted at the top corners. The two ropes were connected to a third 10 metre length of rope, not shown in figure 8.17. The other end of this rope was attached to a float which was moored in the centre of the quarry. Power cables and hydrophone leads, also not shown in figure 8.17, ran from the frame to the shore enabling all the measuring equipment to be set-up on land.

Figure 8.18 shows an underwater picture of the transducer mounted in the frame, taken by a diver using an underwater video camera. The diver's torch is highlighting the transducer, and to the left of the transducer one of the hydrophones can just be made out. From the diver's depth gauge the frame was found to be at a depth of 15 metres, indicating the rope had stretched 5 metres.

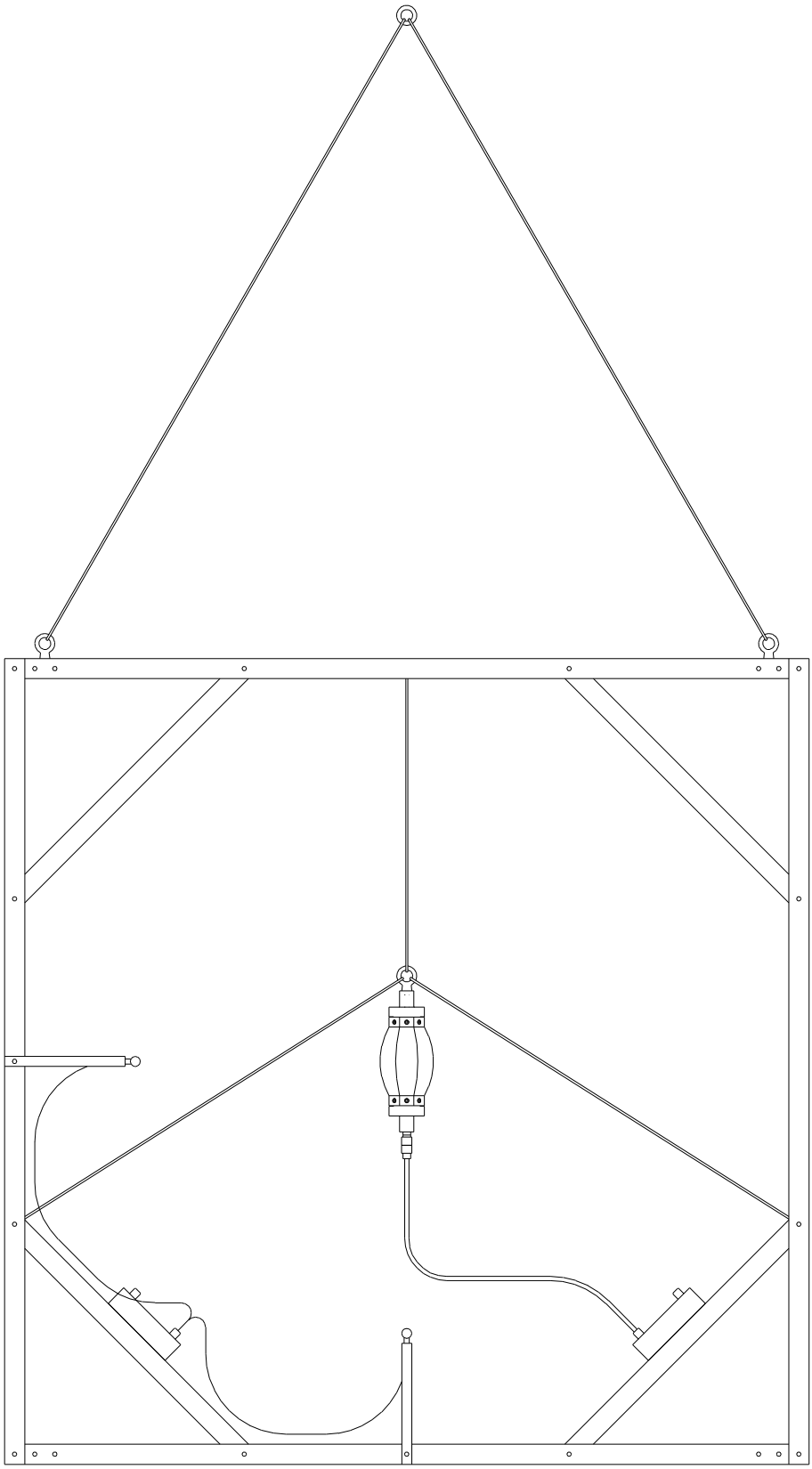

Figure 8.17. Drawing of the 2.5 kHz free-flooded prototype transducer suspended in a 2 metre square calibration frame. The frame has two hydrophones mounted 70 cm from the centre, one on the z-axis and the other on the x-axis of the transducer.

Figure 8.18. Underwater picture of the 2.5 kHz free-flooded prototype transducer suspended in a 2-metre-square calibration frame.

The first measurements to be made were of the admittance response of the transducer. However, since the transducer was connected to a long length of cable it was necessary to perform some calculations to find the true response of the transducer.

The impedance looking into a cable Z_{in} that is connected to a load of impedance Z_L is defined by the following relationship [8.6]:

$$Z_{in} = Z_o \left[\frac{Z_L + Z_o \tanh(\gamma \ell)}{Z_L \tanh(\gamma \ell) + Z_o} \right] \tag{8.4}$$

where Z_o is the characteristic impedance of the cable, γ is the propagation constant, and ℓ is the length of the cable.

Now, from the open-circuit impedance of the cable $Z_{o/c}$,

$$Z_{o/c} = Z_{in}\left(Z_L = \infty\right) = \frac{Z_o}{\tanh(\gamma \ell)} \tag{8.5}$$

and the short-circuit impedance of the cable $Z_{s/c}$,

$$Z_{s/c} = Z_{in}\left(Z_L = 0\right) = Z_o \tanh\left(\gamma\ell\right) \tag{8.6}$$

we find the characteristic impedance is given by

$$Z_o = \sqrt{Z_{o/c} Z_{s/c}} \tag{8.7}$$

and

$$\tanh\left(\gamma\ell\right) = \sqrt{\frac{Z_{s/c}}{Z_{o/c}}} \tag{8.8}$$

Substituting equations (8.7) and (8.8) into (8.4) we get a new definition of the input impedance looking into the cable in terms of the open-circuit and short-circuit impedance of the cable and the load impedance; that is,

$$Z_{in} = Z_{o/c}\left[\frac{Z_L + Z_{s/c}}{Z_L + Z_{o/c}}\right] \tag{8.9}$$

By rearranging equation (8.9) we can get an expression for the load impedance:

$$Z_L = Z_{o/c}\left[\frac{Z_{in} - Z_{s/c}}{Z_{o/c} - Z_{in}}\right] \tag{8.10}$$

Now, assuming that the open-circuit and short-circuit impedance of the cable is known, the impedance of the load can be ascertained by measuring the impedance looking into the cable.

When the transducer was first submerged into the water it behaved as if it were air-backed. This behaviour can be attributed to air bubbles clinging in the interior of the transducer. This is not difficult to imagine, since the surface of the compliant region is extremely rough and pitted. After several hours the impedance response of the transducer was noticeably different. The resonance frequency had increased, as had the 3 dB bandwidth. Finally, a day later the behaviour of the transducer settled down, indicating that most of the air-bubbles had dispersed; that is, the transducer had become fully ‘wetted’. The resonance frequency increased to near the expected value of 2.6 kHz but the dip observed in the numerical results was not noticeable.

The figures 8.19 and 8.20 show respectively the in-water conductance and capacitance responses of the transducer, and table 8.8 list the corresponding properties measured from the these graphs.

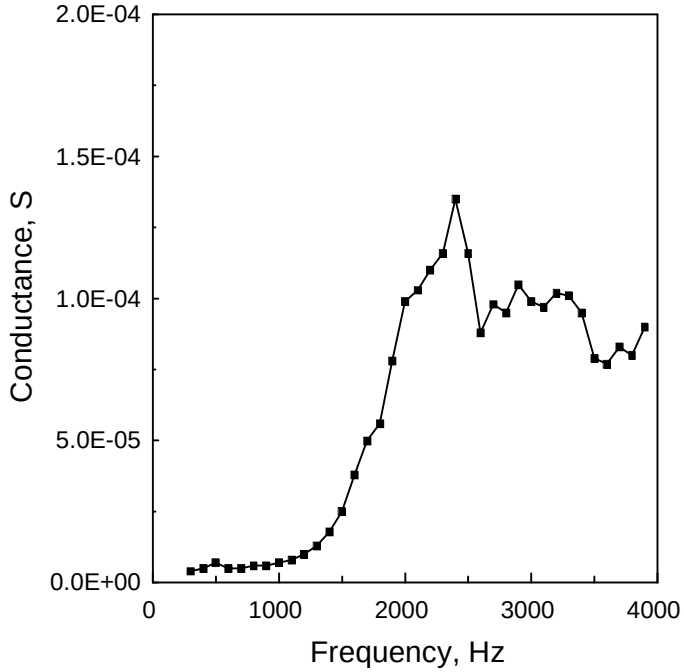

Figure 8.19. Measured in-water conductance response.

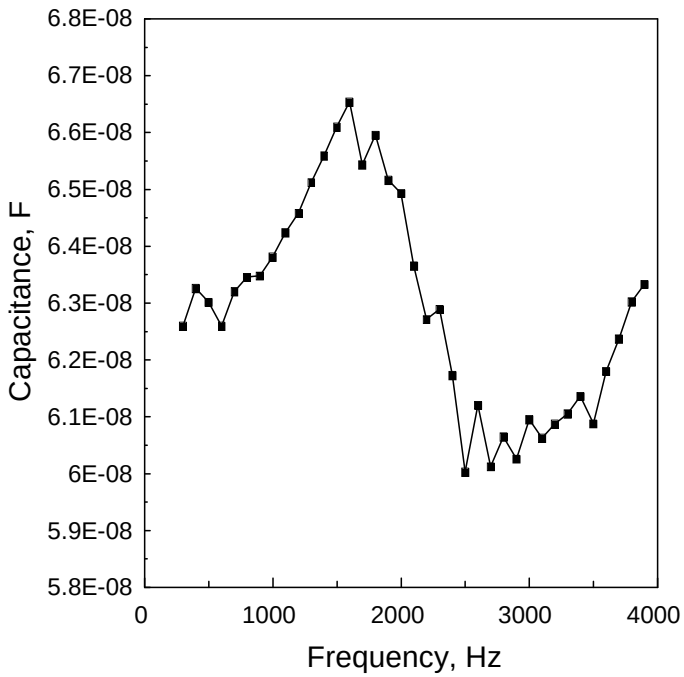

Figure 8.20. Measured in-water capacitance response.

Table 8.10. Parameters derived directly from the measured in-water electrical response.

Parameter	Value[†]
f_{water}	2400 Hz ± 50 Hz
$B(-3\text{ dB})$	> 2200 Hz
Q_M	< 1.1
G_{max}	135 μS
C_e	62 nF

[†] Note: the conductance response of the transducer did not fall below –3 dB of the resonance value within the upper range of frequencies investigated, therefore the bandwidth and quality factor are not precisely defined.

If we compare the measured results taken from the transducer with those predicted by the finite element and boundary element calculations, we see that, like the in-air results, the measured frequency of resonance (2.4 kHz) is somewhat lower than the predicted value (2.61 kHz). As the measured conductance response does not reach the –3 dB level above the resonance frequency within the range of measurements, the 3 dB bandwidth and quality factor are not well defined, and as such no comparison can be made with predicted results. The reduced level of the conductance response is undoubtedly due to extra damping in the structure compared with that modelled. It is also possible that the damping within the foam is higher than expected. Other minor sources of error include the omission of the water between the staves from the numerical model, the omission of the centre bolt from the numerical model, and the assumption of perfect coupling between the staves and the end-plates.

The projector voltage sensitivity, otherwise known as the transmitting voltage response, was measured using the calibrated hydrophone method [8.7]. The transducer was stimulated with a pulsed signal to enabled erroneous measurements from the effects of standing waves, cross-talk, and reflections from boundaries, to be minimised.

The deployment of the transducer and hydrophones was such that the difference in distance between the direct path signal and the first reflection was approximately 30 metres. Given that the lowest frequency to be investigated would be 500 Hz, the maximum number of cycles that could be used was found to be 10. Allowing for a suitable length of time between each pulse to enable

acoustic reflections to disperse, the transducer was stimulated with a pulsed signal of 10 cycles at a burst rate of 200 millisecond.

The equipment used to drive the transducer and record the measurements is listed below:

Hewlett Packard Pulse/Function Generator, Type 8116A
SOLO Power Amplifier, Type 3000
2 Reson Hydrophones
Brüel and Kjær Wideband Conditioning Amplifier, Type 2638
Tecktronix 100 MHz Oscilloscope, Type 2235

The output impedance of the SOLO power amplifier is 4 ohms. Thus, to match the transducer to the power amplifier, a step-up transformer with a turns ratio of 1 to 43 was required. Additionally, to remove the reactive component at resonance, a tuning inductor of 71.2 mH was connected across the secondary of the transformer.

Figure 8.21 shows the projector voltage sensitivity responses in the z- and x-direction. The responses show the resonance frequency to be 2.6 kHz ± 50 Hz, slightly higher than that indicated by the admittance response: again, no cavity resonance is observed around 3.8 kHz. The difference between the two responses at resonance is approximately 1.9 dB, slightly less than that predicted by the numerical model. However, the difference in the measured and predicted magnitudes is pronounced.

Using the relationship

$$10\log_{10}\left(\eta_{ea}\right) = \mathrm{S} - \mathrm{DI} - 10\log_{10}\left(G\right) - 170.9 \tag{8.11}$$

it is possible to estimate the limits of efficiency; that is, the lower and upper values of efficiency. A lower limit for the value of the efficiency can be estimated by taking the source to be omni-directional (DI = 0) with the transmitting sensitivity as measured in the x-direction; similarly an upper limit can be estimated from the higher transmitting sensitivity in the z-direction. The input power in each case is determined from the admittance response. On this basis the efficiency is estimated to lie between 29 % and 45 %. As with the projector voltage sensitivity responses, the efficiency is much lower than expected, indicating a high level of loss within the transducer.

Table 8.11 summarises the results for the free-flooded version of the transducer.

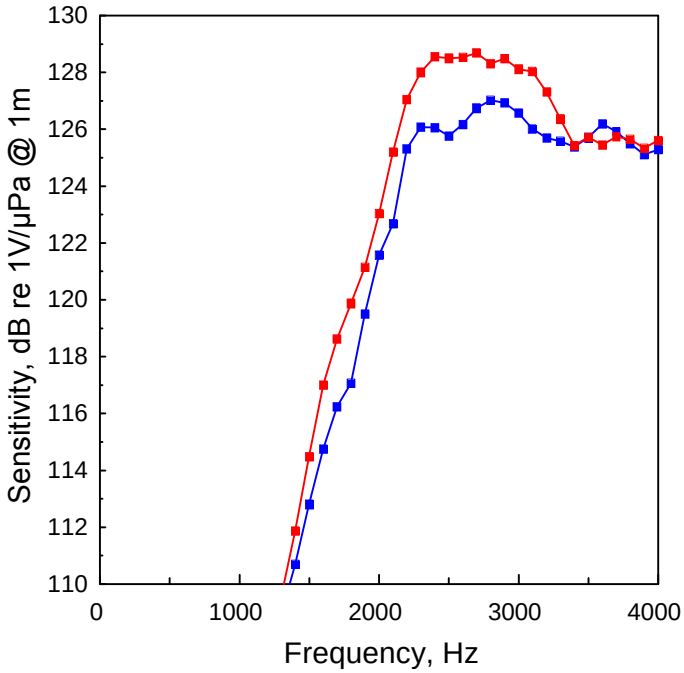

Figure 8.21. Measured projector voltage sensitivity response. Red—response in the z-direction. Blue—response in the x-direction.

Table 8.11. Parameters determined from the measured in-water acoustic responses.

Parameter	Value[†]
f	2600 Hz ± 50 Hz
$B_{x\,axis}(-3\text{ dB})$	> 1840 Hz
$Q_{x\,axis}$	< 1.4
$S_{x\,axis}$	126.8 dB re 1 V/µPa @ 1 m
$B_{z\,axis}(-3\text{ dB})$	1326 Hz
$Q_{z\,axis}$	2.0
$S_{z\,axis}$	128.7 dB re 1 V/µPa @ 1 m
η_{ea}	between 29 % and 45 %

[†] Note: the projector sensitivity response of the transducer in the x-direction did not fall below –3 dB of the resonance value within the upper range of frequencies investigated, therefore the bandwidth and quality factor in this direction are not precisely defined.

Table 8.12. Target specification and projected performance of 2.5 kHz free-flooded flextensional transducer scaled 5.2 : 1.

Parameter	Target	Achieved
Centre frequency	250 – 500 Hz	500 Hz
Operating depth	> 500 m	> 500 m
Total mass	< 250 kg	> 840 kg
Q-factor	< 4	< 2
Source level	> 190 dB re. 1 μPa @ 1 m	< 204 dB re. 1 μPa @ 1 m
Efficiency	> 50 %	< 45 %

If we scale the 2.5 kHz partially free-flooded transducer using the laws described in Chapter 5 we can attempt to assess the suitability of the transducer for use as an ocean acoustic tomography sound source. A scale factor of 5.2 gives a resonance frequency of 500 Hz; the corresponding effect on the other performance parameters are listed in table 8.12 together with the target values. The values of SL were determined by using the relationship between source level and sensitivity;

$$\mathrm{SL} = \mathrm{S} + 20\log_{10}(v) \tag{8.12}$$

where v is the drive voltage. It has been assumed that the output power response of the transducer is linear up to the maximum input voltage.

It must be noted that the values presented in table 8.12 rely on all the components of the transducer scaling linearly. It is unlikely that the compliant foam region will behave in such a manner, moreover its characteristics will be frequency- and depth-dependent. With this in mind, the results for the scaled transducer seem to be encouraging, suggesting that a full-scale device resonating at 500 Hz and operating at 500 m will partially fulfil the target specification. The transducer will have a Q-factor much lower than 4, and a source level way in excess of 190 dB re. 1 μPa @ 1 m. However, the transducer is also marginally less efficient than desired, but of more significance is the weight, over three times greater than the specification value. The increase in weight stems from the large increase in resonance frequency relative to the size of the device, caused by the high stiffness of the cavity in comparison to air-backing. The solution would be to find a material that is equally as strong as Plasticell D300 foam, thus being able to withstand the hydrostatic pressure at 500 m, but that is also more compliant. Possibly other foam materials are available which improve on the Plasticell range in this regard, although only marginal improvement is anticipated. Compliant tubes offer an alternative to foam materials. A further

perceived benefit of using compliant tubes is that they are expected to be much less lossy than foam materials so an improvement in the efficiency might be attainable. Finally, a further suggestion would be the use of either foam or tubes in conjunction with a compressible liquid fill. A suitable material might be the cardon-florine organic compound 'Fluorinert' (FC-72) [8.8]. This fluid has a very low sound speed of 550 m s^{-1} at 12 °C and a density of 1700 kg m^{-3}, resulting in a specific acoustic impedance of 0.935 x 10^6 kg m^{-2} s^{-1}. The specific acoustic impedance of FC-72 is lower than that of sea water, which is approximately 1.54 x 10^6 kg m^{-2} s^{-1}, although obviously much higher than the impedance of air, which has a value of only 420 kg m^{-2} s^{-1}. The compressible fluid would probably be most effective if used in combination with compliant tubes since there would be more volume available to fill. However, the use of a fluid fill inside the cavity would once again necessitate the need for a rubber boot, although this would alleviate the problem of having to waterproof the stack.

Thus, it can be seen that there is considerable scope for further optimisation of the flextensional transducer. The most important aim would be to reduce the stiffness of the compliant region. We also might choose to reduce the volume of piezoelectric ceramic in light of the high acoustic power output, which would help to reduce the weight of the transducer. In addition, the low Q-factor leaves room for optimising the dimensions of the staves. From Chapter 5 it was seen that reducing the ratio of stave thickness to device length would increase the Q-factor but reduce the size and hence weight of the device for a specified resonance frequency.

8.3 Conclusions

In this chapter a solution for overcoming the depth limitations of an air-backed flextensional transducer has been proposed, in the form of a free-flooded device. This design incorporated a compliant region to reduce the internal impedance, thereby improving performance. Finite element and boundary element calculations revealed that partially free-flooding the transducer had the effect of increasing the resonance frequency, while reducing the quality factor, acoustic power output, and efficiency. The large increase in the frequency of resonance is rather worrisome since a significantly larger device would be required to realise a frequency of 500 Hz. This being the case, the weight requirement would not be achievable. However, with the exception of weight, the transducer satisfies all the requirements of an ocean acoustic tomography sound source.

The construction of a transducer incorporating the free-flooding concept in conjunction with an internal compliant region has been described. Results from the electrical and acoustic responses to the transducer did not compare as well to the predicted result as they had done for the air-backed transducer described in the previous chapter. The predicted resonance frequency showed good agreement: however, the quality factor, acoustic power and efficiency were not so accurately predicted. The 3 dB bandwidth was much greater than anticipated, indicating a higher level of damping in the transducer. This level of damping has resulted in low efficiency, with a corresponding effect on the acoustic power output.

An important point to note is that the tests on the transducer were carried out at a depth of 15 metres. As the operating depths is increased it is envisaged that the performance of the transducer would worsen; that is, increasing resonance frequency and reducing power output. This is due to the water pressure compressing the foam and hence reducing its compliance. However, it has not been possible to test this assumption, and sea-trails are essential to confirm the performance of the transducer at a depth of 500 metres.

In conclusion, a transducer that could operate as an ocean acoustic tomography source has been designed and manufactured. However, in order to meet the depth requirement, the performance of the transducer has been sacrificed to some extent. Improvements in the way internal compliance is introduced could help to restore performance, though this requires further investigation.

8.4 References

[8.1] M. Kronengold and W. J. Toulis, 'Directional 420-Hz Sound Source', *IEEE Trans. Geoscience Electronics*, 6(4), 204-211, (1968).

[8.2] J. Ahmad, D. T. I. Francis, and R. F. W. Coates, 'A Fluid-Filled Flextensional Device for Ocean Acoustic Tomography', *Proc. OCEANS '95*, 2021-2026, (1995).

[8.3] W. J. Toulis, 'Acoustic-Backing Techniques for Transducers and Radiators', *J. Acoust. Soc. Am.*, 37(2), 250-256, (1965).

[8.4] R. S. Woollett, 'Trends and Problems in Sonar Transducer Design', *IEEE Trans. Ultrasonics Eng.*, 10, 116-124, (1963).

[8.5] R. S. Woollett, 'Basic Problems Caused by Depth and Size Constraints in Low-Frequency Underwater Transducers', *J. Acoust. Soc. Am.*, 68(4), 1031-1037, (1980).

[8.6] J. Dunlop and D. G. Smith, Telecommunications Engineering, 2nd Edition, (Chapman and Hall, 1989), 184-185.

[8.7] R. J. Bobber, *Underwater Electroacoustic Measurements*, (Navel Research Laboratory, 1970), Chapter 2.

[8.8] Y. Le Gall, D. Boucher, X. Lurton, and A. M. Bruneau, 'Great Depth, High Efficiency, Broadband, Reliable Low Frequency Transducer for Acoustical Tomography, *Proc. OCEANS '94*, 2, 284-288, (1994).

Chapter 9

POWER LIMITATIONS

9.1 Introduction

The maximum acoustic power output of a transducer will be limited either by the properties of the acoustic medium or the internal features of the design.

Factors which limit the acoustic power handling capability of a transducer and which are functions of the piezoelectric ceramics have been summarised by Berlincourt, *et al.*, as follows [9.1]:

1. Dynamic strength of the ceramic,
2. Reduction in efficiency due to internal dielectric losses,
3. Reduction in efficiency due to internal mechanical losses,
4. Depolarisation of the ceramic due to electric field,
5. Depolarisation of the ceramic due to temperature rise.

Also of consideration are those factors which are functions of the electrically passive components of the transducer; the dynamic strength, the internal mechanical losses and the thermal effects on these properties.

An additional limitation is imposed by the phenomenon of cavitation of the water medium at the vibrating surface of the transducer. At shallow depths the output power may be limited by cavitation at a level far below that imposed by other factors [9.2].

This chapter reviews the various phenomena that limit the power output of piezoelectric transducers. Methods for assessing the significance of each phenomenon, using finite element techniques or estimations, are described.

9.2 Cavitation Limitation

The alternating acoustic pressure produced at the surface of a transducer is superimposed on the ambient static pressure of the surrounding medium. As the acoustic intensity is increased, the peak pressure may reach a value equal to the ambient pressure. If the intensity is increased still further, the acoustic pressure peaks will exceed the ambient pressure and absolute pressure will be negative for part of the cycle. At this point the medium begins to cavitate. It is found that on the negative half of the acoustic pressure cycle, bubbles form on the surface and just in front of the transducer. These bubbles tend to collapse when positive absolute pressure is re-established.

The onset of cavitation is associated with the presence of inhomogeneities in the medium. These inhomogeneities are called ‘nuclei’ or ‘microbubbles’. The most plausible explanation for the presence of these nuclei is that small microscopic bubbles of air become trapped in cracks or cavities of small solid particles suspended in the liquid [9.3]. Alternatively, nuclei may exist as free air bubbles surrounded by skins of organic impurities that hinder the escape of air into solution [9.4]. In a pressure field, during the negative half of the cycle, the dissolved air in the medium diffuses into these tiny air bubbles. When the negative pressure begins to exceed the ambient pressure the nuclei begin to grow in size as more dissolved air diffuses into the bubble than out of it. Thus, the onset of cavitation is fairly gradual, starting with some harmonic distortion of the pressure waveform. This distortion becomes noticeable before the cavitation bubbles become visible to the naked eyes and may therefore be used as a sensitive indicator of the onset of cavitation [9.2]. At this point the ratio of output to input power decreases, which marks the departure from linearity.

The phenomenon of cavitation gives rise to various undesirable effects [9.2, 9.4, 9.5]. The presence of a large number of bubbles near the transducer drastically reduces the acoustic impedance into which the transducer must operate. This mismatch reduces the radiated acoustic power and increases internal losses. Acoustic power is also lost in absorption and scattering by the cavitation bubble cloud. If the high input power to the transducer is maintained for some time the transducer may overheat and be permanently damaged. Also, the violent action of bubbles collapsing at the surface of the transducer may cause surface erosion.

The theoretical cavitation threshold, at which cavitation may start, can be readily found by calculating the intensity, I_c, for which the peak acoustic pressure, p_c, reduces the absolute pressure to zero. Thus, the cavitation threshold is defined as

$$I_c = \frac{p_c^2}{2\rho c} \tag{9.1}$$

where ρ is the density and c is the sound speed of the medium. At sea level the absolute pressure is reduced to zero if the peak acoustic pressure is equal to 10^5 N m^{-2} (1 atm). This gives a cavitation threshold intensity of $\frac{1}{3}$ W cm^{-2}.

For very pure water free of nuclei, the cavitation threshold can be much higher than the theoretical limit. The amount by which the cavitation threshold exceeds the ambient pressure may be thought of as the tensile strength of the medium. The tensile strength of a medium, however, is highly sensitive to a variety of factors, such as temperature, dissolved air content, and previous history. Since sea water usually contains large amounts of dissolved gases or microscopic bubbles near its surface its tensile strength will be weak at best.

The cavitation threshold of a transducer may be raised by any of the following:

1. Increasing the frequency,
2. Decreasing the pulse length,
3. Increasing the depth.

The process of bubble formation during the cavitation process requires a finite time [9.5]. As the frequency is increased the periods of negative pressure become shorter and the cavitation threshold rises. The cavitation threshold limits as measured and compiled by Esche [9.6] are shown in figure 9.1. The area enclosed between the two curves represents the range of observed values taken under CW operation in fresh water at atmospheric pressure. Note that the frequency dependence is small below 10 kHz, but thereafter the cavitation threshold increases rapidly as frequency increases. Taking the work of Esche [9.6] as a framework, Urick has estimated an average cavitation threshold [9.4]. Figure 9.2 shows this estimated cavitation threshold as the equivalent plane-wave intensity.

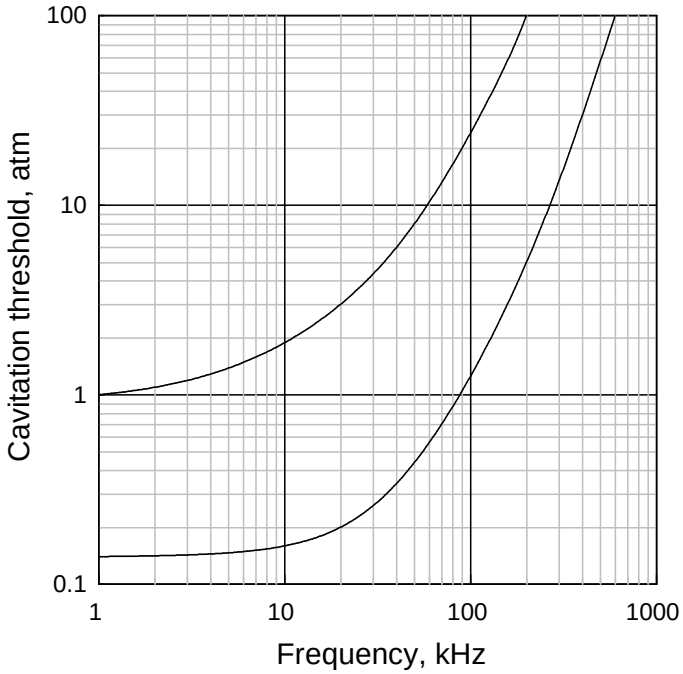

Figure 9.1. Esche's cavitation threshold limits [9.6] (data taken from reference [9.3]). CW data on fresh water at atmospheric pressure.

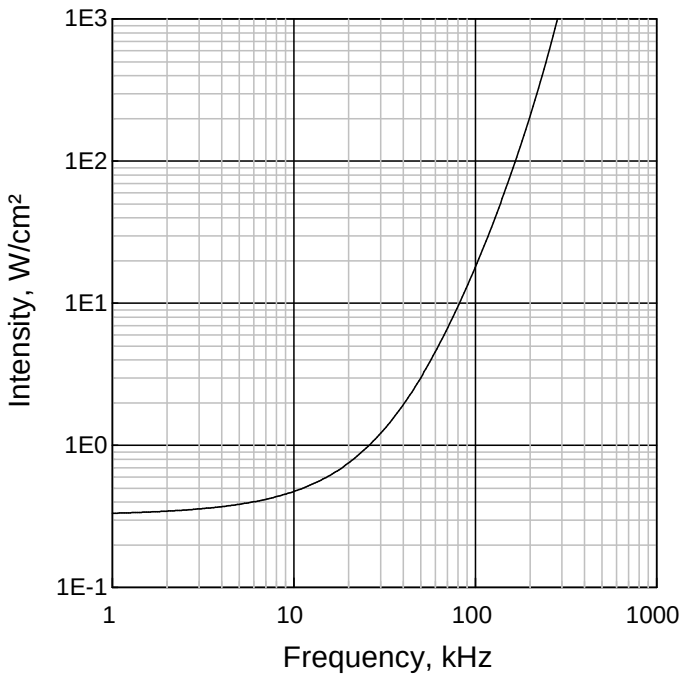

Figure 9.2. Urick's estimated average acoustic intensity as a function of frequency [9.4].

The cavitation threshold can be increased by reducing the pulse length below about 5 milliseconds-seconds [9.5]. This is in agreement with the concept that cavitation nuclei require a finite time interval to grow to a size where the effects are observable.

The effect of an increased depth of operation is to increase the ambient pressure. Since each 10 metres of depth represents an increase in pressure by 10^5 N m^{-2} (1 atm) the cavitation threshold at depth h becomes,

$$I_c(h) = I_c(0)\left[1 + \frac{h}{10}\right]^2 \tag{9.2}$$

where $I_c(0)$ is the cavitation threshold at the surface.

From the above, the maximum CW acoustic power, P_c, that a transducer can radiate at the onset of cavitation may be estimated by using the following relationship

$$P_c = I_c(h)A \tag{9.3}$$

where A is the radiating surface area.

9.3 Mechanical Limitation

Driving a transducer with high power input levels leads to large dynamic stresses. Beyond a certain power, one may exceed the maximum rated dynamic stress of a material (its tensile strength or shear strength) may be exceeded and at this point the material is liable to fail. Depending on the transducer design, the failure will most likely occur within a ceramic element or at the joining between two materials (a glue joint) which is a point of tensile weakness.

The mechanical limitations in transducers operating in the low and medium frequency range, below 100 kHz, can usually be counteracted by the use of mechanical bias [9.7, 9.8]. The application of mechanical bias depends on the transducer design, however, a common method is to run a centre bolt through the middle of the transducer. The maximum mechanical bias which may be tolerated is dependent upon the ceramic composition and the orientation of the stress. Table 9.1 lists approximate limiting values of compressive bias stress for several piezoelectric ceramics.

Table 9.1. Rated compressive and dynamic limits for several piezoelectric ceramics at 25 °C (data taken from reference [9.1] and Vernitron, Ltd., data sheets).

	Navy Type			
	I	II	III	IV
	Vernitron Type			
	PZT-4™	PZT-5A™	PZT-8™	Ceramic-B™
Maximum compressive stress parallel to polar axis, psi	12000	3000	12000	2000
Maximum compressive stress perpendicular to polar axis, psi	8000	2000	8000	2000
Maximum dynamic stress parallel to polar axis, psi	3500	4000	3500	3000

In the high frequency range, above 100 kHz, the small dimensions of the transducers prohibit the use of a tension bolt and hence mechanical limitations in the ceramic may be met. The dynamic strength of piezoelectric ceramics are dependent upon configuration and perfection of fabrication. Table 9.1 lists the maximum recommended dynamic stress level for a number of piezoelectric ceramics.

Finite element techniques for stress analysis have previously been discussed in Chapter 4.

9.4 Electrical Limitation

The maximum electric field that can be applied to a transducer is ultimately limited by the composition of the ceramic employed. The electric field strengths required to depole a variety of piezoelectric ceramics at room temperature are shown in table 9.2. However, an electric field sufficient to cause depolarisation produces extremely high dielectric losses and therefore low efficiencies [9.1]. Thus, such fields are appreciably larger than are applied in practice.

For most piezoelectric transducers, the critical limiting factor is the electrical breakdown of the ceramic [9.10]. The potential that can be safely applied across a dielectric material is finite. If a certain value is exceeded, sparking occurs and the dielectric is said to breakdown. The maximum

Table 9.2. Depoling field for several piezoelectric ceramics at 25 °C [9.9].

	Navy Type			
	I	II	III	IV
	Vernitron Type			
	PZT-4™	PZT-5A™	PZT-8™	Ceramic-B™
a.c. depoling field, kV r.m.s. m^{-1}	>1000	~700	>1000	~400

field that a dielectric material can sustain without breakdown is called its dielectric strength [9.11]. However, electrical breakdown is usually more likely to be caused by flashover between the electrodes. This may occur through the air, or more probably, across the surface of the ceramic where the presence of grease, dirt, or moisture will degrade the dielectric strength.

The limiting electric field which can safely be applied to a transducer cannot be specified accurately as it depends on the material properties of the ceramic and the method of construction. Woollett [9.12] has suggested a limiting field of 200 kV r.m.s. m^{-1} for barium titonate ceramics, and 400 kV r.m.s. m^{-1} for lead zirconate titonate ceramics. Stansfield [9.10] suggests a more conservative figure of 200 kV r.m.s. m^{-1} for both types of ceramic.

9.5 Thermal Limitation

While mechanical and dielectric losses adversely affect efficiency, usually of greater concern is the temperature rise they cause in high-duty-cycle or CW operation of the transducer [9.12]. Under such conditions the transducer is likely to be thermally limited [9.1]. That is, the dielectric and mechanical losses result in the generation of heat within the ceramic material. If the temperature reaches the Curie point of the material it will spontaneously loose its piezoelectric properties. In practice the temperature of the ceramic material must be kept well below this critical point to avoid degradation of the piezoelectric properties. Thus, the temperature limitation may require a lower driving field to be employed than that for low-duty-cycle operation. Table 9.3 lists the Curie point and maximum operating temperature for a number of piezoelectric ceramics.

Table 9.3. Curie temperature and maximum operating temperature for several piezoelectric ceramics (data taken from Vernitron, Ltd., data sheets).

	Navy Type			
	I	II	III	IV
	Vernitron Type			
	PZT-4™	PZT-5A™	PZT-8™	Ceramic-B™
Curie point, °C	328	365	300	115
T_{max}, °C	200	250	175	—

In practice, non-reversible damage may occur in the electrically passive materials before the ceramic is affected. For example, epoxy resin glue, often used in transducer construction, can denature if exposed to temperatures greater than 80 °C for any significant length of time [9.13].

The danger of over-heating can be minimised by choosing a ceramic with low internal losses. Table 9.4 lists the mechanical and dielectric loss factors for a number of piezoelectric ceramics. The low losses of the Navy Type III composition, much lower than Navy Type I ceramics at high drive levels, make it particularly well suited to CW operation in high power transducers.

Finite element techniques for thermal analysis are developed in Chapter 10.

Table 9.4. Mechanical and dielectric loss factors for several piezoelectric ceramics at 25 °C [9.1].

	Navy Type			
	I	II	III	IV
	Vernitron Type			
	PZT-4™	PZT-5A™	PZT-8™	Ceramic-B™
tan δ_m	0.002	0.0133	0.001	0.0025
tan δ_e	0.004	0.02	0.004	0.0059

9.6 References

[9.1] D. A. Berlincourt, D. R. Curran, and H. Jaffe, 'Piezoelectric and Piezomagnetic Materials and their Function in Transducers', in *Physical Acoustics*, 1(a), W. P. Mason, ed., (Academic Press, 1964), 170-270.

[9.2] W. S. Burdic, *Underwater Acoustic System Analysis*, 2nd Edition, (Pretice-Hall, 1991), 86-88.

[9.3] H. G. Flynn, 'Physics of Acoustic Cavitation in Liquids', in *Physical Acoustics*, 1(b), W. P. Mason, ed., (Academic Press, 1964), 57-172.

[9.4] R. J. Urick, *Principles of Underwater Sound*, 3rd Edition, (McGraw-Hill Book Company, 1983), 72-80.

[9.5] D. Stansfield, *Underwater Electroacoustic Transducers*, (Bath University Press and Institute of Acoustics, 1990), 33-36.

[9.6] R. Esche, 'Schwingungskavitation in Flussigkeiten', *Akust. Beih.* (*Acoustica*), 4, AB 208, (1952).

[9.7] H. B. Miller, 'Composite Electromechanical Transducer', U.S. Patent 2,930,912 (29 March 1960); reviewed in *J. Acoust. Soc. Am.*, 33(11), 1648, (1961).

[9.8] H. B. Miller, 'Origin of Mechanical Bias for Transducers', *J. Acoust. Soc. Am.*, 35(9), 1455, (1963).

[9.9] H. Jaffe and D. A. Berlincourt, 'Piezoelectric Transducer Materials', *Proc. IEEE*, 53(10), 1372-1386, (1965).

[9.10] D. Stansfield, *Underwater Electroacoustic Transducers*, (Bath University Press and Institute of Acoustics, 1990), 183-184.

[9.11] J. D. Kraus, *Electromagnetics*, 3rd Edition, (McGraw-Hill, 1984), 72-74.

[9.12] R. S. Woollett, 'Power Limitations of Sonic Transducers', *IEEE Trans. Sonics Ultrasonics*, SU-15(4), 21-227, (1968).

[9.13] R. Coates, D. de Cogan, and P. A. Willson, 'Transmission Line Matrix Modeling Applied to Problems in Underwater Acoustics', *IEEE Oceans '90*, 216-220, (1990).

Chapter 10

NUMERICAL METHODS IN HEAT CONDUCTION

10.1 Introduction

In the previous chapter it was reported that losses within the components of the transducer would manifest itself in the form of heat. In the passive components of the transducer the heat is generated by mechanical losses within the materials. In the active components losses are caused by various phenomena. In the case of piezoelectric materials, mechanical, piezoelectric, and dielectric losses are present. The generation of heat will give rise to an increase in temperature within the transducer, which if excessive could limit the maximum power output, as discussed in the previous chapter. Obviously the extent of this temperature rise depends on the heat-transfer design of the transducer.

In the first section of this chapter a method of calculating the losses within a piezoelectric transducer using FE techniques is described. In subsequent sections a finite element treatment for the three-dimensional heat conduction problem will be derived.

10.2 Calculation of Heat Sources

The material losses which give rise to the generation of heat can be evaluated by extending the finite element techniques presented in Chapter 4.

We may evaluate the heat source distribution with the following formula:

$$\Delta U = \int_{\tau}^{\tau+T} \int_{V} \left[\{T\}^{\mathrm{T}} \frac{d}{dt} \{S\} + \{E\}^{\mathrm{T}} \frac{d}{dt} \{D\} \right] dV dt \tag{10.1}$$

where ΔU is the energy dissipated during a period of time, T. Re-arranging the order of integration we have

$$\Delta U = \int_V \left[\int_\tau^{\tau+T} \{T\}^{\mathrm{T}} \frac{d}{dt}\{S\}\,dt + \int_\tau^{\tau+T} \{E\}^{\mathrm{T}} \frac{d}{dt}\{D\}\,dt \right] dV \tag{10.2}$$

Now, consider the integral

$$\int_\tau^{\tau+T} \left[T \frac{d}{dt} S \right] dt$$

In complex notation, the integral becomes

$$\int_\tau^{\tau+T} \Re e\left\{ \left(T_x + jT_y\right) e^{j\omega t} \right\} \Re e\left\{ \frac{d}{dt}\left(S_x + jS_y\right) e^{j\omega t} \right\} dt$$

Differentiating the strain component with respect to time gives

$$\int_\tau^{\tau+T} \Re e\left\{ \left(T_x + jT_y\right) e^{j\omega t} \right\} \Re e\left\{ j\omega\left(S_x + jS_y\right) e^{j\omega t} \right\} dt$$

Using Euler's† identity, this can be written as

$$\int_\tau^{\tau+T} \Re e\left\{ \left(T_x + jT_y\right)\left[\cos(\omega t) + j\sin(\omega t)\right] \right\} \Re e\left\{ j\omega\left(S_x + jS_y\right)\left[\cos(\omega t) + j\sin(\omega t)\right] \right\} dt$$

Expanding the terms and taking the real components, the expression

$$-\omega \int_\tau^{\tau+T} \left[\left(T_x S_x + T_y S_y\right)\cos(\omega t)\sin(\omega t) + T_x S_y \cos^2(\omega t) + T_y S_x \sin^2(\omega t) \right] dt$$

is obtained, which, by using trigonometric formulae, can be written in terms of functions that may be easily integrated; that is

$$-\tfrac{1}{2}\omega \left[\left(T_x S_x + T_y S_y\right) \int_\tau^{\tau+T} \sin(2\omega t)\,dt + T_x S_y \int_\tau^{\tau+T} \left[1 + \cos(2\omega t)\right] dt + T_y S_x \int_\tau^{\tau+T} \left[1 - \cos(2\omega t)\right] dt \right]$$

Setting $\tau = 0$ and $T = 2\pi/\omega$, the solutions of the various integral are as follows;

$$\int_0^{2\pi/\omega} \sin(2\omega t)\,dt = \left[-\frac{\cos(2\omega t)}{2\omega} \right]_0^{2\pi/\omega} = 0$$

$$\int_0^{2\pi/\omega} \left[1 + \cos(2\omega t)\right] dt = \left[t + \frac{\sin(2\omega t)}{2\omega} \right]_0^{2\pi/\omega} = \frac{2\pi}{\omega}$$

$$\int_0^{2\pi/\omega} \left[1 - \cos(2\omega t)\right] dt = \left[t - \frac{\sin(2\omega t)}{2\omega} \right]_0^{2\pi/\omega} = \frac{2\pi}{\omega}$$

Thus, the original integral evaluates to

$$\int_\tau^{\tau+T} \left[T \frac{d}{dt} S \right] dt = -\pi\left[T_x S_y - T_y S_x \right]$$

---

† Euler's identity: $e^{\pm j\theta} = \cos(\theta) \pm j\sin(\theta)$

which may be more neatly written as

$$\int_{\tau}^{\tau+T}\left[T\frac{d}{dt}S\right]dt=\pi\Im m\left\{TS^{*}\right\}$$

The other term in the integral of equation (10.2) may be evaluated in the same manner:

$$\int_{\tau}^{\tau+T}\left[E\frac{d}{dt}D\right]dt=\pi\Im m\left\{ED^{*}\right\}$$

The energy dissipated per cycle can then be written as

$$\Delta U=\pi\Im m\int_{V}\left[\left\{T\right\}^{\mathrm{T}}\left\{S^{*}\right\}+\left\{E\right\}^{\mathrm{T}}\left\{D^{*}\right\}\right]dV \tag{10.3}$$

The relationships for strain and electric field in terms of the displacements and electric potentials at the nodes, were given in Chapter 4,

$$\left\{S\right\}=\left[B_{u}\right]\left\{u_{n}\right\} \tag{10.4a}$$

$$\left\{E\right\}=-\left[B_{\phi}\right]\left\{\phi_{n}\right\} \tag{10.4b}$$

These may be substituted into the piezoelectric relationships for stress and electric flux density, given in Chapter 2,

$$\left\{T\right\}=\left[c^{E}\right]\left\{S\right\}-\left[e\right]^{\mathrm{T}}\left\{E\right\} \tag{10.5a}$$

$$\left\{D\right\}=\left[e\right]\left\{S\right\}+\left[\varepsilon^{S}\right]\left\{E\right\} \tag{10.5b}$$

to obtain stress and electric flux density relationships in terms of the displacements and electric potentials at the nodes:

$$\left\{T\right\}=\left[c^{E}\right]\left[B_{u}\right]\left\{u_{n}\right\}+\left[e\right]^{\mathrm{T}}\left[B_{\phi}\right]\left\{\phi_{n}\right\} \tag{10.6a}$$

$$\left\{D\right\}=\left[e\right]\left[B_{u}\right]\left\{u_{n}\right\}-\left[\varepsilon^{S}\right]\left[B_{\phi}\right]\left\{\phi_{n}\right\} \tag{10.6b}$$

Substituting equations (10.4a), (10.4b), (10.6a), and (10.6b) into equation (10.3) and re-arranging using rules of manipulation for matrices, we obtain the discrete form

$$\Delta U=\pi\Im m\left\{\begin{matrix}\left\{u_{n}\right\}^{\mathrm{T}}\\ \left\{\phi_{n}\right\}^{\mathrm{T}}\end{matrix}\right\}^{\mathrm{T}}\left[\begin{matrix}\left[K_{uu}\right] & -\left[K_{u\phi}\right]\\ \left[K_{\phi u}\right] & -\left[K_{\phi\phi}\right]\end{matrix}\right]\left\{\begin{matrix}\left\{u_{n}^{*}\right\}\\ \left\{\phi_{m}^{*}\right\}\end{matrix}\right\} \tag{10.7}$$

where the matrices $[K_{uu}]$, $[K_{u\phi}]$, $[K_{\phi u}]$, and $[K_{\phi\phi}]$, are the mechanical, piezoelectric, transposed piezoelectric, and dielectric stiffness matrices respectively, derived in Chapter 4.

The average power dissipated is then

$$P = \frac{\Delta U}{T} = \frac{\omega}{2}\Im m\left\{\begin{matrix}\{u_n\}^{\mathrm{T}} \\ \{\phi_n\}^{\mathrm{T}}\end{matrix}\right\}^{\mathrm{T}}\left[\begin{matrix}[K_{uu}] & -[K_{u\phi}] \\ [K_{\phi u}] & -[K_{\phi\phi}]\end{matrix}\right]\left\{\begin{matrix}\{u_n^*\} \\ \{\phi_n^*\}\end{matrix}\right\} \tag{10.8}$$

Finally, dividing by volume, we obtain the power dissipated per unit volume, or heat generated per unit volume

$$\dot{q} = \frac{P}{V} = \frac{\omega}{2V}\Im m\left\{\begin{matrix}\{u_n\}^{\mathrm{T}} \\ \{\phi_n\}^{\mathrm{T}}\end{matrix}\right\}^{\mathrm{T}}\left[\begin{matrix}[K_{uu}] & -[K_{u\phi}] \\ [K_{\phi u}] & -[K_{\phi\phi}]\end{matrix}\right]\left\{\begin{matrix}\{u_n^*\} \\ \{\phi_n^*\}\end{matrix}\right\} \tag{10.9}$$

10.3 Thermal Equations

When a temperature gradient exists in a body there is an energy transfer from the high-temperature region to the low-temperature region. We say that the energy is transferred by conduction and that the heat-transfer rate per unit area is proportional to the normal temperature gradient

$$\frac{q}{A} \propto \frac{\partial T}{\partial x}$$

When the proportionality constant is inserted, we obtain Fourier's law of heat conduction

$$q = -kA\frac{\partial T}{\partial x} \tag{10.10}$$

where q is the heat-transfer rate and $\partial T/\partial x$ is the temperature gradient in the direction of the heat flow. The constant k is called the thermal conductivity of the material. The minus sign is a consequence of the second law of thermodynamics which requires that heat must flow from higher to lower temperatures.

Using Fourier's law of heat conduction we can derive the basic equations which govern the transfer of heat in a solid.

Consider the general case where the temperature may be changing with time and heat sources may be present. For the three-dimensional elemental volume, figure 10.1, the energy balance yields

$$q_x + q_y + q_z + q_{gen} = q_{x+dx} + q_{y+dy} + q_{z+dz} + \frac{dE}{dt}$$

where q_{gen} is the heat generated within the element and dE/dt is the change in internal energy. The energy quantities are given by

$$q_x = -kdydz\frac{\partial T}{\partial x}$$

$$q_y = -kdxdz\frac{\partial T}{\partial y}$$

$$q_z = -kdxdy\frac{\partial T}{\partial z}$$

$$q_{gen} = \dot{q}dxdydz$$

$$q_{x+dx} = -\left[k\frac{\partial T}{\partial x} + \frac{\partial}{\partial x}\left(k\frac{\partial T}{\partial x}\right)dx\right]dydz$$

$$q_{y+dy} = -\left[k\frac{\partial T}{\partial y} + \frac{\partial}{\partial y}\left(k\frac{\partial T}{\partial y}\right)dy\right]dxdz$$

$$q_{z+dz} = -\left[k\frac{\partial T}{\partial z} + \frac{\partial}{\partial z}\left(k\frac{\partial T}{\partial z}\right)dz\right]dxdy$$

$$\frac{dE}{dt} = \rho c_p dxdydz\frac{\partial T}{\partial t}$$

where ρ is the density, c_p is the specific heat at constant pressure, and $\dot{q}$ is the heat generated per unit volume.

Thus the general three-dimensional heat-conduction equation is

$$\frac{\partial}{\partial x}\left(k_{xx}\frac{\partial T}{\partial x}\right) + \frac{\partial}{\partial y}\left(k_{yy}\frac{\partial T}{\partial y}\right) + \frac{\partial}{\partial z}\left(k_{zz}\frac{\partial T}{\partial z}\right) + \dot{q} = \rho c_p\frac{\partial T}{\partial t} \tag{10.11}$$

which may be expressed in co-ordinate-free notation as

$$\text{div}\left(k\,\text{grad}\,T\right) + \dot{q} = \rho c_p\frac{\partial T}{\partial t} \tag{10.12}$$

Equation (10.12) governs the conduction of heat within the body. We now have to specify the conditions to be satisfied on the boundary.

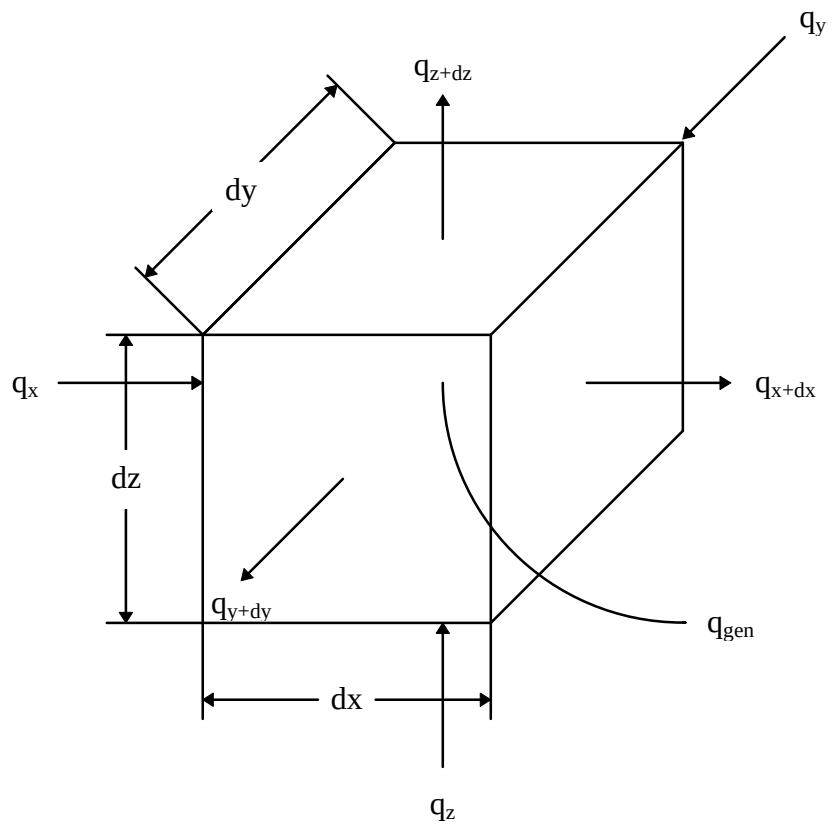

Figure 10.1. Elemental volume for three-dimensional heat-conduction.

We can specify the surface temperature of the body on a part S_1 of the boundary as

$$T = T_\beta \qquad \text{on } S_1 \tag{10.13}$$

where T_β is the given temperature.

If a flow of heat is specified on some part S_2 of the boundary, then we must satisfy

$$(k \operatorname{grad} T)n = q_n \qquad \text{on } S_2 \tag{10.14}$$

where n is the unit vector outward normal to the boundary and q_n is the heat flux per unit surface.

Finally, another commonly used boundary condition is that the flow of heat is proportional to the temperature difference between the surface of the body, and its surroundings. If we impose this condition on a part S_3 of the boundary, we have

$$(k \operatorname{grad} T)n = -h(T - T_\infty) \qquad \text{on } S_3 \tag{10.15}$$

where h is the heat-transfer coefficient and T_∞ is the temperature of the surroundings.

Thus, a mathematical description of the heat conduction problem is

$$\rho c_p \frac{\partial T}{\partial t} - \text{div}\left(k \,\text{grad}\, T\right) = \dot{q} \quad \text{in V} \tag{10.16}$$

$$T = T_\beta \quad \text{on } S_1$$

$$\left(k \,\text{grad}\, T\right)n = q_n \quad \text{on } S_2$$

$$\left(k \,\text{grad}\, T\right)n = -h\left(T - T_\infty\right) \quad \text{on } S_3$$

Finally, if the initial condition

$$T = T_0 \text{ at } t = 0 \tag{10.17}$$

is given, the problem is called the initial boundary value problem of heat conduction. For a steady-state solution, equations (10.16) and (10.17), reduce to the boundary value problem

$$-\text{div}\left(k \,\text{grad}\, T\right) = \dot{q} \quad \text{in V} \tag{10.18}$$

$$T = T_\beta \quad \text{on } S_1$$

$$\left(k \,\text{grad}\, T\right)n = q_n \quad \text{on } S_2$$

$$\left(k \,\text{grad}\, T\right)n = -h\left(T - T_\infty\right) \quad \text{on } S_3$$

10.4 Finite Element Formulation

Using the principles of virtual work, we can change the boundary value problem of heat conduction, equation (10.18), to the weak form [10.1],

$$T = T_\beta \text{ on } S_1 \tag{10.19}$$

$$\int_V \left\{\delta\dot{T}\right\}\left[k\right]\left\{\dot{T}\right\}dV + h\int_{S_3} \left\{\delta T\right\}\left\{T\right\}dS_3 = \dot{q}\int_V \left\{\delta T\right\}dV + q_n\int_{S_2} \left\{\delta T\right\}dS_2 + hT_\infty\int_{S_3} \left\{\delta T\right\}dS_3$$

To generate the matrix relations for a finite element, the temperature is expressed in term of n nodal values via interpolation functions [10.2] N_T:

$$\left\{T\right\} = \left[N_T\right]\left\{T_n\right\} \tag{10.20}$$

where

$$\left\langle N_T \right\rangle = \left\langle N_1 \quad \cdot \quad \cdot \quad \cdot \quad N_n \right\rangle$$

Differentiating equation (10.20) yields

$$\{\dot{T}\} = [B_T]\{T_n\} \tag{10.21}$$

where

$$[B_T] = \begin{bmatrix} \frac{\partial N_1}{\partial x} & \cdots & \frac{\partial N_n}{\partial x} \\ \frac{\partial N_1}{\partial y} & \cdots & \frac{\partial N_n}{\partial y} \\ \frac{\partial N_1}{\partial z} & \cdots & \frac{\partial N_n}{\partial z} \end{bmatrix}$$

Using the above relationships, the energy equation (10.19) can be rewritten as follows:

$$T_n = T_\beta \text{ on } S_1 \tag{10.22}$$

$$[K]\{T_n\} = \{F\}$$

where

$$[K] = \int_V [B_T]^T [k][B_T] dv + h\int_{S_3} \langle N_T \rangle \langle N_T \rangle^T dS_3$$

$$\{F\} = \dot{q}\int_V \langle N_T \rangle dV + q_n \int_{S_2} \langle N_T \rangle dS_2 + hT_\infty \int_{S_3} \langle N_T \rangle dS_3$$

Matrix [*K*] is referred to as the generalised stiffness matrix and {*F*} is known as the generalised load vector.

Prior to solution of equation (10.22) the number of unknown quantities is reduced by applying boundary conditions. Additionally, geometrical symmetry, either axial or mirror, may be exploited to further reduce the number of unknowns. The reduced or modified form of equation (10.22) may then be solved by using a standard method, such as Gauss elimination, or LU decomposition.

Once nodal values of temperature have been determined, we can determine the temperature gradients from equation (10.21), and then the heat flux (heat-transfer rate per unit area) at the nodes can be found from the following equation:

$$\{q''\} = [-k]\{\dot{T}\} \tag{10.23}$$

The methods described in this section have been implemented by the author, in the form of a number of software modules. These extend the capabilities of the finite element and boundary

element software, PHOEBE, so that it can take into account the generation and flow of heat under CW conditions. The testing of this new software is reported in Chapter 11.

10.5 References

[10.1] N. Kikuchi, *Finite Element Methods in Mechanics*, (Cambridge University Press, 1986), Chapter 2.

[10.2] O. C. Zienkiewicz, 'The Finite Element Method', (McGraw-Hill, 1977).

Chapter 11

THERMAL ANALYSIS

11.1 Introduction

As previously seen, the finite element method is adept at modelling mechanical structures. It is equally well suited to solving heat conduction problems.

Using the methods described in Chapter 10, the author has written a number of software modules that extend the finite element and boundary element software, PHOEBE, to take into account the generation and flow of heat under CW conditions. These modules are referred to under the collective name, LETO. In Greek mythology Leto was the daughter of Phoebe and thus seemed an appropriate name for the set of modules that extends the power of PHOEBE into the realms of thermal analysis.

To verify that the new software could correctly predict the temperature profile of transducers operating under CW conditions two different transducer designs were tested. In addition to the measurements of the electrical and acoustic responses of the transducers, the transient temperature rises under CW operation were measured. In each case the temperature response was measured over a suitably long period so that thermal equilibrium was reached. For each transducer the temperature rise was measured for various input voltages. Thus, it was possible to determine the thermal stability of the material properties.

In this chapter the software LETO is briefly described followed by a description of the technique used to verify the temperature rise predicted by this software. The remaining sections present the electrical, acoustic, and thermal test results for a 50 kHz Tonpilz transducer and thermal results for the 2.5 kHz partially free-flooded flextensional transducer previously described in Chapter 8. All these results are compared with predicted values calculated using finite element and boundary element techniques.

11.2 LETO

LETO consists of three distinct software programs, these being the heat source module, the heat conduction module, and the graphics display module. These three software modules, when used in conjunction with PHOEBE, make it possible to determine if a transducer will be thermally limited. This enables the suitability of transducers for applications such as long-range communications to be determined. At the time of writing this author is unaware of a commercial software package which has this capability.

Like PHOEBE, the first two applications run in the MS-DOS environment while the graphics application run under MS-WINDOWS. All three modules take a number of data files as their input and, in the case of the heat source and heat conduction programs, produce output data which are also stored in files. The input and output of data is controlled through the use of control files. A typical set of these is shown in figures 11.1 to 11.3; in this case the control files refer to the Tonpilz transducer described later in this chapter. These files allow C/C++ style comments of the single and multiple line variety. Other lines follow the general format of a keyword followed by the name of a data file which is to be read from or written to. A fuller description of these control files and the format of the file that they refer to is given in Appendix D.

The heat source application, which was takes the displacements and potentials at the nodes, calculated by PHOEBE, as its input, calculates the mechanical, piezoelectric, and dielectric power dissipation, the volume, and the heat generated per unit volume of each element in the mesh. This data can serve as an input to the heat conduction module.

The heat conduction model is a generic application. It can cope with the three kinds of boundary conditions described in Chapter 10: known temperatures at the surface nodes, heat flow from surface elements, and convection from surface elements. The program can also handle heat sources within elements. Using one or more of these conditions the program calculates the temperatures at the nodes.

```
// Heat source input/output control file.
// 50 kHz Tonpilz transducer design by J. Dunn.
// Rotational symmetry of order 16.
// No Mirror symmetry.

// Input files

COORDINATES n.dat
ELEMENTS    e.dat
MATERIALS   m.dat

DISPLACEMENTS     wm1.dat
POTENTIALS        wm1.dat

// Output files

HEATSOURCES h.dat
```

Figure 11.1. Heat source input/output control file “TONPILZ.HS1”.

```
// Heat conduction input/output control file.
// 50 kHz Tonpilz transducer design by J. Dunn.
// Rotational symmetry of order 16.
// No Mirror symmetry.

// Input files

COORDINATES n.dat
ELEMENTS    e.dat
MATERIALS   m.dat

HEATSOURCES       h.dat

BOUNDARYFACES     f.dat
BOUNDARYOUTFLOWS  boutflow.dat

// Output files

TEMPERATURES      t.dat
```

Figure 11.2. Heat conduction input/output control file “TONPILZ.HC1”.

```
// Graphics Display control file.
// 50 kHz Tonpilz transducer design by J. Dunn.
// Rotational symmetry of order 16.
// No Mirror symmetry.

COORDINATES       n.dat
ELEMENTS          e.dat
TEMPERATURES      t.dat
```

Figure 11.3. Graphics display control file “TONPILZ.FE1”.

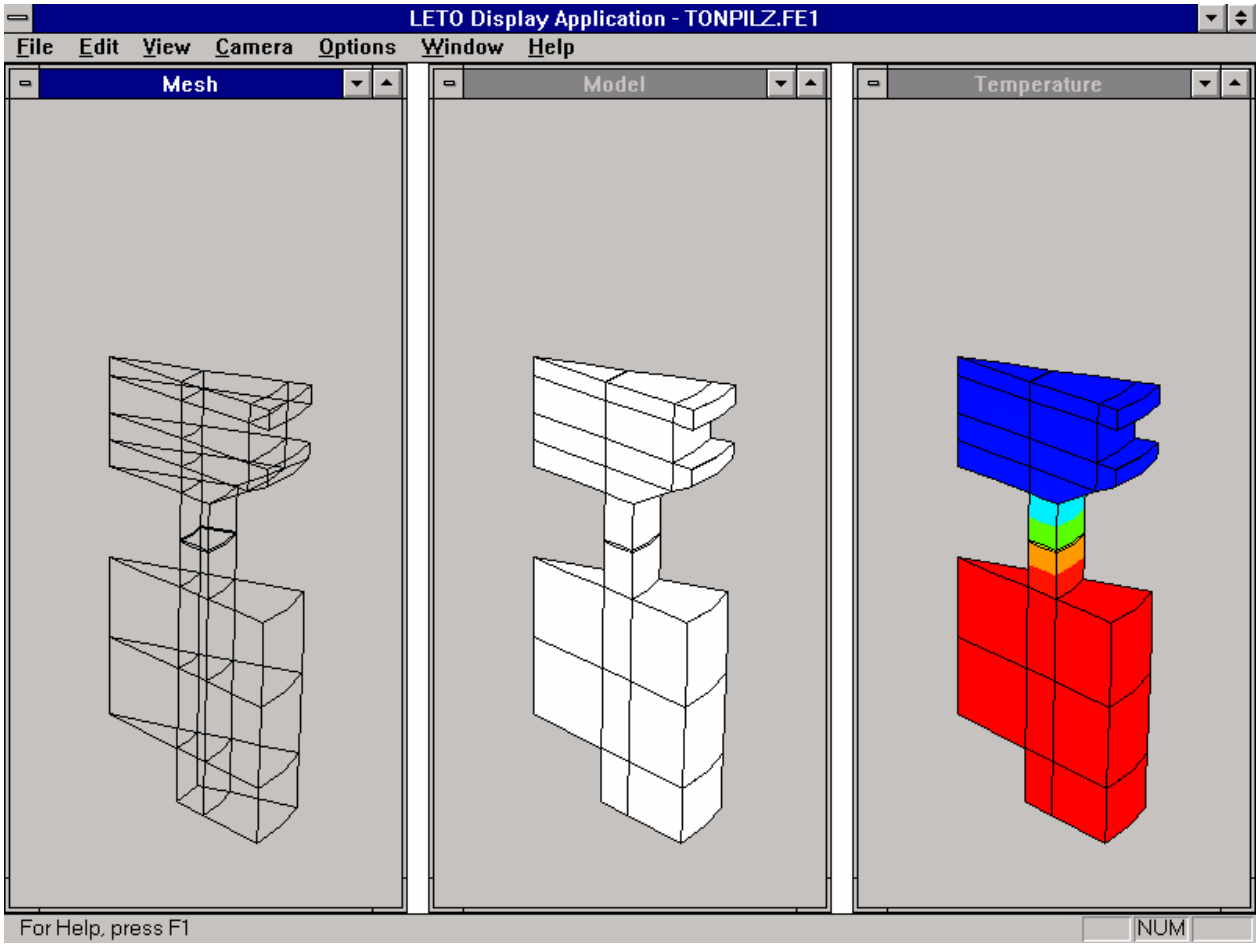

Figure 11.4. A screen shot of the graphics display program, LETO display application, displaying three different views of a sixteenth segment of the 50 kHz Tonpilz transducer described later in this chapter.

It should be noted that the current method of solving the steady-state temperature profile of the transducer assumes that the properties of the materials are thermally inert; that is, the properties of the material do not vary with temperature. This is an acceptable assumption for metals over the temperature range of interest, 0 °C to 100 °C, since the properties of these materials will only exhibit small variations. For other material such as ceramics, glue, or foam this will not be as valid. A possible method of obtaining a more accurate solution would be to update the material properties based on the calculated temperatures within the materials and repeat the analysis. This process could be repeated until a suitable accuracy was achieved. However, for a first approximation a single iteration will suffice.

Finally, the third module allows various views of a modelled structure to be displayed; these being, a mesh view, a model view, and a surface temperature view. A screen shot of this program is

displayed in figure 11.4. In this case the application is being used to view the Tonpilz transducer, which is discussed later in this chapter.

2.3 Temperature Calibration Method

The set-up used to measure temperature change over a period of time is shown in figure 11.5. Obviously it would be very time consuming to measure the complete temperature profile of a transducer. However, if the temperature could be confirmed at a single point then it would be a good assumption that the numerical model was representative. A condition of this presumption is that the chosen spot display a marked change in temperature. Thus, a single temperature probe was fitted to each transducer in the spot considered to be the place of maximum temperature rise. The chosen spot on each transducer was as near as possible to the centre of the piezoelectric material. The probe was a thermistor – a temperature sensitive resistor. The electrical resistance of this device changes with temperature; a positive change in temperature causes an increase in resistance for of a positive temperature coefficient device (P.T.C. thermistor) while the resistance of a negative temperature coefficient device (N.T.C. thermistor) decreases.

The type of thermistor chosen is dependent on a number of factors. Firstly the speed at which the device reacts to a change in temperature, its thermal inertia, is dependent on mass. Thus, the thermistor must be small. Secondly, since the response of a thermistor is not linear it must be calibrated. The tolerance of a device identifies how closely it is matched to another device of the same type. If the tolerance is high, each thermistor must be individually calibrated. Thus, a low tolerance device is preferable. The chosen device was a bead N.T.C. thermistor with a tolerance of 0.2 %.

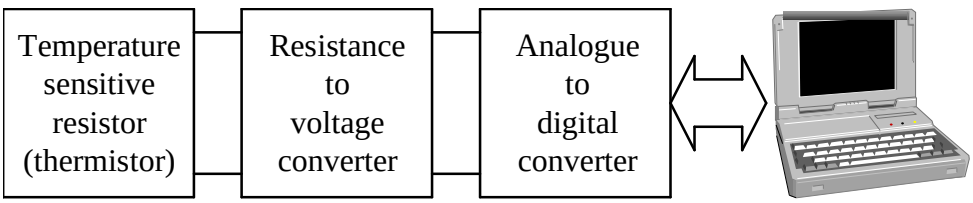

Figure 11.5. Typical equipment required to measure temperature.

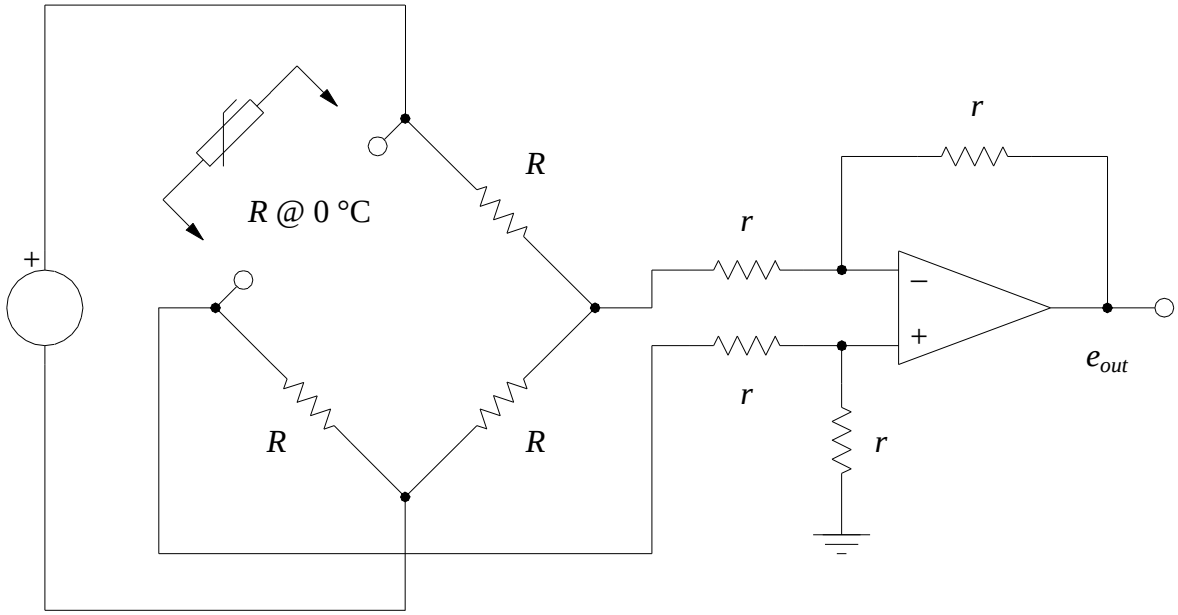

Figure 11.6. Simplified schematic of a resistance-to-voltage converter (RVC).

In order to measure the temperature of the transducer one could simply measure the resistance of the thermistor at set times; for example, every 30 seconds. A more accurate and versatile method is to let a computer record measurements. However, a computer cannot directly measure electrical resistance. First the resistance has to be converted to a voltage and then to a binary number. A circuit which can convert a resistance to a voltage is shown in figure 11.6 (for a complete circuit diagram see Appendix C). The output of this circuit is connected to an analogue-to-digital converter (ADC) which converts a voltage to a binary number. The input to an ADC is usually restricted to the voltage range of 0 V to 2.5 V. Thus, the output of the resistance-to-voltage converter (RVC) must be within this range.

Since the requirement was to observe temperature between the range 0 °C to 100 °C, in order to maximise the accuracy of the measurement taken, the RVC was designed to output 0 V to 2.5 V over this range when connected to the chosen thermistor. The calibration curve of the RVC and thermistor is shown in figure 11.7.

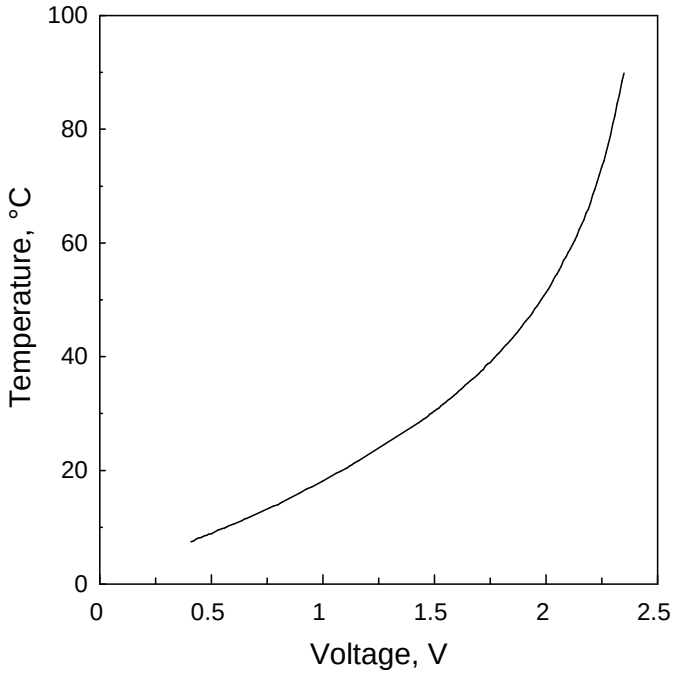

Figure 11.7. Temperature sensor calibration.

11.4 A 50 kHz Tonpilz Transducer

The first device to be tested was an 'off-the-shelf' 50 kHz Tonpilz transducer designed by J. Dunn [11.1]. This transducer was initially designed using the lumped-element approach. The design was then refined using finite-element techniques, resulting in a significant improvement in performance (increased 3 dB bandwidth, and higher electro-mechanical coupling).

The term 'Tonpilz' in German literally means 'vibrating mushroom', an expression first used by Hahnemann and Hecht in 1920 [11.2]. The design of these transducers has been covered by many authors, however, a particularly lucid account is given by Stansfield [11.3]. The Tonpilz transducer design most commonly consists of a piezoelectric stack sandwiched between a head-mass and a tail-mass. To obtain broad band operation, the transducer must have a low quality factor, and this implies a large radiating area and low effective vibrating mass. It can be shown that the effective vibrating mass can be defined as $M_e = M_h(1 + M_h / M_t)$, where M_h is the mass of the head and M_t the mass of the tail [11.4]. Thus, in order to minimise the effective vibrating

mass, the head mass must be small, the tail mass being an order of magnitude larger. Thus, the tail is usually steel or brass, while the head is aluminium or titanium.

Dunn's transducer consists of an aluminium head, a PZT-4 stack, and a mild steel tail. Technical schematics and a comprehensive parts list for this 50 kHz Tonpilz transducer can be found in Appendix B. The cross-section drawing of the device is repeated in figure 11.8, and photographs, taken at various angles, are shown in figures 11.9 to 11.11.

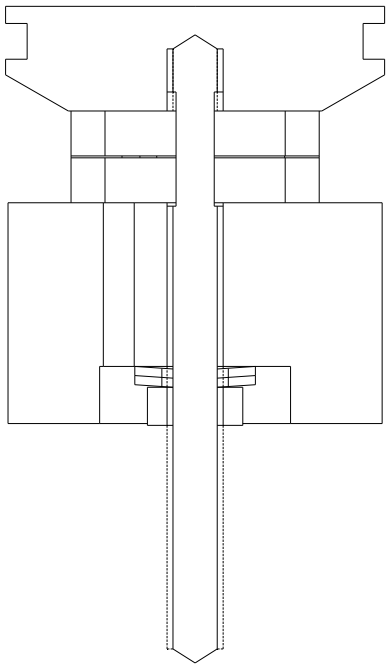

Figure 11.8. Technical drawing of the 50 kHz Tonpilz transducer (scale 2 : 1).

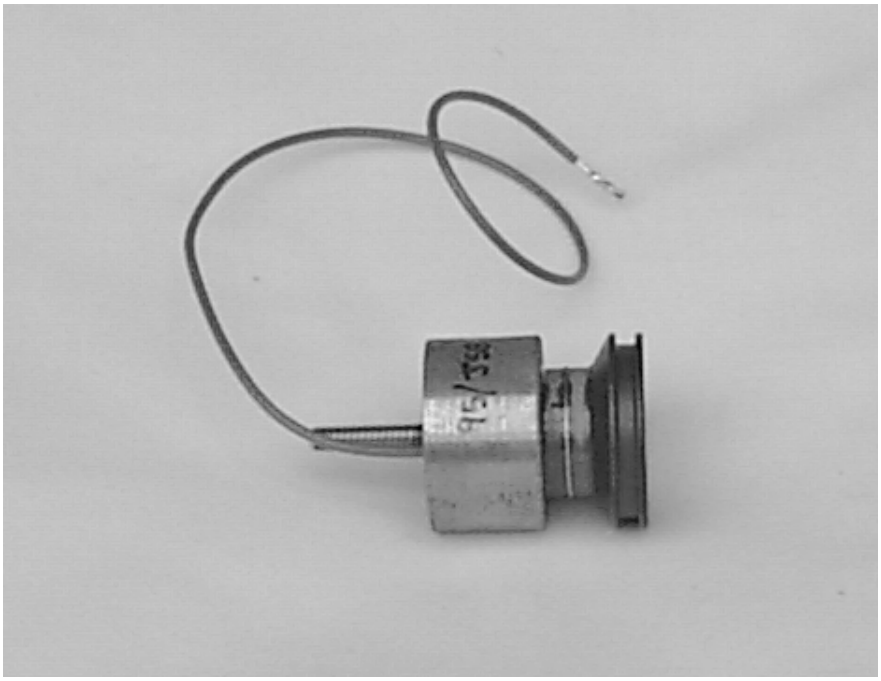

Figure 11.9. 50 kHz Tonpilz transducer (horizontal view).

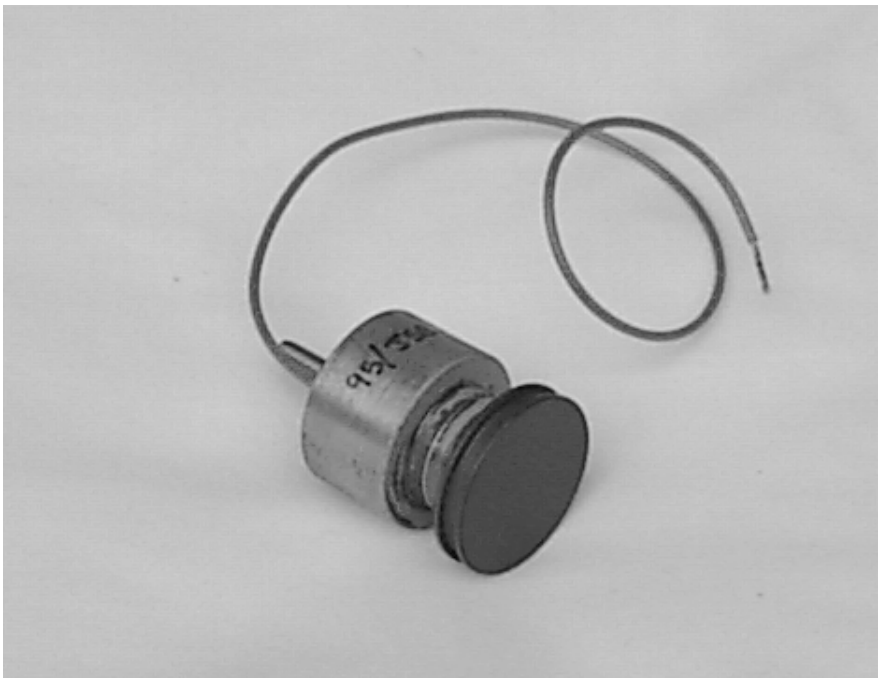

Figure 11.10. 50 kHz Tonpilz transducer (head-end view).

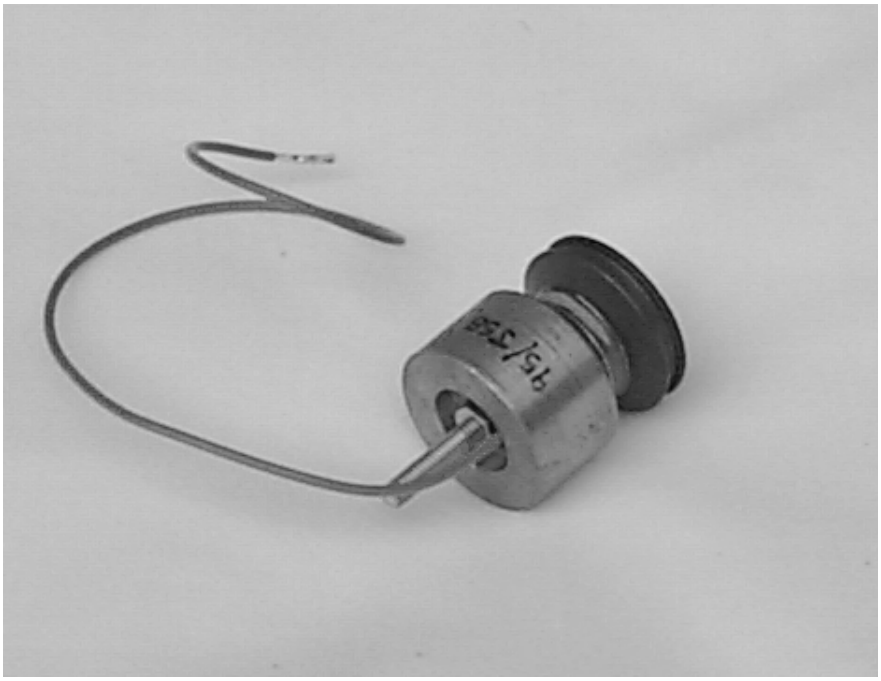

Figure 11.11. 50 kHz Tonpilz transducer (tail-end view).

The excitation of a Tonpilz transducer causes the head-mass to vibrate in antiphase with the tail-mass. To avoid radiation from the front face being cancelled by that from other parts the transducer it is usually mounted in a watertight air-filled case, so that only the front face is in contact with the water. Figure 11.12 shows a cross-section view of the transducer mounted inside a watertight housing that was designed by the author. The housing is of split construction, the top half containing the Tonpliz element, while the other half accommodates the electrical connections. The ingress of water is prevented by the use of 'O'-ring seals between the transducer head and the housing and between the two halves of the housing.

In order to model the transducer using PHOEBE, a mesh had to be generated. Figure 11.13 depicts the complete structural mesh (for clarity the hidden lines have been removed) which consists of 336 elements. By invoking rotational symmetry, the structural mesh has been reduced to a one sixteenth segment that contains only 21 elements, shown in figure 11.14, consisting of 10 head elements, 2 piezoelectric elements, 1 glue joint element (optional) representing all the glue joints in the transducer, and 8 tail elements. The finite element model of the transducer has been simplified in a number of ways. The most obvious is the omission of the centre bolt. This has

meant that the bolt hole through the tail and the bolt thread which penetrates a short distance into the head have been ignored. The small hole that provides access for the electrical wire which connects to the brass shim has also been ignored.

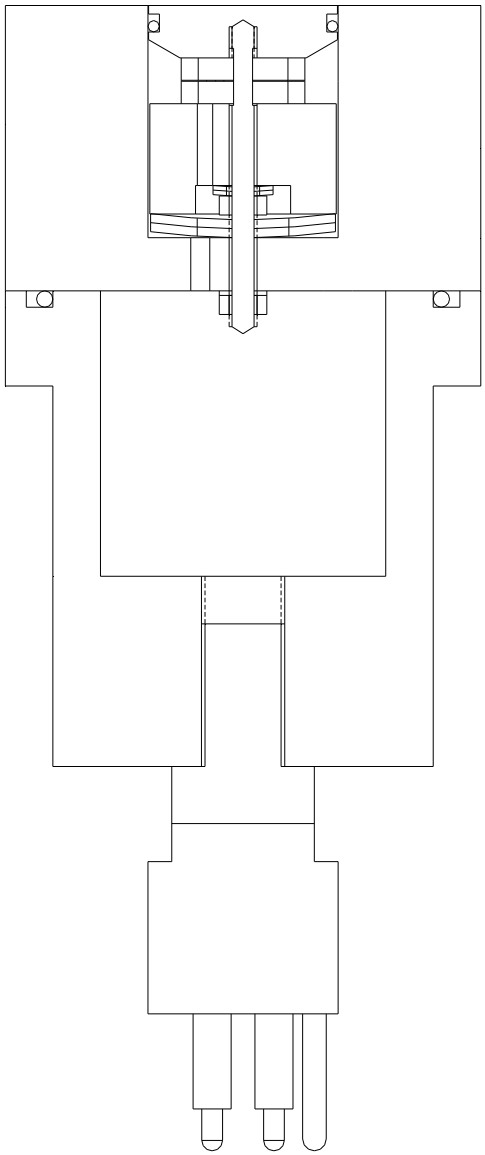

Figure 11.12. Technical drawing of the 50 kHz Tonpilz transducer and housing (scale 1 : 1). The Tonpilz element is contained within the top half of the housing, the rest of the housing serves to accommodate the electrical connections.

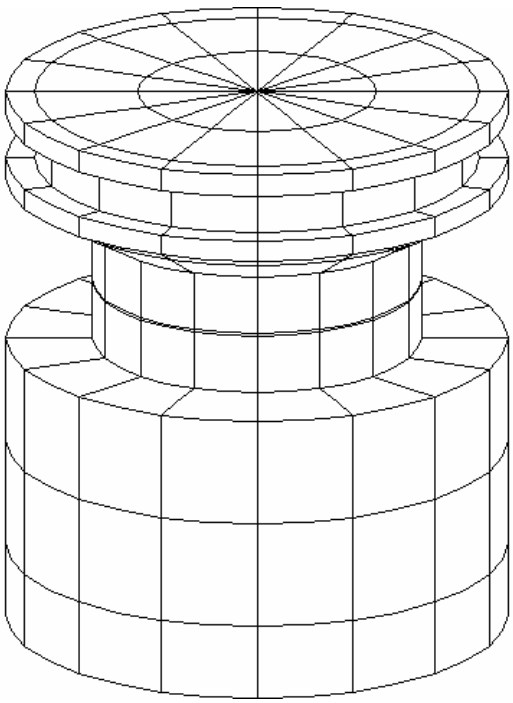

Figure 11.13. Structural mesh (hidden lines have been removed for clarity).

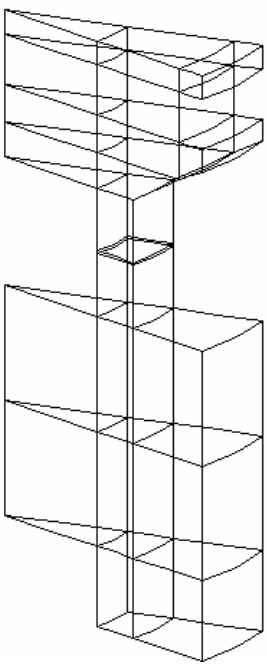

Figure 11.14. Finite element mesh.

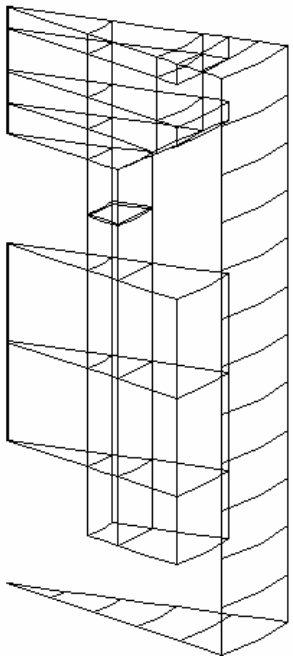

Figure 11.15. Finite element and boundary element mesh.

The choice of glue joint thickness for this transducer was very difficult, as the calculated results where found to be highly dependent on its dimension. Consequently two sets of results are presented, the first assumes no glue joints while the second has a single glue joint of 0.12 mm between the ceramic elements that represents all the glue joints within the structure.

Table 11.1 lists the materials used for each component of the transducer, and their properties.

Table 11.1. Transducer materials and their properties.

Part	Material	Density (kg m^{-3})	Young's modulus (10^3 MPa)	Poisson's ratio	Mechanical quality factor Q_m
Ceramic	PZT-4™	See table 2.2			
Glue joint	Araldite	1180	6.5	0.40	10
Tail	Mild Steel	7700	195.0	0.28	2000
Head	Aluminium	2710	68.91	0.30	1000

As only the front face of the transducer is in contact with the water, not all of the external faces of the finite element mesh can serve as the boundary element mesh. In this case only three surface elements on the front face of the head contribute to the boundary element mesh. However, the boundary element mesh must form a closed structure, and hence extra elements have been generated which form a shell around the transducer. These surface elements, which are not related to the finite element mesh, are assumed to be rigid. They do not represent the actual housing (which would require many more elements) but they do provide a means of representing to a good accuracy the acoustic loading on the front face of the transducer. Both the finite element mesh and the boundary element mesh are shown in figure 11.15.

11.4.1 Electrical Behaviour

In this section the various electrical responses of the transducer, predicted by finite element and boundary element analysis, are presented. These are compared directly with the responses measured from the transducer. The methodology used to analyse the responses is identical to that used for the 5 kHz air-backed flextensional transducer. This being the case, the results should be self-explanatory, and in order to avoid repetition only the importance points will be discussed.

The theoretical in-air and in-water admittance and capacitance responses calculated using a model without glue joints are shown in figures 11.16 to 11.19, the responses calculated using a model with glue joints are shown in figures 11.20 to 11.23, and the measured responses are shown in figures 11.24 to 11.27. The in-air performance characteristics, both theoretical and measured, derived from the aforementioned responses, are listed in table 11.2, and the component values of the equivalent circuit which represents the electrical response of the transducer are given in table 11.3. Table 11.4 presents the values taken from the in-water responses. These results generally compare well with Dunn's [11.1] (f_{air} = 49.36 kHz, Q_M = 3.2, and $k^2 \geq 0.168$).

As with the 5 kHz air-backed flextensional transducer, the values of resonance frequency concur, the model without glue joint showing a better in-air agreement. For other values the model with glue joints exhibits a more accurate match. The measured level of mechanical damping is in-between the two predicted results, the model without glue joint underestimating the damping

while the model with glue joint produced an overestimation. The values for low-frequency capacitance compare reasonably with the expected value, 772.9 pF, calculated by equation (6.1).

Table 11.2. Parameters derived directly from the predicted and measured in-air electrical responses.

Parameter	Theoretical value		Experimental value
	(no glue joints)	(with glue joints)	
f_{air}	53.715 kHz	51.897 kHz	54.34 kHz
k^2	0.289	0.277	0.155
Q_m	500	120	279
G_m	34.06 mS	7.53 mS	5.66 mS
C_{LF}	681 pF	684 pF	713 pF
tan δ_e	0.003	0.003	0.01

Table 11.3. Components of the in-air equivalent circuits.

Parameter	Theoretical value		Experimental value
	(no glue joints)	(with glue joints)	
L_m	44.2 mH	49.6 mH	77.6 mH
C_m	196.8 pF	189.8 pF	110.5 pF
R_m	29.4 Ω	132.7 Ω	176.7 Ω
C_e	484.2 pF	494.6 pF	602.5 pF
R_e	1.5 MΩ	1.5 MΩ	410 kΩ

Table 11.4. Parameters derived directly from the predicted and measured in-water electrical responses.

Parameter	Theoretical value		Experimental value
	(no glue joints)	(with glue joints)	
f_{water}	53 kHz	51 kHz	50 kHz
Q_M	3.50	3.20	2.73
G_M	229.3 μS	185.9 μS	175.3 μS
$G_{\max}$	259.7 μS	223.7 μS	200 μS
C_e	474.6 pF	495.5 pF	725.7 pF

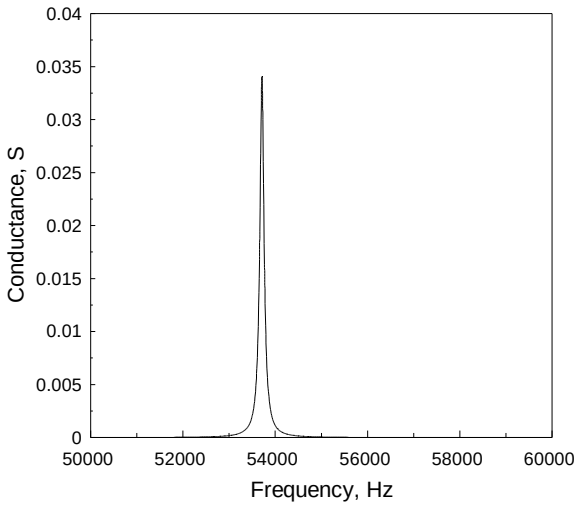

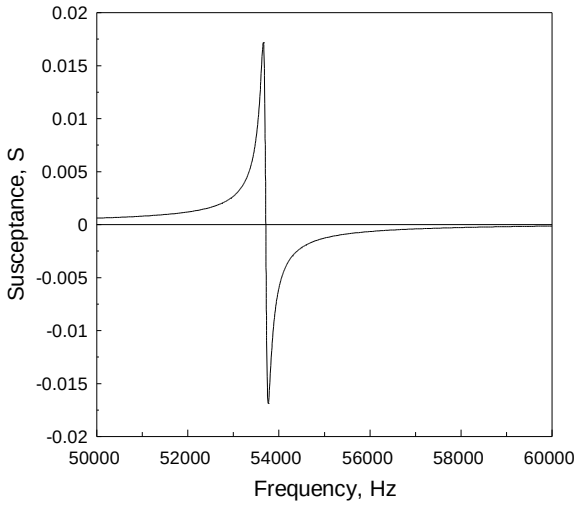

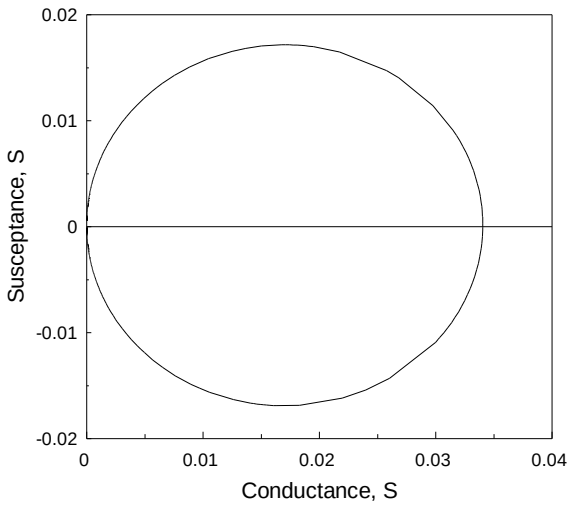

Figure 11.16. Predicted in-air admittance response (no glue joints).

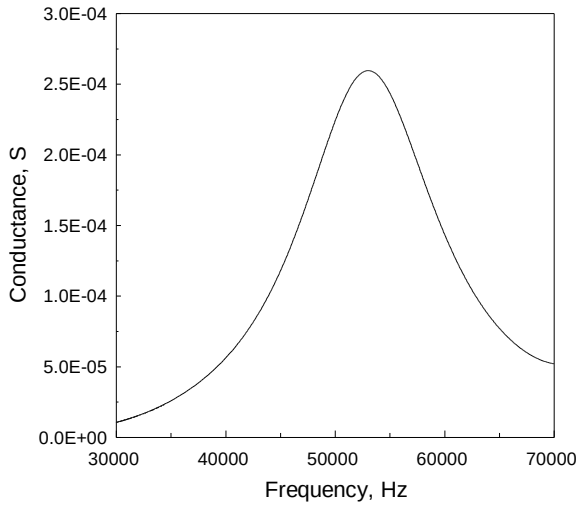

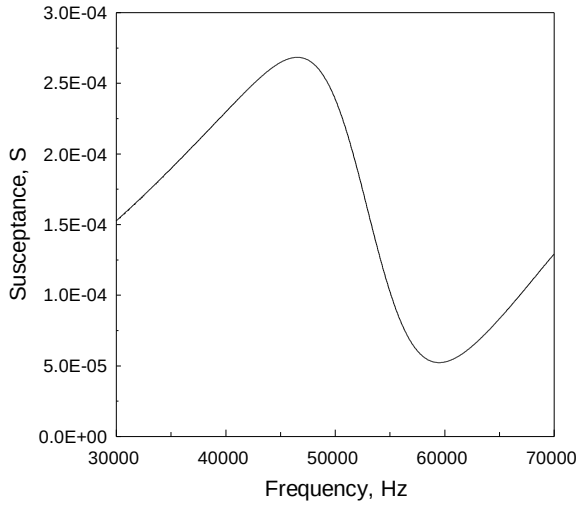

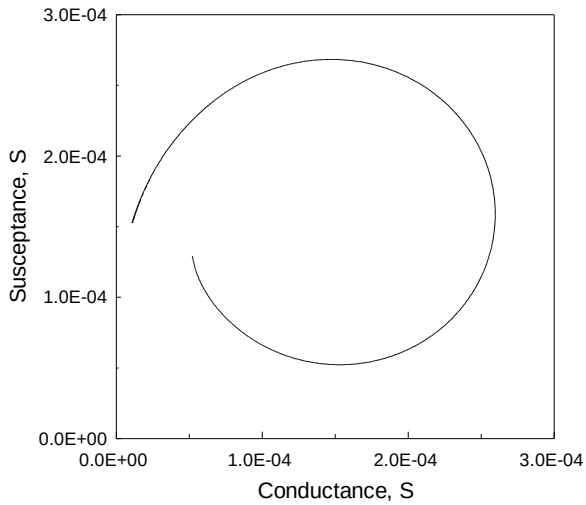

Figure 11.17. Predicted in-water admittance response (no glue joints).

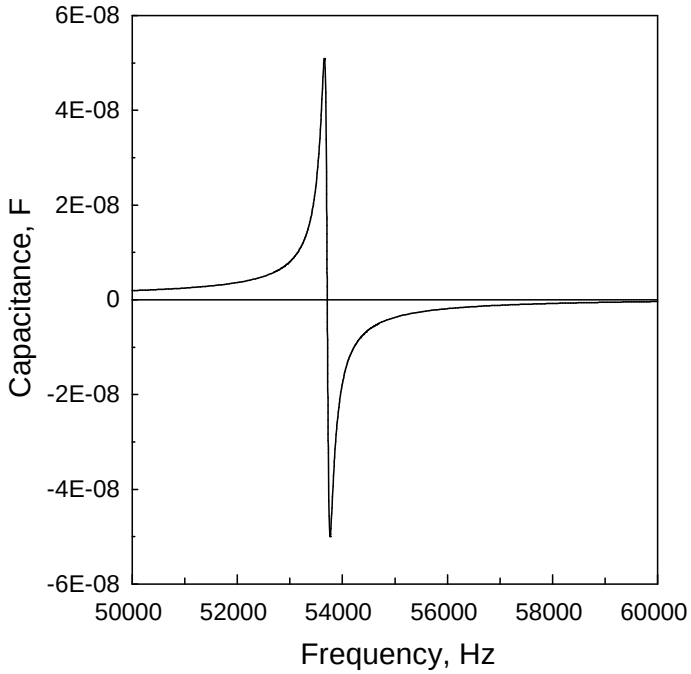

Figure 11.18. Predicted in-air capacitance response (no glue joints).

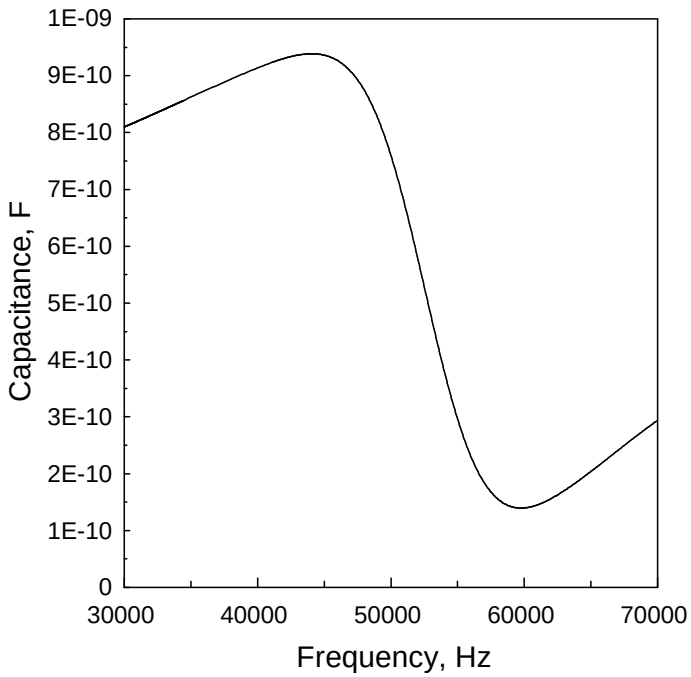

Figure 11.19. Predicted in-water capacitance response (no glue joints).

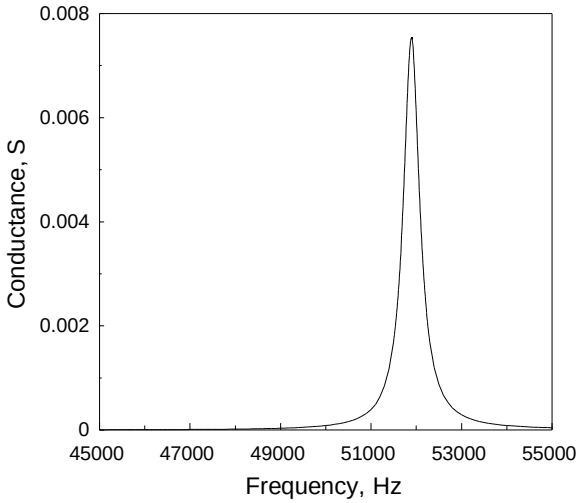

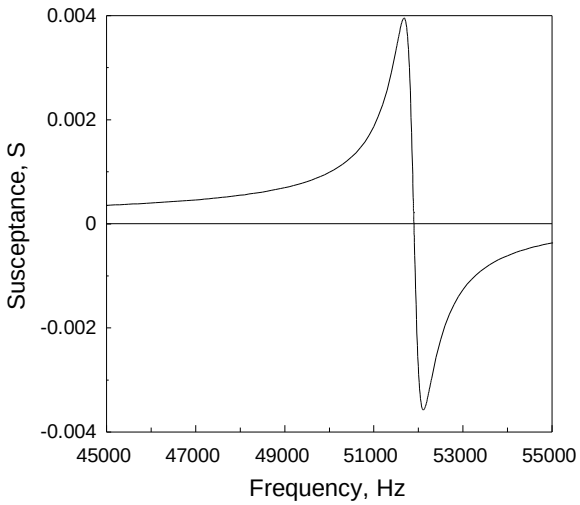

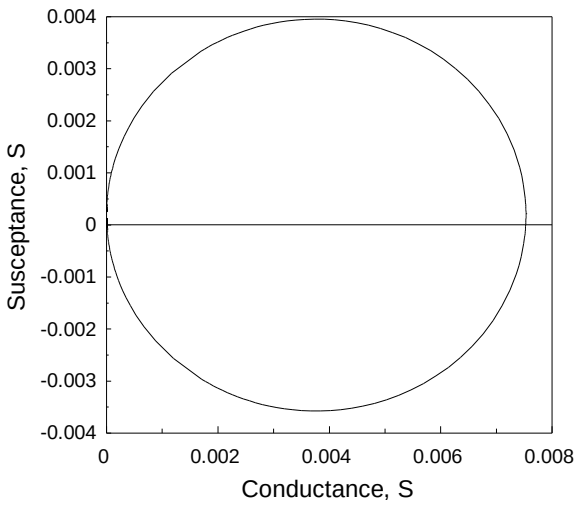

Figure 11.20. Predicted in-air admittance response (with glue joints).

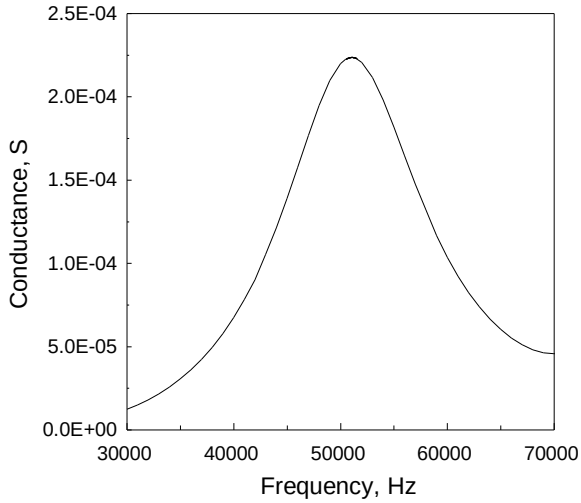

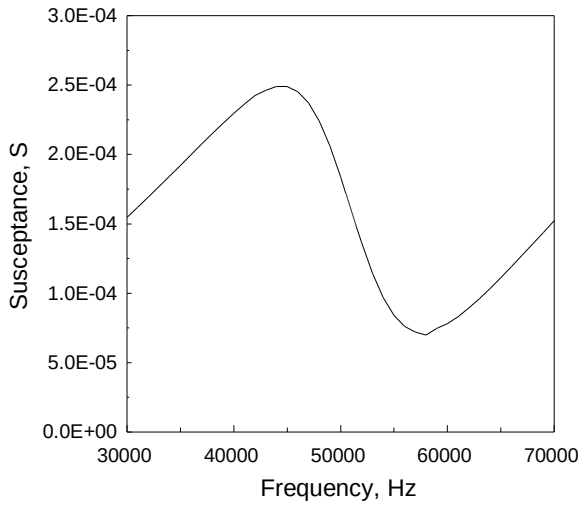

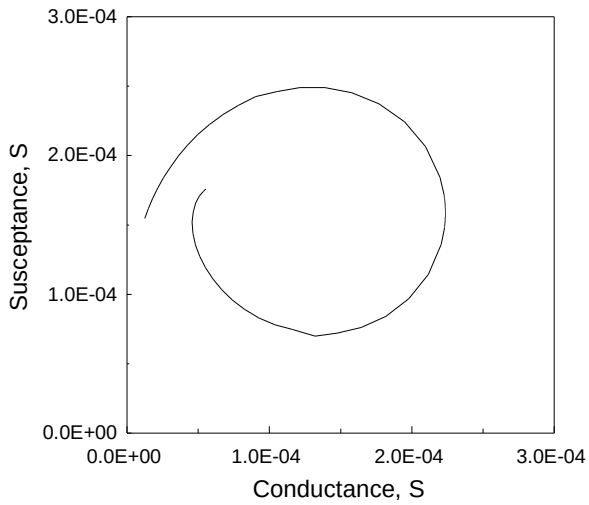

Figure 11.21. Predicted in-water admittance response (with glue joints).

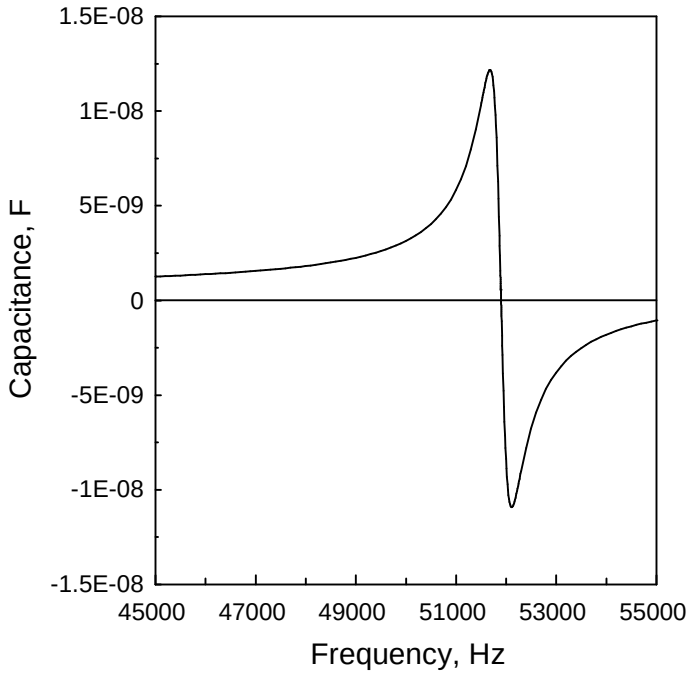

Figure 11.22. Predicted in-air capacitance response (with glue joints)

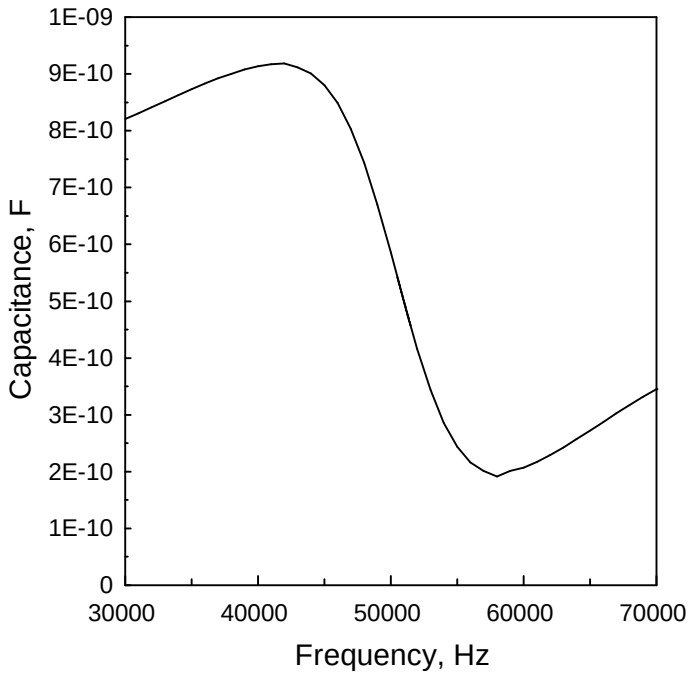

Figure 11.23. Predicted in-water capacitance response (with glue joints).

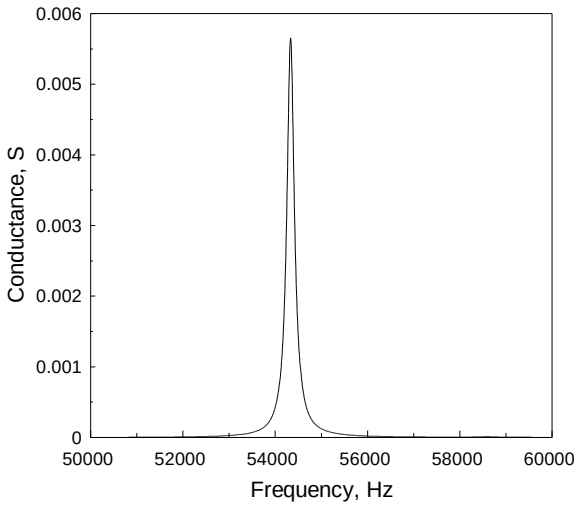

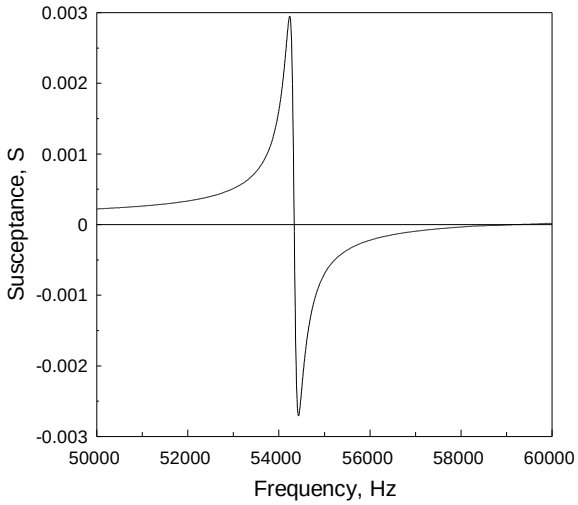

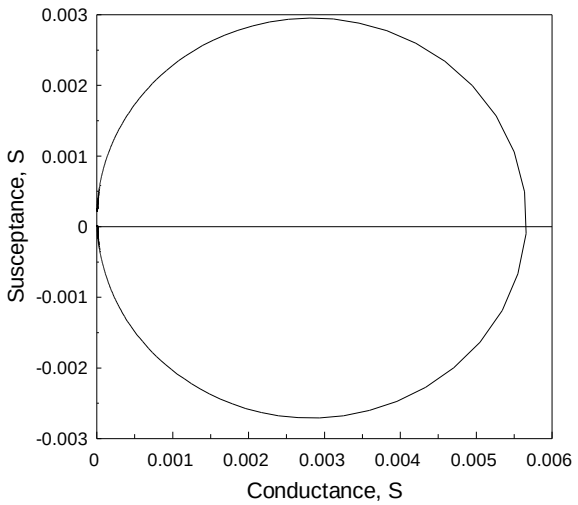

Figure 11.24. Measured in-air admittance response.

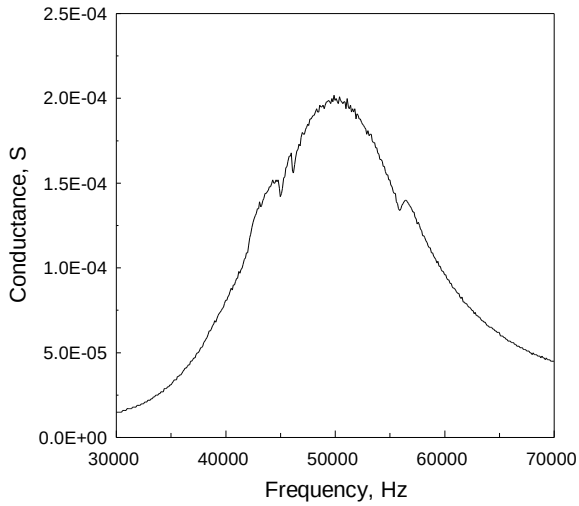

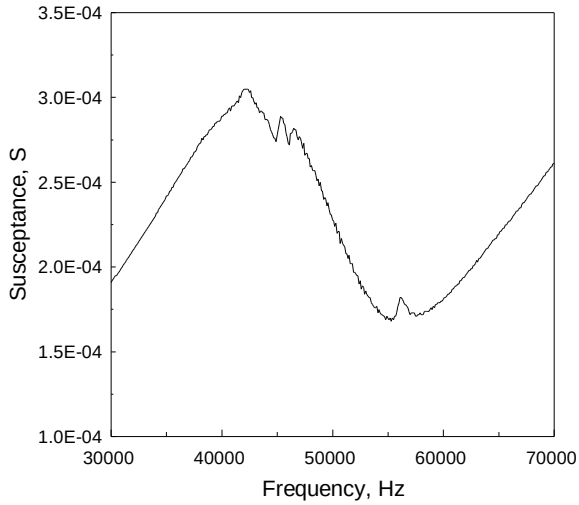

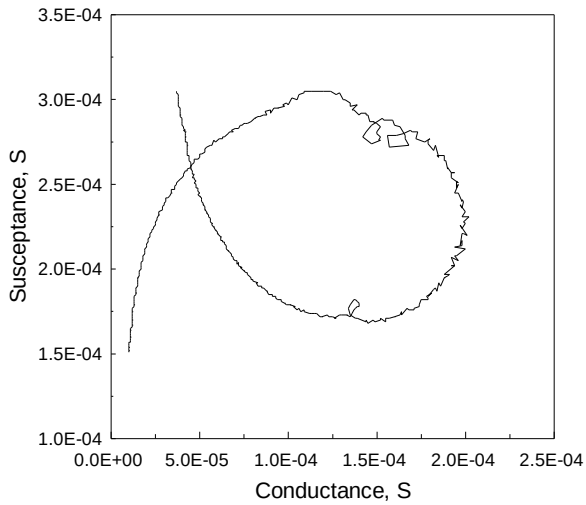

Figure 11.25. Measured in-water admittance response.

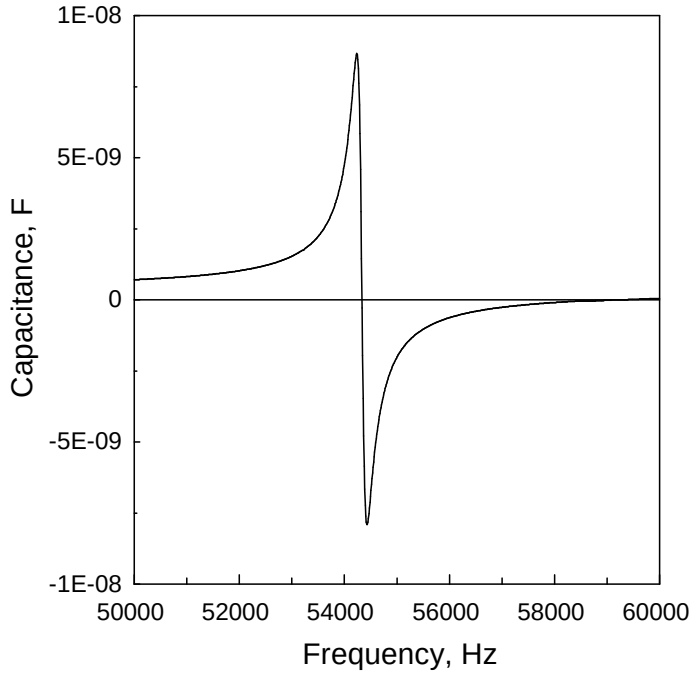

Figure 11.26. Measured in-air capacitance response.

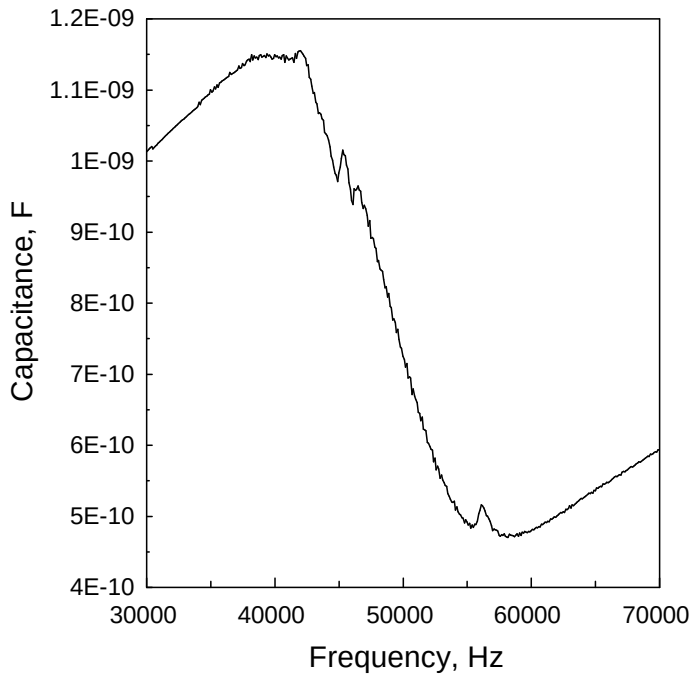

Figure 11.27. Measured in-water capacitance response.

Table 11.5. Predicted and measured efficiencies.

Parameter	Theoretical value		Experimental value
	(no glue joints)	(with glue joints)	
η_{ma}	99.3 %	97.5 %	96.7 %
η_{em}	88.3 %	83.1 %	87.7 %
η_{ea}	88.7 %	81.0 %	84.8 %

From the in-air and in-water responses it is possible to estimate the values the mechanical-acoustic, electro-mechanical, and electro-acoustic efficiencies. These are listed in table 11.5. The theoretical and measured values of efficiency exhibit good agreement, the measured efficiency lying in-between the values predicted from the two models.

11.4.2 Mechanical Behaviour

The displacement fields predicted by the two models (with and without glue joints) were almost identical and so the discussion here covers both sets of results.

The displacement field of the transducer at resonance when operating in water is shown in figure 11.28. It can be seen that the head-to-tail displacement ratio is large, as expected, since the head is much lighter than the tail. The head of the transducer exhibits very little flexure motion, a design aim of Dunn. This minimal bending motion of the head at the resonance frequency of the transducer is essential if performance is to be optimised for wide bandwidth operation.

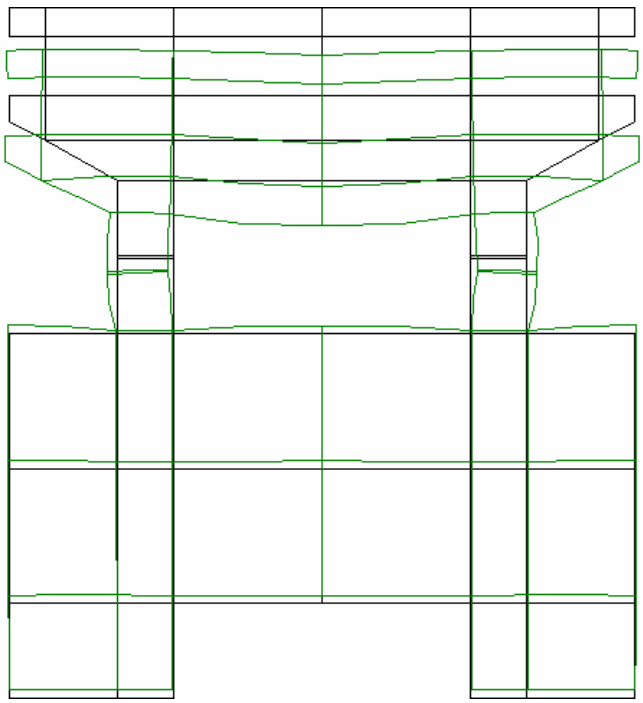

Figure 11.28. Predicted in-water relative displacement field of the 50 kHz Tonpilz transducer at resonance, shown for the model with glue joints. The displacement field for the model without glue joints is virtually identical. Solid lines—at-rest position. Dotted lines—displaced position.

11.4.3 Acoustic Behaviour

The projector voltage sensitivity was determined using the calibrated hydrophone method [11.5]. The transducer was suspended in the centre of an acoustic tank (30 x 12 x 10 feet) with a hydrophone placed at a distance of one metre along the perpendicular from the centre of the radiating face. The transducer was stimulated with a pulsed signal of 10 cycles at a burst rate of 200 millisecond.

The equipment used to drive the transducer and record the measurements is listed below:

Hewlett Packard Pulse/Function Generator, Type 8116A
EIN RF Power Amplifier, Type 240L
Brüel and Kjær Hydrophone, Type 8103
Brüel and Kjær Wideband Conditioning Amplifier, Type 2638
Tecktronix 100 MHz Oscilloscope, Type 2235

The output impedance of the EIN RF power amplifier is 50 ohms. Thus, to match the transducer to the power amplifier, a step-up transformer with a turns ratio of 1 to 10 was required. To remove the reactive electrical component of the transducer at resonance a 14.0 mH tuning coil was connected across the secondary of the transformer.

The predicted projector voltage sensitivity responses on the acoustic axis of the transducer modelled without and with glue joints are shown in figures 11.29 and 11.30 respectively, while the measured response is shown in figure 11.31. The acoustic responses show improved agreement in the values of resonance frequency and quality factor in comparison with those determined from the in-water admittance responses. The values of resonance frequency predicted by the two models are 54.0 kHz ± 25 Hz and 52.0 kHz ± 25 Hz, corresponding to discrepancies of 3.8 % and 0 % relative to the measured value of 52.0 kHz ± 500 Hz. The values of quality factor (3.1 and 3.0 for the models, 3.0 measured) can be considered to be identical within the measurement tolerances.

The magnitudes of the predicted sound pressure level at resonance are approximately 4.5 dB for no glue joints, and 2.5 dB with glue joints, greater than the measured value. However, in both cases some of the discrepancy can be probably be attributed to the models predicting a narrower beamwidth and hence greater directivity index.

The directivity of a modelled transducer is easily calculated from the difference between the power output on the acoustic axis and the total power output. The directivity of the real transducer can be estimated if it is assumed that it behaves as a circular piston in an infinite baffle. Using the following relationship [11.6]

$$\mathrm{DI} = 10\log_{10}\left(\frac{4\pi A}{\lambda^2}\right) \tag{11.1}$$

the directivity index, DI, is found to be in the region of 8.4 dB.

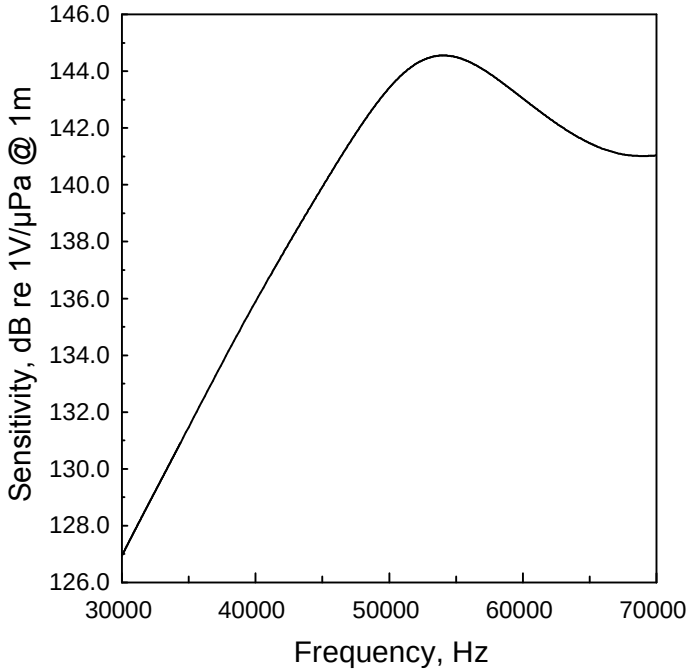

Figure 11.29. Predicted in-water acoustic response (no glue joints).

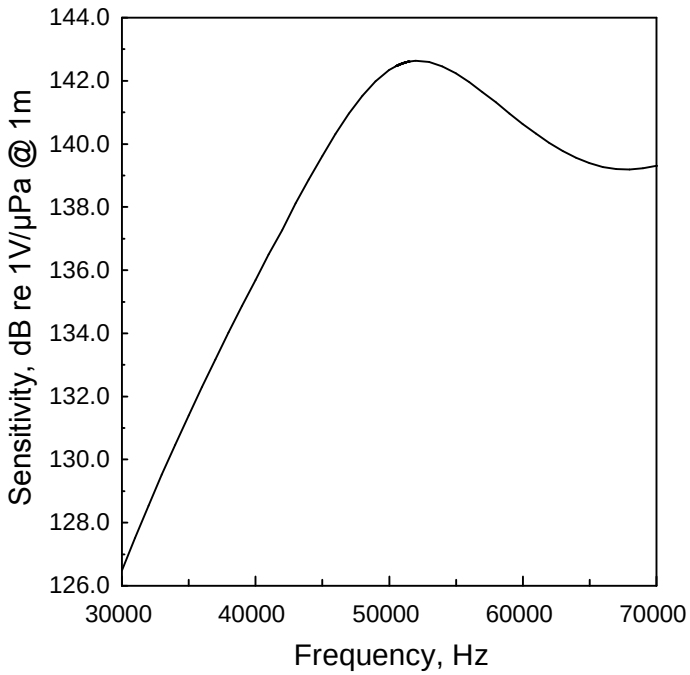

Figure 11.30. Predicted in-water acoustic response (with glue joints).

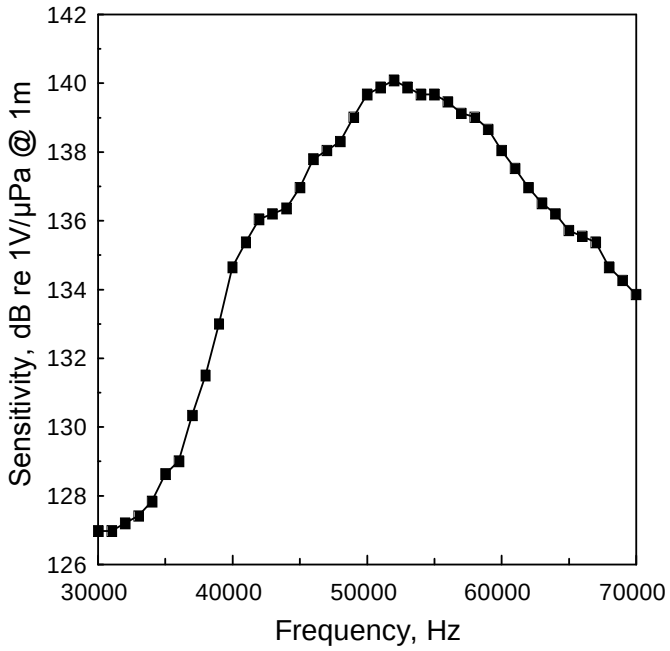

Figure 11.31. Measured in-water acoustic response.

Having found an approximate value for DI it is possible to estimate of the efficiency of the transducer. A value of 63 % was calculated. This may seem to be rather low but it must be noted that the calculation of efficiency is very sensitive to measurement errors. Also the 'O'-ring seal, not included in the model, between the head of the transducer and the housing will have some damping effect, reducing the radiated power and lowering efficiency.

Table 11.6 summarises the performance characteristics derived from the theoretical and measured acoustic responses.

Table 11.6. Parameters determined from the predicted and measured in-water acoustic responses.

Parameter	Theoretical value		Experimental value
	(no glue joints)	(glue joints)	
f	54.0 kHz ± 25 Hz	52.0 kHz ± 25 Hz	52.0 kHz ± 500 Hz
Q	3.1	3.0	3
S	144.6 dB re 1 V/μPa @ 1 m	142.6 dB re 1 V/μPa @ 1 m	140.1 dB re 1 V/μPa @ 1 m
DI	9.5 dB	9.9 dB	8.4 dB
η_{ea}	98.9 %	96.6 %	63 %

11.4.4 Thermal Behaviour

Using the software modules developed by the author it is possible to extend the numerical examination of the behaviour of the transducer. We can now investigate the power dissipated in each component of the transducer, arising from mechanical, piezoelectric, and dielectric losses. With this information we can calculate the steady-state temperature profile of the transducer.

Using LETO to calculate the power dissipated in the transducer, the efficiency was found to be 99.1 % for no glue joints and 95.9 % with glue joints. This is approximately the same as those calculated by PHOEBE (98.9 % and 96.5 %) where the efficiency is determined from the ratio of acoustic power output to electrical power input. Quantitative values of losses for the two models are given in tables 11.7 and 11.8. It may be noted that piezoelectric losses are not listed. This is because reliable data for piezoelectric loss factors are not currently available. However, the facility to model this type of loss has been included in the software so that it may be taken into account when such data become available.

The mechanical loss in each component would be expected to be proportional to the amplitude of vibration, volume of material, and the damping factor. This is indeed the case. Without glue joints most of the losses occur in the ceramic stack. This is to be expected since the stack experiences the largest deformation per cycle and also has the highest damping factor. With the inclusion of the glue joints the effect is stark. Almost 80 % of the losses in this model are caused by the glue joints.

Table 11.7. Predicted percentages of power dissipated in the various components of the transducer (no glue joints)

Component	Percentage of power dissipated		
	Mechanical	Dielectric	Total
Ceramic	63.49 %	23.36 %	86.85 %
Glue joints	—	—	—
Head	10.02 %	—	10.02 %
Tail	3.13 %	—	3.13 %

Table 11.8. Predicted percentages of power dissipated in the various components of the transducer (with glue joints)

Component	Percentage of power dissipated		
	Mechanical	Dielectric	Total
Ceramic	12.44 %	5.44 %	17.88 %
Glue joints	79.50 %	—	79.50 %
Head	2.02 %	—	2.02 %
Tail	0.60 %	—	0.60 %

In order to calculate the temperature profile of the transducer we need to known the thermal conductivity of the various components that make up the device. These are listed in table 11.9.

Finally, the boundary conditions need to be specified. The radiating face of the transducer is in contact with water and hence heat will be lost by convection at this surface. This is the third type of boundary condition, as listed in Chapter 10, Section 10.3, where the flow of heat is proportional to the temperature difference between the surface of the body and the surroundings. The flow of heat from the radiating face into the surrounding water depends on the heat-transfer coefficient. If the average value of this coefficient is taken to be representative over the surface of the radiating face then the methods described in Appendix A can be used determine its value. Since the transducer was mounted such that its face is perpendicular to the water surface, this face can be treated as a vertical plate, where the characteristic length is assumed to be equal to the square root of the surface area of the radiating face. In Appendix A several different empirical relationships are listed that are suitable for calculating the average heat-transfer coefficient from a vertical plate, the value of which depends on the fluid temperature, taken to be 25 °C, and the surface temperature of the radiating face, which is proportional to the excitation voltage.

Table 11.9. Thermal conductivities of the transducer materials.

Part	Material	Thermal conductivity ($W\ m^{-1}\ K^{-1}$)
Ceramic	PZT-4™	2.1
Glue joint	Araldite	0.5
Tail	Mild Steel	43.0
Head	Aluminium	177.0

Table 11.10. Average heat-transfer coefficient for various input voltages.

Peak input voltage (V)	Average heat-transfer coefficient† ($W\ m^{-2}\ K^{-1}$)	
	(no glue joints)	(with glue joints)
500	384.1	510.6
600	413.2	549.2
700	439.5	612.8
800	463.6	645.6

† calculated using equation (A.2).

Table 11.10 lists the values of this coefficient calculated using equation (A.2) for various input voltages. The rest of the transducer is surrounded by a thin layer of air. Within such small layers of air only very small convection currents are likely to occur and the heat will mostly be lost by conduction. Since the thermal conductivity of air is very low the heat loss from these surfaces will be negligible and it is therefore reasonable to treat these surfaces as being insulated.

Figure 11.34 shows the general temperature profile of the transducer at thermal equilibrium. It can be seen that the speed at which heat is conducted through the various components of the transducer is important in determining the ultimate temperature within the transducer. In the case of the Tonpilz transducer the ceramic stack between the head and tail acts as a insulator. Thus, the highest temperature is observed in the tail. On the other hand, the temperature of the head is only a few degrees above the water temperature. This is because any heat within the head is quickly conducted to the radiating surface. Thus, the temperature of the head is determined by the rate at which heat is lost through convection; that is, the average heat-transfer coefficient.

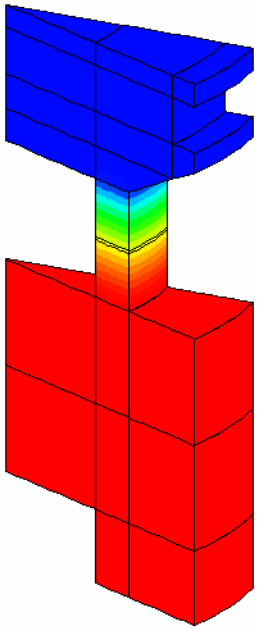

Figure 11.32. Predicted temperature profile at resonance (temperatures depend on drive voltage).

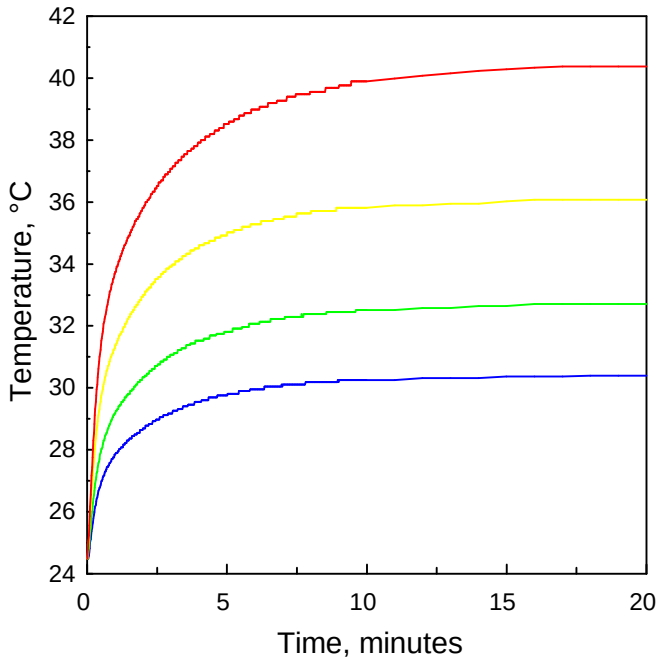

Figure 11.33. Measured thermal response at resonance for various input voltages. Red—800 V peak. Yellow—700 V peak. Green—600 V peak. Blue—500 V peak.

Table 11.11. Predicted rise in temperature, above the ambient temperature, at the mid point on the outer surface of the stack, for various input voltages.

Peak input voltage (V)	Temperature rise (°C)	
	(no glue joints)	(with glue joints)
500	4.22	19.93
600	5.93	28.25
700	7.92	37.60
800	10.18	48.62

Table 11.12. Maximum predicted rise in temperature, above the ambient temperature, within the transducer for various input voltages.

Peak input voltage (V)	Temperature rise (°C)	
	(no glue joints)	(with glue joints)
500	5.24	20.80
600	7.40	29.49
700	9.92	39.30
800	12.78	50.84

Table 11.13. Measured rise in temperature, above the ambient temperature, at the mid point on the outer surface of the stack, for various input voltages.

Peak input voltage (V)	Change in temperature (°C)
500	6.00
600	8.10
700	11.28
800	15.18

Table 11.14. Percentage error between the predicted and measured rise in temperature, above the ambient temperature, at the mid point on the outer surface of the stack, for various input voltages.

Peak input voltage (V)	Percentage error	
	(no glue joints)	(with glue joints)
500	–30 %	232 %
600	–27 %	248 %
700	–30 %	233 %
800	–33 %	220 %

Table 11.11 lists the temperature rise at the mid point, on the outer surface of the stack, for various input voltages. Table 11.12 lists the maximum temperature rise within the transducer, for the same input voltages.

In order to validate the theoretical steady-state temperature rise of the 50 kHz transducer a temperature probe was mounted at the mid point, on the outer surface of the stack. The transducer was driven at its resonance frequency by a pure sine wave, over a time period long enough for thermal equilibrium to be reached (20 minutes), and the thermal evolution recorded, starting from the water temperature (24.5 °C). The experiment was performed for input voltages of 500, 600, 700, and 800 V peak. Figure 11.33 shows the measured thermal evolution for the different input voltages and table 11.13 records the corresponding temperature rise at thermal equilibrium.

Table 11.14 compares the accuracy of the theoretical results with the measured results. The comparison shows that, like the admittance values, the model without glue joints under predicted the rise in temperature while the model with glue joints resulted in an over prediction; in the worst cases the errors are –34 % and 248 % for models without and with glue joints respectively.

It may be noted that an estimate of the efficiency of the transducer can be made from the thermal results, by recognising that the ratio of the measured to predicted temperature rise is equal to the ratio of the measured to predicted power dissipated within the transducer. For this to be true we have to assume that the heat generated within the transducer is only lost through convection into the water (a reasonable assumption) and the convection heat-transfer coefficient is identical to that used in the finite element calculations (minor discrepancies are tolerable). The power dissipated in the transducer P_i is given by

$$P_i = \left(1 - \eta_{ea}\right) v^2 G_{max} \tag{11.2}$$

where η_{ea} is the electro-acoustic efficiency, v is the r.m.s. input voltage, and G_{max} is the peak in-water conductance at resonance. Thus, the ratio of measured to predicted temperature rise is

$$\frac{T(measured)}{T(predicted)} = \frac{\left[1 - \eta_{ea}(measured)\right]}{\left[1 - \eta_{ea}(predicted)\right]} \frac{G_{max}(measured)}{G_{max}(predicted)} \tag{11.3}$$

Re-arranging in terms of $\eta_{ea}(measured)$ we get

$$\eta_{ea}(measured) = 1 - \left[1 - \eta_{ea}(predicted)\right] \frac{T(measured)}{T(predicted)} \frac{G_{max}(predicted)}{G_{max}(measured)} \qquad (11.4)$$

Now, substituting the values into equation (11.4) we find $\eta_{ea}(measured)$ = 0.983 using the theoretical value from the model without glue joints, and $\eta_{ea}(measured)$ = 0.986 from the other model.

The efficiency calculated from the thermal results (98.3 % to 98.6 %) is within the range of the theoretical efficiency (99.1 % without and 97.8 % with glue joints) and much higher than the acoustically measured efficiency (63 %). This would suggest that the previously measured efficiency at resonance is somewhat under its true value.

The above analysis is based on the premise that the data for the thermal conductivities of the materials is accurate, in particular the thermal conductivity of the piezoelectric ceramics. However, manufacturing tolerances for piezoelectric ceramics are known to be wide (standard tolerances of ±20 % are typically quoted by manufacturers). This may be fairly significant, particularly when we consider that the temperature in the 50 kHz Tonpilz transducer depends rather critically on the thermal conductivity of the piezoelectric ceramics.

11.2.5 Power Limitations

Electrical limit—Using an electrical field limit of 200 kV r.m.s. m^{-1} [11.7], where the thickness of the piezoelectric ceramics rings is 3 x 10^{-3} m, the limiting voltage v_{max} = 600 V r.m.s.

Cavitation limit—From equation (9.2) we can define a relationship for the minimum depth below which cavitation is likely to occur; that is,

$$h = 10\left(\sqrt{\frac{P_{max}}{I_c(0)A}} - 1\right) \qquad \text{for } P_{max} \geq I_c(0)A \qquad (11.5)$$

where $I_c(0)$ is the cavitation threshold at the surface, P_{max} is the maximum acoustic power radiated by the transducer and A is area of the radiating surface. The maximum acoustic power output, P_{max}, can be expressed as

$$P_{max} = \exp_{10}\left(\frac{\mathrm{S} + 20\log_{10}(v_{max}) - \mathrm{DI} - 170.9}{10}\right) \tag{11.6}$$

Using the values for projector voltage sensitivity, S, and directivity index, DI, listed in table 11.6, the power output is found; P_{max}(*predicted – no glue joints*) = 94.7 W, P_{max}(*predicted – with glue joints*) = 94.7 W, and P_{max}(*measured*) = 40.4 W. Then from figure (9.2) the cavitation threshold at resonance frequency is determine; $I_c(0)$ = 3 W cm^{-2} @ 50 kHz. Finally, substituting the appropriate values into equation (11.4) the minimum operating depth is found; *h*(*theoretical – no glue joints*) = 15.1 m, *h*(*theoretical – with glue joints*) = 12.8 m, and *h*(*measured*) = 6.4 m.

Thermal limit—the highest temperature reach within the transducer is below any critical temperature where damage might be done for drive voltages up to at least the recommended limit (for a water temperature of up to at least 25 °C and a limiting voltage of 600 V r.m.s.).

11.5 A 2.5 kHz Flextensional Transducer

In this section the previous analysis of the 2.5 kHz partially free-flooded flextensional transducer presented in Chapter 8 is extended to include its thermal behaviour.

11.5.1 Thermal Behaviour

The methodology used to analyse the thermal behaviour of the 2.5 kHz partially free-flooded flextensional transducer follows that used for the 50 kHz Tonpilz transducer.

The power dissipation in the transducer can be calculated using LETO. It is found that the efficiency is 97.8 %, a value slightly higher than that calculated by PHOEBE (97.2 %). The percentage loss in each component is listed in table 11.15. Significantly, most of the power is dissipated in the foam region, indicating that it is absorbing a lot of acoustic power.

It was speculated in Chapter 8 that the major cause of loss in the transducer was due to the compliant region, and this theory is now substantiated. The other components conform to the trend previously seen with the Tonpilz transducer.

Once again, in order to calculate the unknown temperature we need to know the thermal conductivities of the various components of the transducer (these are listed in table 11.16) and the boundary conditions. The boundary conditions for the flextensional are slightly more difficult to calculate than for the Tonpilz transducer. An empirical formula does not exist for this complex shape. However, there are relationships for other geometries which will serve as a good a approximation. For example, the flextensional transducer can be treated as a vertical cylinder, an irregular solid, or a sphere. It was found that the various different formulae gave very similar values for the average heat-transfer coefficient at a given voltage: however the chosen geometry was the sphere. The average heat-transfer coefficient for various input voltages are listed in table 11.17.

Figure 11.34 shows the temperature profile of the transducer at thermal equilibrium. Table 11.18 lists the temperature rise at the centre point, on the surface of the plate at the foam interface, for various input voltages. Table 11.19 lists the maximum temperature rise within the transducer, for the same input voltages.

In order to validate the predicted steady-state temperature rise of the flextensional transducer a temperature probe was mounted at the mid point, on the outer surface of the stack. The transducer was driven at its resonance frequency by a pure sine wave, over a time period long enough for thermal equilibrium to be reached (5 hours), and the thermal evolution recorded, starting from the water temperature (17 °C). The experiment was performed for input voltages of 500, 600, 700, and 800 V peak. Figure 11.35 shows the measured thermal evolution for the different input voltages and table 11.20 records the corresponding temperature rise at thermal equilibrium.

Table 11.21 compares the accuracy of the theoretical results with the measured results. The comparison shows that the model has under-predicted the temperature observed in the transducer, in the worst case the error is -77 %.

Table 11.15. Predicted percentages of power dissipated in the various components of the transducer.

Component	Percentage of power dissipated		
	Mechanical	Electrical	Total
Ceramic	10.51 %	2.68 %	11.19 %
Glue joints	24.91 %	—	24.91 %
Insulators	0.47 %	—	0.47 %
End-plates	0.05 %	—	0.05 %
Staves	4.66 %	—	4.66 %
Foam	55.52 %	—	55.52 %
Cavity fluid	1.20 %	—	1.20 %

Table 11.16. Thermal conductivities of the transducer materials.

Part	Material	Thermal conductivity ($W\ m^{-1}\ K^{-1}$)
Ceramic	PZT-4™	2.1
Glue joints	Araldite	0.5
Insulators	MACOR™	1.46
End-plates	Stainless steel	20.0
Staves	Aluminium	177.0
Foam	D300	0.048
Cavity fluid	Water	0.6

Table 11.17. Average heat-transfer coefficients for various input voltages.

Peak input voltage (V)	Average heat-transfer coefficient[†] ($W\ m^{-2}\ K^{-1}$)
500	108.8
600	116.6
700	123.7
800	130.2

[†] Calculated using equation (A.7).

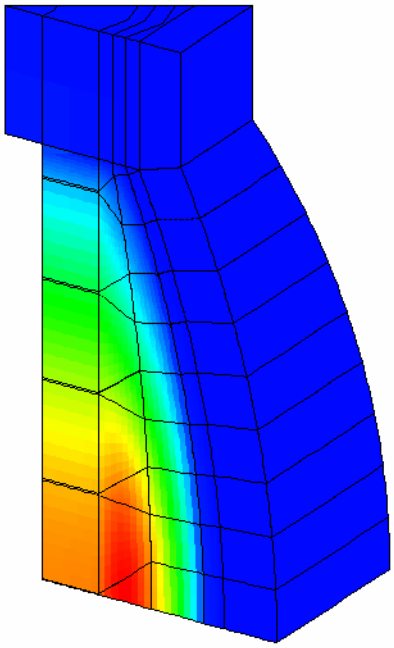

Figure 11.34. Predicted temperature profile at resonance (temperatures depend on drive voltage).

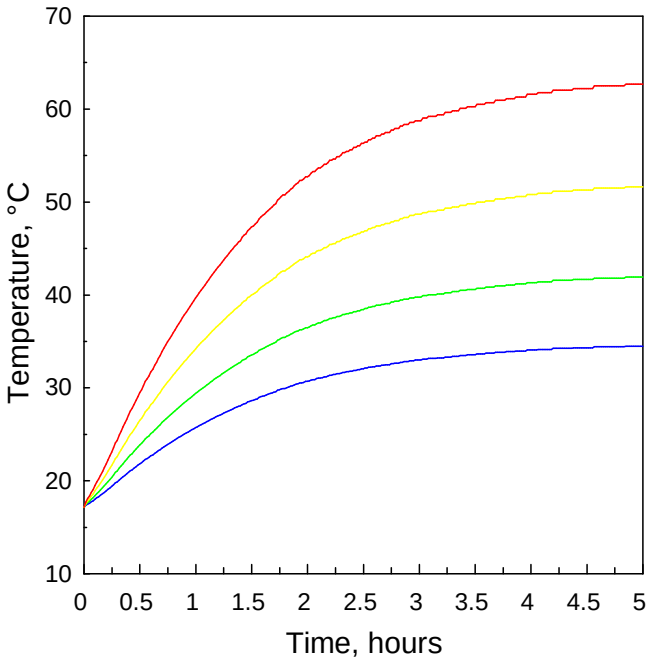

Figure 11.35. Measured thermal response at resonance for various input voltages. Red—800 V peak. Yellow—700 V peak. Green—600 V peak. Blue—500 V peak.

Table 11.18. Predicted rise in temperature, above the ambient temperature, at the mid point on the outer surface of the stack, for various input voltages.

Peak input voltage (V)	Temperature rise (°C)
500	4.10
600	5.90
700	8.02
800	10.47

Table 11.19. Maximum predicted rise in temperature, above the ambient temperature, within the transducer for various input voltages.

Peak input voltage (V)	Temperature rise (°C)
500	4.67
600	6.72
700	9.13
800	11.92

Table 11.20. Measured rise in temperature, above the ambient temperature, at the mid point on the outer surface of the stack, for various input voltages.

Peak input voltage (V)	Change in Temperature rise (°C)
500	17.35
600	24.78
700	34.50
800	45.54

Table 11.21. Percentage error between the predicted and measured rise in temperature, above the ambient temperature, at the mid point on the outer surface of the stack, for various input voltages.

Peak input voltage (V)	Percentage error
500	–76 %
600	–76 %
700	–77 %
800	–77 %

As before, the efficiency of the transducer can estimate from the thermal results. From table 8.6 we have G_{max}(*predicted*) = 413 μS and from table 8.10 G_{max}(*measured*) = 135 μS, and earlier in this section we determined η_{ea}(*predicted*) = 0.978. Then, from table 11.18, for an input voltage of 500 V peak, *T*(*predicted*) = 4.10 °C, and from table 11.20, for the corresponding input voltage, *T*(*measured*) = 17.35 °C. Proceeding in the same manner as for the Tonpilz transducer, we substitute these values into equation (11.4) and find η_{ea}(*measured*) = 0.715.

The efficiency calculated from thermal measurements (71.5 %) is much better than previously estimated, although it is still much worse than predicted (97.8 %). This over-estimation of the efficiency of the device is the major source of error between the predicted and measured temperature rise. It is suspected that the true damping factor in the foam is higher than that used in the numerical model.

11.5.2 Power Limitations

Electrical limit—Using an electrical field limit of 200 kV r.m.s. m^{-1} [11.7], where the thickness of the piezoelectric ceramics rings is 6 x 10^{-3} m, the limiting voltage v_{max} = 1200 V r.m.s.

Cavitation limit—Proceeding in the same manner as for the Tonpilz transducer, the predicted results indicate that the power output would be cavitation-limited at depths less than 3.4 m. However, the measured results show that the transducer will not cavitate at any depth.

Thermal limit—The recommended maximum continuous operating temperature for Plasticell foams is 60 °C. The predicted results indicate that the temperature rise within the transducer will not be great enough to effect the foam at drive voltages up to at least 800 V peak. However, from the measured results it can be seen that the free-flooded flextensional transducer with the foam insert is thermally limited. The exact thermal limit is difficult to predict from the measured results since we only know the temperature rise at the mid point, on the outer surface of the stack. The theoretical results imply that the temperature in the foam would be slightly higher than that found in the stack. Assuming, as predicted, that the temperature in the foam is hotter than in the stack it is estimated that the applied input voltage should certainly not exceed 800 V peak

(assuming a water temperature of 17 °C) if the transducer is to be used under CW operating conditions for extended periods of time.

From figure 11.35 we see that the transducer would have to be driven under CW operating conditions for a considerable length of time before the temperature rise becomes significant. For short periods of time the transducer would therefore be electrical limited. As the operation time is increased the input voltage must be reduced in order to prevent the transducer reaching its thermal limit. Further development of LETO would enable the evolution of the temperature with time to be studied in more detail and provide a prediction of the voltage limit for a given operating time.

11.6 Conclusions

In this chapter two transducers have been modelled using the finite element and boundary element software, PHOEBE, in conjunction with the thermal software, LETO. Varying degrees of success were achieved. In each case the resonance frequency of the transducer was accurately predicted. However, the numerical models produced mixed results for the values of quality factor, efficiency, acoustic power, and temperature rise.

For the 50 kHz Tonpilz transducer the theoretical results showed good cohesion with experimental measurements. Due to the difficulty of predicting the thickness of the glue joints in the transducer it was modelled with and without glue joints for comparison purposes. The model without glue joints underestimated the damping in the structure while the other model resulted in an overestimation.

Thermal analysis for the 2.5 kHz partially free-flooded flextensional transducer has been presented. The flextensional transducer revealed a limitation of the thermal software. The software relies on the user to determine the heat-transfer coefficient at surfaces where convection occurs. The coefficient can be calculated only for simple geometries for which empirical relationships are known. For complex geometries the most appropriate empirical relationship has to be selected. However, in many cases a minor error in the estimation of the heat-transfer coefficient does not result in a serious miscalculation of the temperature rise in the transducer. The thermal results suffered from insufficient damping in the numerical model.

The thermal analysis revealed that the Tonpliz transducer would not be thermally limited under CW operation, but rather cavitation-limited at shallow depths (15.1 metres predicted from the numerical model without glue joints, 12.8 metres predicted from the numerical model with glue joints, 6.4 metres estimated from measurements), and electrically limited at greater depths. The predicted results for the free-flooded flextensional transducer indicated that it would be cavitation-limited at depths less than 3.4 metres and electrically limited at greater depths. However, since the transducer was significantly less efficiency than predicted it was found that it was actually thermally limited under CW operation.

Although the thermal rise for the two transducers was not very accurately predicted, the results were of the same order as the measurements, and the differences could be accounted for. Thus, the software gives the user a reasonable idea about the thermal behaviour of the transducer, which is sufficiently reliable to determine if the transducer will be thermally limited under CW operation.

A key reason for the differences has been identified as the level of damping in transducer structures, and this is suggested as an important subject for further research. In particular, better knowledge of the damping properties of materials is desirable.

For applications where the transducer is required to be driven continually for a period of time it is more important to know the transient behaviour of the transducer; that is, the speed at which the temperature rises when power is applied, and how quickly the temperature is dissipated when the power is removed. For example, from the experimental measurements it was observed that the 50 kHz Tonpliz transducer heated up very quickly, while the temperature evolution in the 2.5 kHz partially free-flooded flextensional transducer was considerably slower.

To predict the transient behaviour of a transducer the finite element problem would have to be solved in the time domain. Implementation of this method would allow the properties of the materials to be updated as the temperature within the various materials changed. To do so, PHOEBE and the LETO would be used in a user controlled loop. First the displacements at the nodes would be calculated and from these the heat sources. Then, the transient thermal evolution could be computed, and at this point the material properties would be updated and the displacements at the nodes and the heat sources recalculated. The calculation of the thermal

evolution would be continued from the previous end point. This process would be repeated until thermal stability is reached, or the required operating time had expired, or a maximum limit was reached in one or more of the materials.

Implementation of a time-domain solution was beyond the time constraints of this thesis.

11.7 References

[11.1] J. R. Dunn, 'Some Aspects of Transducer Design by Finite Element Techniques', in *Progress in Underwater Acoustics*, H. M. Merklinger, ed., (Plenum Press, 1987), 639-645.

[11.2] W. Hahnemann and H. Hecht, 'Die Grundform des mechanisch-akustischen Schwingungskörpers. (Der Tonpilz.)', *Physik. Zeitschr.*, 21, 187-192, (1920).

[11.3] D. Stansfield, *Underwater Electroacoustic Transducers*, (Bath University Press and Institute of Acoustics, 1990), Chapters 7 and 8.

[11.4] D. Stansfield, *Underwater Electroacoustic Transducers*, (Bath University Press and Institute of Acoustics, 1990), 182.

[11.5] R. J. Bobber, *Underwater Electroacoustic Measurements*, (Naval Research Laboratory, 1970), Chapter 2.

[11.6] D. Stansfield, *Underwater Electroacoustic Transducers*, (Bath University Press and Institute of Acoustics, 1990), 160-162.

[11.7] D. Stansfield, *Underwater Electroacoustic Transducers*, (Bath University Press and Institute of Acoustics, 1990), 183-184.

Chapter 12

CONCLUSIONS AND FURTHER WORK

12.1 Conclusions

In this thesis the application and development of finite element techniques for the design and analysis of underwater acoustic transducers has been reported. The research has been motivated by the lack of suitable low-frequency transducers with the required performance characteristics for applications in ocean acoustic tomography.

Before embarking on the design and modelling work a number of possible technologies were investigated. First, motor technologies that could potentially drive a flextensional transducer were reviewed. Suitable materials must be able to expand or contract under the control of an external stimulus, thus converting input energy into acoustic output energy. Three such materials were explored; namely, piezoelectric, electrostrictive, and magnetostrictive materials. The suitability of each material was assessed and consequently piezoelectric ceramics were chosen as the preferred materials. The main benefit of electrostrictive and magnetostrictive materials over piezoelectric materials was the higher power output. However, as the required power output was not excessive and in light of the difficulty of implementing these materials, due to their non-linear behaviour, they were rejected in favour of piezoelectric ceramics. A further reason for selecting piezoelectric ceramics is their comparative low cost and ease of availability.

Thereafter, a selection of flextensional transformer technologies were considered for suitability as an ocean acoustic tomography sound source. Of particular interest was the class I flextensional transducer, otherwise known as the ‘barrel-staved’ flextensional. The shape of the device means that it is readily suited to arrangement in a vertical line array to achieve horizontal directivity and so reduce unwanted acoustic energy transmission to the ocean floor and sea surface. It was also anticipated that of all the flextensional designs the class I transducer would offer the best chance of meeting the depth requirements.

A study of the literature revealed that there is an insufficient understanding of the workings of the class I flextensional transducer. Although the transducer has been previously investigated using a theoretical approach in the 1960s, very little further analysis of the design has been reported since then. More accurate predictions can be obtained from finite element modelling, which has not been used in a comprehensive study of the mechanical behaviour of the class I design, although it has been extensively applied to class IV and V flextensional transducers. Thus, accurate design criteria have not been developed for the class I flextensional transducer, as it has been for the other two classes.

The finite element (FE) approach combined with the boundary element (BE) method provides a detailed description of the structural and acoustic performance of a transducer. This method has been used to assist in the design process; although computationally intensive it has allowed a much broader design scope than would have been feasible with a purely empirical approach. The numerical software, PHOEBE, has been applied to the study class I flextensional transducers, with a view to establishing some basic design rules. Both slotted-shell and staved-shell profiles have been investigated where the ultimate goal has been to achieve low-frequency, high-power, and high-efficiency performance from a small and lightweight device.

A rigorous examination of the influence of the various design parameters on the transducer's performance has been undertaken. More specifically, the shell material, the number of staves or slots, the thickness and curvature of the shell, and the radius at the end of the transducer have been investigated.

Numerical analysis using the FE method coupled with the BE method led to an increased understanding of the general principles that govern the operation of class I flextensional transducers. The ability to study the effects of design changes illustrates the power of the numerical method in assisting in the design process. It was seen that the performance characteristics of a class I flextensional transducer are governed chiefly by the material properties and thickness and curvature of its shell. For a particular shell thickness there is a corresponding curvature for achieving optimum quality factor. The optimum number of slot or staves would appear to be 8 when considering performance gain and ease of manufacturing. Finally the end-plate should be stiffer than the shell for good coupling between stack and shell, and as small as possible in order to reduce weight.

Using the results from the modelling process a design for an ocean acoustic tomography transducer was developed that met the frequency, quality factor, acoustic power, and efficiency requirements, but failed to achieve the specified weight and operating depth. However, the device was only marginally overweight and hence was not considered to be a problem.

To validate the theory a 5 kHz air-backed class I flextensional transducer based on a scaled version of the ocean acoustic tomography design was assembled. The device was rigorously tested and the measured characteristics were found to compare very well with the values predicted from finite element and boundary element calculations. The discrepancy between the theoretical and experimental results was attributed to the differences between the numerical model and the prototype device, these being due to the simplifications applied to the finite element model in order to reduce its complexity and the variation of material properties from their expected values.

The initial research focused on an air-backed transducer design which is only capable of working down to a depth of approximately 100 metres. The specification for an ocean acoustic tomography source requires an operational depth in excess of 500 metres. Thus, a means of providing depth capability had to be considered. Two methods were thought to be appropriate for the class I flextensional transducer geometry: (a) operating the transducer as a free-flooded device, with the inclusion of compliant tubes to reduce the internal impedance; (b) operating the transducer as a free-flooded device, using a compliant material, such as a closed-cell foam, to partially fill the interior in order to reduce the internal loading on the shell. Both of these options favoured the use of a convex shell profile since it enabled a greater volume of compliant material to be fitted into the cavity, helping to restore performance. The latter method was selected as it was thought to offer simpler and cheaper construction.

FE and BE calculations revealed that partially free-flooding the transducer had the effect of increasing the resonance frequency, while reducing the quality factor, acoustic power output, and efficiency. The large increase in resonance frequency was significant since a much larger device would be required to realise a frequency of 500 Hz. This being the case, the weight requirement could not be achieved. However, with the exception of weight, the transducer design satisfied all the requirements of an ocean acoustic tomography sound source, assuming scaling laws can be applied.

On the basis of the numerical results a 2.5 kHz partially free-flooded class I flextensional transducer was constructed. Testing of the device confirmed the theoretical results, although the agreement was not as good as it had been for the air-backed transducer. This greater divergence between the results is to be expected since the structure of the transducer is more complex and difficult to model. The discrepancy between the theoretical and experimental results was also attributed to the variation of material properties from their expected values.

By scaling the measured performance characteristics of the 2.5 kHz partially free-flooded class I flextensional transducer, it was possible to make a tentative assessment of the suitability of the transducer for use as an ocean acoustic tomography sound source. The results suggested that a device resonating at 500 Hz and operating at 500 m would have a Q-factor much lower than 4, and a source level way in excess of 190 dB re. 1 μPa @ 1 m. However, the transducer would also be marginally less efficient than desired, and the weight would be over three times greater than the specification value.

Thus, the coupled FE and BE method has enabled the design of a class I flextensional transducer that could be used as an ocean acoustic tomography source to be developed. The design was implemented and subsequent testing verified the numerically-predicted performance characteristics. A simple but effective pressure compensation system has been used that will allow the transducer to operate down to depths of at least 500 metres, significantly greater than conventional air-backed designs that are limited to approximately 100 metres. The device is omnidirectional with a high acoustic power output. Furthermore, the device is extremely broad band.

In the modelling work described, the acoustic power output of the transducer was assumed to be limited by the maximum electrical field that could be safely applied to the ceramic stack, a valid assumption for most transducers. However, the power output might alternatively be limited by cavitation, mechanical failure, or thermal failure, any of which would impose a limit on the maximum drive field that could be employed. In order to accurately determine the maximum acoustic power output of the transducer it was essential to determine which limitation applied.

At a depth of 500 metres the maximum acoustic intensity before the onset of cavitation is approximately 867 W cm^{-2}. Thus, we can safely rule out cavitation. Mechanical failure is usually associated with high frequency transducer designs where excessive dynamic stresses cause fatigue failure. Depending on the transducer design, the failure will most likely occur within a ceramic element or at the joining between two materials. For low frequency transducers, problems of mechanical failure at glue joints within the stack of the transducer are avoided by using a centre bolt to apply a compressive force strong enough to prevent the stack from going into tension, even at maximum drive levels. Since a centre bolt has been fitted to the transducer we can also neglect the likelihood of mechanical failure. Heating of the transducer due to mechanical losses and also piezoelectric and dielectric losses within the ceramics is usually only significant when high-duty-cycle or CW operation is required. For ocean acoustic tomography applications extremely-low-duty-cycle operation is required (for example, a 10 millisecond pulse every hour) and therefore thermal limitations within the transducer will not be encountered. Thus, the original assumption that the transducer is electrically limited is valid.

The investigation of the performance of the class I flextensional transducer and the subsequent development of the design has been biased towards the requirements of an ocean acoustic tomography source. However, the results presented in this thesis apply equally to other applications that might suit the flextensional transducer. An important area is that of long-range communications transducers, where low-frequency and wide-bandwidth are beneficial performance characteristics. Even though the propagation losses at low frequencies are low, a high power capability is desirable for long-range operation since the signal-to-noise ratio is improved.

Communications application requires continuous operation of the transducer over long periods of time. Under such conditions losses within the transducer are more likely to be significant and the transducer may be thermally limited. To investigate this possibility new FE software was developed which extended the existing finite element and boundary element software, PHOEBE, so that it could take into account the generation and flow of heat under CW conditions. The new software allows the mechanical, piezoelectric, and dielectric power dissipation within a transducer to be determined. It also enables the steady-state temperature rise to be calculated. Thus, the new software, when used in conjunction with PHOEBE, makes it possible to determine if a

transducer will be thermally limited under CW operation. This enables the suitability of transducers for applications such as long-range communications to be determined.

Two types of transducer were modelled using the finite element and boundary element software, PHOEBE, in conjunction with the thermal software developed by the author; namely, a 50 kHz Tonpilz transducer and the previously described 2.5 kHz partially free-flooded class I flextensional transducer. The thermal behaviour of both transducers was reasonably accurately modelled and the discrepancies could be accounted for.

Thus, a FE treatment has been developed for predicting if a transducer will be thermal limited under CW operation. The method is based on the existing software, PHOEBE, and new software written by the author. PHOEBE calculates the electrical, mechanical, and acoustic behaviour of the transducer, while the author's software evaluates the heat dissipation and the resulting temperature rise. This procedure has been successfully applied to different transducer designs and the results have been verified experimentally.

In conclusion, it has been seen that FE techniques can be usefully employed in the design of underwater transducers. The accuracy of the method essentially depends on how well the FE model represents the actual transducer and the reliability of the material data available, especially the values of damping factors. In most cases it is necessary to simplify the model in some way, the level of which will depend on the complexity of the transducer, the frequency of operation, and the processing power of the computer used to solve the problem. When simplifications are necessary, it is up to the designer to decide how this can best be achieved; that is, which components can safely be removed or simplified without overly affecting the accuracy of the results.

12.2 Further Work

The research presented in this thesis offers a great potential for further work. More experimentation would be desirable to establish the true acoustic performance of the 2.5 kHz partially-free-flooded class I flextensional transducer at depth. Changes in the acoustic power output and efficiency of the transducer could be monitored with increasing depth so as to establish the effect that hydrostatic pressure has on the compliant foam region. However, this work would require a deep water location. The deepest locations in the UK are about 300 metres (for example, Loch Morar and Loch Ness) and sea depth greater than 500 metres only occur beyond the continental shelf. More suitable sites may be found in the Mediterranean, where sufficient depths are reached fairly close to the coast.

Further development of the partially free-flooded design is possible. In particular, alternative materials or methods for increasing the compliance of the cavity could usefully be explored. This might include the investigation of other foam materials or maybe compliant tubes. Another possibility is the use of either foam or tubes in conjunction with a compressible liquid fill.

The thermal work was concerned primarily with solving the problem of the steady-state temperature distribution within a transducer under continuous operation. This method could also be used to approximate the behaviour of transducers driven using pulsed transmission where the pulse cycle has repetition time much less than the time constant of the change in temperature. However, to calculate the transient behaviour the thermal FE problem would have to be solved in the time domain.

Another area for further work concerns the determination of the surface heat transfer coefficients that govern the rate at which heat is lost from the surface of the transducer by convection. In this thesis the natural convection coefficients have been determined from empirical relationships. However, coefficients can only be calculated for simple geometries for which empirical relationships are known, for more complex geometries an estimate must be made. It is envisaged that improved results would be achieved by employing a numerical treatment of natural convection heat transfer.

It is known that changes in temperature cause changes in the dimensions of materials. Thus, the heat generated within a transducer will result in thermomechanical stresses due to different rates of thermal expansion, either caused by variation in temperature within a material, or by materials with different thermal expansion coefficients. It is likely, in some cases (essentially high-frequency designs), that the addition of thermomechanical stresses and dynamic stresses could limit acoustic power output. FE methods could be implemented to calculate thermomechanical stresses.

Finally, one of the main hindrances to producing accurate numerical predictions was identified as being caused by a lack of reliable data on the properties of materials. Furthermore, the properties of many materials are stress- and temperature-dependent. Therefore, methods of accurately measuring characteristics of materials under a variety of conditions would be extremely beneficial.

Appendix A

EMPIRICAL RELATIONS FOR FREE CONVECTION

A.1 Introduction

The average heat-transfer coefficient $\bar{h}$ is given by

$$\bar{h} = \frac{k}{x}\overline{\mathrm{Nu}} \tag{A.1}$$

where k is the thermal conductivity of the fluid, $\overline{\mathrm{Nu}}$ is the average Nusselt number of the fluid, and x is the characteristic length of the boundary surface.

The value of $\overline{\mathrm{Nu}}$ for free convection can be determined from empirical relations[†]. A simple relationship is,

$$\overline{\mathrm{Nu}} = C\,\mathrm{Ra}^{m} \tag{A.2}$$

where Ra is Rayleigh number of the fluid, and C and m are constants which depend on the geometry of the problem and the magnitude of Ra (see table A.1).

Other relations for the average Nusselt number are as follows.

Vertical planes and cylinders:

$$\overline{\mathrm{Nu}} = 0.68 + \frac{0.67\,\mathrm{Ra}^{1/4}}{\left[1+\left(0.492/\mathrm{Pr}\right)^{9/16}\right]^{4/9}} \qquad \text{for Ra} < 10^{9} \tag{A.3}$$

$$\overline{\mathrm{Nu}} = \left[0.825 + \frac{0.387\,\mathrm{Ra}^{1/4}}{\left[1+\left(0.492/\mathrm{Pr}\right)^{9/16}\right]^{8/27}}\right]^{2} \qquad \text{for } 10^{-1} < \text{Ra} < 10^{12} \tag{A.4}$$

where Pr is the Prandtl number of the fluid.

[†] J. P. Holman, *Heat Transfer*, 7th Edition, (McGraw-Hill Book Co., 1992), Chapter 7.

Table A.1. Constants for use with equation (A.2) for isothermal surfaces.

Ra	*C*	*m*
Vertical plates and cylinders Characteristic length = height of plate or length of cylinder		
$10^4 - 10^9$	0.59	$\frac{1}{4}$
$10^9 - 10^{13}$	0.10	$\frac{1}{3}$
Horizontal cylinders Characteristic length = diameter of cylinder		
$10^4 - 10^9$	0.53	$\frac{1}{4}$
$10^9 - 10^{12}$	0.13	$\frac{1}{3}$
Upper surface of heated plate or lower surface of cooled plate Characteristic length = square root of the surface area		
$2 \times 10^4 - 8 \times 10^6$	0.54	$\frac{1}{4}$
$8 \times 10^6 - 10^{11}$	0.15	$\frac{1}{3}$
Lower surface of heated plate or upper surface of cooled plate Characteristic length = square root of the surface area		
$10^5 - 10^{11}$	0.27	$\frac{1}{4}$
Vertical cylinder with height = diameter Characteristic length = diameter		
$10^4 - 10^6$	0.775	0.21
Irregular solids Characteristic length = distance fluid particle travels in boundary layer		
$10^4 - 10^9$	0.52	$\frac{1}{4}$

Horizontal cylinders:

$$\overline{\mathrm{Nu}} = 0.36 + \frac{0.518\,\mathrm{Ra}^{1/4}}{\left[1+\left(0.559/\mathrm{Pr}\right)^{9/16}\right]^{4/9}} \qquad \text{for } 10^{-6} < \mathrm{Ra} < 10^9 \qquad \text{(A.5)}$$

$$\overline{\mathrm{Nu}} = \left\{ 0.60 + 0.387 \left[\frac{\mathrm{Ra}}{\left[1+\left(0.559/\mathrm{Pr}\right)^{9/16}\right]^{16/9}} \right]^{1/6} \right\}^2 \qquad \text{for } 10^{-5} < \mathrm{Ra} < 10^{12} \qquad \text{(A.6)}$$

Spheres:

$$\overline{\mathrm{Nu}} = 2 + 0.50\,\mathrm{Ra}^{1/4} \qquad \text{for } 3 \times 10^5 < \mathrm{Ra} < 8 \times 10^8 \qquad \text{(A.7)}$$

In all cases the properties of these equations are evaluated at the film temperature T_f. The film temperature is the arithmetic mean between the temperature of the boundary surface and the surrounding fluid; that is,

$$T_f = \frac{T_\beta + T_\infty}{2} \tag{A.8}$$

where T_β is the temperature at the boundary and T_∞ is the temperature of the fluid.

The requirement is to evaluate the average heat-transfer coefficient at the boundary surface. First an estimate of the surface temperature T_β must be made. Re-arranging Newton's cooling law

$$q = \bar{h}A\left(T_\beta - T_\infty\right) \tag{A.9}$$

in terms of T_β, yields

$$T_\beta = \frac{q}{\bar{h}A} + T_\infty \tag{A.10}$$

where A is the surface area of the boundary and q is the heat-transfer rate. The value of q can be determined by noting that at thermal equilibrium the rate at which heat is generated must be equal to the rate at which heat is lost. Thus,

$$q = \left(1 - \eta_{ea}\right)v^2 G \tag{A.11}$$

where η_{ea} is the electro-acoustic efficiency, v is the r.m.s. input voltage, and G is the conductance. The value of the average heat-transfer coefficient has to be estimated. An approximate value of $\bar{h}$ for free convection in water is 500 W m^{-2} K^{-1}.

Calculating q and using the estimate for $\bar{h}$ it is possible to determine the approximate boundary-surface temperature T_β, and from this the approximate film temperature T_f. The Ra of water may then be calculated from

$$\mathrm{Ra} = \frac{g\beta\rho^2 c_p}{\mu k}\left(T_\beta - T_\infty\right)x^3 \tag{A.12}$$

where the value of $\dfrac{g\beta\rho^2 c_p}{\mu k}$ is determined at the film temperature (values listed in table A.2).

The next step is to determine $\overline{\mathrm{Nu}}$ using one of the equations listed that is appropriate to the geometry of the boundary surface. Depending on the formula used to calculate $\overline{\mathrm{Nu}}$, a value for Pr determined at the film temperature may be required (values listed in table A.2).

Table A.2. Properties of Water

Temperature (°C)	k (W m^{-1} K^{-1})	Pr	$\frac{g\beta\rho^2 c_p}{\mu k}$ (m^{-3} K^{-1})
4.44	0.575	11.35	1.91×10^{9}
10.00	0.585	9.40	6.34×10^{9}
15.56	0.595	7.88	1.08×10^{10}
21.11	0.604	6.78	1.46×10^{10}
26.67	0.614	5.85	1.91×10^{10}
32.22	0.623	5.12	2.48×10^{10}
37.78	0.630	4.53	3.30×10^{10}
43.33	0.637	4.04	4.19×10^{10}
48.89	0.644	3.64	4.89×10^{10}
54.44	0.649	3.30	5.66×10^{10}
60.00	0.654	3.01	6.48×10^{10}
65.55	0.659	2.73	7.62×10^{10}
71.11	0.665	2.53	8.84×10^{10}
76.67	0.668	2.33	9.85×10^{10}
82.22	0.673	2.16	1.09×10^{11}

Finally, substituting the values of the thermal conductivity k of water at the film temperature (values listed in table A.2), x, and $\overline{\mathrm{Nu}}$ into equation (A.1) a new value for the average heat-transfer coefficient $\bar{h}$ is found. The process can then be repeated until a suitable accuracy is achieved.

Appendix B

TECHNICAL DRAWINGS

B.1 5 kHz Air-backed Class I Flextensional Transducer.

B.2 2.5 kHz Free-flooded Class I Flextensional Transducer.

B.3 50 kHz Tonpilz Transducer.

Technical drawings of these transducers follows.

B.1 5 kHz Air-backed Class I Flextensional Transducer

A cross-section of the assembled transducer is shown in drg. no. F5k/1.

Components

1x Mild steel (AlSl-316) endplate1 (see drg. no. F5k/2)
1x Mild steel (AlSl-316) endplate2 (see drg. no. F5k/3)
8x Aluminium ($AlMgSi_3$) stave (see drg. no. F5k/4)
1x M8 Stainless steel (A2) stress bolt (see drg. no. F5k/5)

Standard components

8x PZT4™ ring, 20 mm O.D., 8 mm I.D., 6 mm thickness
2x MACOR™ ring, 20 mm O.D., 8 mm I.D., 2.4 mm thickness
16x M4 Stainless steel (A4 marine grade) countersink bolt, 8 mm thread
2x Eye hook

Other Materials

PFTE wire, grade ‘C’ insulation
Insulation tape
Monel 400 metal gauss, 48 swg
ARALDITE™, 2019

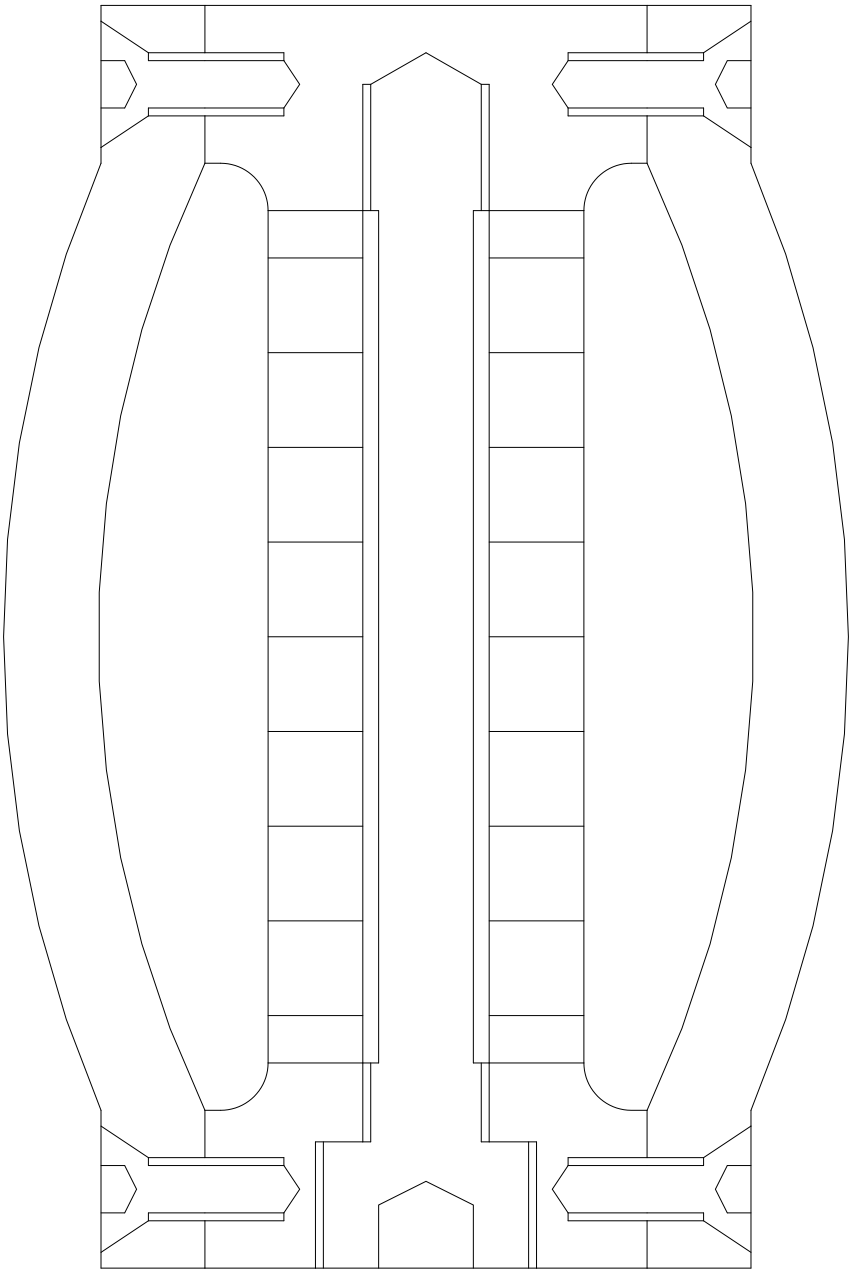

5 kHz FLEXTENSIONAL TRANSDUCER ASSEMBLY (DRG. NO. F5k/1)	CROSS-SECTION VIEW
	SCALE: 2 to 1

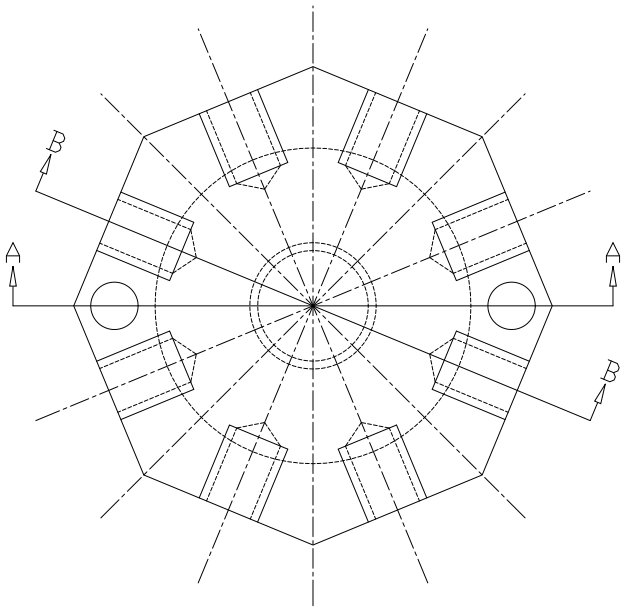

SECTION AA

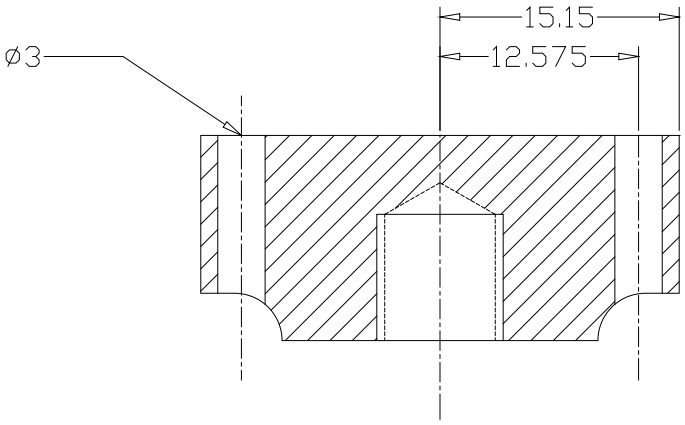

SECTION BB

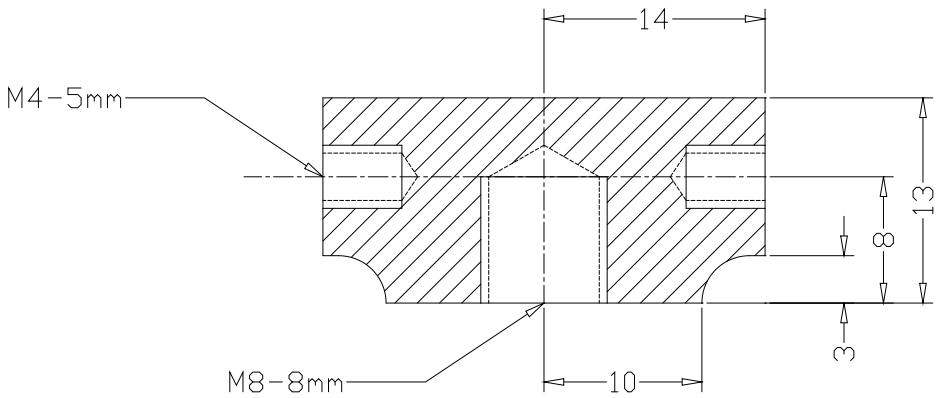

MILD STEEL

5 kHz FLEXTENSIONAL TRANSDUCER	DIMENSIONS IN MILLIMETRES
ENDPLATE1 (DRG. NO. F5k/2)	SCALE: 2 to 1

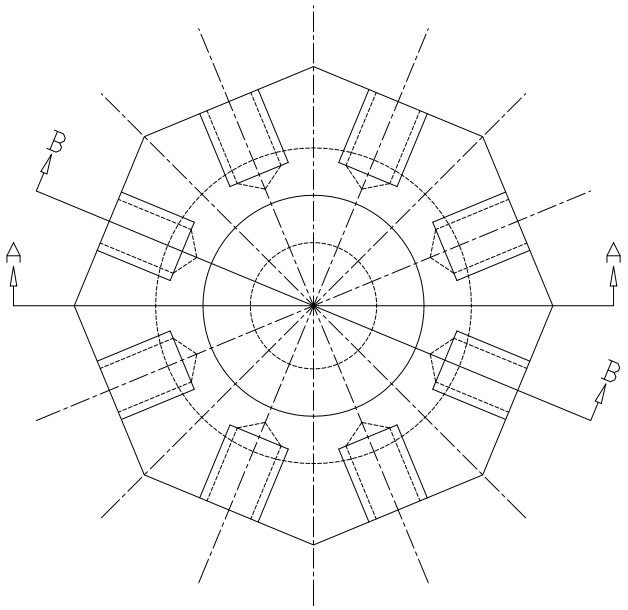

SECTION AA

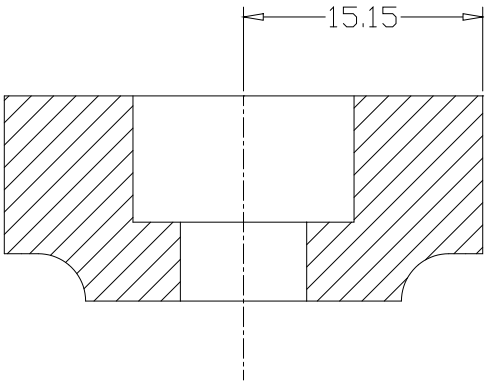

SECTION BB

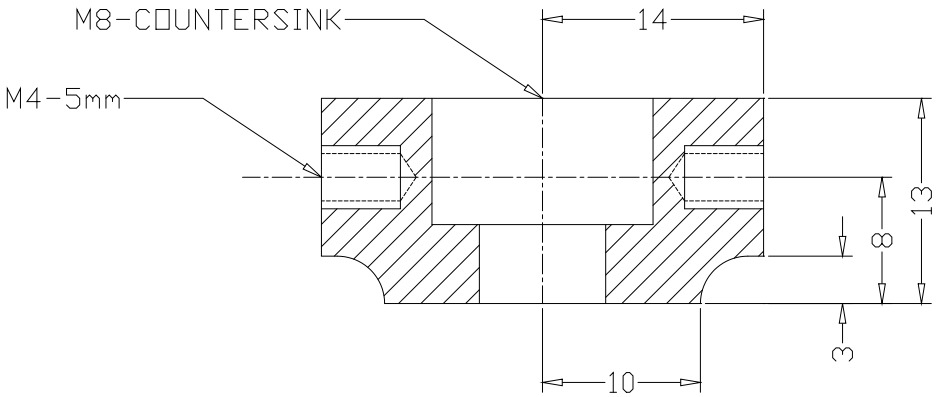

MILD STEEL

5 kHz FLEXTENSIONAL TRANSDUCER	DIMENSIONS IN MILLIMETRES
ENDPLATE2 (DRG. NO. F5k/3)	SCALE: 2 to 1

SECTION AA

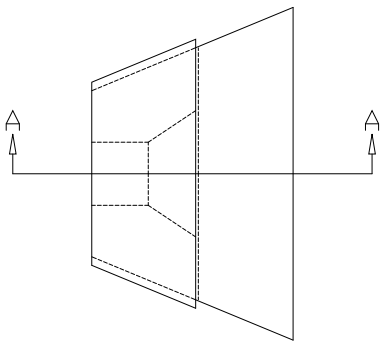

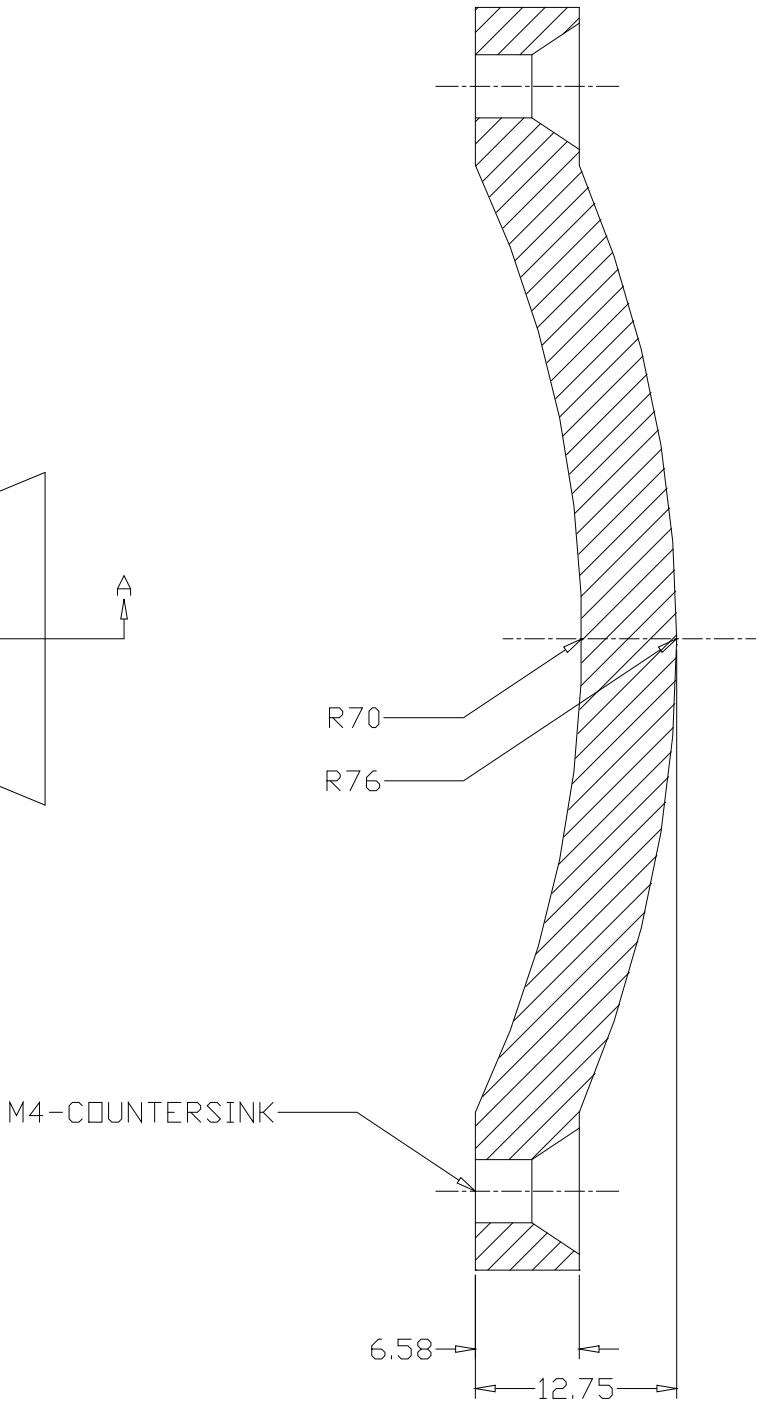

ALUMINIUM (HARD ANODIZED)

5 kHz FLEXTENSIONAL TRANSDUCER STAVE (DRG. NO. F5k/4a)	DIMENSIONS IN MILLIMETRES
	SCALE: 2 to 1

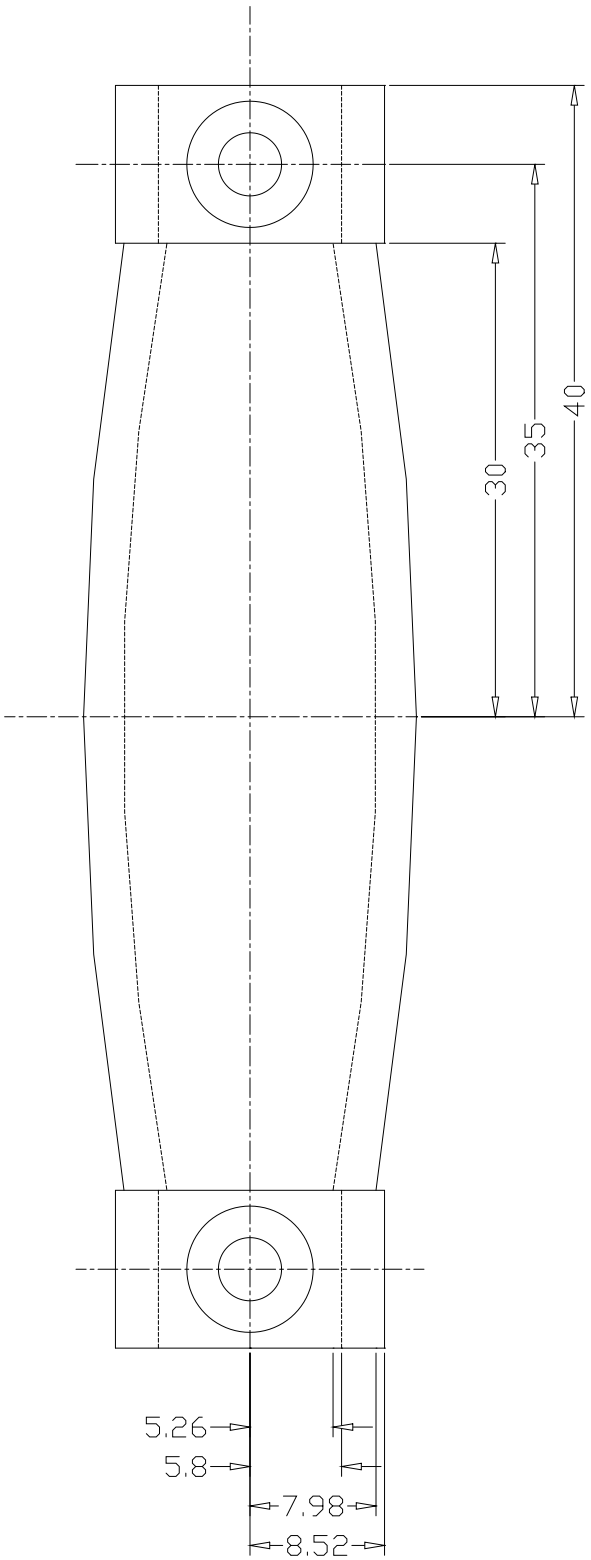

5 kHz FLEXTENSIONAL TRANSDUCER	DIMENSIONS IN MILLIMETRES
STAVE (DRG. NO. F5k/4b)	SCALE: 2 to 1

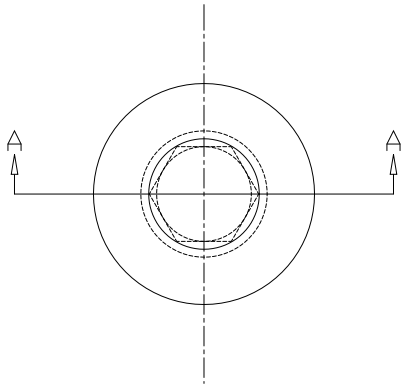

SECTION AA

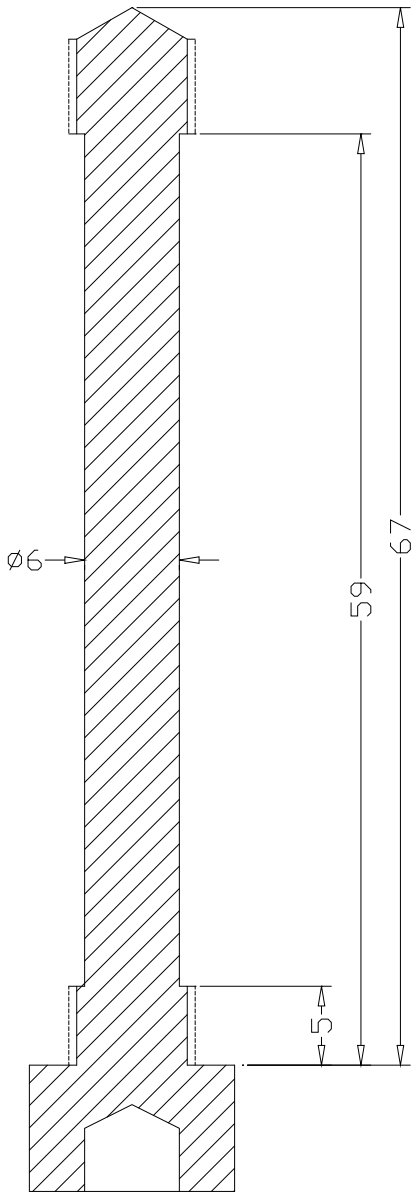

M8 STAINLESS STEEL CAP BOLT

5 kHz FLEXTENSIONAL TRANSDUCER BOLT (DRG. NO. F5k/5)	DIMENSIONS IN MILLIMETRES SCALE: 2 to 1

B.2 2.5 kHz Free-flooded Class I Flextensional Transducer

A cross-section of the assembled transducer is shown in drg. no. F2k5/1.

Components

1x Hard anodised aluminium (HE-30) cap1 (see drg. no. F2k5/2)
1x Hard anodised aluminium (HE-30) cap2 (see drg. no. F2k5/3)
1x Stainless steel (A4-316 marine grade) endplate1 (see drg. no. F2k5/4)
1x Stainless steel (A4-316 marine grade) endplate2 (see drg. no. F2k5/5)
8x Hard anodised aluminium (HE-30) stave (see drg. no. F2k5/6)
1x Foam (PLASTICELL™ D300) compliant region (see drg. no. F2k5/7)
1x Nylon tube, 20 mm O.D., 10 mm I.D., 170.5 mm length
1x M10 Stainless steel (A4 marine grade) studding, 240 mm length

Standard components

26x PZT4™ ring, 50 mm O.D., 20 mm I.D., 6 mm thickness
2x MACOR™ ring, 50 mm O.D., 20 mm I.D., 6 mm thickness
16x M6 Stainless steel (A4) cap bolt, 25 mm thread
16x M6 Stainless steel (A4) cap bolt, 30 mm thread
1x M12 Stainless steel (A4) Eye bolt
2x M10 Stainless steel (A4) washer
2x M10 Stainless steel (A4) nut
1x 4 pin WET-CON™
2x ‘O’ Ring, 31.6 mm I.D., 2.4 mm cross-section diameter

Other Materials

PFTE wire, grade ‘C’ insulation
Monel 400 metal gauss, 48 swg
ARALDITE™, 2019
SCOTCHCAST™

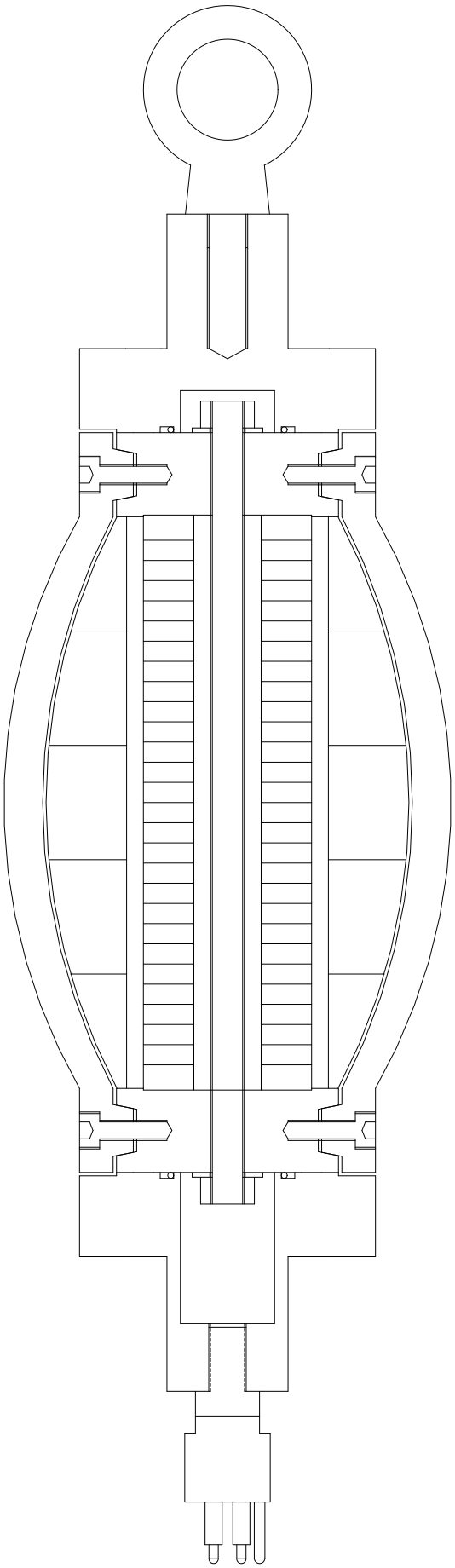

2.5 kHz FLEXTENSIONAL TRANSDUCER ASSEMBLY (DRG. NO. F2k5/1)	CROSS-SECTION VIEW
	SCALE: 1 to 2

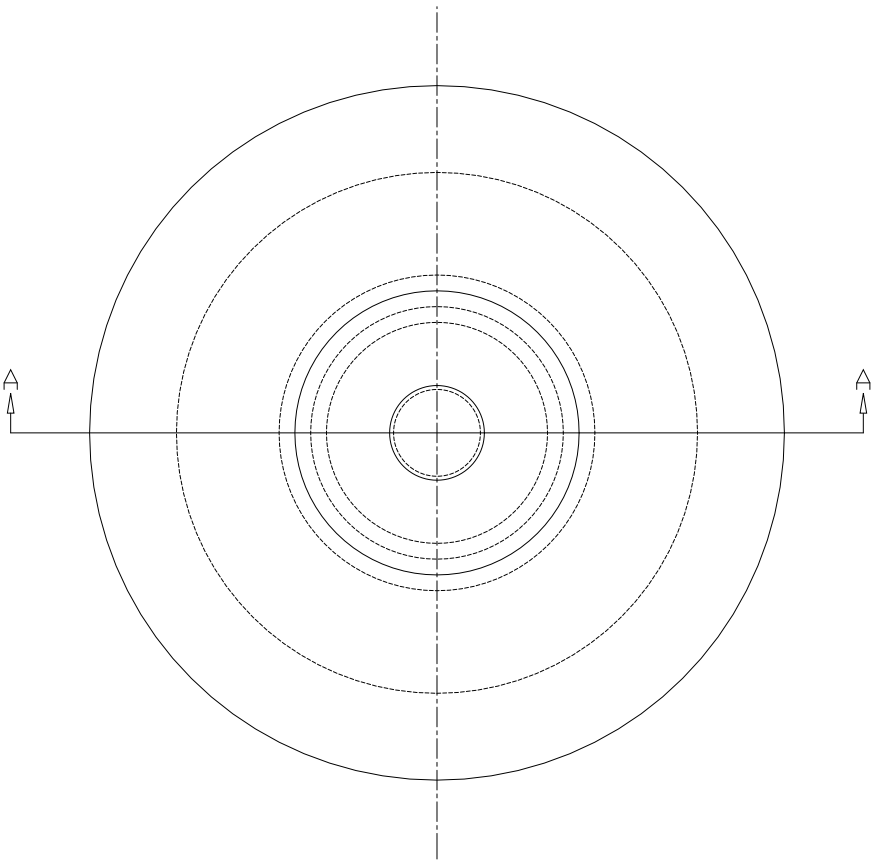

SECTION AA

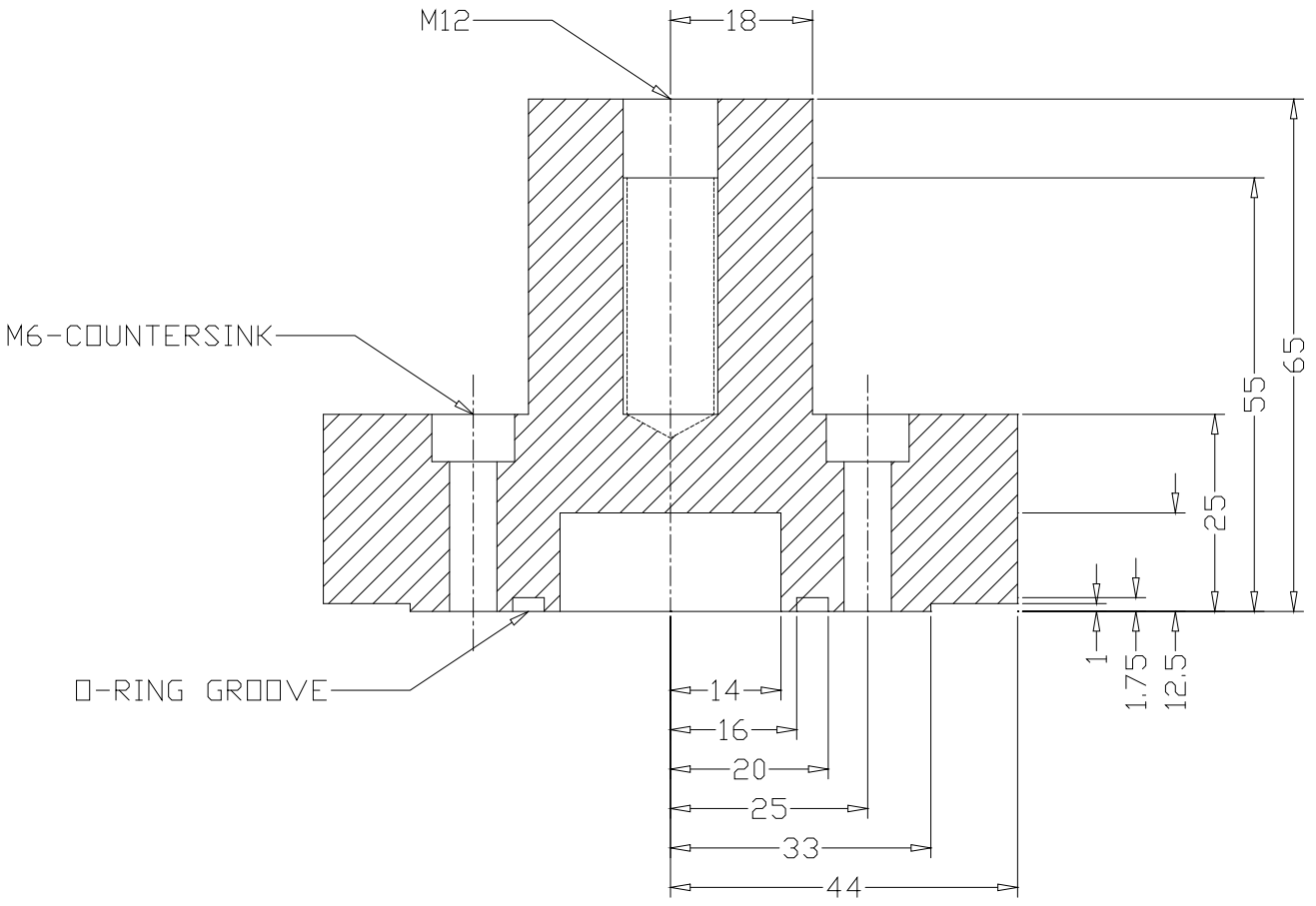

2.5 kHz FLEXTENSIONAL TRANSDUCER	DIMENSIONS IN MILLIMETRES
CAP1 (DRG. NO. F2k5/2)	SCALE: 1 to 1

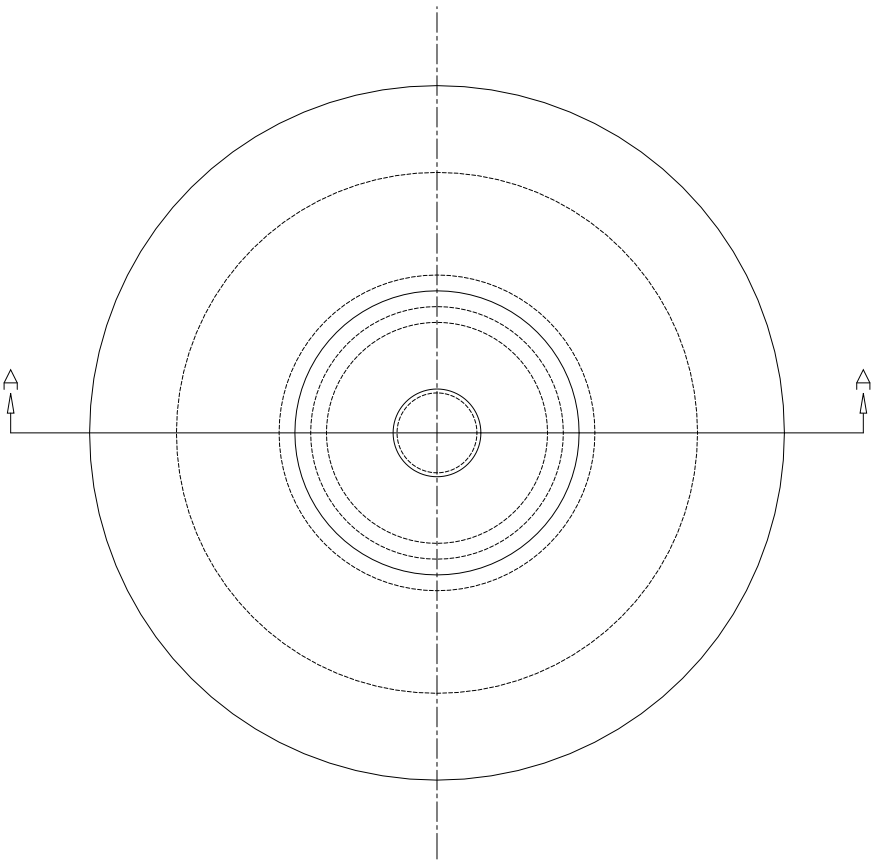

SECTION AA

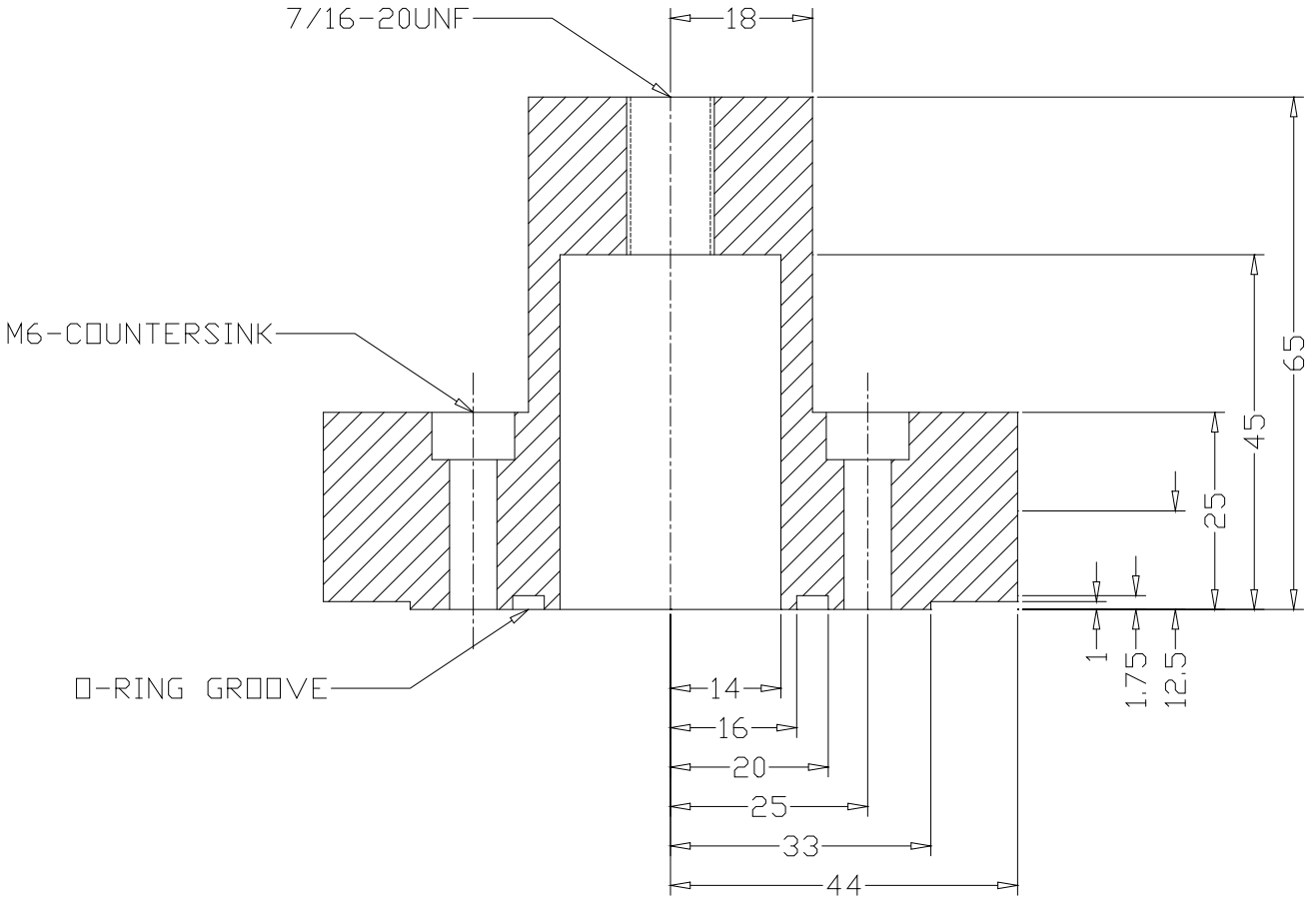

2.5 kHz FLEXTENSIONAL TRANSDUCER CAP2 (DRG. NO. F2k5/3)	DIMENSIONS IN MILLIMETRES SCALE: 1 to 1

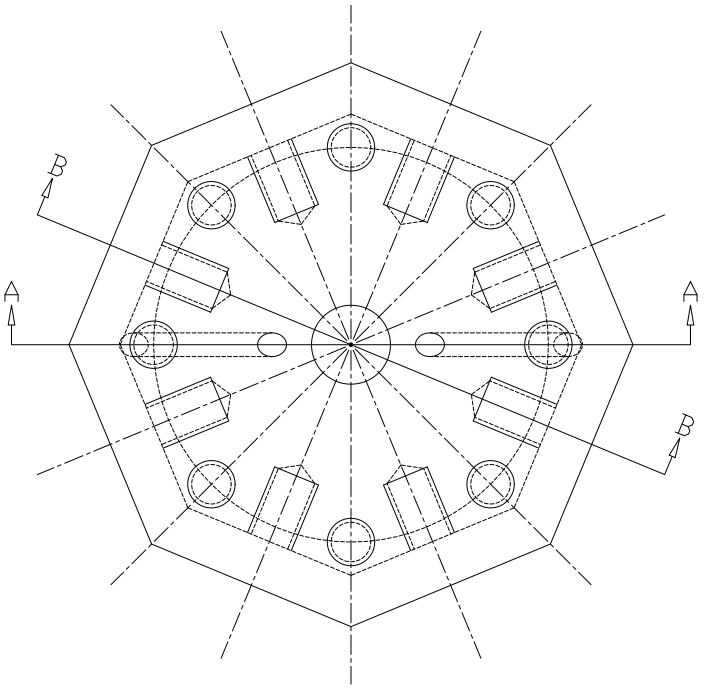

SECTION AA

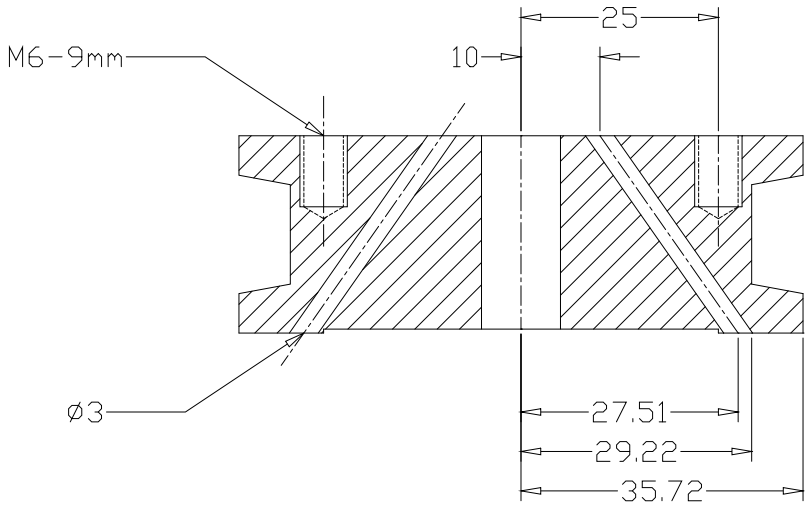

SECTION BB

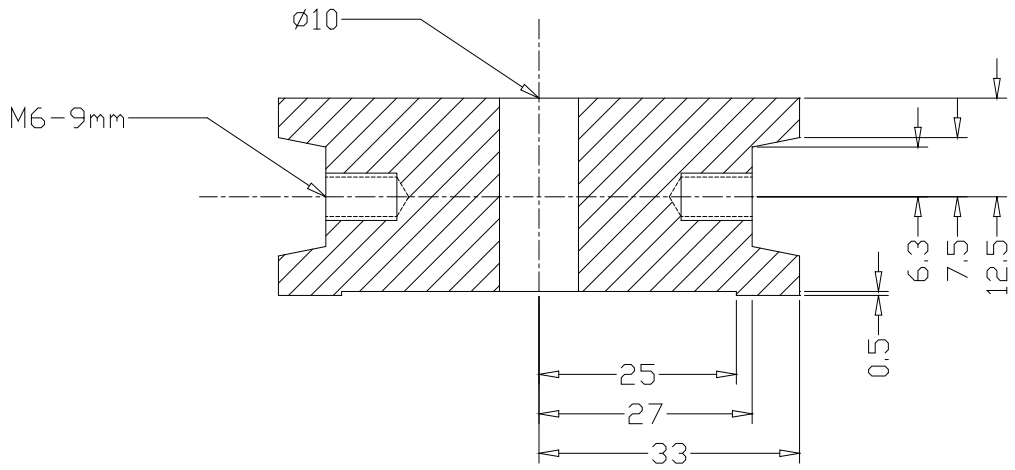

2.5 kHz FLEXTENSIONAL TRANSDUCER	DIMENSIONS IN MILLIMETRES
ENDPLATE1 (DRG. NO. F2k5/4)	SCALE: 1 to 1

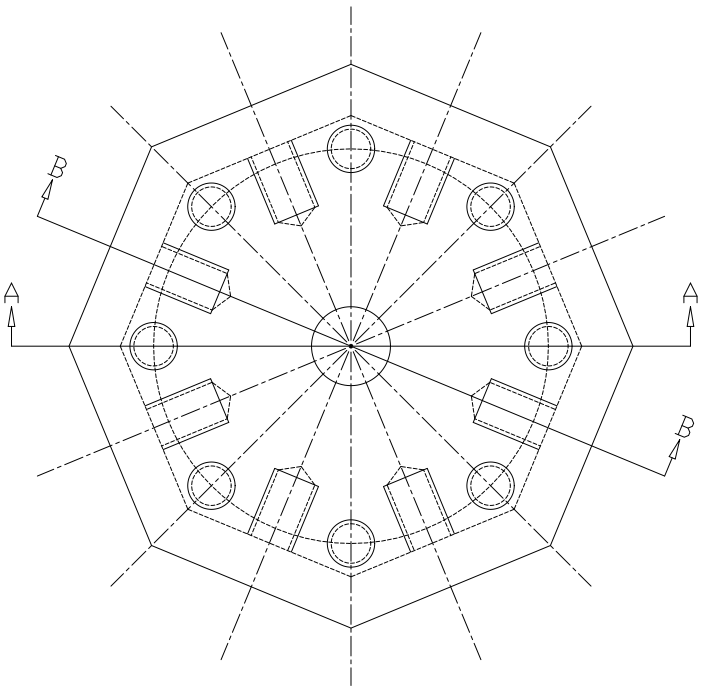

SECTION AA

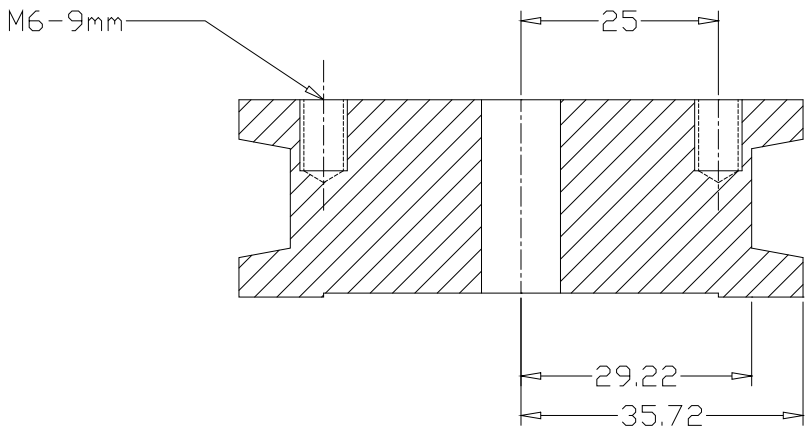

SECTION BB

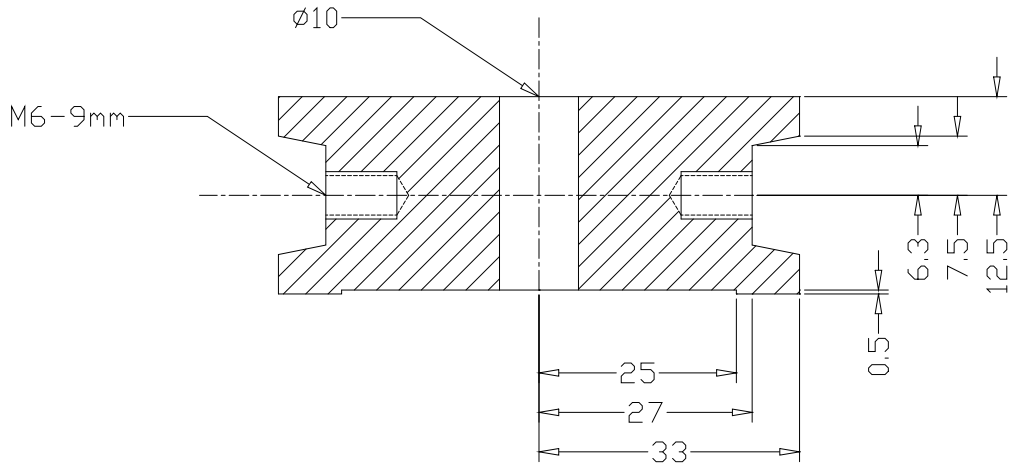

2.5 kHz FLEXTENSIONAL TRANSDUCER ENDPLATE2 (DRG. NO. F2k5/5)	DIMENSIONS IN MILLIMETRES SCALE: 1 to 1

SECTION AA

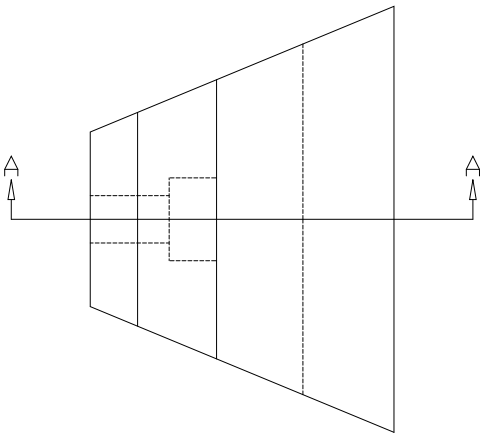

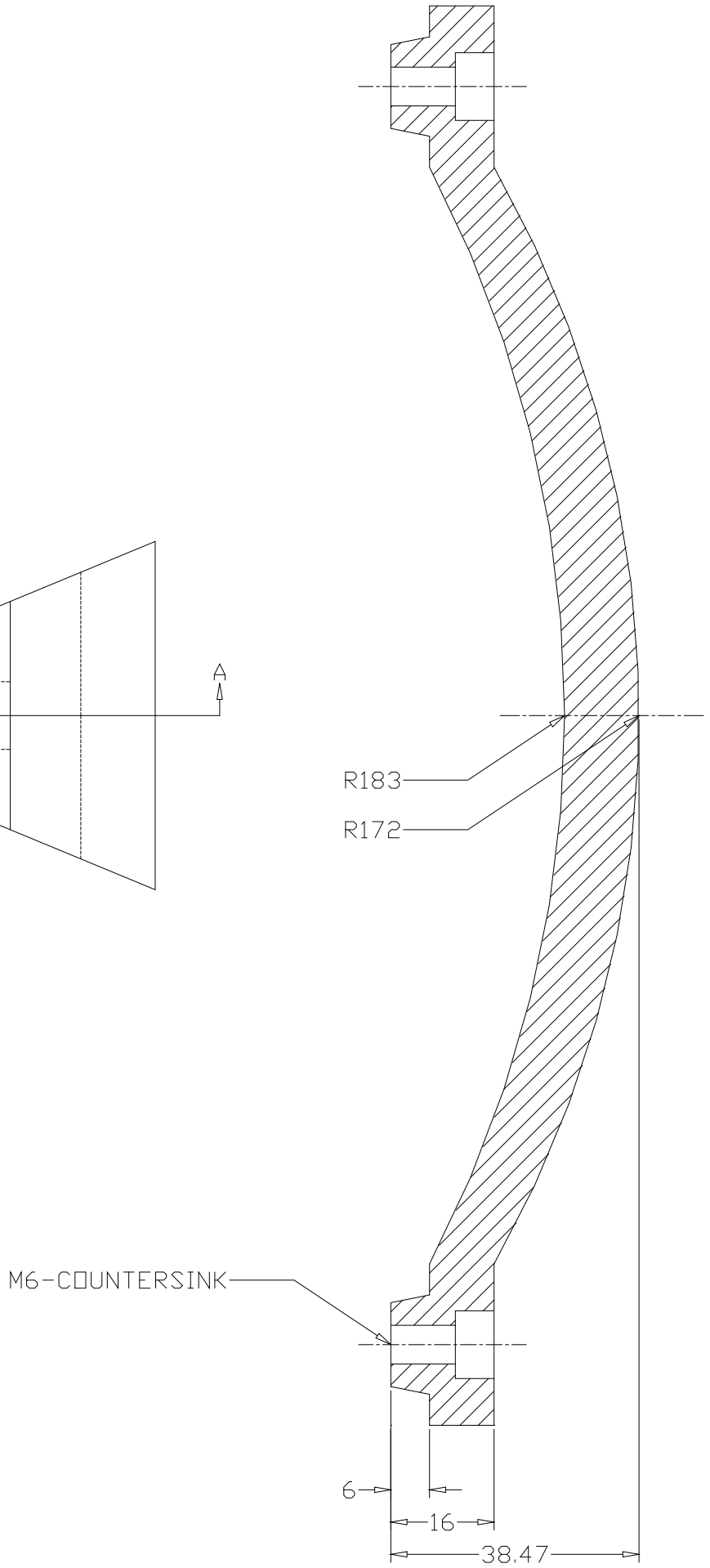

2.5 kHz FLEXTENSIONAL TRANSDUCER STAVE (DRG. NO. F2k5/6a)	DIMENSIONS IN MILLIMETRES
	SCALE: 1 to 1

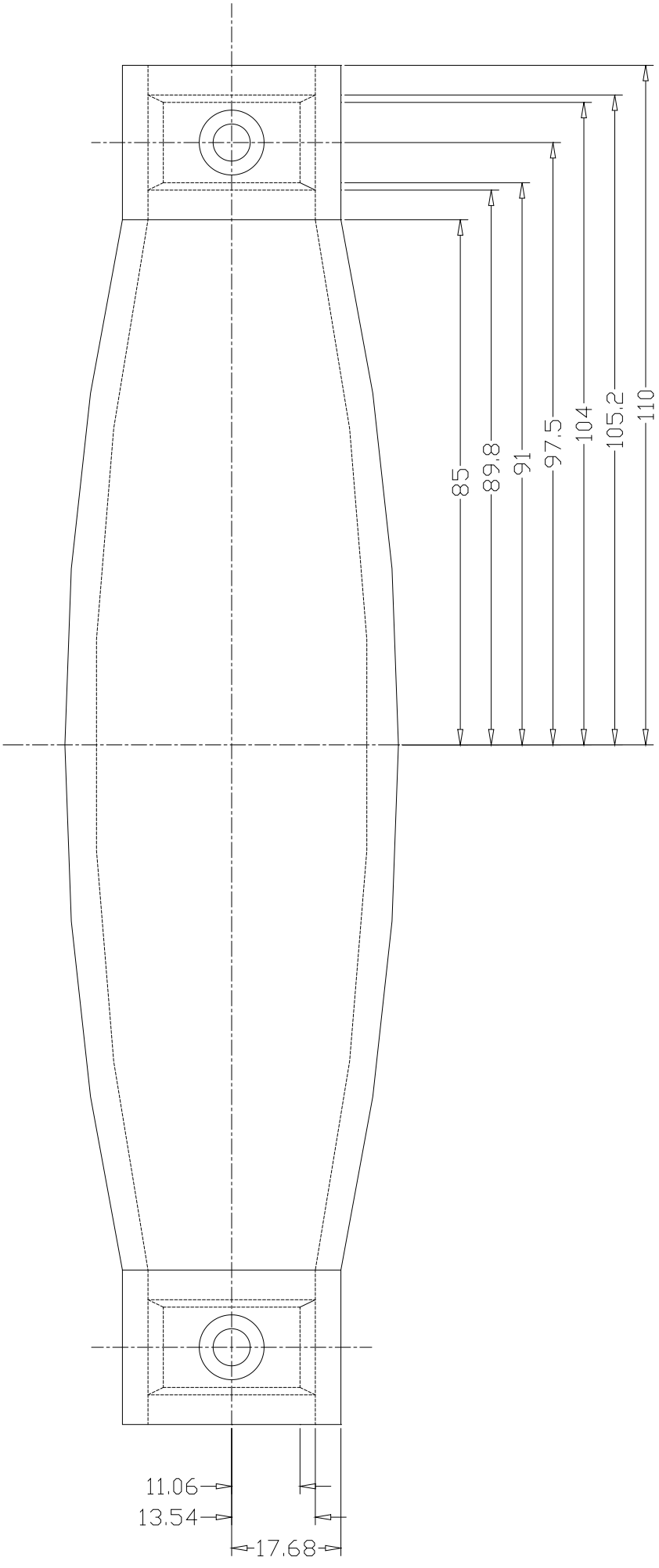

2.5 kHz FLEXTENSIONAL TRANSDUCER STAVE (DRG. NO. F2k5/6b)	DIMENSIONS IN MILLIMETRES
	SCALE: 1 to 1

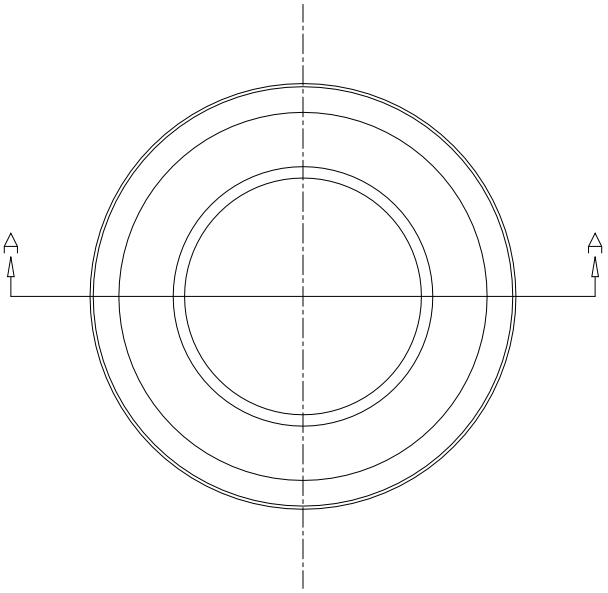

SECTION AA

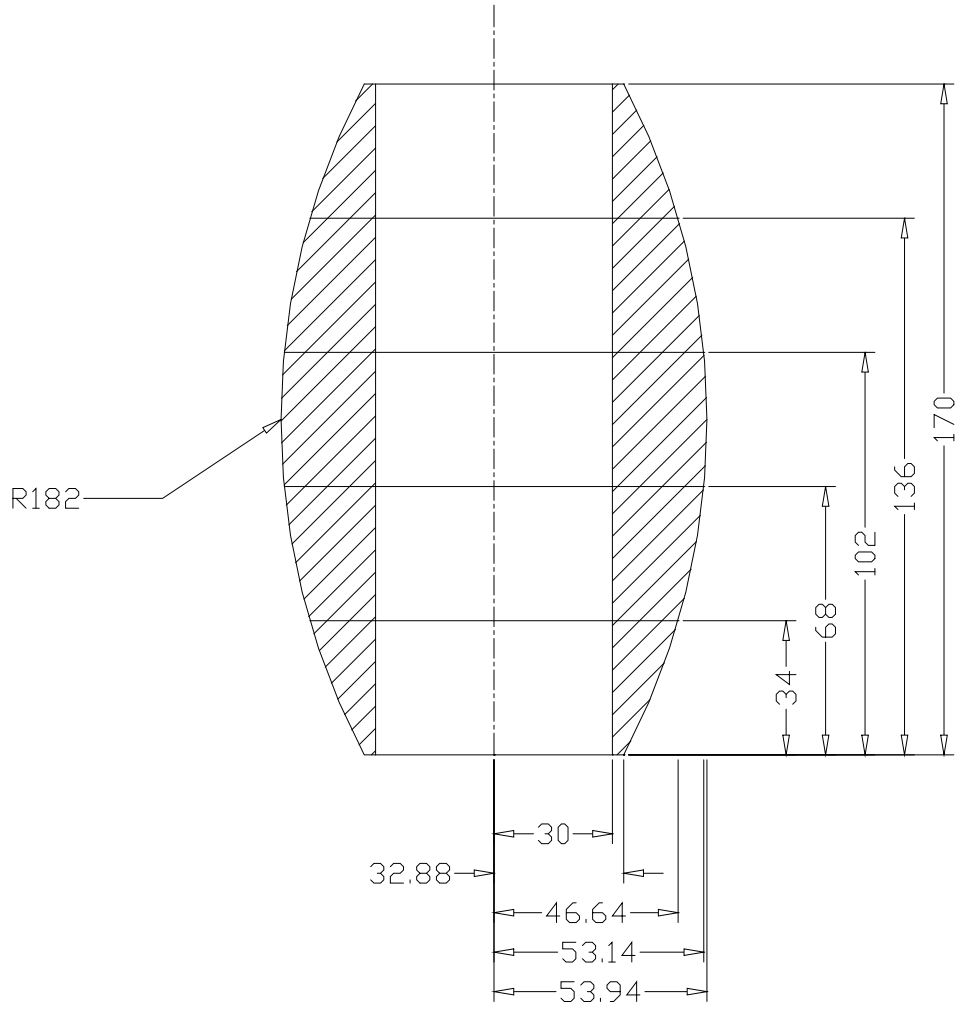

2.5 kHz FLEXTENSIONAL TRANSDUCER FOAM (DRG. NO. F2k5/7)	DIMENSIONS IN MILLIMETRES
	SCALE: 1 to 2

B.3 50 kHz Tonpilz Transducer

A cross-section of the assembled transducer and housing is shown in drg. no. T50k/1.
A cross-section of the assembled transducer is shown in drg. no. T50k/2.

Components

1x Hard anodised aluminium head (see drg. no. T50k/3)
1x 0.005" Brass shim (see drg. no. T50k/4)
1x Mild steel tail (see drg. no. T50k/5)
1x Stainless steel stud (see drg. no. T50k/6)
1x Hard anodised aluminium (HE-30) mounting (see drg. no. T50k/7)
1x Hard anodised aluminium (HE-30) cover (see drg. no. T50k/8)

Standard components

2x PZT4™ ring, 16.5 mm O.D., 12.0 mm I.D., 3.0 mm thickness
2x 4BA Stainless steel lock nut
1x 4BA Solder tag
2x Disc spring washer, 8 mm O.D., 4.2 mm I.D., 0.4 mm thickness, 0.6 mm free height
2x Disc spring washer, 25 mm O.D., 12.25 mm I.D., 1.2 mm thickness, 2.0 mm free height
4x M4 Stainless steel cap bolt, 20 mm thread
1x 4 pin WET-CON™
1x ‘O’ Ring, 0.864" I.D., 0.07" cross-section diameter
1x ‘O’ Ring, 1.987" I.D., 0.103" cross-section diameter

Other Materials

PFTE wire, grade ‘B’ insulation
Insulation tape
ARALDITE™

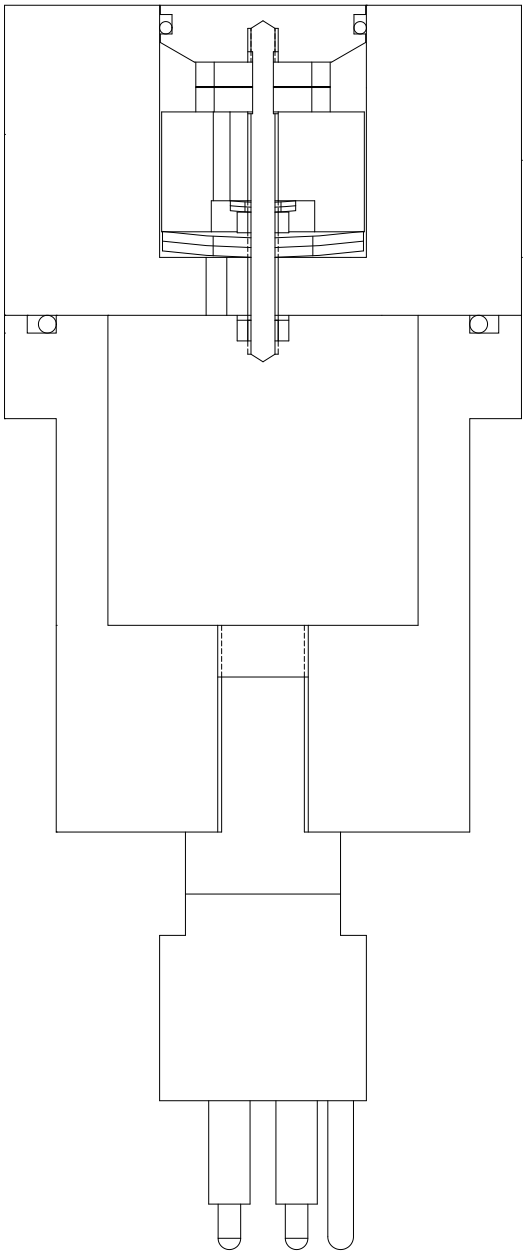

50 kHz TONPILZ TRANSDUCER ASSEMBLY (DRG. NO. T50k/1)	CROSS-SECTION VIEW
	SCALE: 1 to 1

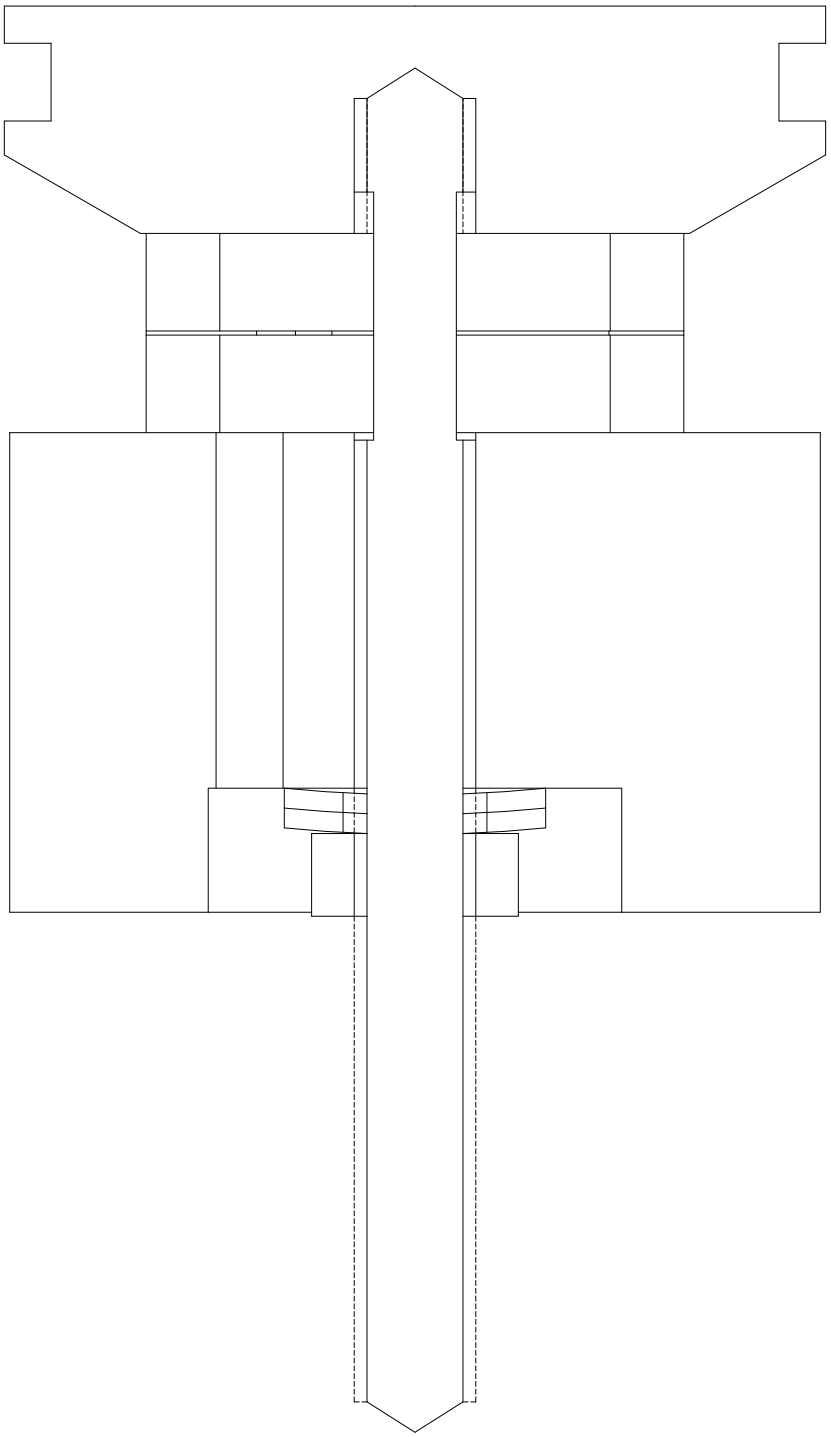

50 kHz TONPILZ TRANSDUCER ELEMENT (DRG. NO. T50k/2)	CROSS-SECTION VIEW
	SCALE: 4 to 1

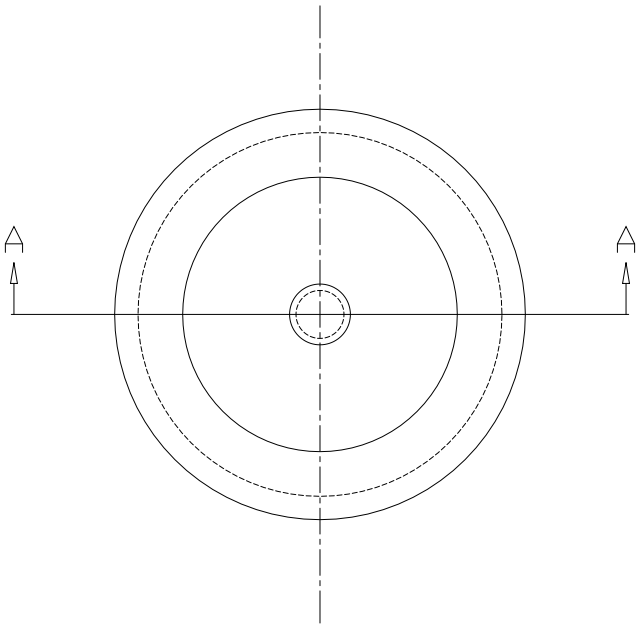

SECTION AA

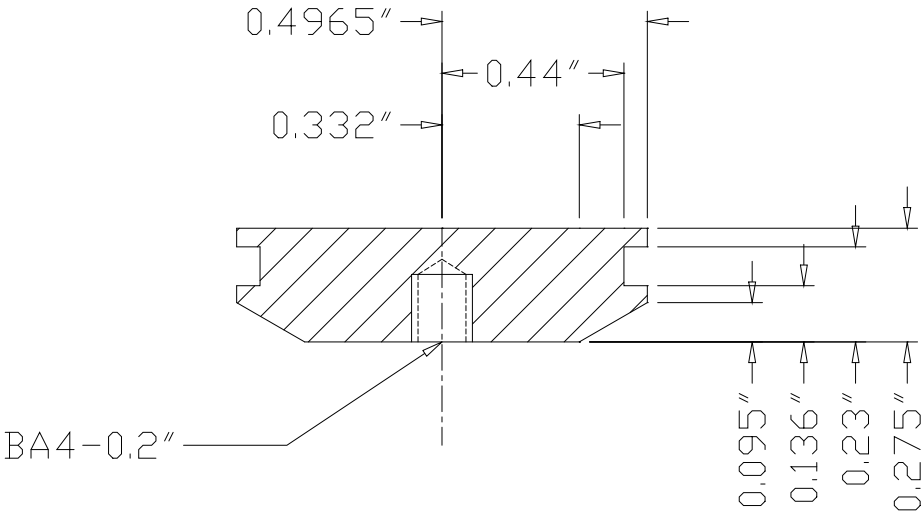

ALUMINIUM (HARD ANODIZED)

50 kHz TONPILZ TRANSDUCER HEAD (DRG. NO. T50k/3)	DIMENSIONS IN INCHES
	SCALE: 2 to 1

0.005″ BRASS SHIM

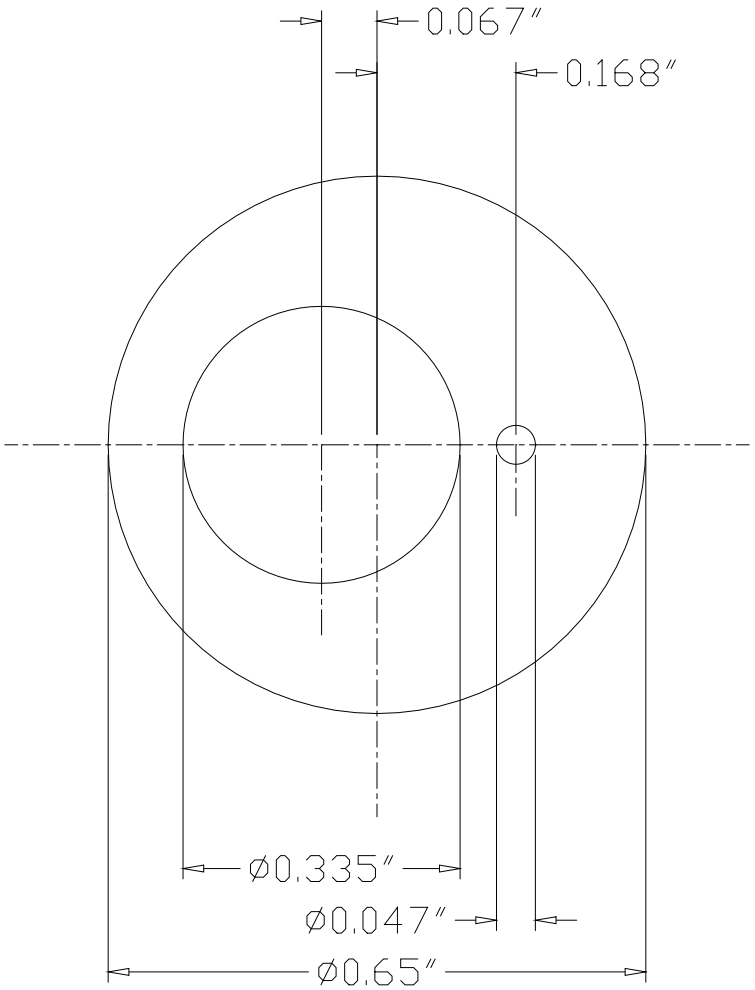

50 kHz TONPILZ TRANSDUCER	DIMENSIONS IN INCHES
SHIM (DRG. NO. T50k/4)	SCALE: 4 to 1

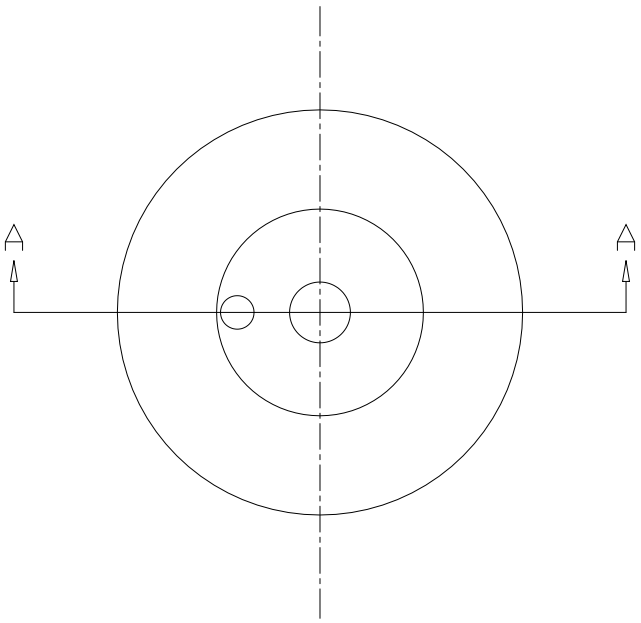

SECTION AA

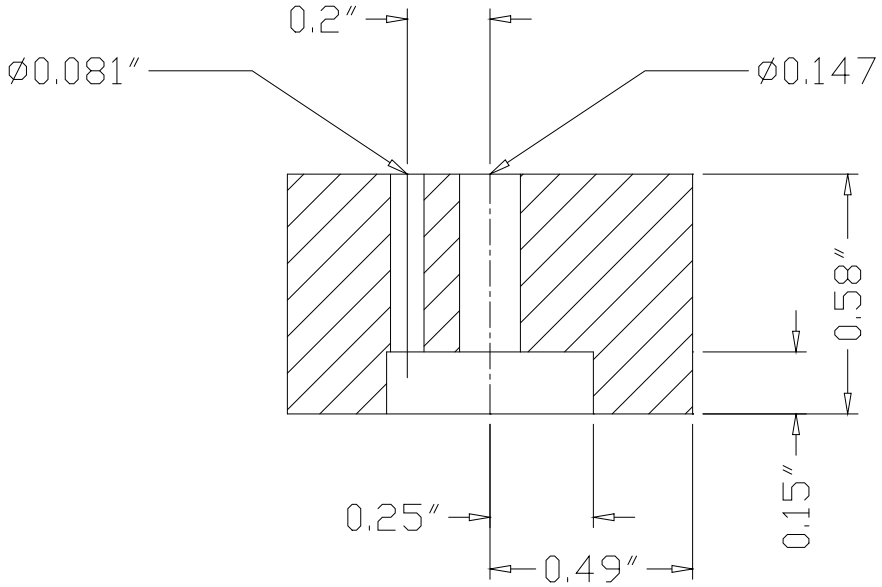

MILD STEEL

50 kHz TONPILZ TRANSDUCER	DIMENSIONS IN INCHES
TAIL (DRG. NO. T50k/5)	SCALE: 2 to 1

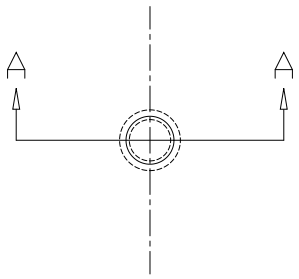

SECTION AA

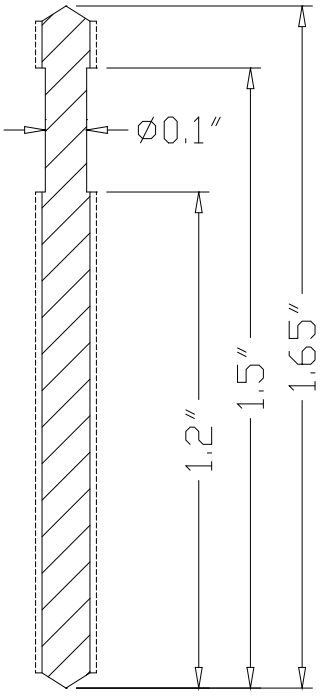

4BA STAINLESS STEEL STUDDING

50 kHz TONPILZ TRANSDUCER	DIMENSIONS IN INCHES
STUD (DRG. NO. T50k/6)	SCALE: 2 to 1

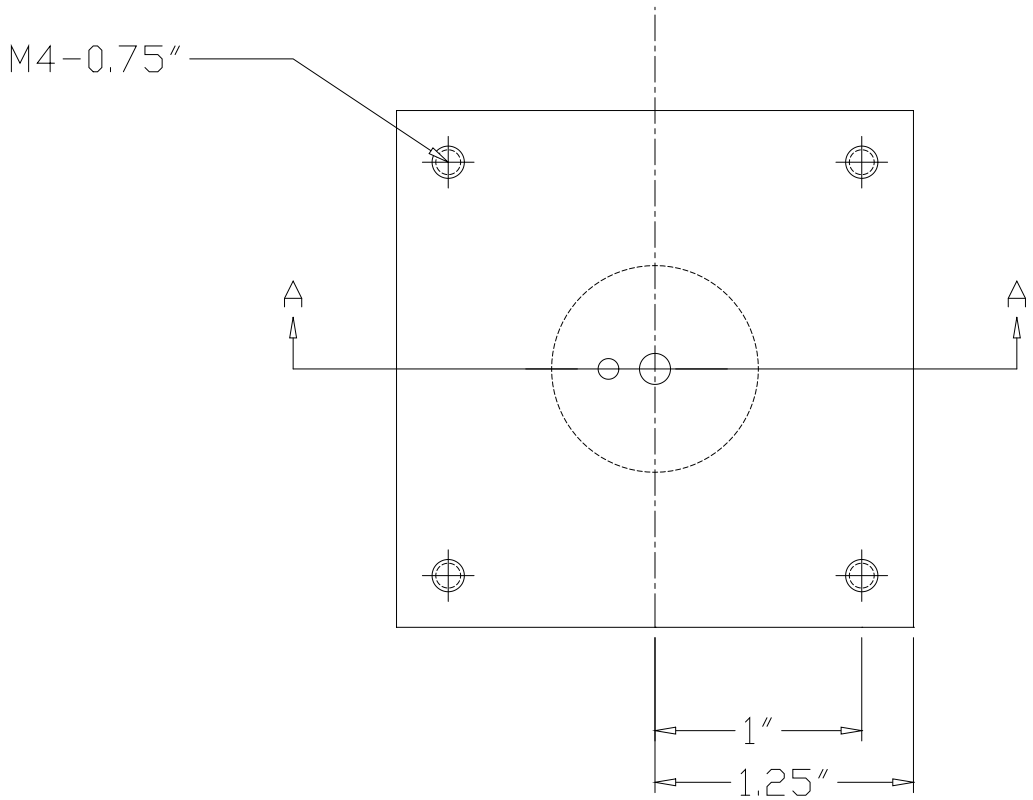

SECTION AA

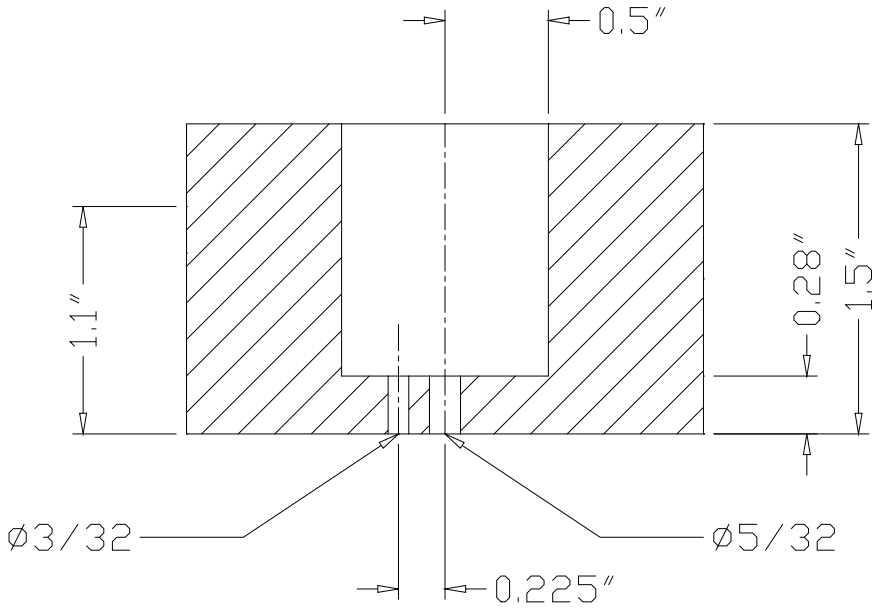

ALUMINIUM (HARD ANODIZED)

50 kHz TONPILZ TRANSDUCER MOUNTING (DRG. NO. T50k/7)	DIMENSIONS AS STATED SCALE: 1 TO 1

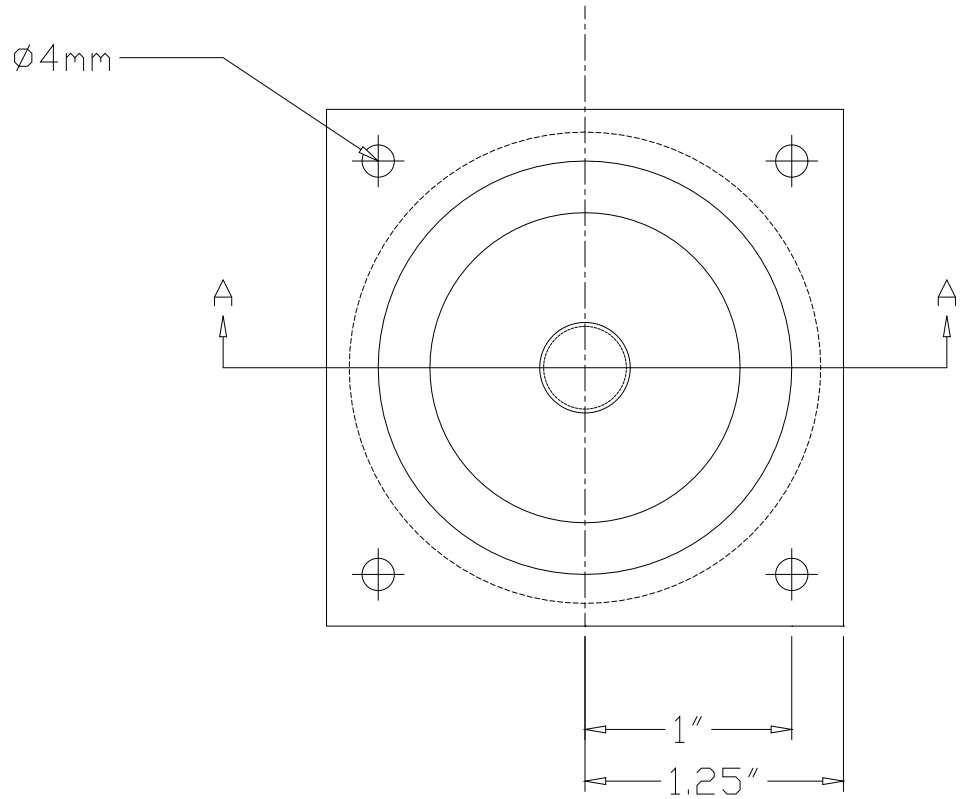

SECTION AA

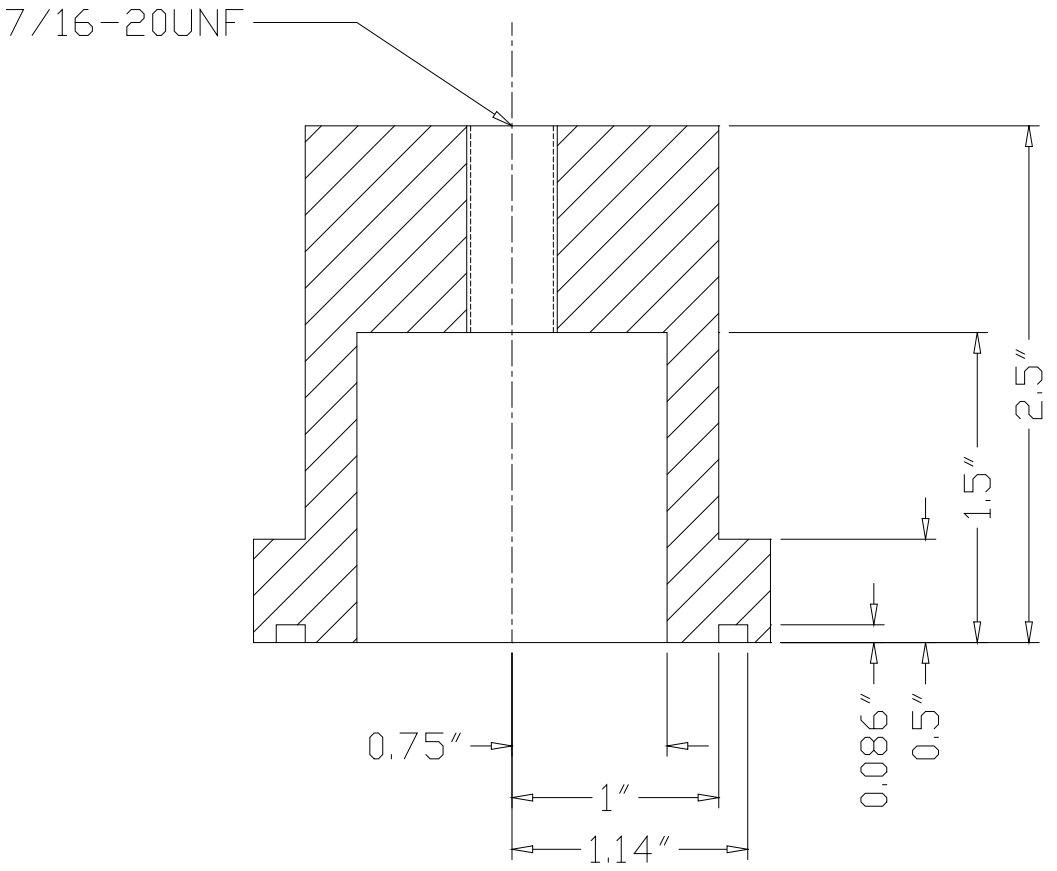

ALUMINIUM (HARD ANODIZED)

50 kHz TONPILZ TRANSDUCER	DIMENSIONS AS STATED
COVER (DRG. NO. T50k/8)	SCALE: 1 to 1

Appendix C

CIRCUIT DIAGRAMS

C.1 Resistance to voltage converter.

Schematic diagrams of these circuits follows.

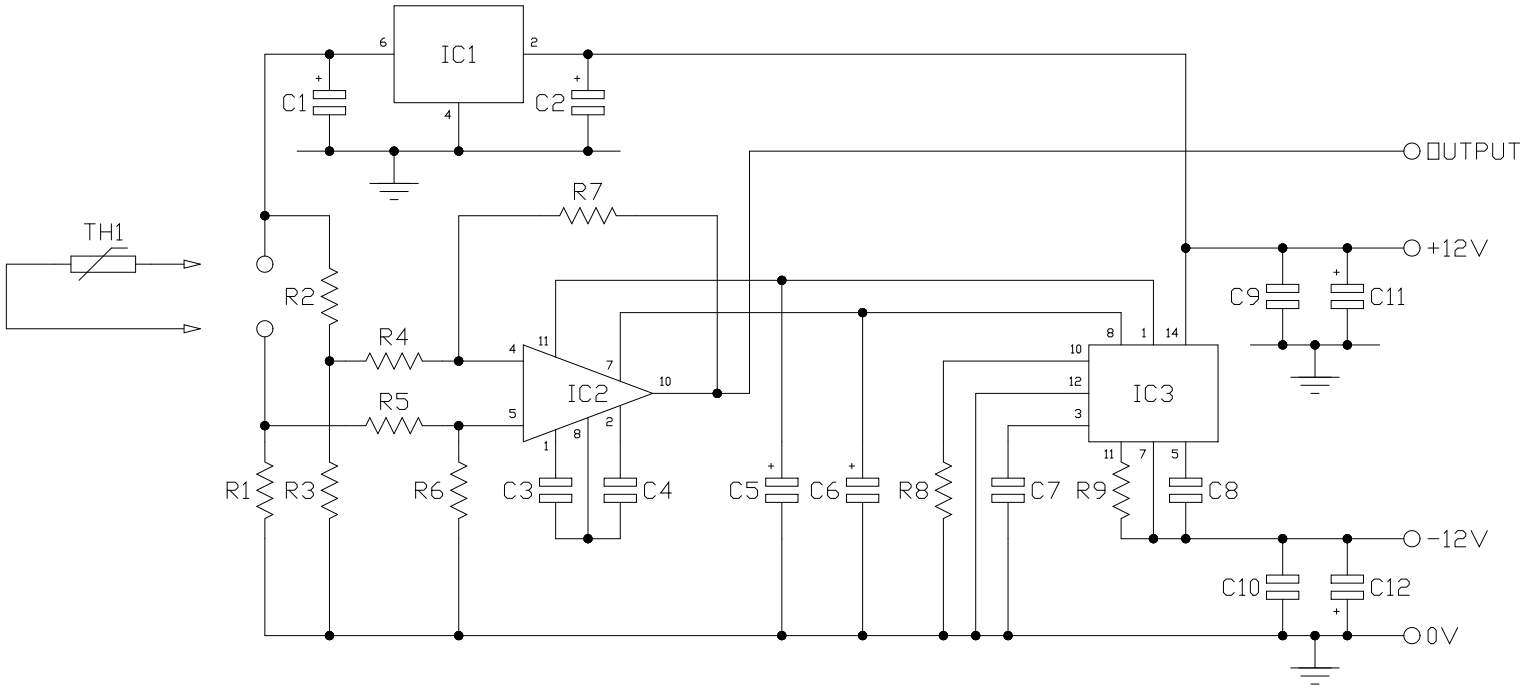

RESISTORS

R1,R2,R3	32k4 METAL FILM 0.1%
R4,R5,R6,R7	100k METAL FILM 0.1%
R8	15k METAL FILM 1%
R9	71k5 METAL FILM 0.1%

THERMISTOR

TH1	N.T.C. 10k @ 25°C

CAPACITORS

C1,C2,C5,C6	4u7F TANTALUM 16V
C3,C4	0u1F MYLAR
C7,C8,C9,C10	1000pF CERAMIC
C11,C12	470uF ELECTROLYTIC 16V

INTEGRATED CIRCUITS

IC1	REF195GP
IC2	RC4194N
IC3	TSC7650A

Appendix D

LETO FILE FORMATS

D.1 Control Files

The input and output data files used by the three applications that make up LETO are specified in control files. The heat sources module, heat conduction module, and graphics display module use control files with file extensions ".HS1", ".HC1", and ".FE1" respectively. Typically these files consist of keyword and filename pairs, where the keyword identifies the type of data contained in the file. Comments can also be included in LETO control files. Both C and C++ style comments are supported. The traditional C comment format, where /* begins a comment and */ ends it, can be used to write multi-line comments. The C++ comment token is the double-slash (//) sequence. Whenever the sequence appears everything to the end of the line is a comment. Each application requires a mandatory set of data files. In additional, some optional files may also be used. The mandatory and optional data file that may be included in the control files are listed below.

Heat sources application control file

Mandatory input files:
COORDINATES, ELEMENTS, MATERIALS, DISPLACEMENTS, and POTENTIALS.

Mandatory output files:
HEATSOURCES.

Heat conduction application control file

Mandatory input files:
COORDINATES, ELEMENTS, and MATERIALS.

Optional input files:

KNOWNTEMPERATURES, HEATSOURCES, and/or FACES plus BOUNDARYINFLOWS and/or BOUNDARYOUTFLOWS.

Mandatory output files:

TEMPERATURES.

Graphics display application control file

Mandatory input files:

COORDINATES and ELEMENTS.

Optional input files:

TEMPERATURES.

D.2 Data Files

The format of the data files that the various keywords refer to is as follows.

COORDINATES

Header line	<total number of nodes>	integer value
	<number of solution nodes>	integer value
	<rotational symmetry>	integer value
	<mirror symmetry in the yz-plane>	Boolean value
	<mirror symmetry in the xz-plane>	Boolean value
	<mirror symmetry in the xy-plane>	Boolean value
Other lines	<x co-ordinate>	real value
	<y co-ordinate>	real value
	<z co-ordinate>	real value

DISPLACEMENTS & POTENTIALS

Header line	< number of solution nodes >	integer value
	<excitation frequency>	real value
	<peak voltage>	complex value
	<peak current>	complex value
Other lines	<node number>	integer value
	<x displacement>	complex value
	<y displacement>	complex value
	<z displacement>	complex value
	<potential>	complex value

TEMPERATURES

Header line	<number of solution nodes>	integer value
	<excitation frequency>	real value
	<peak voltage>	complex value
	<peak current>	complex value
Other lines	<temperature>	real value

ELEMENTS

Header line	<number of elements>	integer value
	<nodes per element>	integer value
	<rotational symmetry>	integer value
	<mirror symmetry in the yz-plane>	Boolean value
	<mirror symmetry in the xz-plane>	Boolean value
	<mirror symmetry in the xy-plane>	Boolean value
Other lines	<node number list (1…n)>	integer list

FACES

Header line	<number of elements>	integer value
	<nodes per element>	integer value
	<rotational symmetry>	integer value
	<mirror symmetry in the yz-plane>	Boolean value
	<mirror symmetry in the xz-plane>	Boolean value
	<mirror symmetry in the xy-plane>	Boolean value
Other lines	<node number list (1…n)>	integer list

HEATSOURCES

Header line	<number of elements>	integer value
	<excitation frequency>	real value
	<peak voltage>	complex value
	<peak current>	complex value
Other lines	<mechanical dissipation>	real value
	<piezoelectric dissipation>	real value
	<dielectric dissipation>	real value
	<volume of element>	real value
	<power dissipation per unit volume>	real value

MATERIALS

Header line	<number of elements>	integer value
Other lines	<material number>	integer value (0 to 9 reserved for piezoelectric materials)
	<polarisation direction>	integer value (only applicable to piezoelectric materials: (-1)—negative polarisation along the z-axis, 1—positive polarisation along the z-axis, 0—radial polarisation about the z-axis)

KNOWNTEMPERATURES

Lines	<node number>	integer value
	<temperature>	real value

BOUNDARYINFLOWS

Lines	<face number>	integer value
	<heat flux>	real value

BOUNDARYOUTFLOWS

Lines	<face number>	integer value
	<heat-transfer coefficient>	real value
	<fluid temperature>	real value

Material properties files are not directly referred to in LETO control files. They are indirectly referenced through a MATERIALS file which defines the material to element mapping. To enable this mapping, each material properties file is assigned a unique filename of the form "matpr???.dat" where the question marks are replaced by a unique number which is used to represent the material. Numbers in the range 0 to 9 are reserved for piezoelectric materials. The structure of these files is given below.

MATERIALPROPERTIES

<material name>	text (maximum of 80 characters)
<density>	real value
<elastic matrix>	complex 6x6 matrix
<piezoelectric matrix>	complex 6x3 matrix (only applicable to piezoelectric materials)
<dielectric matrix>	complex 3x3 matrix (only applicable to piezoelectric materials)
<conductivity matrix>	real 3x3 matrix

Appendix E

PUBLICATIONS

D. T. I. Francis, J. A. Ahmad, C. Bayliss, and R. F. W. Coates, 'Finite and Boundary Element Modelling of Class III Flextensional Transducers for Ocean Acoustic Tomography', in *Proc. Underwater Acoustics*, L. Bjørnø, ed., (European Commission, 1994), Vol. 1, 512-520.

D. T. I. Francis, C. Bayliss, J. A. Ahmad, and R. F. W. Coates, 'The Development of a Low Frequency Barrel-Stave Transducer for Tomographic Applications Using Finite Element and Boundary Element Modelling', *Proc. OCEANS '94*, 371-376, (1994).